NEW INFRARED TOOLS TO MEASURE THE SOLAR CORONAL MAGNETIC FIELD

A THESIS SUBMITTED TO THE GRADUATE DIVISION OF THE UNIVERSITY OF HAWAIʻI AT MĀNOA IN PARTIAL FULFILLMENT OF THE REQUIREMENTS FOR THE DEGREE OF

DOCTOR OF PHILOSOPHY

IN

ASTRONOMY

AUGUST 2017

By

Gabriel Ionel Dima

Thesis Committee:

Jeffrey Kuhn, Chairperson
Svetlana Berdyugina
Veronica Bindi
Rolf Kudritzki
Shadia Habbal

Keywords: solar corona, polarimetry, infrared, Hanle effect

ACKNOWLEDGMENTS

I've been in graduate school for eight years now and the number of people that have helped or touched my life is staggering. Writing this part of my dissertation has actually been the most difficult emotionally.

I am grateful for all the support I have received over these past eight years from the faculty and staff as a graduate student at the Institute for Astronomy both in Manoa and on Maui. I am especially grateful to Ilia Roussev and his wife Elena who took care of me like I was family. Equally grateful I am to Jeff Kuhn who convinced me to change direction in my thesis and I ended up learning a lot about instrumentation, data collection and analysis. Or at least I learned enough to realize just how much more there is to know!

I want to thank my family, especially my mother and stepfather, who supported me morally and financially through all these years and who always believed I had what it took to be a scientist. I am also grateful to my friend Joanna who also supported me and moved with me to Maui so that I could collect the data I needed for my dissertation.

Another big thanks goes to my friend Jabran Zahid who brought me into his own research and showed me how fun it is to pursue an idea and collaborate closely with someone.

I want to give a special thanks to all my committee members who put up with my seemingly endless emails trying to coordinate signatures. A big thanks goes to Rolf and Svetlana who helped put my mind at ease about the future right when I needed it the most. Also I want to thank Shadia for agreeing to be on my committee on short notice and Veronica for taking time from her travels to attend the meetings and defense. I also want to thank and remember John Madey, who served on my committee until his passing in 2016, for offering useful feedback on my early dissertation proposals.

Finally I wanted to say thank you to my grandparents who passed away during my PhD. They taught me mathematics and without them I would categorically not be where I am today.

ABSTRACT

Although the Sun is by far the closest star we can study, we are just beginning to understand more about the processes taking place both inside and outside its photosphere. Magnetic fields likely play a significant part in many of the dynamic processes observed in the solar corona, but we still lack the ability to routinely measure the magnetic fields in the corona directly. To address this problem new diagnostic tools based on coronal emission lines and their polarized properties are necessary. During my dissertation work I explored a new way to measure weak ($<$10G) coronal magnetic fields using linearly polarized infrared emission lines. A theoretical model was developed to invert linearly polarized measurements of simultaneous forbidden/permitted coronal emission lines and obtain a solution for the vector magnetic field. This was complemented by ground-based measurements using the SOLARC telescope (Haleakalā, Maui) as well as analysis of multi-line observations obtained during the March 29 2006 total solar eclipse. The main focus was analyzing linear polarization from three coronal emission lines: FeXIII 1075nm, SiX 1430nm and HeI 1083nm. These lines were observed both during the March 29 2006 total solar eclipse and using SOLARC. While the FeXIII1075 is routinely used as a diagnostic tool of the solar corona, the potential for the SiX1430 and HeI1083 lines as coronal diagnostic tools have not been explored observationally before. Based on linearly polarized observations of these lines we obtained several important results: the emission line ratio FeXIII1075/SiX1430 can be used as a temperature diagnostic and as a way to discriminate between coronal models; discovery of unexpectedly large polarization amplitudes for the SiX1430 hinting at a need to review our understanding of how this line is formed; confirmation of the presence of diffuse polarized HeI1083 emission in the solar corona with polarization orientation offset from tangential to the solar limb. The results reported here, and hands-on experience with telescope operation during the project, have shown a decrease in sensitivity of measurements using SOLARC which needs to be addressed both in terms of upgrading the camera and mirror system and the data reduction pipeline.

TABLE OF CONTENTS

LIST OF TABLES

LIST OF FIGURES

CHAPTER 1
INTRODUCTION

From a scientific standpoint, the Sun is unique because it is the only star close enough to Earth that features on its surface can be resolved. Studying it has led to fundamental scientific discoveries in nuclear physics, general relativity and particle physics. It represents a huge open air laboratory to study extreme physics difficult to simulate on Earth and as detection capabilities improve more is being revealed about the nature and structure of our closest star.

A lot of emphasis in modern solar physics is placed on studying the dynamic activity that takes place in the outer atmosphere of the Sun called the solar corona (Figure 1.1). One reason for this emphasis is that this activity has measurable impacts in the near-Earth environment. As we expand further into space and away from the Earth's protective magnetic field we are exposed more and more to the effects of Sun-driven space weather. The magnetic field is theorized to play a key role in coronal dynamics but we still have incomplete knowledge of its origin and evolution (Mackay & Yeates 2012).

The leading theory for the origin of the solar magnetic field is dynamo action in the convection region (Charbonneau 2014). As the field is produced differential rotation in different solar layers and latitudes causes the field to rise towards the solar surface. Bundles of strong magnetic field (B$\sim$1000G) reaching the photosphere suppress convection and produce dimmer (cooler) regions called sunspots which have been observed for hundred of years. The first evidence that the Sun is magnetized was originally discovered in such regions (Hale 1908) because the radially oriented magnetic fields induce strong Zeeman splitting in photospheric absorption lines (see Figure 1.2 for a dramatic example of this effect). As spatial resolution and sensitivity of measurements increased it became obvious that magnetic fields are not limited to sunspots but are present over the entire surface of the Sun and may actually play a larger role in coronal processes than was previously understood (Centeno et al. 2007; Gošić et al. 2014). Systematic mapping of the radial photospheric magnetic fields were started in the 1950s (Babcock & Babcock 1952; Babcock 1959) and continued through the intervening 60 years. In the last decade, photospheric vector magnetic field

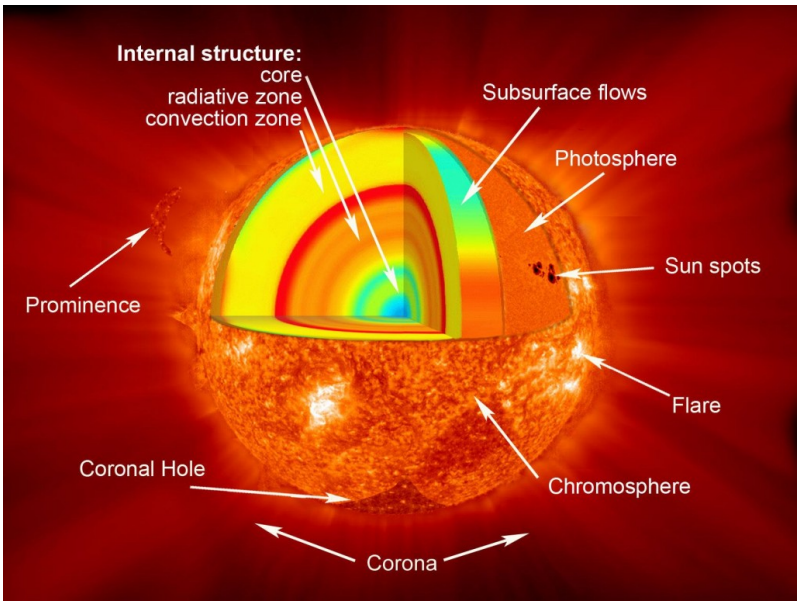

Figure 1.1: Sketch showing the principal components of the solar interior and atmosphere. Most of the geo-effective solar activity takes place in the corona, whereas our current ability to measure magnetic fields routinely is limited to just the narrow photospheric layer of the Sun. (source: NASA Solar Ultraviolet Magnetograph Investigation).

measurements have become routine with satellite missions like Hinode (Kosugi2007) and SDO (Solar Dynamic Observatory, Pesnell et al. 2012) as well as ground-based measurements using SOLIS (Synoptic Optical Long-Term Investigations of the Sun, Keller et al. 2003).

Taking advantage of the wealth of photospheric observations a large number of coronal simulations have been developed: potential field, linear and non-linear force free, and magnetohydrodynamic (MHD) (reviews by Mackay & Yeates 2012; Wiegelmann et al. 2015). Many of them have achieved a remarkable level of success in explaining a number of phenomena, e.g., coronal mass ejections (Forbes et al. 2006; Chen 2011; Lionello et al. 2013), flares (Benz 2008), prominences (Labrosse et al. 2010) and coronal holes (Downs et al. 2012). However, they remain largely unconstrained by real-time coronal magnetic observations. Therefore, a number of problems remain unresolved. For example, understanding the way in which free energy is stored in the corona prior to eruptions is largely unknown (Judge et al. 2013). To distinguish between the aforementioned models, it is now critical to place more constraints on the coronal magnetic field. Developing a method to directly measure vector magnetic fields will significantly improve understanding of heating and dynamics in

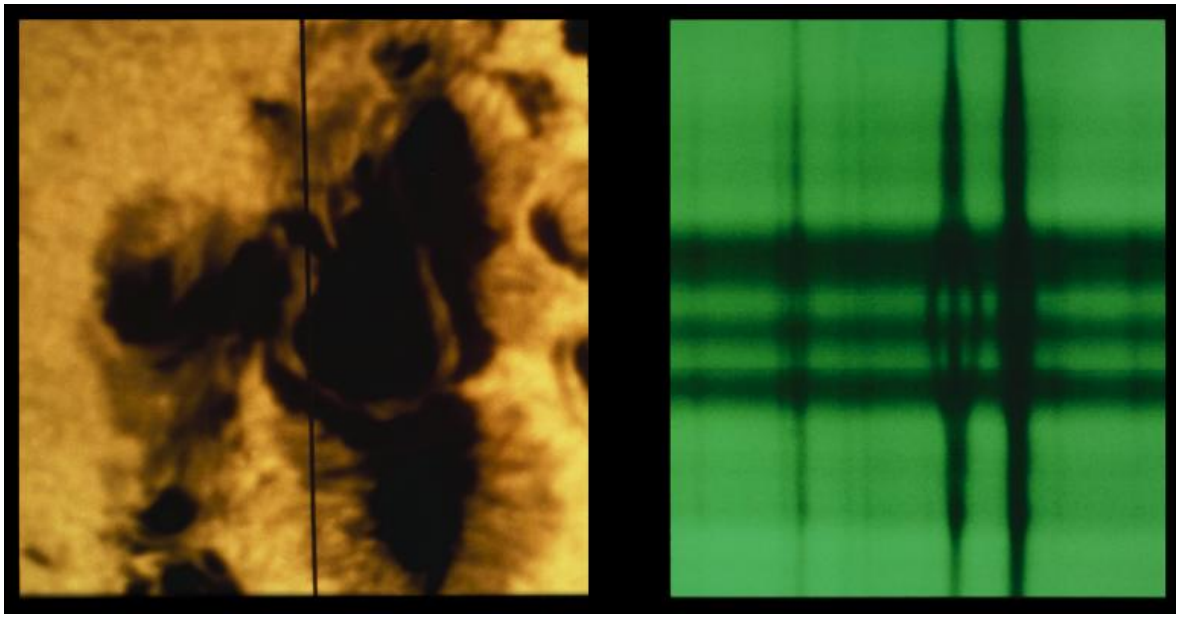

Figure 1.2: Images showing an active region observed in white light on the photosphere (left) and the slit-spectra obtained near the FeI 525nm absorption line showing Zeeman splitting due to the strong radial fields (4100G) inside the active region (dark in left image). Reproduced from: https://www.noao.edu/image_gallery/html/im0404.html

the Sun's atmosphere.

The ever higher resolution images of the corona reveal how rich and varied the plasma behavior really is. Once the 4m Daniel K. Inouye Solar Telescope (DKIST) telescope begins observations in 2020, it will most likely reveal new aspects of the corona. Now is a good time to prepare new tools and methods that can be applied to the type of details that observations using DKIST will provide.

1.1 Background

Optical measurements of the coronal magnetic field are complicated because the polarization signals are generally weak and because a volume of coronal plasma along the line-of-sight (LOS) contributes to each measurement. The main limitation lies in the difficulty of observing the weak circularly polarized emission signals that are required for Zeeman magnetometry. A better approach based on permitted-forbidden line pairs and the Hanle effect has significant advantages:

- It only relies on measuring linearly polarized emission signals which are typically two (or more)

orders of magnitude larger than circularly polarized emission lines.

- Uses emission lines at longer infrared (IR) wavelengths where we greatly benefit from reduced scattered light from the Earth's atmosphere and increased sensitivity.

- This new approach can be developed into a powerful method that can be applied directly to high spatial resolution measurements that first light IR instrument(s) on DKIST will bring.

The scope of the present research is intrinsically tied to the new approach for measuring the coronal magnetic field as underlined above. The key concepts are briefly introduced in the sections below. More background information is given throughout Chapters 2 and 3 that deal with specific topics within the aims of this research project.

Coronal magnetic field measurements

Measuring the coronal vector magnetic field is still a major challenge because of the intrinsic weakness of the field (<10G) and the faint brightness of coronal emission compared to the solar disc ($\sim 10^{-6}$B$_\odot$) Magnetic fields in the solar photosphere were first measured early in the 20th Century (Hale 1908). Throughout the following century, the quality of such measurements was improved culminating with the launch of the Solar Dynamics Observatory (SDO) satellite in 2010 (Pesnell et al. 2012). Among other observations SDO maps the vector magnetic field over a large fraction of the solar photosphere using the Helioseismic and Magnetic Imager (MHI) instrument (Schou et al. 2012). In comparison, attempts to measure the coronal magnetic field have not progressed as fast. This is because the photosphere and corona are in fundamentally different plasma regimes, with the former characterized by dense relatively cool plasma (T$\sim$5,700K, $n_e \sim 10^{14}$cm^{-3}), while the latter is very hot and tenuous (T$\sim$1,500,000K, $n_e \sim 10^7 - 10^9$cm^{-3}). Furthermore, the theory and few measurements of the coronal magnetic field revealed that it is very weak (<10G) over most of the volume apart from just above active regions (Kuhn 1995; Lin et al. 2004). Techniques presently used for measuring the coronal magnetic fields are summarized here.

1. *Techniques based on Zeeman effect in coronal forbidden lines*

The Zeeman effect refers to the splitting of degenerate sub-states in the upper level of anatomic line

transition due to the presence of a magnetic field (e.g. Landi Degl'Innocenti & Landolfi 2004). This causes a single line profile to split into several components with orthogonal circular polarization states (Figure 1.2). Magnetometry based on the longitudinal Zeeman effect measures the separation between the components to constrain the strength of the field along the line of sight of the measurement.

Near-IR coronal forbidden emission lines (FELs) are important diagnostics of the coronal plasma and magnetic fields because they allow for sensitive measurements of longitudinal field flux density of a few Gauss by measuring circular polarization (Judge 1998). Although this method has great potential for characterizing the coronal magnetic field, it is difficult to apply as it requires very sensitive polarimetric measurements, i.e., 10^{-4} circular polarization amplitude for a magnetic flux density of a few Gauss (Lin et al. 2000).

2. *Radio continuum polarization measurements*

In contrast to measurements based on the Zeeman effect, radio polarization measurements are specific to large scale estimates of the coronal field. Two types of techniques, gyroresonant and bremsstrahllung emission are developed, and they provide field strength information in different layers of the corona (Lee et al. 1997). Moreover, they are most sensitive to strong fields typically found in active regions. Other applications of radio magnetometry are measurements based on Faraday rotation of distant sources (Patzold et al. 1987), or Faraday rotation of polarized solar radiation (Alissandrakis & Chiuderi Drago 1995). However, such measurements always require a known background source of polarized radiation.

Strong magnetic fields, above 100G, present far below 1.5 $R_{\odot}$ can be detected using gyroresonance radiation in microwave and decametric wavelengths (White 2005). Shocks through the solar corona can cause type II radio bursts inducing band splitting that can be used to determine the ambient magnetic field along the path of the shocks propagating through the solar corona (Smerd et al. 1975; Cho et al. 2007).

Introduction to Forbidden/Permitted Hanle magnetic diagnostics

The Hanle effect describes a change in the polarization of atomically scattered optical radiation due to the presence of a magnetic field which splits atomic levels into 2J+1 magnetic sublevels (J is the total angular momentum) via the Zeeman effect. If sublevels of the upper transition are unevenly populated through their coupling to an anisotropic solar radiation field, then the emission line can be polarized. If the Zeeman splitting is comparable to the natural line-width (i.e., the Larmor frequency is smaller than, or comparable to the line spontaneous transition rate), quantum mechanically induced wavefunction interferences will modify the scattering polarization magnitude and rotate the polarization plane by an amount that depends on the field - this is the Hanle effect (Landi Degl'Innocenti & Landolfi 2004).

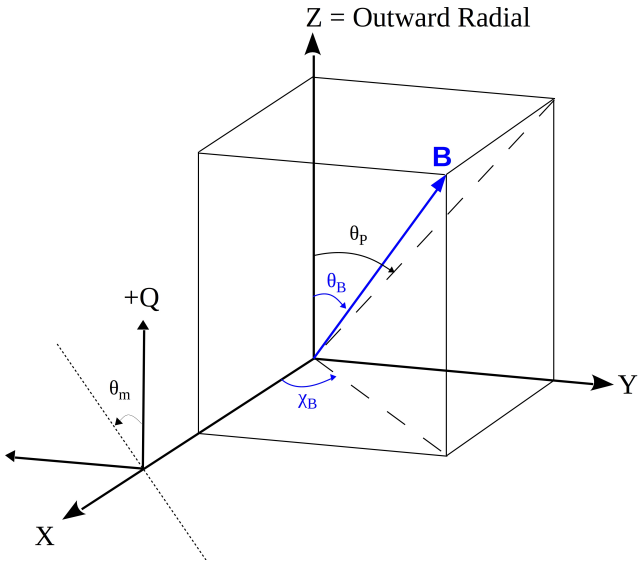

Figure 1.3: Geometry of the magnetic field located in the plane of the sky (corresponding to ZY plane). The +Z direction indicates the local outward radial direction. Therefore, moving around the solar limb corresponds to a rotation about the X axis, which is taken to coincide with the line of sight. The projected angle of the magnetic field on the plane of sky $\theta_{\rm P}$ is measured clockwise, while the angle of polarization $\theta_{\rm m}$ is measured counter-clockwise adhering to the common polarimetric convention. The reference direction for the polarization measurement is oriented along the outward radial direction (from Dima et al. 2016).

The coronal vector magnetic field at a point in the corona is uniquely described by the magnetic flux density $|\mathbf{B}| \equiv \mathrm{B}$, the inclination angle $\theta_{\rm B}$(with respect to the local outward solar radial direction)

and the azimuth angle χ_B in a plane perpendicular to the radial direction (Figure 3.1). For a scattering geometry where the emission takes place in the plane-of-sky (POS) we can freely choose the reference axis for the χ_B angle to coincide with the line of sight axis. In the unsaturated Hanle regime, when the atomic Larmor frequency is comparable to the inverse upper-level lifetime, the linear polarization of an emission line is sensitive to all three B-vector parameters, while in the saturated Hanle regime (when the Larmor frequency is much larger than the inverse lifetime) only the angles (θ_B, χ_B) influence the linear polarization. The B value at which the transition between the two regimes takes places is not a sharp value. In fact, a gradual loss of sensitivity takes place above the critical field strength B_H, which depends on the Lande factor g' and the lifetime τ' of the upper level:

$$B_H = \frac{\hbar}{\mu_B g' \tau'} \tag{1.1.1}$$

where μ_B is the Bohr magneton.

At typical coronal field strengths, coronal FELs are effectively in the saturated Hanle regime due to their large upper level lifetimes (House 1974). The critical field strength for such lines is around 10^{-4}G. Therefore, only the orientation of the field vector on the plane of the sky θ_P (Figure 3.1) can be constrained through linear polarization measurements of FELs. In contrast, emission lines in the unsaturated Hanle regime have linear polarization measurements which are sensitive to both the orientation and strength of the magnetic field vector. However, the effects on the linear polarization parameters Q and U are degenerate between orientation and strength so simply observing one linearly polarized emission line in the unsaturated Hanle regime still does not yield complete information about the magnetic field. The dependence of the two types of emission lines on magnetic field parameters can be visualized through Hanle diagrams that show how Stokes Q and U values change depending on the magnetic field (Figure 1.4). A true Hanle diagram for an unsaturated line would have to be three-dimensional because unsaturated Hanle emission lines are sensitive to both field strength B and orientation angles (θ_B, χ_B). Setting one of the angles constant (e.g. $\theta_B = 90°$) it is possible to visualize how the other two parameters (B,χ_B) influence the linear polarization parameters.

A powerful coronal field diagnostic follows from simultaneous measurements of the optical scat-

tering linear polarization of combined forbidden and permitted spectral lines. Early work on the possibility of using permitted lines with different Hanle sensitivity (Bommier et al. 1981) considered the HeI 587nm and HeI 1083nm lines. They used these lines for measuring prominence magnetic fields located in or very near the plane of the sky. Using linear polarization observations of the HeI D3 permitted line combined with forward calculations of field configurations (López Ariste & Casini 2003; Merenda et al. 2006) provided constraints on the magnetic field configurations of solar prominences.

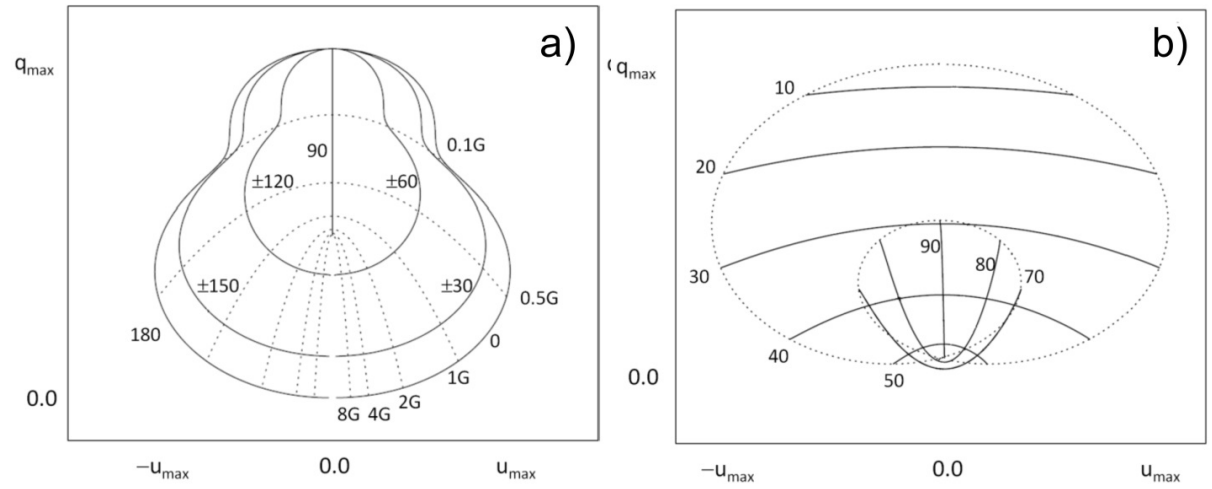

Figure 1.4: Hanle diagrams showing how unsaturated (a) and saturated (b) Stokes Q and U parameters vary depending on the magnetic field properties. For the unsaturated Hanle regime in (a) θ_B = 90° and solid lines correspond to constant azimuth χ_B angles as marked while constant magnetic field strengths are shown with dotted lines. In (b) lines of constant inclination (θ_B) angle are shown as solid lines while the azimuth (χ_B) varies between -90° to 90° from left to right along the solid lines. The dotted lines in (b) correspond to constant azimuth $\chi_B = \pm 90°$.

Neutral species in the corona are new diagnostics of coronal magnetic fields

Ultraviolet (UV) coronal lines, such as hydrogen Lyman (Ly) series lines, have the potential to measure the entire magnetic vector field because they are the most intense lines emitted in the solar corona (Bommier & Sahal-Brechot 1982; Raouafi et al. 2009; Vial & Chane-Yook 2016). The Hanle effect saturates in the Ly α, β, γ lines at 54G, 14G and 6G, respectively. Ly β and γ are suitable for coronal magnetism studies, while Ly α is more appropriate for the transition region since fields there are closer to the critical field strength. Currently the major drawback to UV polarimetry is

the fact that it is limited to space facilities (not implemented yet), or rocket experiments like the CLASP experiment (Ishikawa et al. 2011) which delivered just a single measurement.

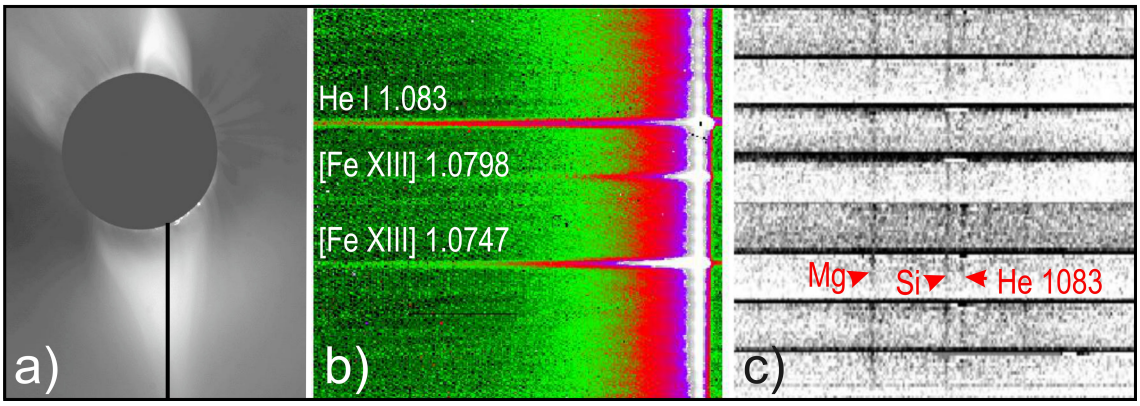

Figure 1.5: HeI 1083nm and nearby FeXIII lines observed in the solar corona. (a) White light corona image obtained during the 1994 eclipse with a long slit ($\sim$2000″) placed along a streamer. (b) Corresponding spectra showing nearly constant brightness in the HeI line, extending to several radii (from Kuhn et al. 1996). (c) Imaging spectropolarimetry data obtained with SOLARC showing constant polarized brightness (Stokes Q) in the HeI line (from Moise et al. 2010).

The second most abundant component of the corona and solar wind after hydrogen is helium. Observations of neutral helium usually happen in the cooler chromosphere (e.g. in prominences and spicules, Figure 1.1) and its optical 587.5 nm and infrared 1083 nm lines are employed to measure magnetic fields in these structures using the Zeeman or saturated Hanle effects (e.g. Centeno et al. 2008). Much higher in the corona around 9 $R_\odot$ neutral helium has been detected in the UV 58.4 nm line (Lallement 2002).

Most interestingly HeI emission at very low elongations from the solar limb has also been observed during eclipse condition in 1994 using the IR triplet transition at 1083 nm (Figure 1.5a,b; Kuhn et al. 1996). Daytime coronagraphic observations using the Scatter-free Observatory for Limb, Active Regions, and Coronae (SOLARC Kuhn et al. 2003) telescope revealed diffuse coronal HeI 1083 linearly polarized emission (Figure 1.5c; Kuhn et al. 2007; Moise et al. 2010). No neutral atomic or molecular species can survive for prolonged time under million-degree coronal conditions unless they are continuously supplied from external sources. If the lifetimes of these species in the corona are longer than their radiative lifetimes, they can scatter light from the solar photosphere

and, therefore, can be observed in polarized emission lines. Moise et al. (2010) explained the weak diffuse HeI emission as coming from neutral He atoms desorbed from circumsolar dust grains that become collisionally excited to the metastable ground triplet He state due to higher electron densities in coronal streamers. This model assumes that circumsolar dust has an inner radius between 2-4 $R_\odot$ which acts to neutralize solar wind ionized He. Past 2 $R_\odot$ the weak magnetic field ($<$0.1G) only rotates the HeI plane of polarization by $<10^\circ$ (Figure 3 in Dima et al. 2016). Such an effect can be tested through more careful measurements of the angle of polarization of the HeI 1083 emission line.

The presence of neutral helium in the solar corona at distances up to many solar radii and its successful detection through ground-based spectropolarimetric coronographic measurements opens a new window into solar coronal magnetism studies. The advantage of observing neutrals in the corona is that they are suitable for unsaturated Hanle effect measurements.

The IR HeI 1083 nm line has a significant advantage for coronal studies because the Sun radiates about 107 times more infrared photons (per wavelength interval) than it does in the UV. Furthermore, the near IR part of the solar spectrum is important for ground-based observations because virtually all spurious scattered-light noise sources in coronal observations decline with increasing wavelength (Kuhn et al. 2003). The light scattered by HeI in the corona is affected by the local magnetic field through the Hanle effect. Since the HeI 1083 nm line is a permitted transition (short radiative lifetime of the upper level), its Hanle sensitivity is just right for coronal magnetic fields around 0.1-8G.

This research gap was addressed by the present project both by theoretical and experimental studies as shown in Chapters 3 and 6.

1.2 Research objectives and thesis structure

The overarching goal of this project is to measure the weak coronal magnetic field using linearly polarized IR emission lines. To achieve this, both theoretical modelling and ground-based measurements were employed. The latter consists of analysing a set of eclipse observations as well as obtaining, processing and interpreting new observations with the SOLARC telescope located on

Haleakalā, Maui.

Specific objectives are:

- Develop a theoretical model to invert linearly polarized measurements of simultaneous saturated/unsaturated coronal emission lines and obtain the vector magnetic field.
- Begin monthly coronal observing program with SOLARC to achieve a set of measurements reliable for magnetic field analysis.
- Analyse the data using the inversion model and compare to magnetic field models from MHD simulations to distinguish between different simulations.

Chapter 2 outlines results from spectropolarimetric measurements obtained during the March 29, 2006 total solar eclipse over a wide field of view in the corona in the 1-2 μm spectral range. This spectral window includes both the forbidden FeXIII 1075 and SiX 1430 lines, as well as the permitted HeI 1083 line, giving a unique opportunity to study the polarization properties of these lines simultaneously. The chapter is prepared as a manuscript and presents an analysis of the data and offers an interpretation of the observations based on comparisons with forward integrated synthetic polarized observables from MHD models of the corona.

Chapter 3 is a published paper (Dima et al. 2016) detailing how concurrent linear polarization measurements of near-infrared forbidden and permitted lines together with Hanle effect models can be used to calculate the coronal vector magnetic field. In the unsaturated Hanle regime both the direction and strength of the magnetic field affect the linear polarization, while in the saturated regime the polarization is insensitive to the strength of the field. The relatively long radiative lifetimes of coronal forbidden atomic transitions implies that the emission lines are formed in the saturated Hanle regime and the linear polarization is insensitive to the strength of the field. By combining measurements of both forbidden and permitted lines, the direction and strength of the field can be obtained. For example, the SiX 1430 nm line shows strong linear polarization and has been observed in emission over a large field-of-view (out to elongations of $0.5R_{\odot}$). The paper describes an algorithm that combines linear polarization measurements of the SiX1430 nm forbidden line with linear polarization observations of the HeI 1083 nm permitted coronal line to obtain the

vector magnetic field. To illustrate the concept, the paper assumes that the emitting gas for both atomic transitions is located in the plane of the sky. The further development of this method and associated tools are considered a critical step toward interpreting the high spectral, spatial and temporal infrared spectro-polarimetric measurements that will be possible when the Daniel K. Inouye Solar Telescope (DKIST) is completed in 2020.

Chapter 4 is a technical review of the SOLARC facility, a 0.46m reflecting coronagraphic solar telescope located very near the top of Haleakalā(around an altitude of 3048m) on the island Maui. This telescope is particularly well suited for accurate spectropolarimetric measurements due to its off-axis unobscured optical system. The telescope itself is housed in a small dome attached to the Zodiacal Light building near the construction site for the new 4-m DKIST telescope.

Chapter 5 describes data reduction methods applied to spectropolarimetric observations specific to SOLARC spectrograph settings and designs adapted for this research. The topics addressed are: (1) Elimination of modal noise; (2) Dark and bias reduction; (3) Extracting individual spectra; (4) Flat-fielding; (5) Calculation of Stokes parameters from polarized spectra; and (6) Disc center calibration.

Chapter 6 deals with analysis of measurements obtained using the SOLARC telescope. Details of a typical observing day are given and analysis is performed for two representative sets of measurements of co-spatial emission lines. Having aquired measurements of HeI1083 and FeXIII1075 for two target regions we present an example Hanle inversion following the theoretical modelling outlined in Chapter 3.One of the target regions shows consistent HeI1083 measurements and the polarization observatons intersects the model grids generating reasonable solutions tentatively supporting the approach in Dima et al. (2016). Independent verification of such a measurement would open up an incredible opportunity to measure the coronal magnetic field using a new infrared diagnostic tool on larger datasets. This has great potential to discriminate among MHD models with different heating physics. In addition, an example of mismatch between measurement and model grids is explored and discussed. One day of measurements produced co-spatial measurements of FeXIII1075 and SiX1430 at multiple positions around the solar limb. Although work is still ongoing to infer line intensities from these meaurements, we discuss the observed correlation between polarization angles

for the two lines and the implications for better understanding the line-of-sight problem in coronal observations.

The last chapter in this thesis, **Chapter 7**, summarises the key findings of all work conducted as part of this project, and contains a number of suggestions for potential future research directions.

BIBLIOGRAPHY

Alissandrakis, C. A., & Chiuderi Drago, F. 1995, Sol. Phys., 160, 171

Babcock, H. W., & Babcock, H. D. 1952, PASP, 64, 282

Babcock, H. D. 1959, ApJ, 130, 364

Benz, A. O. 2008, Living Reviews in Solar Physics, 5, 1

Bommier, V., Sahal-Brechot, S., & Leroy, J. L. 1981, A&A, 100, 231

Bommier, V., & Sahal-Brechot, S. 1982, Sol. Phys., 78, 157

Centeno, R., Socas-Navarro, H., Lites, B., et al. 2007, ApJ, 666, L137

Centeno, R., Trujillo Bueno, J., Uitenbroek, H., & Collados, M. 2008, ApJ, 677, 742-750

Charbonneau, P. 2014, ARA&A, 52, 251

Chen, P. F. 2011, Living Reviews in Solar Physics, 8, 1

Cho, K.-S., Lee, J., Gary, D. E., Moon, Y.-J., & Park, Y. D. 2007, ApJ, 665, 799

Dima, G., Kuhn, J., & Berdyugina, S. 2016, Frontiers in Astronomy and Space Sciences, 3, 13

Downs, C., Roussev, I. I., van der Holst, B., Lugaz, N., & Sokolov, I. V. 2012, ApJ, 750, 134

Forbes, T. G., Linker, J. A., Chen, J., et al. 2006, Space Sci. Rev., 123, 251

Gošić, M., Bellot Rubio, L. R., Orozco Suárez, D., Katsukawa, Y., & del Toro Iniesta, J. C. 2014, ApJ, 797, 49

Hale, G. E. 1908, ApJ, 28, 315

House, L. L. 1974, PASP, 86, 490

Ishikawa, R., Bando, T., Fujimura, D., et al. 2011, Solar Polarization 6, 437, 287

Judge, P. G. 1998, ApJ, 500, 1009

Judge, P. G., Habbal, S., & Landi, E. 2013, Sol. Phys., 288, 467

Keller, C. U., Harvey, J. W., & Giampapa, M. S. 2003, Proc. SPIE, 4853, 194

Kuhn, J. R. 1995, Infrared tools for solar astrophysics: What's next?, 89

Kuhn, J. R., Penn, M. J., & Mann, I. 1996, ApJ, 456, L67

Kuhn, J. R., Coulter, R., Lin, H., & Mickey, D. L. 2003, Proc. SPIE, 4853, 318

Kuhn, J. R., Arnaud, J., Jaeggli, S., Lin, H., & Moise, E. 2007, ApJ, 667, L203

Kosugi, T., Matsuzaki, K., Sakao, T., et al. 2007, Sol. Phys., 243, 3

Labrosse, N., Heinzel, P., Vial, J.-C., et al. 2010, Space Sci. Rev., 151, 243

Lallement, R. 2002, The Century of Space Science, Volume I, 1191

Landi Degl'Innocenti, E., & Landolfi, M. 2004, Astrophysics and Space Science Library, 307

Lionello, R., Downs, C., Linker, J. A., et al. 2013, ApJ, 777, 76

Lee, J., White, S. M., Gopalswamy, N., & Kundu, M. R. 1997, Sol. Phys., 174, 175

Lin, H., Penn, M. J., & Tomczyk, S. 2000, ApJ, 541, L83

Lin, H., Kuhn, J. R., & Coulter, R. 2004, ApJ, 613, L177

López Ariste, A., & Casini, R. 2003, ApJ, 582, L51

Mackay, D. H., & Yeates, A. R. 2012, Living Reviews in Solar Physics, 9, 6

Merenda, L., Trujillo Bueno, J., Landi Degl'Innocenti, E., & Collados, M. 2006, ApJ, 642, 554

Michalek, G., Gopalswamy, N., & Yashiro, S. 2007, Sol. Phys., 246, 399

Moise, E., Raymond, J., & Kuhn, J. R. 2010, ApJ, 722, 1411

Patzold, M., Bird, M. K., Volland, H., et al. 1987, Sol. Phys., 109, 91

Pesnell, W. D., Thompson, B. J., & Chamberlin, P. C. 2012, Sol. Phys., 275, 3

Raouafi, N.-E., Solanki, S. K., & Wiegelmann, T. 2009, Solar Polarization 5: In Honor of Jan Stenflo, 405, 429

Schou, J., Scherrer, P. H., Bush, R. I., et al. 2012, Sol. Phys., 275, 229

Smerd, S. F., Sheridan, K. V., & Stewart, R. T. 1975, Astrophys. Lett., 16, 23

Steenburgh, R. A., Biesecker, D. A., & Millward, G. H. 2014, Sol. Phys., 289, 675

Vial, J.-C., & Chane-Yook, M. 2016, Sol. Phys., 291, 3549

Wiegelmann, T., Petrie, G. J. D., & Riley, P. 2015, Space Sci. Rev.,

White, S. M. 2005, Chromospheric and Coronal Magnetic Fields, 596, 10.1

@mss @mss

CHAPTER 2
USING A NEW INFRARED SIX CORONAL EMISSION LINE FOR DISCRIMINATING BETWEEN MAGNETOHYDRODYNAMIC MODELS OF THE SOLAR CORONA DURING THE 2006 SOLAR ECLIPSE

ABSTRACT

The data analysis is based on linearly polarized infrared observations over the 1-2 μm range obtained during the 2006 total solar eclipse by a team of researchers including Jeffrey Kuhn and Shadia Habbal who form my dissertion committee. The observations covered a 6×6 $R_\odot$field of view in the solar corona and were obtained using a fiber-based spectograph. The data yielded linearly polarized measurements of the FeXIII 1.075 μm, HeI 1.083 μm, and for the first time SiX 1.430 μm emission lines. To interpret the measurements, we used forward integrated synthetic emission from two magnetohydrodynamic models for the same Carrington rotation with different heating functions and magnetic boundary conditions. We found that the FeXIII 1.075/SiX 1.430 emission ratio can be used as a temperature diagnostic for the solar corona and is consistent with coronal material at a temperature around 1.5 MK. This observation together with the radial variation of the continuum polarization amplitude was used to discriminate between the two coronal models. The observed polarized amplitudes for the SiX 1.430 μm line are found to be on average 5% higher than the predicted values from available atomic models for the line. This discrepancy indicates a need for a closer look at some of the model assumptions for the collisional coefficients, as well as new polarized observations of the line to rule out any unknown systematic effect in the present data. One of fibers located at 1.5 $R_\odot$ measured a HeI 1.083 μm intensity signal consistent with previous eclipse measurements around 5×10^{-7} $B_\odot$. However, given the nature of the observations it is not possible to completely rule out contamination with emission from prominence material not obscured by the lunar limb.

2.1 Introduction

The observed dynamic behavior of the Sun is strongly influenced by the solar magnetic field, which originates inside the Sun, rises through the photosphere and finally expands to fill the coronal volume and interplanetary space. Parts of the solar magnetic field are measured remotely and nearly continuously at the photosphere (e.g. Solar Dynamics Observatory/Helioseismic and Magnetic Imager – SDO/HMI, Schou et al. (2012)) and in situ near the Earth (Advanced Composition Explorer – ACE, Smith et al. (1998)). However, much of the dynamic behavior observed (coronal mass ejections, flares and waves) takes place inside the layers above the photosphere, in the solar corona where there are no routine direct measurements of the coronal magnetic field. A large number of models have been developed over the past decade to fill in the coronal magnetic field gap in these measurements. These models, in the form of static magnetic field extrapolations and time-dependent magnetohydrodynamic (MHD) simulations are now routinely used to calculate coronal magnetic field solutions that satisfy the boundary measurements (e.g. Wiegelmann et al. 2015, for a review and references therein). However, we still lack the ability to routinely measure the vector coronal magnetic field directly which would help further constrain the solutions and physical processes that are modeled.

Part of the problem is that coronal emission is intrinsically much fainter than the solar disc (10^{-6} $B_{\odot}$ right next to the limb) and decreases exponentially with radius away from the Sun. Outside total solar eclipses, both ground and space observatories need to use coronagraphs to block the glare from the disc and scattered light from the telescope itself from interfering with the measurements (Kuhn et al. 2003). So far the most precise direct measurements of the coronal magnetic field have been obtained through optical spectropolarimetry in the infrared (Kuhn et al. 1996; Lin et al. 2000, 2004; Tomczyk et al. 2008). Polarimetric infrared(IR) coronal observations measure the Zeeman effect (e.g., Arnaud & Newkirk 1987; Kuhn 1995) in the forbidden FeXIII 1.0747 μm line (hereafter FeXIII1075). Attempts to measure the coronal magnetic field strength currently depend on the ability to detect very weak Zeeman splitting through Stokes V (circular) polarization observations. However, in the corona where the field is only a few Gauss, the Stokes V signal is very weak

(typically 10^{-4}) in spectral lines that are dominated by much stronger linear scattering polarization amplitudes (e.g. Stokes Q and U of order 10^{-2}, (Lin et al. 2004). Penn (e.g., 2014) provides a larger context of all coronal magnetometry techniques but the promise of the 4m Daniel K. Inouye Solar Telescope (DKIST) is to use near-IR coronal lines to routinely observe the so far seldom measured weak solar coronal magnetic field.

The IR spectrum is particularly useful for ground-based studies of the corona for several reasons: lower scattering of disc light from telescope optical elements and decreasing scattering from the Earth's atmosphere at wavelengths below 1.8 μm (Kuhn et al. 2003). Both observations (Kuhn et al. 1996) and calculations (Judge 1998) have described new IR forbidden lines that could be useful as spectropolarimetric diagnostics. The discovery of the HeI1.083 μm line (hereafter HeI1083) far into the corona (Kuhn et al. 1996) has made it feasible to measure coronal fields in the 1-10 G range using only linear polarimetry of the HeI1083 line and other forbidden coronal lines – such as the newly characterized SiX 1.4301 μm (hereafter SiX1430) line (Dima et al. 2016). Early measurements of HeI1083 revealed diffuse coronal neutral triplet-state He associated with streamers (Kuhn et al. 1996). This initial measurement was eventually confirmed to have near solar origin through ground-based spectropolarimetric observations using the Scatter-free Observatory for Limb, Active Regions, and Coronae (SOLARC) telescope on Haleakala (Kuhn et al. 2007; Moise et al. 2010). The diffuse HeI emission is apparently caused by collisional excitation of singlet-state neutral He from electrons in the higher density regions inside streamers (Moise et al. 2010).

Although the SiX1430 line has been highlighted as a potentially useful coronal diagnostic (Judge 1998) only a handful of observations have been reported during eclipses (Münch et al. 1967; Olsen et al. 1971; Kuhn et al. 1996) and one published ground measurement not taken during an eclipse (Penn & Kuhn 1994). Historically the observation focus has been on the FeXIII1075 line for coronal polarimetric studies because of its stronger intensity and lack of large sky absorption bands. However, the corona is not expected to have a homogeneous temperature structure or an average temperature that remains constant throughout the solar cycle. Therefore, it is critical that we characterize and expand the emission lines diagnostics for more ions that sample regions with different temperatures. As a case in point SiX1430 has a peak ionization temperature of 1.1 MK while

FeXIII1075 peaks near 1.6 MK Arnaud & Rothenflug (1985).

During the March 29 2006 total solar eclipse coronal spectropolarimetric measurements were obtained over a 6×6 $R_\odot$ field of view (FOV) with a 1-2 μm spectral range. This window includes both the forbidden FeXIII1075 and SiX1430 lines as well as the permitted HeI1083 line, providing a unique opportunity to study the linear polarization properties of these lines simultaneously. This paper presents an analysis of these data and offers an interpretation based on comparisons with forward integrated synthetic polarized observables through two different MHD models of the corona for the day of the eclipse.

2.2 Observations

For this analysis, we worked on two types of data:

1. Polarized spectra obtained during the eclipse from which linearly polarized emission line and continuum intensities are extracted.

2. Synthetic images for FeXIII1075, SiX1430 and continuum calculated from forward integration of optically thin polarized emission through two coronal MHD models with different heating models and boundary conditions.

2.2.1 Eclipse measurements

Solar eclipses are ideal for ground-based measurements of coronal emission since the normally bright terrestrial sky background is very low. However, eclipses are short-lived and offer only fleeting glimpses into coronal physics. Observed of the total solar eclipse took place on March 29, 2006 at a site in the Libyan Sahara (N24° 33′ 59″ and E17° 57′ 16″). Second contact occurred at 10:13:57 UT when the Sun was at an altitude of +67° and azimuth 154° (Habbal et al. 2006). Measurements were taken throughout totality which lasted approximately 4 minutes and 6 seconds and attained a magnitude of 1.051. The sky remained clear throughout the eclipse.

The observations were taken using a near-infrared imaging spectropolarimeter designed specifically for coronal imaging spectroscopy. This instrument comprises five major optical components:

simple telescope, linear polarizer, an optical fiber bundle, grating spectrograph and a camera. The telescope consists of an off-axis spherical mirror with a 7.5 cm diameter and an effective focal length of 0.6 m. At the mirror focus lies an array of 127 optical fibers, spaced uniformly to sample the corona out to 4 $R_\odot$, with a spatial resolution of about $7.5'$. The labelled fiber locations relative to the solar disc are shown in Figure 2.1. The fiber bundle was not fitted with a lens array so the 50 μm fiber cores collected light from a circular area $16''$ in diameter. The telescope was slightly out of focus with a radius of defocus of around $8.5'$.

A computer controlled linear polarizer was placed in front of the fiber array and used to modulate the incoming beam from the telescope. The polarizer rotated by 45° between exposures so that the linear polarization state of the coronal light can be obtained from a combination of four exposures (hereafter a set of four consecutive exposures are referred to as one frame). The order of the exposures in each frame is I+U, I+Q, I-U and I-Q, where I, Q, U are the Stokes parameters. Over the duration of the eclipse 32 exposures were taken, each 5 seconds in duration. An unknown mechanical problem caused the image to jog slightly right at exposure number 17 with the approximate location of the solar disc after the shift shown by the dashed circle in Figure 2.1.

The optical fibers outputs were arranged into a linear array, with the fibers packed closely together. This linear array becomes the effective entrance slit of a Littrow-configuration reflecting grating spectrograph. The spectrograph produces a separate 2-pixel FWHM-wide spectrum from each fiber, with a resolving power of approximately 500. A 1024×1024 liquid nitrogen-cooled HgCdTe array camera, manufactured by Raytheon, Inc. was used to record 127 spectra simultaneously during each exposure. Up the ramp readout (2 Hz frequency) was used to reduce the effect of read-noise. A short-pass filter was positioned before the detector to block light outside the 1-1.9 μm wavelength range.

2.2.2 MHD models

Two three-dimensional MHD simulations of the corona were used to generate synthetic polarized emission exposures of the white light continuum and the SiX1430 and FeXIII1075 lines. The MHD simulations were computed using the MAS model developed by Predictive Sciences Incorporated

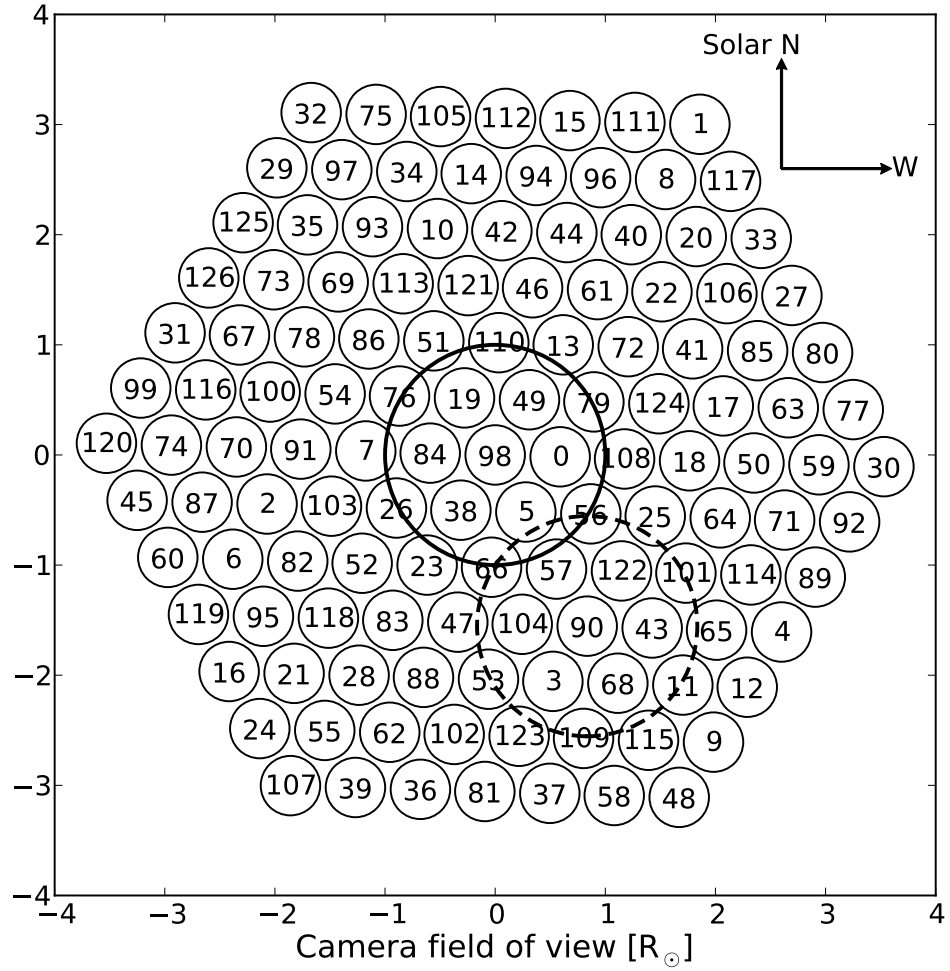

Figure 2.1: Approximate location on the fiber array of the solar disc during the first half of the eclipse (thick solid black circle) and during the second half (thick dashed black circle). The numbers are labels assigned to each fiber and the small circles are drawn only to guide the eye and do not represent the full image area sampled by each fiber due to telescope defocus.

(see Lionello et al. 2009, for details). The principal differences between the two simulations lie in the heating model used and the boundary photospheric magnetic field map. One model leads to a cooler overall corona and will be referred thereafter as the "cool model" while the other model will be referred to as the "warm model" since they lead to different density-weighted average temperatures of the corona (Figure 2.2). The average density in the corona decreases slightly faster for the cooler model. The warm model was computed in the days leading up to the eclipse so did not benefit from having the most complete photospheric magnetic field map covering the day of the eclipse. This simulation, its heating model and a comparison to white-light eclipse images, is discussed in Mikić et al. (2007). The cool model was produced recently and uses a heating model similar to Downs et al. (2013). The full-sun photospheric boundary conditions for the radial magnetic field are derived from output of the LMSAL Evolving Surface-Flux Assimilation Model (Schrijver & De Rosa 2003) for 12UT, just after totality.

The simulation domain is defined in heliocentric spherical polar coordinates. The radial domain extends from r=1 $R_\odot$ to r=20 $R_\odot$ with the radial mesh spacing increasing smoothly outwards: near the limb the radial spacing is $\Delta r = 7.3 \times 10^{-4}$ $R_\odot$, which increases to $\Delta r = 3.0 \times 10^{-4}$ $R_\odot$ near r=2 $R_\odot$. Near r=20 $R_\odot$ the radial spacing becomes $\Delta r = 1$ $R_\odot$. The parts of the simulation domain that are expected to contribute all the significant flux for the synthetic observations lie within 2.5 $R_\odot$. The co-latitude θ varies between $[0, \pi]$ and has variable spacing between the poles and the equator: the spacing near the poles is $\Delta\theta = 0.1$ rad and decreases to $\Delta\theta = 0.01$ rad near the equator. The azimuth ϕ varies between $[-\pi, \pi]$ and has a constant mesh spacing of $\Delta\phi = 0.016$ rad throughout the simulation domain.

For our purposes, the end product of each simulation consists of a data cube containing electron density, temperature and the vector magnetic field in each cell. This data cube is used in conjunction with the analysis tool FORWARD (Gibson et al. 2016) to generate synthetic polarized emission of electron scattered continuum (K-corona) and the SiX1430 and FeXIII1075 lines. FORWARD is a flexible tool that generates emission maps with varying spatial resolution and line-of-sight (LOS) depth. For both the continuum and the line emission, we used a square grid centered on the Sun with square pixels of dimension 0.01×0.01 $R_\odot$. Along each LOS the emission is integrated

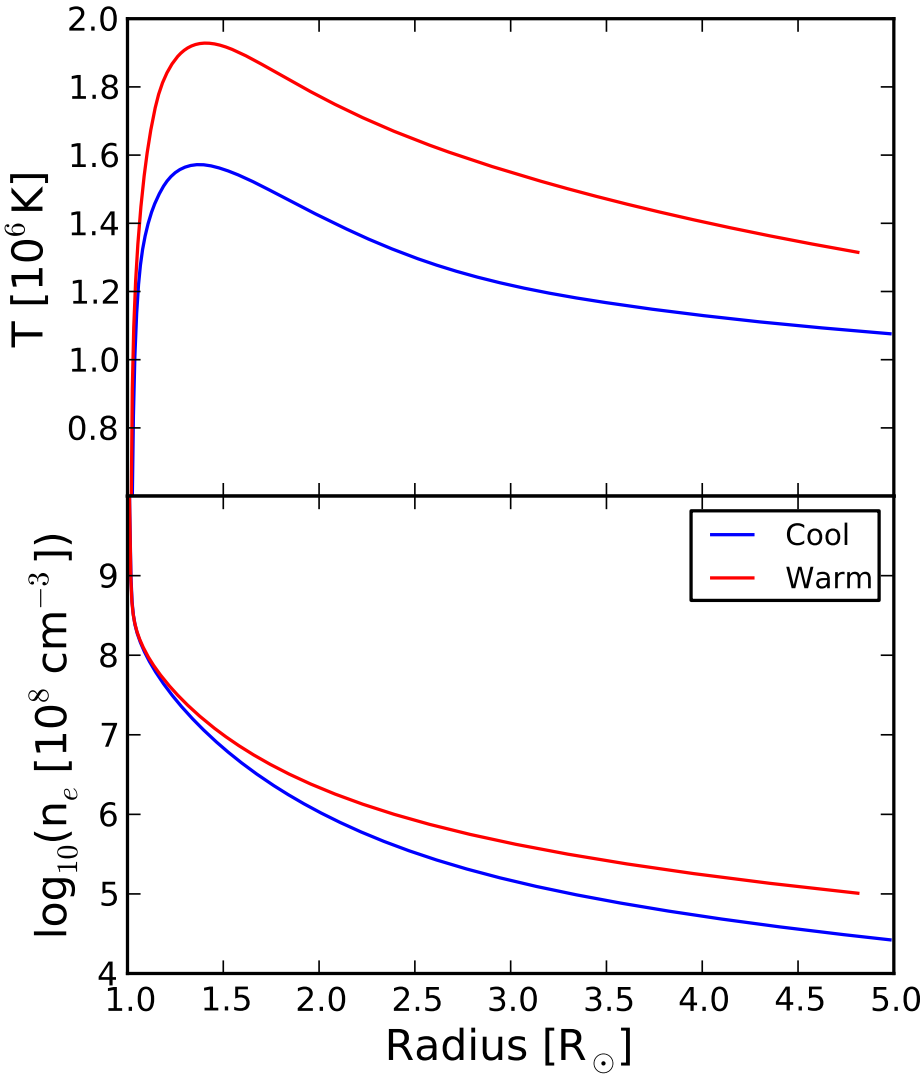

Figure 2.2: Radial variation of the angle averaged, n_e^2 weighted temperature (top) and density (bottom) for the warm (red) and cool (blue) MHD models. It is noticeable that the cool MHD model has averaged temperatures lower that the warm model by around 400,000 K at all radii apart from a small region very close to the limb. In turn, the reduced temperature causes the density throughout most of the corona to be lower in the cool model.

using 110 steps with 0.02 rad step size. This integration path is centered on the plane of the sky (plane perpendicular to the LOS and passing though the center of the Sun). The MHD simulations use spherical coordinate grids so integrating using constant angular increments rather than constant cartesian increments, ensures that a LOS further from the limb does not undersample the simulation domain. The continuum synthetic image dimensions are 3.5×3.5 $R_\odot$, while for the line intensities the grid dimensions are 2.0×2.0 $R_\odot$ since line emission is comparatively much fainter beyond this radius.

The FORWARD model for continuum includes only Thomson scattered light from free electrons in the K-corona (Minnaert 1930). Apart from the K-corona the real coronal continuum has a contribution of light scattered by circumsolar dust particles referred to as the F-corona. The exact distribution and particle size composition of the dust is still an active area of research so currently only empirical radial brightness profiles of the F-coronal exist (Dolei et al. 2015; Koutchmy & Lamy 1985; Saito et al. 1977). Most F-corona brightness distributions are calculated from observations with the Large Angle and Spectrometric Coronagraph (LASCO, Brueckner et al. 1995) which has a FOV limited to radii above 2 $R_\odot$. Instead we use the F-corona model brightness distribution calculated by van de Hulst (1950) from a compilation of eclipse observations. This model has the advantage of covering the full radial range all the way down to the limb of the Sun and provides absolute values for the F-corona brightness as well as average values for the K-corona at solar minimum and maximum. Below $r<5$ $R_\odot$ the F-corona emission is negligibly polarized so no polarized contributions from the F-corona are included in the synthetic polarized brightness (Mann 1992; Koutchmy & Lamy 1985). The elongation dependent F-corona contribution is calculated and added using equation 7 from van de Hulst (1950):

$$F(r) = 14.88r^{-7} + 4.99r^{-2.5} \tag{2.2.1}$$

where F(r) is the F-corona brightness in units of 10^{-8} $B_\odot$ as a function of elongation r measured in $R_\odot$.

Linearly polarized emission coefficients for the SiX1430 and FeXIII1075 lines are calculated using atomic models for the SiX and FeXIII ions included in the FORWARD code (Judge & Casini 2001).

The atomic models include corrections for depolarizing collisions with electrons and protons due to cascades from excited levels and mixing of the Zeeman substates (Judge et al. 2006). Given the low density of the solar corona we make the reasonable assumption that emission for these lines is optically thin so calculating the total polarized emission involves adding the emission coefficients in each pixel along a particular LOS.

The final output from the FORWARD integrated emission is a set of noise-free images showing Stokes I, Q, U for the continuum, FeXIII1075 and SiX1430 lines corresponding to each MHD model.

2.3 Data Analysis and Results

2.3.1 Eclipse Measurements

From each exposure 127 spectra are extracted by correcting for spectral warping in the wavelength direction and calculating the intensity along each fiber through a quadratic interpolation over the pixels illuminated in the spatial direction of the array. This produces a set of 32×127 eclipse spectra together with 127 sky spectra covering the wavelength range 1-1.9 μm. One example of a raw extracted spectrum obtained from fiber 76 (core of the fiber located at 1.02 $R_\odot$) is shown in Figure 2.3, with emission lines identified. Noticeable below 1.3 μm is the strongly decreasing filter throughput. To account for the large differences in filter response between different parts of the spectrum we calculate ratios of integrated emission line intensities and the measured nearby continuum. This is a good approximation if the filter response is flat over the width of the lines and the continuum is flat over the width of the instrument point spread function (PSF). For this experiment the measured instrumental PSF has a full width at half maximum (FWHM) of around 23.5 Å. Near FeXIII1075 and HeI1083 there are only a small number of sky absorption lines so I expect the integrated line intensity to continuum ratio to be preserved without the need for any correction factor. However, because SiX1430 is located in a region with very dense sky absorption lines (Figure 2.4a) the PSF convolution causes the measured continuum near the line to underestimate the real continuum near the line by a factor of 0.46. This factor is calculated from convolving high resolution solar disc spectra (Wallace et al. 1996) with a theoretical PSF and estimating the

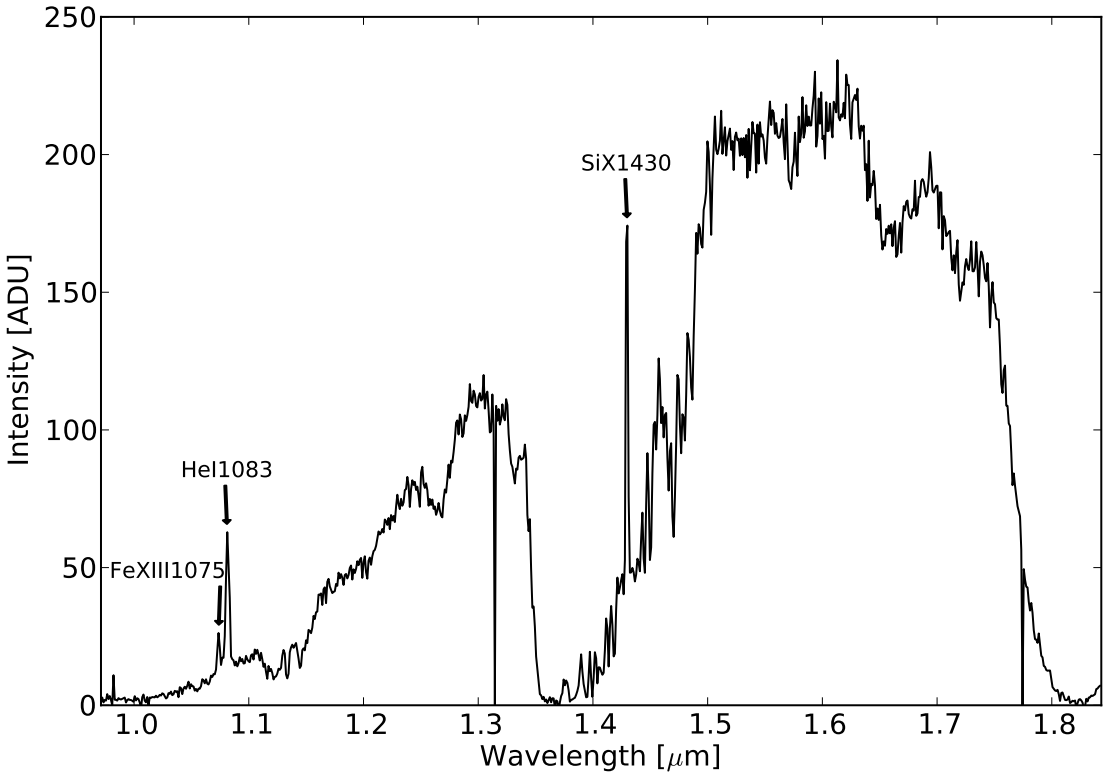

Figure 2.3: Raw spectrum extracted from fiber 76 at exposure 7. The filter transmission varies strongly across the spectral region and the throughput is significatly depressed near 1.1 μm. Interesting coronal emission lines are indicated on the spectrum. Also noticeable is the depression in the spectrum between 1.35-1.5μm due to the large number of atmospheric absorption lines and the large width of the instrument response function.

needed correction for the measured continuum (Figure 2.4b, c).

To extract line information, we fit line profiles to spectra for each exposure instead of stacking all the collected spectra. Each spectrum is first continuum corrected by subtracting the corresponding scaled sky spectrum for a specific fiber. After performing the continuum subtraction, a Gaussian function is fitted to each line. Figure 2.5 shows the line profile fits for the first exposure in Fiber 54 as an example.

Eclipses are inherently dynamic events because the lunar disk moves quickly across very bright regions of the corona. During totality, the apparent lunar disk radius was 1.051 $R_\odot$. Therefore, at second contact the lunar disk occults as much as 0.1 $R_\odot$ of the solar corona on the West limb while 4 minutes later at third contact the lunar disk occults as much as 0.1 $R_\odot$ of the corona on the

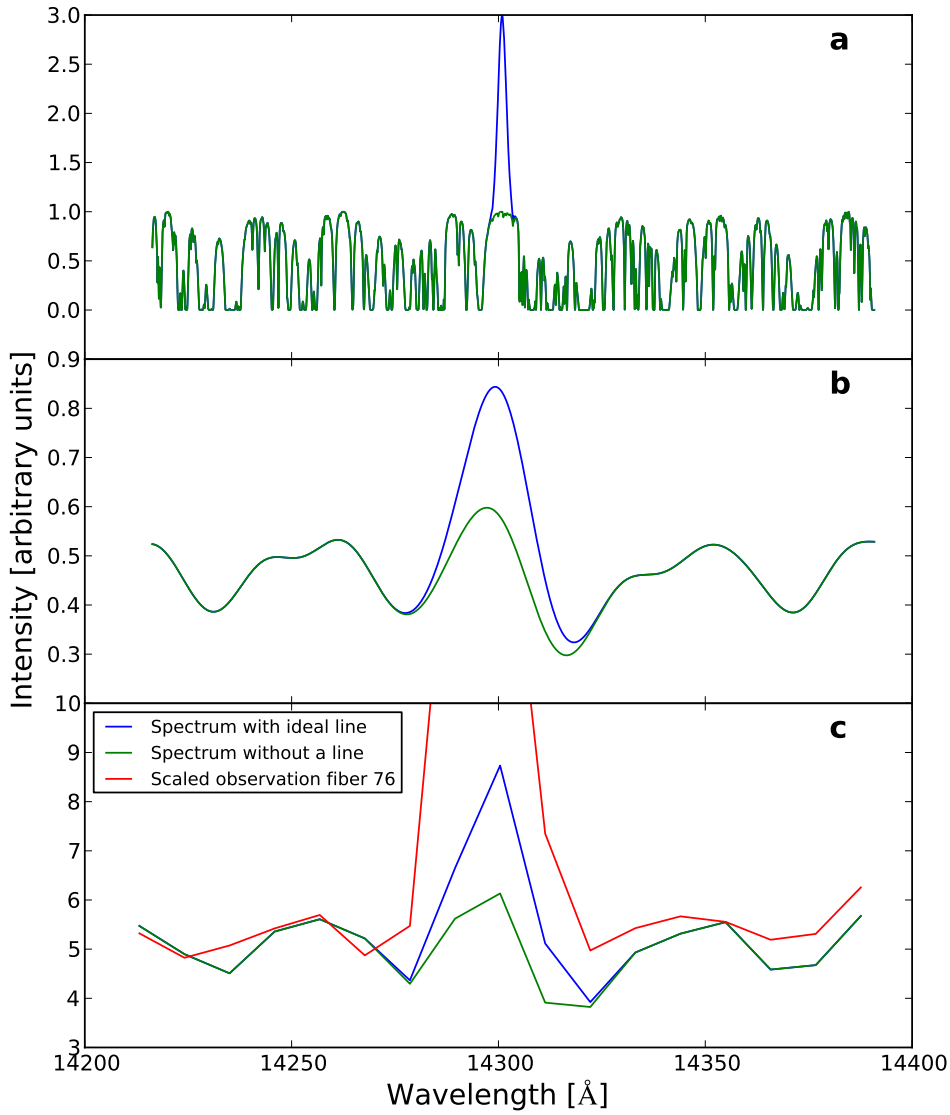

Figure 2.4: Spectral region from the atlas by Wallace et al. (1996) around the SiX1430 line observed at high spectral resolution (a). A synthetic SiX1430 emission line is added for comparison with line properties comparable to the available high resolutions observations of this line (Penn & Kuhn 1994). The effect of convolving the high-resolution spectrum with a broad PSF (FWHM = 23.5 Å) is shown in panel b. Panel c shows this convolved spectrum sampled at our instrument spectral resolution of 10.9 Å. Also shown in panel c is a scaled measured spectrum from fiber 76 (see Figure 2.16). The correspondence of the continuum features can be clearly seen (modulated by array gain and observing noise).

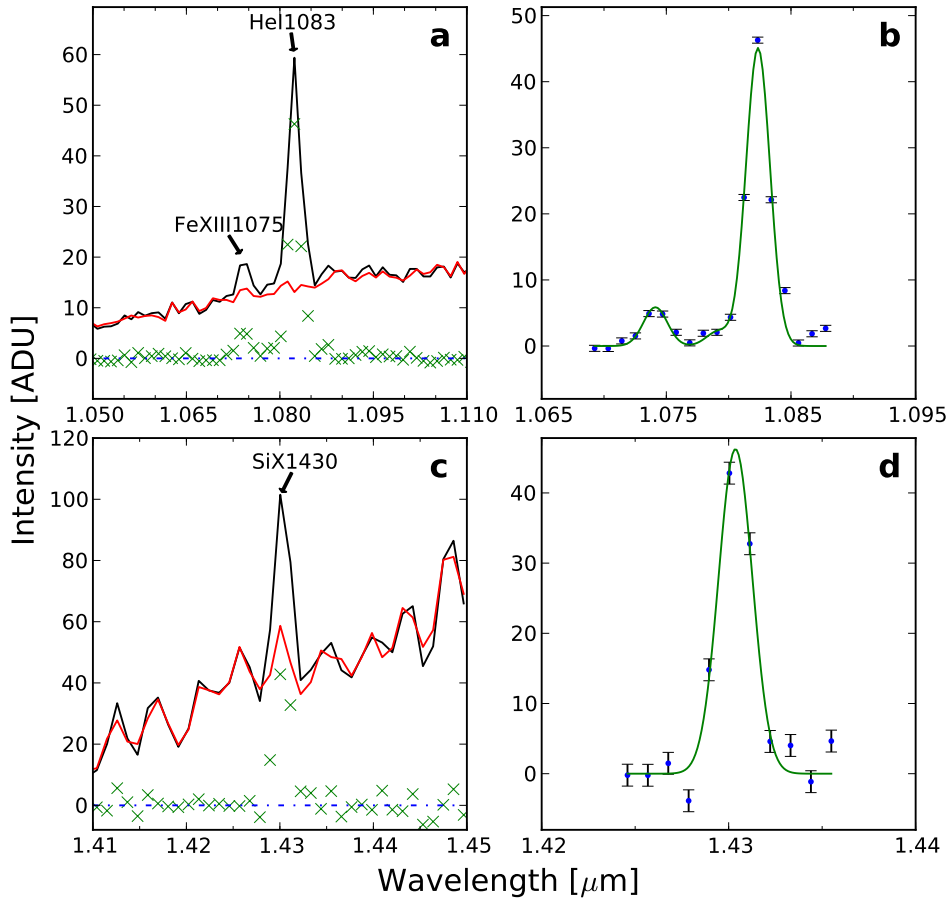

Figure 2.5: Fits for the FeXIII1075, HeI1083 and SiX1430 emission lines for the first exposure of fiber 54 (see Figure 2.16). Panels a and c show the data (black line) and the scaled/shifted sky spectrum (red line) along with the residual (green crosses in a, c and blue dots in b, d) after continuum subtraction. The line profiles are shown in solid green lines panels b and d.

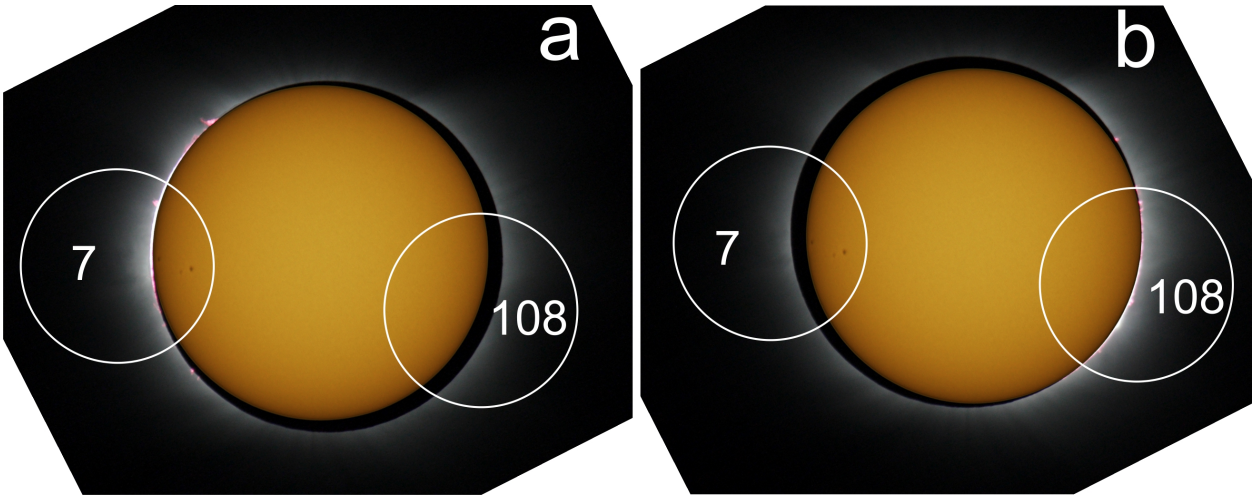

Figure 2.6: Relative positions between the moon and Sun disc at second (a) and third contact (b). The white discs represent approximate sizes for the size of the defocus radius. As the eclipse progresses both continuum and line intensities decrease during the eclipse for fiber 7 and increase for fiber 108. (Photo credit Odd Høydalsvik)

East limb. Figure 2.6 shows the coronal regions occluded by the moon together with fibers 7 and 108 and the effective image region sampled by each fiber due to the defocus. The defocused image together with the moving lunar disc lead to measurements in near limb fibers that show brightness variations during the measurement sequences. Figure 2.7 shows how this variation is different for fibers 7 and 108 located on opposite sides of the Sun.

After measuring the line and continuum intensity for each exposure Stokes Q and U parameters are calculated by fitting a function of the form

$$\mathrm{F(t) = I(t) + U\cos\left(t\frac{\pi}{2}\right) + Q\sin\left(t\frac{\pi}{2}\right)} \tag{2.3.1}$$

In this case, t is the exposure number counting the first exposure as t = 0 and Q and U are the corresponding linear Stokes parameters for a particular sequence of measurements. The function I(t) is a first or second order polynomial that accounts for the intensity variation due to the eclipse. Figure 2.7 shows examples of fits to the intensities for fibers 7 and 108. In principle, this procedure is imperfect since the occulting moon blocks emission from regions with different polarization brightness. This may lead to the situation where each exposure is actually measuring light from slightly

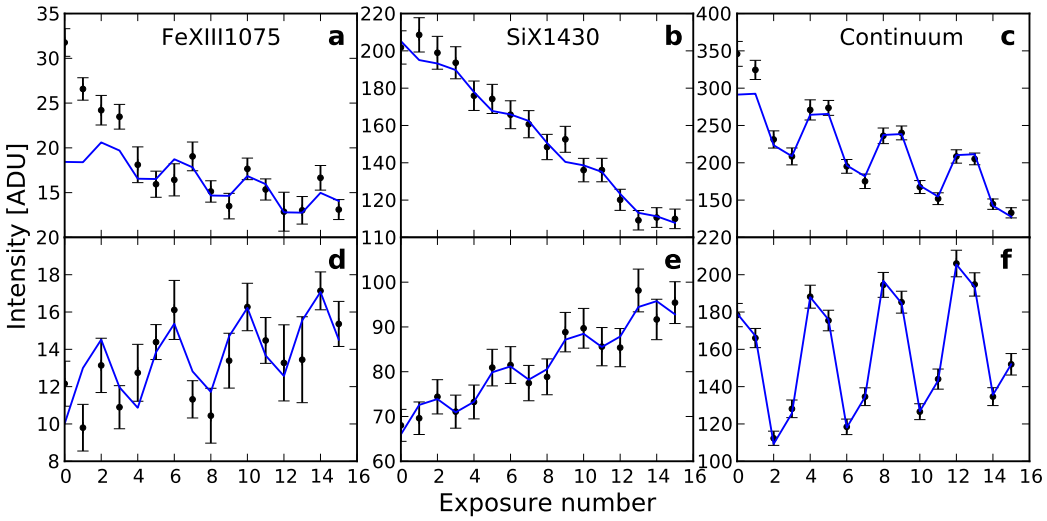

Figure 2.7: Line and continuum brightness variation for fiber 7 (a-c) and fiber 108 (d-f). Fits for the line and continuum polarization values are shown in blue. Right at the start of the eclipse some fibers like 7 show steeper gradients in the first few exposures and then settle into a more regular variation. For fiber 7 we only used exposures 4-15 for the fit. Since fiber 7 is on the W limb as the eclipse progresses more light is obscured and a progressive decrease is observed in the amount of light measured for the lines and continuum. Conversely, fiber 108 is located on the E limb and the brightness in lines and continuum increases. The short period variation is due to the rotating linear polarizer.

different regions of the corona. However, our eclipse simulations performed using synthetic emission maps where the intrinsic polarization is known a priori (see Section 2.3.2) show this procedure is robust in recovering the polarized signal.

From this fit, Stokes parameters Q and U are automatically obtained while the value of Stokes I is calculated as the average over all the measurements in a sequence with an error corresponding to the spread in intensity measurements. For intuitive purposes during the remaining analysis we choose to work in terms of the concepts of linear polarization angles and polarization amplitudes which are related to Stokes I, Q, U through the relations:

$$\text{Polarization amplitude} = \frac{\sqrt{\mathrm{Q}^2 + \mathrm{U}^2}}{I} \tag{2.3.2}$$

$$\text{Polarization angle} = 0.5 \arctan\left(\frac{\mathrm{U}}{\mathrm{Q}}\right) \tag{2.3.3}$$

To ensure the polarization angle is correctly calculated, an "arctan2"-type function should be applied. This function accounts for the signs of the U an Q values so that together with the factor of 0.5 equation 2.3.3 correctly maps the polarization angle over the domain [-90°, 90°] in all quadrants of the trigonometric circle.

The sky spectra used to perform the continuum correction are shifted along the wavelength direction by fractions of a pixel due to an unknown systematic effect. This effect couples with the broad PSF of the instrument to impose a limitation on the accuracy of the continuum correction and subsequent line fitting. Errors introduced are characterized by a linear relationship between the standard deviation of the continuum subtraction residuals and the continuum intensity (Figure 2.8). If Poisson noise was the dominant source of noise the relationship between the residual standard deviation and the intensity would be $\sigma_{\mathrm{I}} \propto \sqrt{\mathrm{I}}$. The best linear fits are different for the continuum near SiX1430 and the continuum near FeXIII1075 and are respectively given by:

$$\sigma_{\mathrm{r}} = 0.045^{+0.001}_{-0.001} I_{\mathrm{c}} + 0.38^{+0.03}_{-0.03} \tag{2.3.4}$$

$$\sigma_{\mathrm{r}} = 0.012^{+0.001}_{-0.001} I_{\mathrm{c}} + 0.54^{+0.02}_{-0.02} \tag{2.3.5}$$

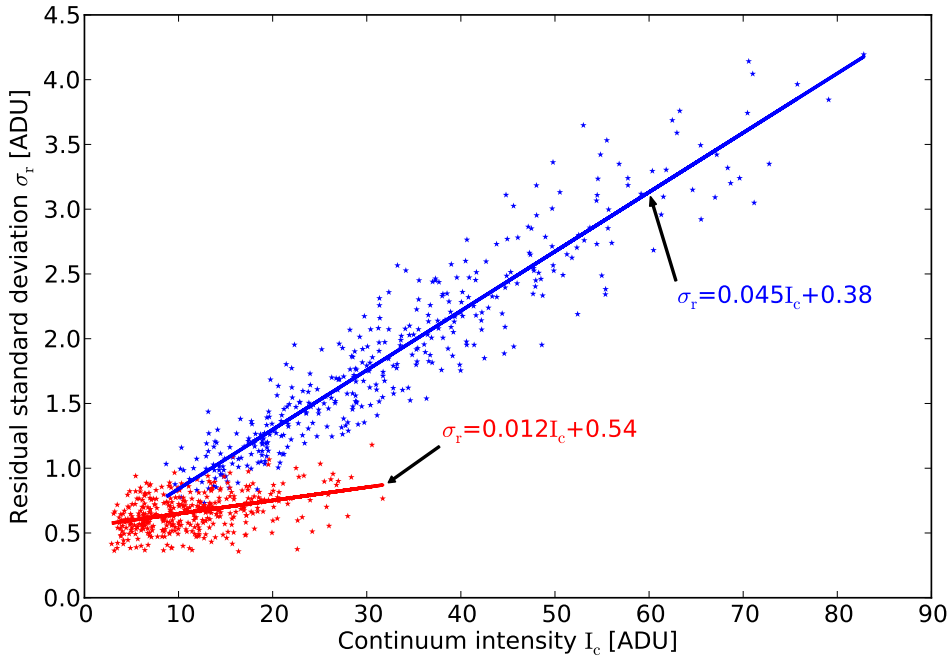

Figure 2.8: Relationship between the continuum brightness and residuals after sky subtraction near SiX1430 (blue points) and FeXIII1075 (red points). The best linear fit relationship is shown along with the equation for each line. The difference in slope between the fits in the different line regions is caused by the larger number of sky absorption lines near the SiX1430 line compared to the FeXIII1075 line and the convolution with a large instrumental PSF (compare the jagged continuum regions near the two lines seen in Figure 2.5a,c).

The variation in the slope of the noise relationships near the two lines can be attributed to the presence of a large amount of blended terrestrial absorption lines near SiX1430 compared to FeXIII1075. The second constant term is due to detector noise and plays a larger role in detecting the FeXIII1075 and HeI1083 lines due to decreased throughput for that spectral region. Calculating these noise parameters is important because it serves as a guide to adding comparable levels of noise in the synthetic observables as discussed in the following section.

2.3.2 Synthetic observations

The emission maps are noise-free with resolutions limited only by the simulation pixel sizes. Increasing the resolution of the images higher than the simulation resolution will not increase information since the simulation is uniform inside the cell sizes. To eliminate systematic effects between the real and synthetic observations potentially caused by the fitting method, we manipulated the synthetic

images to closer resemble the observations by simulating an artificial eclipse and telescope defocus using the following steps:

1. Linear polarization modulation is introduced in the 32 exposures by adding or subtracting the synthetic Stokes Q and U images to the Stokes I images using the same polarizer sequence employed during the eclipse measurements: I+U, I+Q, I-U and I-Q.

2. Variability due to the motion of the lunar disc is simulated by moving a digital lunar disc with diameter 1.05 $R_\odot$ over the sharp synthetic images in 32 time steps. Pixels inside the lunar disc are set to zero brightness.

3. The resulting "eclipsed" polarized images are then convolved with a circularly uniform top-hat function with radius 0.58 $R_\odot$ that approximates the image defocus effect.

4. Each of the resulting exposures are then sampled at the same approximate spatial positions as the eclipse fibers resulting in a data set of 32 noise-free polarized brightness sequences for the continuum, FeXIII1075 and SiX1430 lines in each fiber.

Figure 2.9 gives an example comparison between the measured and simulated noise-free synthetic observables for fibers 7 and 56. We recover polarized continuum intensity variations qualitatively and quantitatively similar to the eclipse observations. There is greater discrepancy between the synthetic and observed polarized line emission variation as well as amplitude variation due to the polarizer. The reason for the discrepancy is twofold: the MHD models do not necessarily simulate the exact coronal distributions for SiX1430 and FeXIII1075 emission; the synthetic emission maps are noise-free whereas the observations contain noise.

The final analysis step is to gradually introduce noise in the observations quantitatively similar to the noise we measure in the observations (Equations 2.3.4, 2.3.5). Noise is added at each exposure by randomly sampling a normalized distribution with a standard deviation proportional to the intensity at that exposure. This proportionality factor is changed progressively to show the effect noise has on the measured polarization angles and amplitudes. For the continuum, polarization properties are generally not affected by the introduced noise since the polarization amplitude (over 10%) is typically much larger than the noise level (maximum around 5%) whereas the synthetic

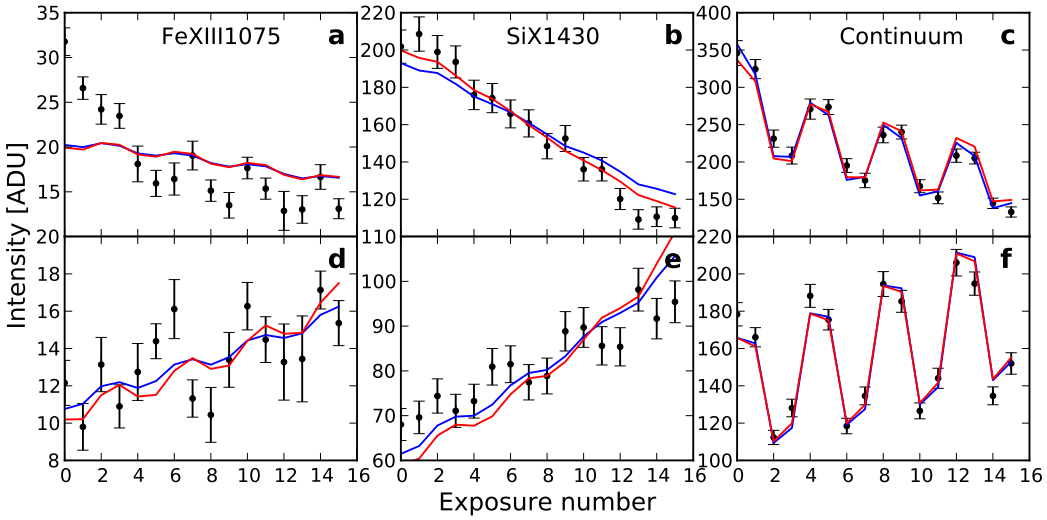

Figure 2.9: Comparisons between the observed (black point with errors) and synthetic polarized intensity variation (blue and red lines). Red solid lines represent the warm MHD model results while blue solid lines represent the cool model. Fibers 7 (a-c) and 108 (d-f) are shown. The synthetic emission is scaled so that the averages line up with the measurements. The continuum variation is well reproduced but synthetic line emission tends to show decreased polarization amplitudes compared to the measurements. The slopes of the trends is different because the MHD models are not perfect representations of the true corona.

line polarization amplitudes are typically closer to $2-3\%$, so much smaller than the realistic noise levels.

2.4 Discussion

Considering the size of the dataset we split our analysis into four topics:

1. Linearly polarized observations of SiX1430 and FeXIII1075 and comparisons with theoretical expectations for this line.

2. Using the line intensity ratio FeXIII1075/SiX1430 as a temperature diagnostic to characterize an "average" coronal temperature and compare with the MHD models.

3. Continuum polarization amplitude radial variation and stability of the F-corona.

4. Discussion of the measured HeI1083 emission.

2.4.1 Polarization of SiX1430 and FeXIII1075

The FeXIII1075 coronal line has been the target of eclipse expeditions and ground-based observations because of its relative brightness and lack of contamination from sky absorption bands (Arnaud & Newkirk 1987; Tomczyk et al. 2008; Habbal et al. 2003; Lin et al. 2004). Polarized properties of this line are well understood and backed by observations (Sahal-Brechot et al. 1977; House 1974, 1977; Habbal et al. 2001; Judge 1998). In contrast, SiX1430 has only been observed a handful of times and has always been found to be slightly weaker in intensity that FeXIII1075 (Penn & Kuhn 1994; Kuhn et al. 1996). However, no polarized measurements of SiX1430 has so far been demonstrated so its polarimetric potential is unknown. We present here the first linearly polarized measurements of the SiX1430 emission line which show unexpectedly large polarization amplitudes compared to the predicted values. The reasons for the discrepancy lie in the underlying model atomic physics, or in the spatial distribution of the emission in the solar corona which is a strong function of the electron density.

To argue for this, we adopt an aggregate approach by building distributions of the polarized angles and amplitudes for the SiX1430 and FeXIII1075 lines for all the fibers where observations are available. Similar distributions are created from the synthetic datasets by restricting the analysis to the fibers where measurements are also available. Both MHD models produce nearly identical polarized distributions so we restrict the analysis to only using the warm model but the analysis could equally be applied to the cool model. In this sense, this analysis is not useful for distinguishing between the two MHD models. To understand the effects of measurement noise, distributions are created for synthetic emission with three noise levels (0%, 2.5% and 5%) meant to approximate the measurement noise (equations 2.3.4 and 2.3.5). The resulting polarization angle and amplitude distributions are shown in Figures 2.10, 2.11, respectively.

Since both lines are forbidden magnetic dipole transitions, the theoretical expectation is that the angle distributions would be peaked near the direction perpendicular to the solar limb. Eddy et al. (1973) and (Arnaud & Newkirk 1987) show observed polarized angle distributions for FeXIII1075 that are peaked near radial orientations. This result can be compared to Figure 2.10 that shows both the noise-free synthetic and measured angle distribution for the FeXIII1075 and SiX1430 lines are

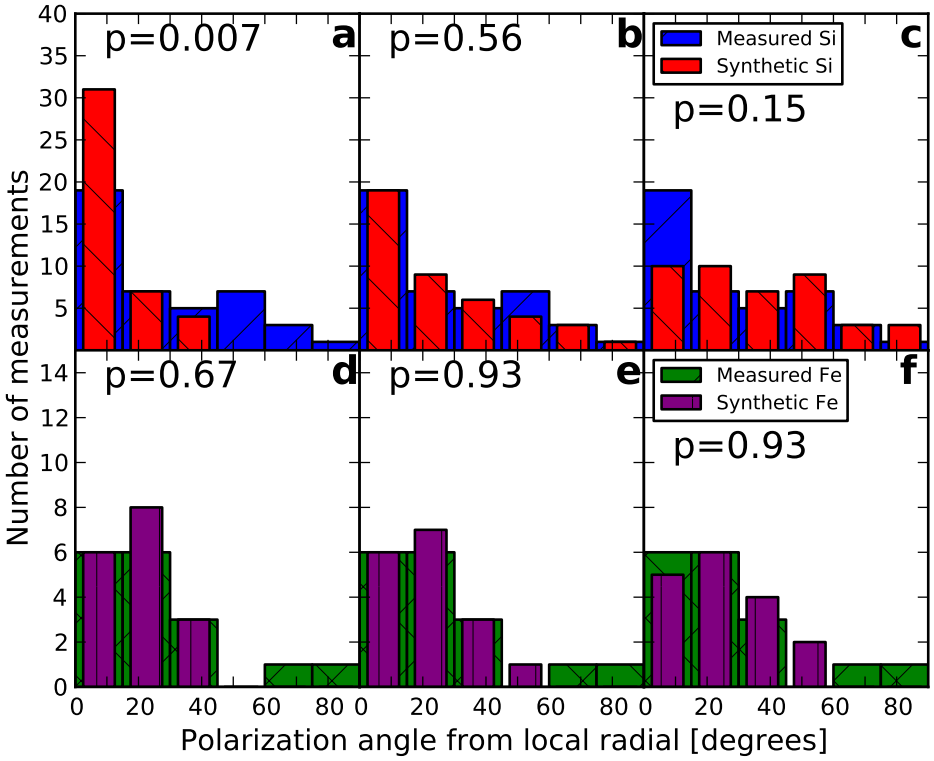

Figure 2.10: Distribution of polarization angles measured from the local radial direction in each fiber for SiX1430 (a-c) and FeXIII1075 (d-f). Random errors proportional to line intensities are introduced in the synthetic measurements with the proportionality factors: 0% (a, d), 2.5% (b,e) and 5% (c, f). There is noticeable flattening in the synthetic angle distributions as larger errors are introduced. The width of all the bins is 15°, but the synthetic bins are drawn with narrower widths to improve visibility. The p values in each subplot are calculated using a Kolmogorov-Smirnov test for each pair of distributions.

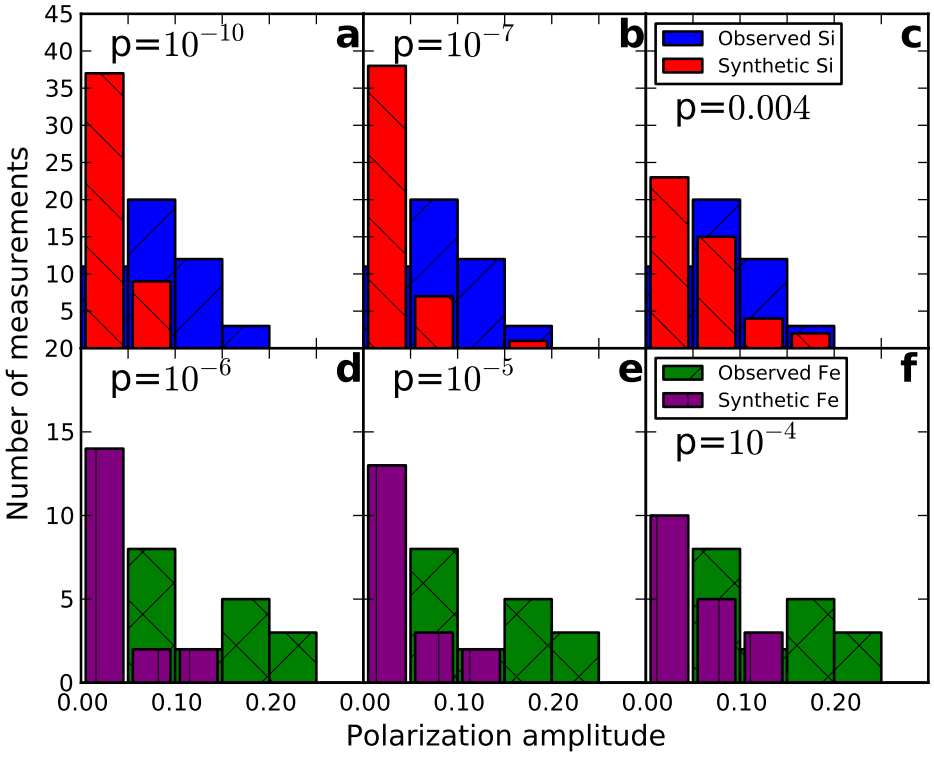

Figure 2.11: Distribution of polarization amplitudes measured in each fiber for SiX1430 (a-c) and FeXIII1075 (d-f). Random errors proportional to line intensities are introduced in the synthetic measurements with the proportionality factors: 0% (a, d), 2.5% (b,e) and 5% (c, f). It is noticeable that even for realistically large noise levels (c, f) the synthetic polarization amplitude still tend to underestimate the measured distributions. Compare this with Figure 2.10c,f where the synthetic polarized angles distributions at similar noise levels tend to overestimate the flatness of the observed distribution. The width of all the bins is 0.5, but the synthetic bins are drawn with narrower widths to improve visibility. The p values in each subplot are calculated using a Kolmogorov-Smirnov test for each pair of distributions.

in qualitative agreement with a distribution peaked near linear polarized orientations perpendicular to the local solar limb. As noise is increased progressively in the synthetic emission, the angle distributions tend to become flatter as the noise leads to larger errors in the angle fits. For realistic values of noise (Figure 2.10c,f) the effect is more pronounced for SiX1430 where we have a larger sample size of 44 measurements than FeXIII1075 where we only have 17 measurements with lower S/N. The discrepancy in the number of observations for both lines is due to decreased sensitivity near the FeXIII1075 line due to a drop in filter transmissivity.

To compare the observed and synthetic distributions we computed the two-sided Kolmogorov-Smirnov (KS) test for each pair to decide if the samples are drawn from the same parent distribution. The resulting probabilities that the two distributions are drawn from the same parent distributions are shown in individual panels in Figure 2.10. For SiX1430 the 2.5% noise distribution shows the best agreement with the observations ($p = 0.56$) while the 5% noise distribution shown much smaller agreement ($p = 0.16$) indicating that noise levels larger than this will lead to poorer agreement. The results for FeXIII1075 are less conclusive since there are comparatively fewer observations to compare the models with.

The measured polarization amplitude distributions (Figure 2.11) show a peak near polarized amplitudes of 0.075 for SiX1430 and a poorly defined peak for the sample of FeXIII1075 detections. In contrast, all the synthetic distributions are peaked near 0.025. Adding realistic levels of noise tends to broaden the synthetic distributions but still preserves the low polarization amplitude peak for both SiX1430 and FeXIII1075. The KS test comparing the observations and noisy distributions shows increasing agreement for higher levels of noise but the p-values remain exceedingly low. It is conceivable that adding more noise to the simulations may bring better agreement but this destroys the polarization angle agreement with the observations indicating that the cause of the discrepancy is not the noise but some underlying assuming in the synthetic models.

Our interpretation of these findings is that the observed SiX1430 emission is more strongly polarized than predicted by the combination of the MHD and atomic physics models used in producing the synthetic emission. Strong polarization for SiX1430 would show both enhanced polarized amplitude and the polarization orientation angle would be more robust to measurement noise. This

explains why, despite the relatively large noise, the observed polarized angles remain closely distributed near radial orientations. It is harder to draw any strong conclusions about FeXIII1075 because of the smaller sample sizes involved. Furthermore, the noise for FeXIII1075 is harder to model because it is dominated by the constant detector noise term (second term in 2.2.1), rather than the term proportional to the line intensity.

Several factors affect the polarization amplitude of the line: (1) the anisotropy of the radiation exciting the line; (2) the amount of depolarization due to isotropic collisions; and (3) the relative ratio between collisional and photoexcitation in the line.

1. The anisotropy of the radiation is a geometric effect and increases with the distance of the scattering atom from the disc of the Sun. Atoms higher in the corona scatter more anisotropic radiation and will consequently be more strongly polarized. If this effect explained the observed discrepancy, more SiX atoms would have to be radiating from farther away than closer to the limb. This is hard to achieve without requiring large amount of emission from larger radii out in the corona. We could not achieve this even after forcing ad hoc, unrealistically flat electron density distributions in the MHD models.

2. Isotropic collisions of electrons with the excited magnetic sublevels and cascades down from higher excited states will tend to depolarize the line. Thus, higher electron densities tend to result in lower line polarizations. One way to test this is to artificially decrease the electron density to levels where this effect becomes negligible. However, performing this test in the MHD models did not have a large enough effect on the line polarization amplitudes to correct the observed discrepancy.

3. Part of the line is excited through isotropic collisions which do not induce polarization in the upper level of the line but do contribute to the total intensity of the line. The ratio between the collisional and radiative excitation of the line could be the source of the observed discrepancy in the polarization amplitude. There are two ways to alter this ratio, either by decreasing the number of collisions or by altering the collisional coefficients that couple the density to the amount of excitation in the line. As discussed in the points above, lowering the density did

not increase the polarized amplitude of the line enough to account for the discrepancy. We conclude that a closer look at the collisional coupling coefficients in the FORWARD model may help explain the discrepancy as well obtaining new polarized observations of the SiX1430 line to account for any undetected systematic effect in the present measurements.

2.4.2 FeXIII1075/SiX1430 as a coronal temperature diagnostic

Strong emission from highly ionized species like SiX and FeXIII indicates that the solar corona is a very hot, highly ionized plasma environment. An interesting problem to answer is how much does the "average" temperature of the solar corona vary over time. This issue is important to study because temperature in turn affects which emission lines are brighter at particular times in the solar cycle. There is already some evidence that the average temperature of the corona does vary in time. Arnaud & Newkirk (1987) pointed out that FeXIV5303 emission was enhanced over the FeXIII1075 line during the 1977-1980 observing period leading up to the peak of cycle 19. Analysis of in situ plasma composition over solar cycle 23 and the beginning of cycle 24 have led a number of studies to conclude that the average charge states of Si and Fe decreased significantly (von Steiger & Zurbuchen (2011); Kasper et al. (2012); Lepri et al. (2013). These studies concluded that the coronal temperature was decreasing during the second part of solar cycle 23 when the eclipse occurred. Habbal et al. (2010) looked at the same in situ data and concluded that the coronal temperature was steady over cycle 23 but did indicate a decrease from the temperature in cycle 22. Landi & Testa (2014) analyzed remote sensing measurements of emission line ratios at the base of long lived streamers over the period covering cycles 22-24, and concluded that the temperature of the corona during cycle 23 did not change appreciably.

The present measurements of FeXIII1075 and SiX1430 emission over a large FOV with small scale inhomogeneities diffused by the telescope defocus offer an opportunity to study whether the warm or the cool MHD models are in better agreement with the average coronal temperature. This is possible because ion populations in the rarefied corona are strong functions of temperature and weak functions of density so the intensity ratio for these lines is also a strong function of temperature and a weak function of density. Utilizing the CHIANTI atomic database (Dere et al. 1997; Landi et

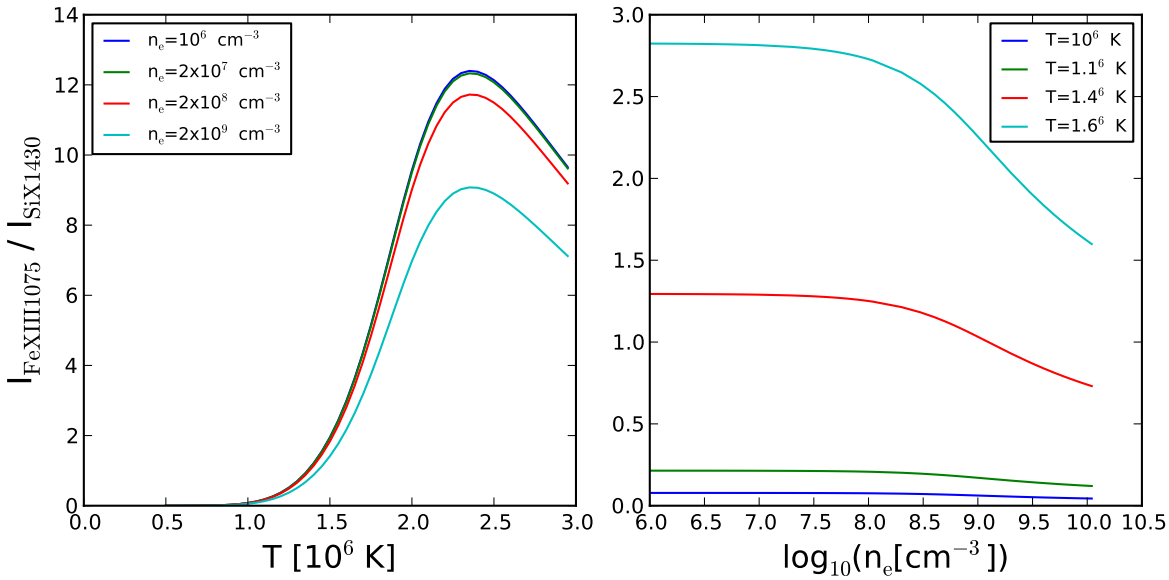

Figure 2.12: Variation of the FeXIII1075/SiX1430 line ratio with temperature(left) and density(right) assuming constant emission measures. The line ratio for relevant densities in the solar corona ($10^6 < n_e < 5 \times 10^8$ cm^{-3}) does not vary with density but does show a steep sensitivity to the temperature for relevant coronal temperature (10^6 K $< T < 2 \times 10^6$ K).

al. 2013) we calculated how the ratio FeXIII1075/SiX1430 varies as a function of temperature and density (Figure 2.12). At typical coronal densities ($n_e < 10^8$ cm^{-3}) the ratio is constant, but for typical coronal temperatures in the range 1-2 MK it shows larger variation which make it a good temperature diagnostic.

Comparing the observed and synthetic distributions of line ratios we see that the observations tend to be in better agreement with the warm model (Figure 2.13). The line ratio averages fall at 1.7 ± 0.5 for the observations and warm model and at 1.0 ± 0.2 for the cool model. Interpreting these values based on the curves shown in Figure 2.12, this corresponds to an average value for the coronal temperature around 1.5 ± 0.05 MK for the observations and warm model and 1.35 ± 0.05 MK for the cool model.

For each MHD model we calculate a n_e^2 weighted average temperature over the entrie coronal

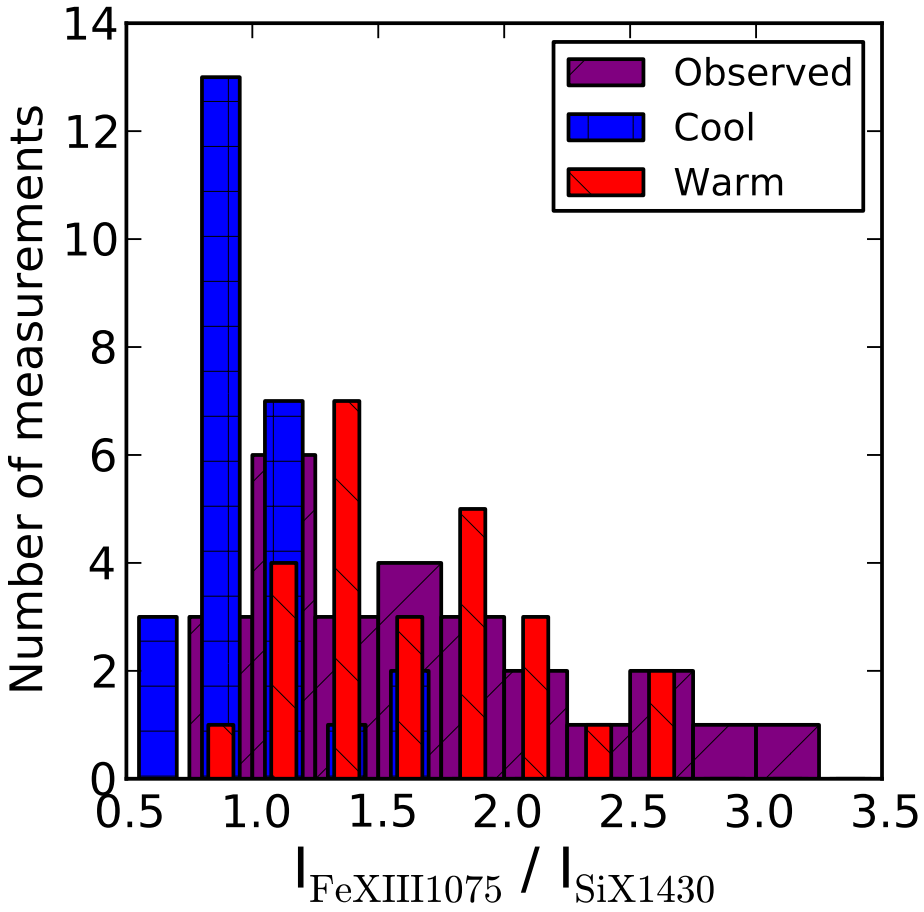

Figure 2.13: Distributions of FeXIII1075/SiX1430 ratios for the observations and synthetic emission from both MHD models. The width of all the bins is 0.25, but the synthetic bins are drawn with narrower widths to improve visibility.

volume at radii larger than 1.05 $R_\odot$using the formula

$$T_{cor} = \frac{\sum_{r=1.05}^{5} \sum_{\theta=0}^{\pi} \sum_{\phi=-\pi}^{+\pi} n_e^2 T}{\sum_{r=1.05}^{5} \sum_{\theta=0}^{\pi} \sum_{\phi=-\pi}^{+\pi} n_e^2} \tag{2.4.1}$$

The choice of a limiting inner radius is motivated by observation that the innermost corona is obscured during most of the eclipse. Midway through the eclipse the moon obscures 0.05 $R_\odot$ of the corona on all sides of the Sun so it is reasonable to assume that on average emission below this threshold is hidden from the detector. The resulting values for the temperature are 1.5 MK for the warm model and 1.3 MK for the cool model. These values are in good agreement with the temperatures determined from the emission line ratios and indicate that the observations tend to be in better agreement with the warm model. Further evidence that the warm model is in better agreement with the observations is presented in the following section discussing the continuum polarized amplitude variation with radius.

2.4.3 Continuum

The observed continuum polarization orientation is consistent with previous measurements of Thomson scattering polarization from free electrons in the corona (van de Hulst 1950). This type of scattering is characterized by linear polarization tangential to the solar limb, which we observed in most of the fibers where a reliable continuum signal is measurable (Figure 2.14). The continuum polarization amplitude increases up to 1.5 $R_\odot$ and then decreases with radius (Figure 2.15). This is consistent with previous observations of the continuum polarization amplitude and is due to the increasing contribution to the continuum from the weakly polarized F-corona. The scatter in the polarization amplitude measurements going around the solar limb is due to the changing LOS through different parts of the coronal density distribution(van de Hulst 1950).

The synthetic continuum polarization amplitudes obtained from Thomson scattering alone tend to overestimate the measurements at all radii, but agree better with the observations below 1.5 $R_\odot$ compared to further out. The real corona contains both scattered light from electrons (K-

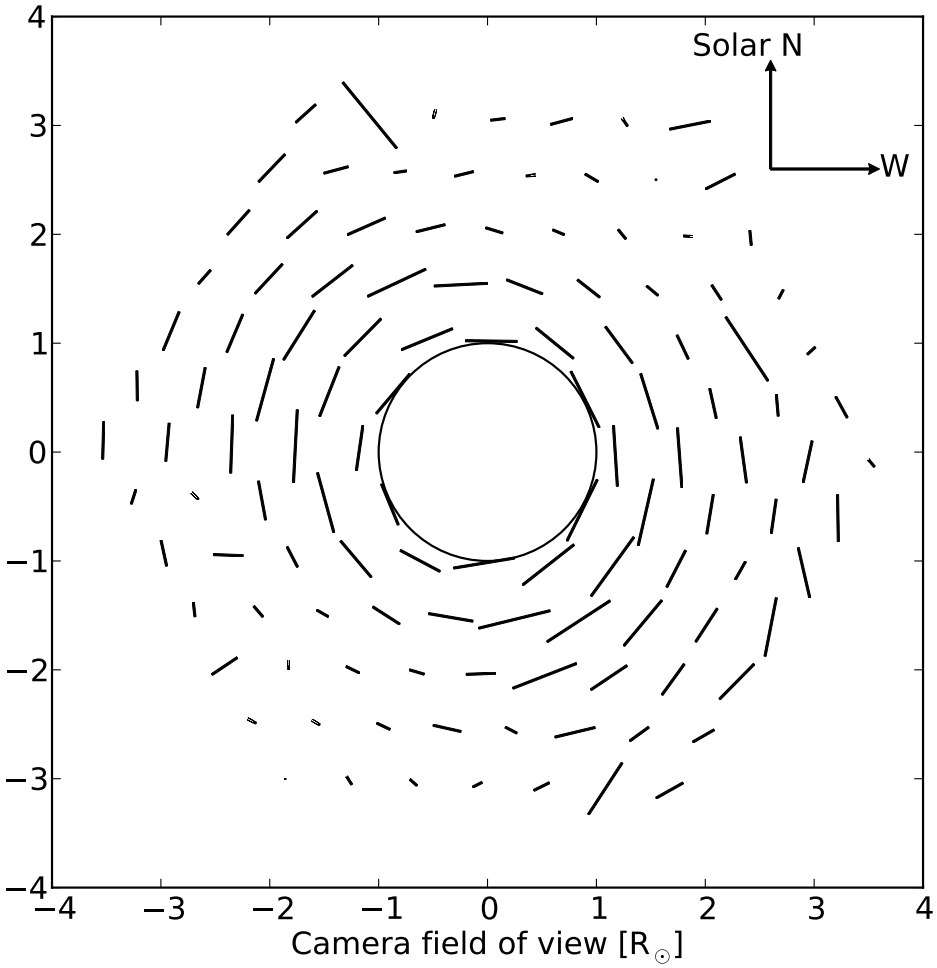

Figure 2.14: Continuum polarization vectors with lengths scaled to the polarization amplitudes. Some fibers far from the limb (r>2.5 $R_\odot$) have low S/N which leads to the anomalous orientations. The measured continuum polarization is tangential to the limb as expected from Thomson scattering off free electrons.

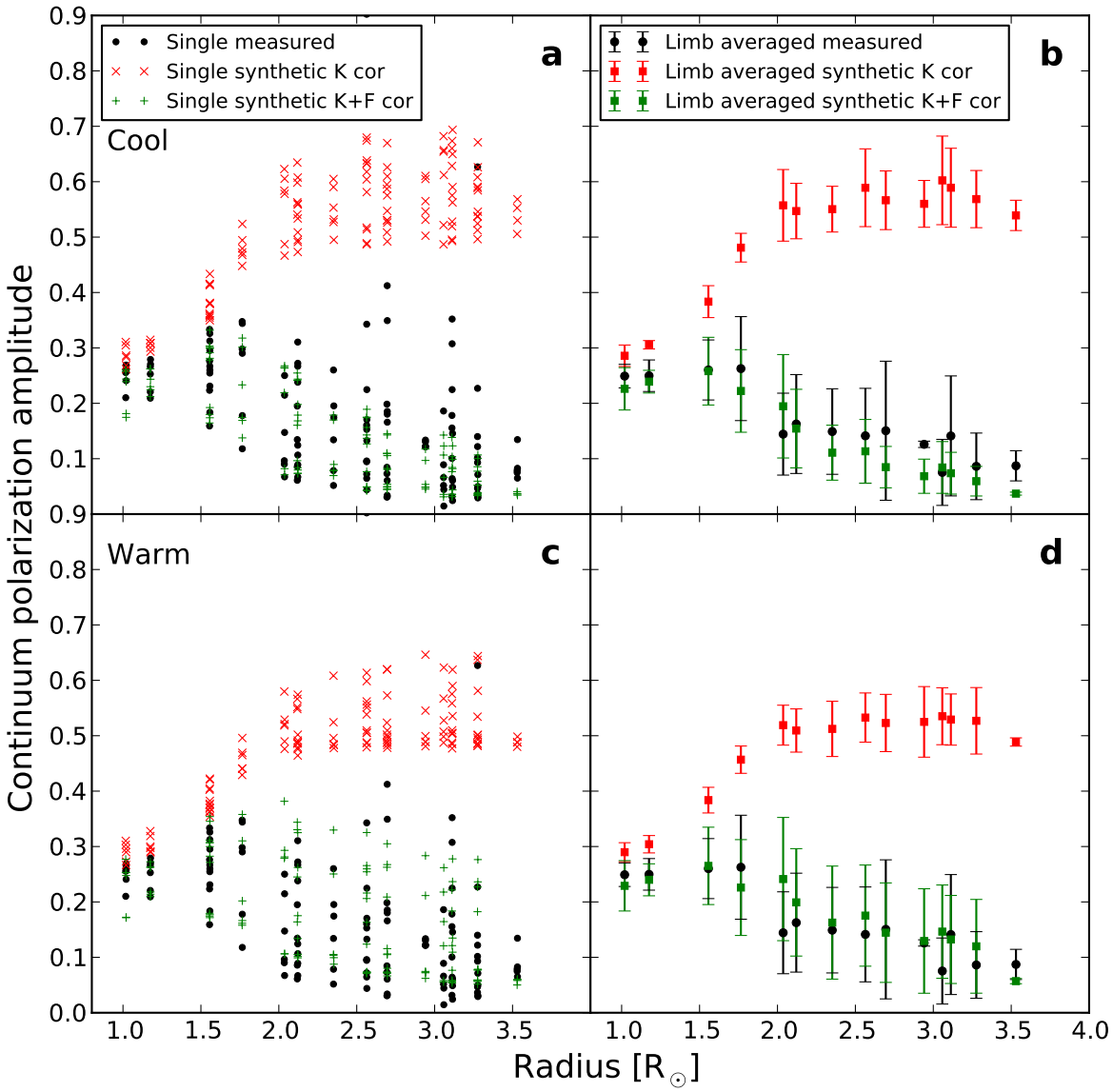

Figure 2.15: Observed continuum polarization amplitudes compared with the synthetic polarized amplitudes from the cold (a, b) and warm (c, d) MHD simulations. Panels a, c show individual measurements in each fiber while panels b, d show the limb averaged values together with the associated standard deviations for each radius bin. The red points correspond to synthetic emission due to the K-corona only which the green points are synthetic emission with F-corona corrections added.

corona) and from dust (F-corona) and while the F-corona contributes more further out from the limb the contribution is not negligible even very close to the limb. van de Hulst (1950) provides a set of corrections to the total continuum brightness that account for the F-corona down to the limb of the Sun (equation 2.2.1). Adding this correction to the continuum brightness improves the agreement between the observations and models surprisingly well. Given the limitations in the observations and intrinsic differences between the models and the real corona, individual fiber measurements do not agree exactly but performing an averaging around the limb at each radial location (Figure 2.15b,d) gives a better idea of the agreement between models and observations. Comparing the cold and warm MHD model distributions, we see that, within uncertainties, both models approximate the averages and spread in the observations at radii below 2.5 $R_\odot$. Both models reproduce the polarization amplitude peak at 1.5 $R_\odot$, with the cooler model underestimating the amount of polarization at radii above 2.5 $R_\odot$. This effect may be explained by the steeper falloff in the electron density at larger radii in the cool model compared to the warm model (Figure 2.2b). Having fewer electrons to scatter light at larger radii leads to smaller contributions to the K-corona brightness which in turn leads to decreased polarized amplitudes for the same F-coronal contribution to the total intensity.

The agreement between the observations and models suggests that the relative contributions between the F and K components to the continuum has remained relatively constant over the past 70 years since van de Hulst (1950) published their work. This conclusion is supported by Saito et al. (1977) who studied F-corona brightness temporal variations at radii larger than 3 $R_\odot$ over the Skylab period and concluded that it is constant to 10%. Morgan & Habbal (2007) also found that F-coronal brightness remains unchanged over the solar cycle in the visible at heights between 3-6 $R_\odot$. Solar eclipses offer the unique opportunity to study the F-corona stability in the regions very close to the limb while space based observatories can only observe down to 2 $R_\odot$.

2.4.4 HeI1083 emission

The 1994 detection of HeI1083 emission reaching far from the limb into the corona is an important clue that our understanding of the coronal structure may be incomplete. At coronal temperatures,

there should be no detectable emission from neutral He in ionization equilibrium. Since then ground-based observations of the line outside of eclipse conditions (Kuhn et al. 2007; Moise et al. 2010) have achieved polarized detections of this line. The emission signal is weak (polarized brightness of order 10^{-8}) so confirming measurements are difficult. Because a lenslet optical feed for the fibers in this experiment could not be obtained in time for the eclipse, these measurements have marginal sensitivity. In retrospect, the attempt to spatially de-alias the measurements by defocusing the image on the fiber bundle also limited our sensitivity, but one of the fibers detected a HeI1083 signal that is not consistent with chromospheric emission. Clarifying this detection is an important goal since HeI1083 is the only permitted IR line available and it has the potential to unlock new magnetic field diagnostics in the corona through the Hanle effect (Dima et al. 2016).

The 2006 eclipse afforded another opportunity to detect this line and measure its linearly polarized properties. Some HeI1083 emission was detected in twelve fibers located in two clusters on either side of the limb during the two parts of the eclipse (Figure 2.16). One cluster of six fibers is located on the NE limb (fibers 26, 7, 76, 54, 86 and 51) and the other cluster is located on the SW limb (fibers 109, 58, 115, 11, 65 and 9).

HeI1083 intensities measured in each fiber are shown in Figure 2.17 and fibers are grouped together according to the approximate locations on the image before and after the middle of the eclipse, although the image displacement before and after is only approximately known. Most fibers show HeI1083 intensity that is much larger than the diffuse flux observed previously. These observed fiber signals also vary due to the moon's progression across the presumed near-limb chromospheric emission. An additional check for a cool chromospheric source of this HeI signal comes from looking for simultaneous emission from the Paschen HI 1.282 μm line (hereafter HI1282). We find that all but two fibers show strongly correlated HI1282 emission (Figure 2.18) which is further evidence that this bright, time-varying HeI emission comes from cool chromospheric material contaminating the fibers due to the telescope defocus.

We note that the linear relationship between the HeI1083 and HI1282 emission appears to have two regimes. The slope of the relationship for all the fibers changes once the HeI1083 emission falls below about 3×10^{-6} $B_{\odot}$. Plotting the ratio HeI1083/HI1282 af a function of HeI1083 intensity

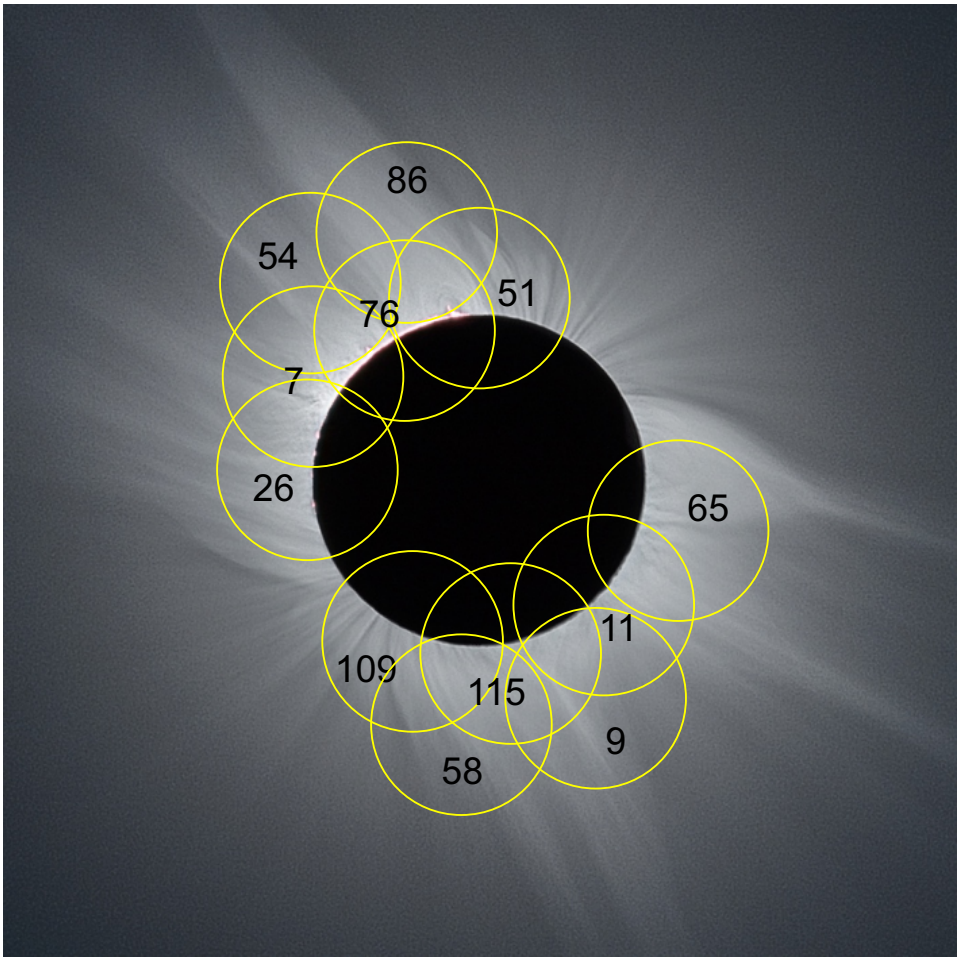

Figure 2.16: Fibers where HeI1083 emission is detected during the eclipse shown over a processed white light image of the corona obtained on the day of the eclipse. Fiber 86 can be seen to straddle a large streamer but it is also located near an elongated prominence.

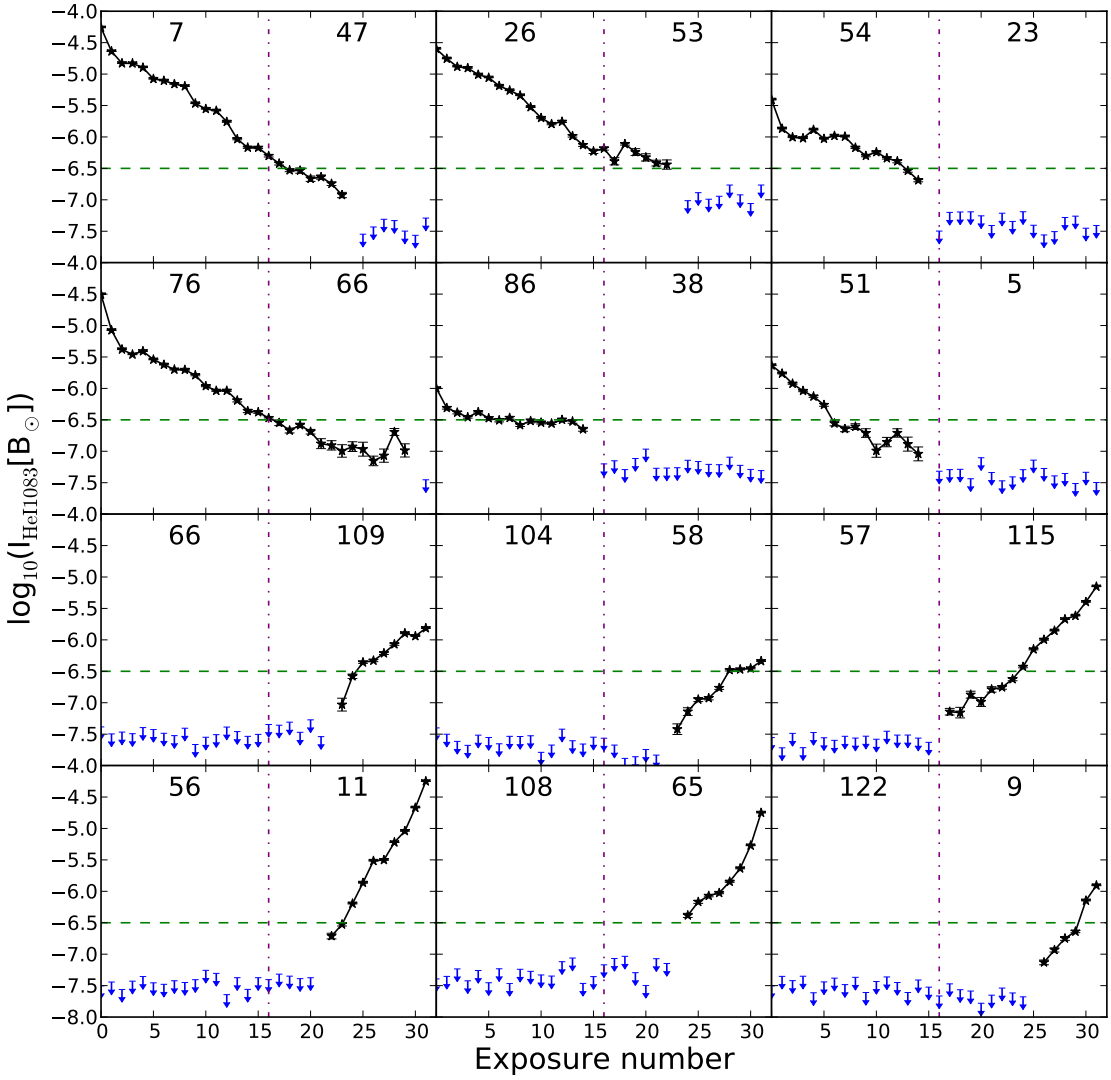

Figure 2.17: Measured HeI1083 line brightness for all the fibers where it is detected. The numerical fiber labels are shown in each panel with the first number corresponding to fibers in the first half of the eclipse and the second number corresponding to the fiber number observing approximately the same coronal region during the second half of the eclipse. The arrows indicate upper limits on detections corresponding to 3σ of the continuum noise near the line. The purple dot-dash line indicates the moment the image shifted. Green dashed lines indicate the measured intensity for HeI1083 during the 1994 eclipse (Kuhn et al. 1996).

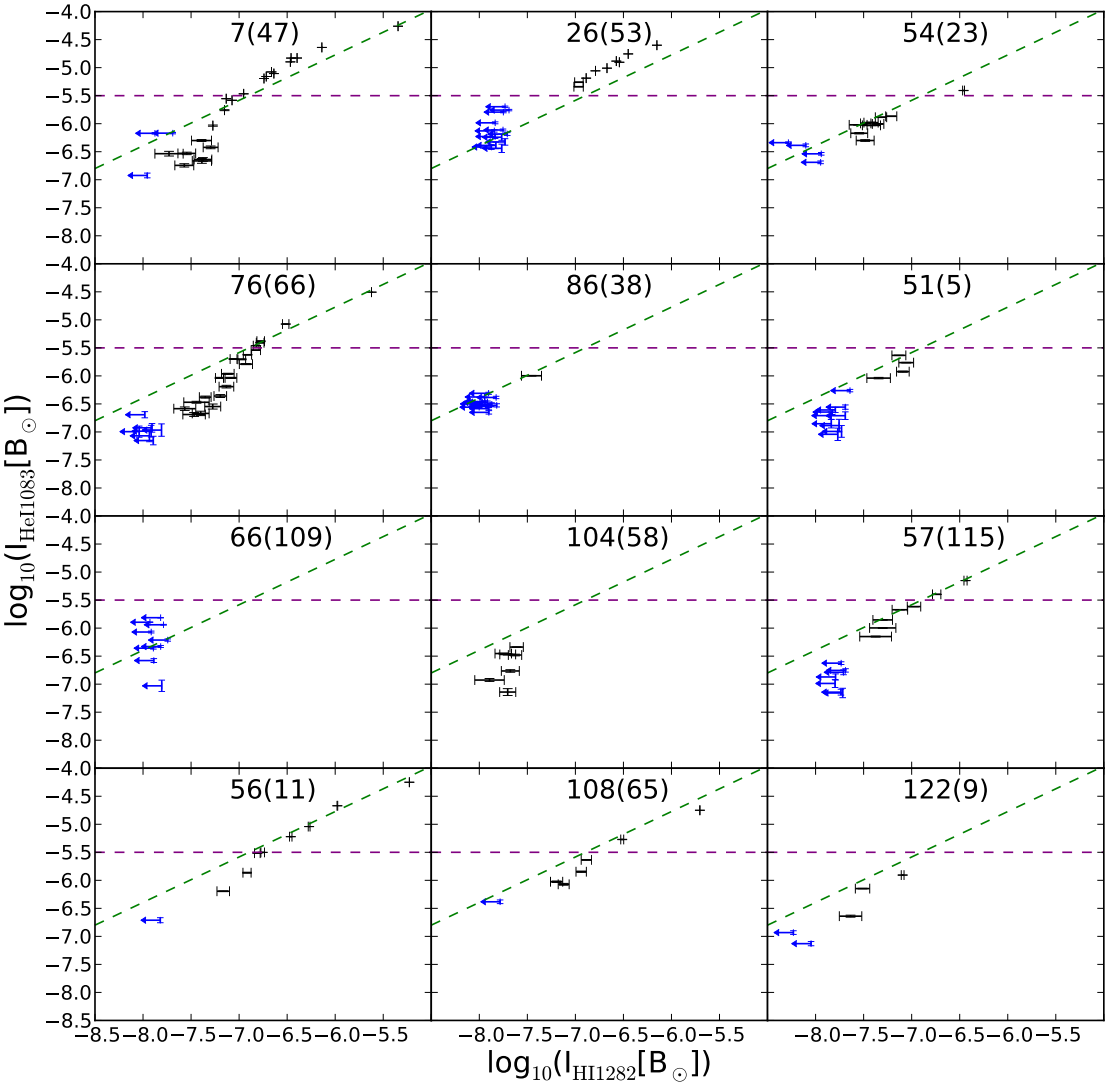

Figure 2.18: Correlation between the HeI1083 and the HI1281 line intensities for the same fiber labels as in Figure 2.17. All points shown are HeI1083 detections while upper limits for the HI1281 line are indicated by the blue arrows. Correlations between the two lines are seen in most of the fibers apart from 86 and 66. The green dashed line is a visual aid indicating the approximate relationship between emission from the two lines for HeI1083 intensities above 3×10^{-6} $B_{\odot}$. The purple dashed line indicates the intensity level where most of the fibers show a change in the correlation.

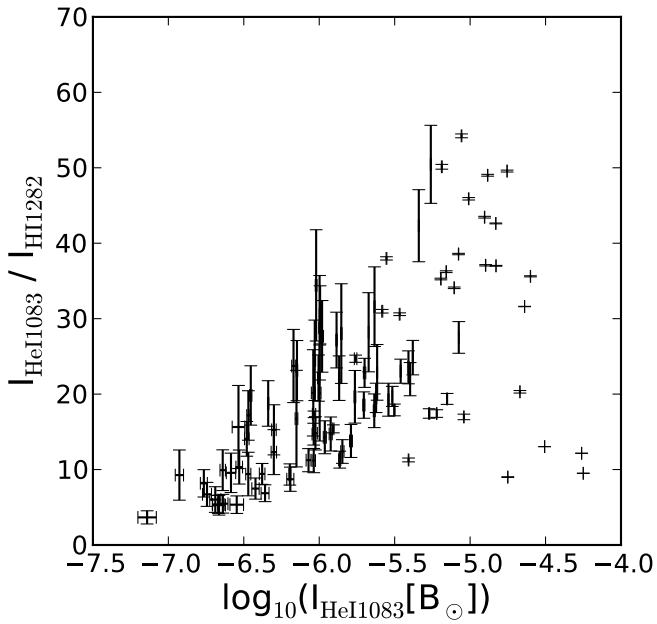

Figure 2.19: Relationship between the HeI1083/HI1282 emission ratio and the total HeI1083 emission. Data from all fibers is shown.

(Figure 2.19) also indicates the relationship between the emission in the two lines has different regimes. One interpretation for the variation is that chromospheric HeI and HI emission has a different radial extent with HeI emission appearing much stronger at smaller radii. At this time we will leave further interpretation of this relationship for future work since it likely requires modeling of the distribution of HeI and HI emission in chromospheric and prominence material.

Fibers 86 and 109 shows no detectable HI1282 emission at the 2×10^{-8} $B_\odot$ level correlated with the detected HeI1083 emission. Fiber 109 has relatively rapidly varying HeI1083 emission that increases over the last 8 exposures to 2×10^{-6} $B_\odot$. Fiber 86, however, shows nearly constant HeI1083 brightness at a signal level that remains relatively constant and is around the bright limit of 3×10^{-7} $B_\odot$ level reported by Kuhn et al. (1996). Analyzing the HeI1083 emission for fiber 86 reveals a polarized amplitude around 0.1 (Figure 2.20) which places the polarized brightness around 3×10^{-8} $B_\odot$ which is consistent with SOLARC measurements reported by Moise et al. (2010). However, even though the fiber core is located at a radius of 1.5 $R_\odot$, the continuum in this fiber does show some variability during the eclipse which indicates this fiber may also have contamination from a prominence source contained in the defocused illumination of this fiber, despite the lack of

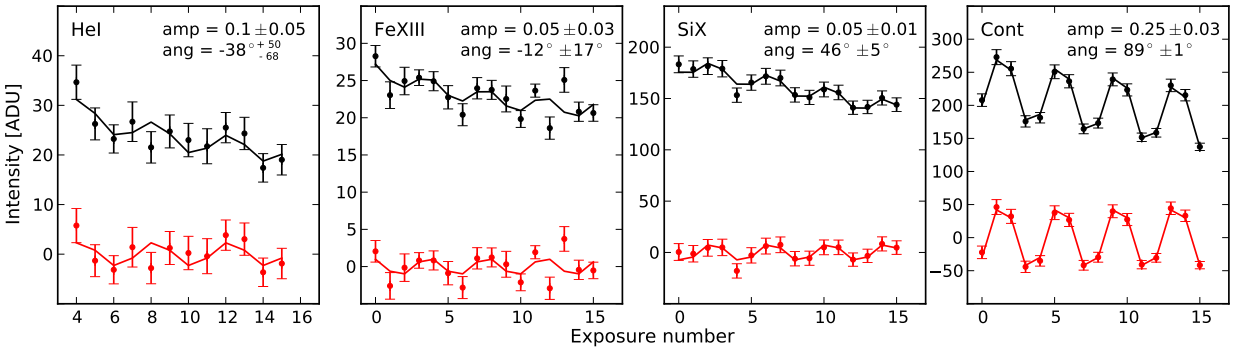

Figure 2.20: Line intensity and continuum measurements and polarimetric fits for fiber 86. The black points represent the observed values together with the polarized fits to the data. The red points show only the polarized brightness variation with the total intensity subtracted. Calculated polarized amplitudes and angles (measured in the local solar radial frame) are given in the upper right hand corners of each panel.

correlated HI1282 emission.

Absent a direct disc center calibration, the values shown in Figures 2.17 and 2.18 are calibrated using the synthetic emission from the MHD models. Because the telescope defocus effectively smears out small scale inhomogeneities in the corona, as long as the MHD models accurately approximate the white light brightness on scales larger than the defocus radius, the synthetic emission can serve as an adequate proxy for the disk calibration. This eclipse measurement interpretation suffers from a relatively poor spatial sampling function due to the image defocus with all of the fibers where HeI1083 emission is detected showing variation in the continuum indicating likely contamination with chromospheric sources. As a proof of concept of the dual-line method (Dima et al. 2016), if we assume that the coronal magnetic field is only weakly varying then we can combine the SiX1430 and HeI1083 measurements to deduce the local coronal field and direction. For example, we find that the HeI1083 signal at fiber 86 has a polarization amplitude of 0.1, but a poorly defined direction while the SiX1430 signal shows polarization with a well-defined angle. We can use the forbidden line polarized angle to constrain the inclination and azimuth of the magnetic field in the local radial coordinate frame. Using the HeI atomic modeling code "Hanle and Zeeman Light" (HAZEL, Asensio Ramos et al. 2008) we can create expected polarized emission grids for a variety of magnetic field strengths and orientations (Figure 2.21). Comparing the measured HeI1083 polarization amplitude with these grids yields an upper limit around 2 G for the magnetic field strength. However, since

the HeI1083 polarization angle is poorly constrained by the present data the orientation of the field is also poorly constrained.

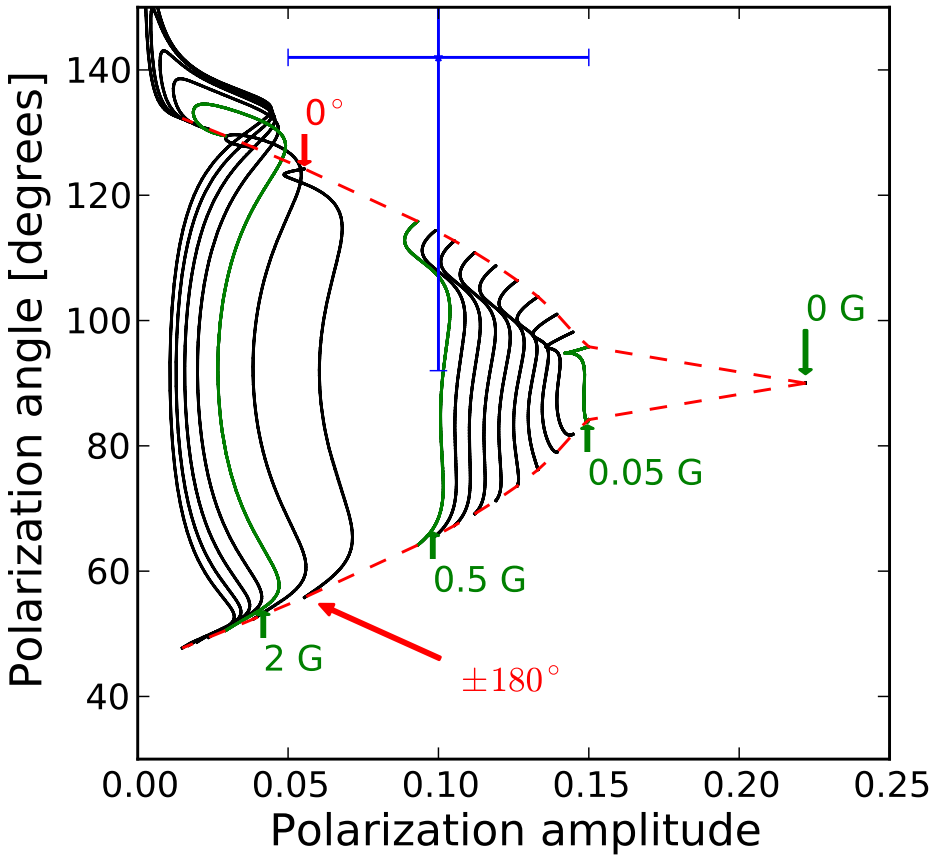

Figure 2.21: Example of a model grid for polarized HeI1083 emission assuming emission from a source located at a radius of 1.5 $R_\odot$ constructed using the method described in Dima et al. (2016). The black and green lines represent constant magnetic field strength contours with a few values shown for reference. The red dashed lines represent constant magnetic azimuth angle contours. The blue cross represents the measured HeI1083 polarization in fiber 86 where the angle is highly uncertain but the polarization amplitude is more tightly constrained. The polarized amplitude can be used to set a constraint on the strength of the magnetic field since the field strength increases approximately monotonically towards the left of the plot.

2.5 Conclusions

During the 2006 total solar eclipse linearly polarized coronal emission was measured in the near-IR 1-2 μm region over a wide field of view covering 7 $R_\odot$. The observations yielded detections of the

FeXIII1075, HeI1083, HI1282 and SiX1430 emission lines in many of the fibers near the limb of the Sun.

To understand the solar corona better we need more IR emission line diagnostic tools in preparation of the type of observations possible with the next generation solar telescopes. Observing combinations of lines like SiX1430 and FeXIII1075 that peak in intensity at different temperatures is a powerful temperature diagnostic of the corona. Furthermore, the SiX1430 emission line is measured to have an unexpectedly large polarization amplitude (around 7.5%). Outside coronal conditions, ground-based observations of the corona have to contend with very bright background sky emission that make very dim coronal line intensity measurements difficult to obtain. Having a stronger polarized signal makes detection through spectropolarimetry significantly easier since the sky is essentially unpolarized close to the solar limb and can be subtracted out

Comparison of line and continuum observations with synthetic emission from two MHD models with different heating functions and boundary conditions shows that the warmer MHD model indicates closer agreement with the available data. The density-weighted average coronal temperature of the model was consistent with a corona near a temperature of 1.5 MK based on a new interpretation of the FeXIII1075/SiX1430 ratio. This is supported by the observed radial variation of the continuum polarization amplitude which agrees with the electron density falloff in the warmer MHD model. This conclusion is based on the assumption that the F-corona brightness has remained steady over the past 70 years.

We detected HeI1083 emission in 12 near-limb fibers. Most of the fibers show correlated emission in the HI1282 Paschen line. The slope of the correlation varies depending on the strength of the HeI1083 emission hinting at some underlying chromospheric mechanism for producing the two lines. One fiber located at 1.5 $R_\odot$ yielded a possible detection of the diffuse coronal HeI1083 signal at the 3×10^{-7} $B_\odot$ level but contamination from chromospheric light could not be ruled out since the continuum in the fiber showed variation during the eclipse.

BIBLIOGRAPHY

Altrock, R. C. 2004, Sol. Phys., 224, 255

Arnaud, M., & Rothenflug, R. 1985, A&AS, 60, 425

Arnaud, J., & Newkirk, G., Jr. 1987, A&A, 178, 263

Asensio Ramos, A., Trujillo Bueno, J., & Landi Degl'Innocenti, E. 2008, ApJ, 683, 542-565

Bommier, V., Sahal-Brechot, S., & Leroy, J. L. 1981, A&A, 100, 231

Brueckner, G. E., Howard, R. A., Koomen, M. J., et al. 1995, Sol. Phys., 162, 357

Casini, R., & Judge, P. G. 1999, ApJ, 522, 524

Dima, G., Kuhn, J., & Berdyugina, S. 2016, Frontiers in Astronomy and Space Sciences, 3, 13

Dere, K. P., Landi, E., Mason, H. E., Monsignori Fossi, B. C., & Young, P. R. 1997, A&AS, 125,

Dolei, S., Spadaro, D., & Ventura, R. 2015, A&A, 577, A34

Downs, C., Lionello, R., Mikic, Z., Linker, J., & Velli, M. M. 2013, AGU Fall Meeting Abstracts,

Eddy, J. A., Lee, R. H., & Emerson, J. P. 1973, Sol. Phys., 30, 351

Gibson, S. E., Kucera, T. A., Rastawicki, D., et al. 2010, ApJ, 724, 1133

Gibson, S., Kucera, T., White, S., et al. 2016, Frontiers in Astronomy and Space Sciences, 3, 8

Habbal, S. R., Woo, R., & Arnaud, J. 2001, ApJ, 558, 852

Habbal, S. R., Arndt, M. B., Nayfeh, M. H., et al. 2003, ApJ, 592, L87

Habbal, S. R., Kuhn, J., Mickey, D., et al. 2006, Solar Physics and Solar Eclipses (SPSE 2006), 27

Habbal, S. R., Morgan, H., Johnson, J., et al. 2007, ApJ, 663, 598

Habbal, S. R., Morgan, H., Druckmüller, M., & Ding, A. 2010, ApJ, 711, L75

House, L. L. 1974, PASP, 86, 490

House, L. L. 1977, ApJ, 214, 632

van de Hulst, H. C. 1950, Bull. Astron. Inst. Netherlands, 11, 135

Ishikawa, R., Bando, T., Fujimura, D., et al. 2011, Solar Polarization 6, 437, 287

Judge, P. G. 1998, ApJ, 500, 1009

Judge, P. G., & Casini, R. 2001, Advanced Solar Polarimetry – Theory, Observation, and Instrumentation, 236, 503

Judge, P. G., Low, B. C., & Casini, R. 2006, ApJ, 651, 1229

Kasper, J. C., Stevens, M. L., Korreck, K. E., et al. 2012, ApJ, 745, 162

Kuhn, J. R. 1995, Infrared tools for solar astrophysics: What's next?, 89

Kuhn, J. R., Penn, M. J., & Mann, I. 1996, ApJ, 456, L67

Kuhn, J. R., Coulter, R., Lin, H., & Mickey, D. L. 2003, Proc. SPIE, 4853, 318

Kuhn, J. R., Arnaud, J., Jaeggli, S., Lin, H., & Moise, E. 2007, ApJ, 667, L203

Koutchmy, S., & Lamy, P. L. 1985, IAU Colloq. 85: Properties and Interactions of Interplanetary Dust, 119, 63

Landi, E., Young, P. R., Dere, K. P., Del Zanna, G., & Mason, H. E. 2013, ApJ, 763, 86

Landi, E., & Testa, P. 2014, ApJ, 787, 33

Lepri, S. T., Landi, E., & Zurbuchen, T. H. 2013, ApJ, 768, 94

Lin, H., Penn, M. J., & Tomczyk, S. 2000, ApJ, 541, L83

Lin, H., Kuhn, J. R., & Coulter, R. 2004, ApJ, 613, L177

Lionello, R., Linker, J. A., & Mikić, Z. 2009, ApJ, 690, 902

Liu, Y., & Lin, H. 2008, ApJ, 680, 1496-1507

López Ariste, A., & Casini, R. 2003, ApJ, 582, L51

Mann, I. 1992, A&A, 261, 329

Merenda, L., Trujillo Bueno, J., Landi Degl'Innocenti, E., & Collados, M. 2006, ApJ, 642, 554

Minnaert, M. 1930, ZAp, 1, 209

Mikić, Z., Linker, J. A., Lionello, R., Riley, P., & Titov, V. 2007, Solar and Stellar Physics Through Eclipses, 370, 299

Moise, E., Raymond, J., & Kuhn, J. R. 2010, ApJ, 722, 1411

Morgan, H., & Habbal, S. R. 2007, A&A, 471, L47

Münch, G., Neugebauer, G., & McCammon, D. 1967, ApJ, 149, 681

Olsen, K. H., Anderson, C. R., & Stewart, J. N. 1971, Sol. Phys., 21, 360

Penn, M. J., & Kuhn, J. R. 1994, ApJ, 434, 807

Penn, M. J. 2014, Living Reviews in Solar Physics, 11

Saito, K., Poland, A. I., & Munro, R. H. 1977, Sol. Phys., 55, 121

Sahal-Brechot, S., Bommier, V., & Leroy, J. L. 1977, A&A, 59, 223

Schou, J., Scherrer, P. H., Bush, R. I., et al. 2012, Sol. Phys., 275, 229

Schuster, A. 1879, MNRAS, 40, 35

Schrijver, C. J., & De Rosa, M. L. 2003, Sol. Phys., 212, 165

Smith, C. W., L'Heureux, J., Ness, N. F., et al. 1998, Space Sci. Rev., 86, 613

von Steiger, R., & Zurbuchen, T. H. 2011, Journal of Geophysical Research (Space Physics), 116, A01105

Tomczyk, S., Card, G. L., Darnell, T., et al. 2008, Sol. Phys., 247, 411

Wallace, L., Livingston, W., Hinkle, K., & Bernath, P. 1996, ApJS, 106, 165

Wiegelmann, T., Petrie, G. J. D., & Riley, P. 2015, Space Sci. Rev.,

CHAPTER 3
HANLE EFFECT INVERSION ALGORITHM

ABSTRACT

Measuring the coronal vector magnetic field is still a major challenge in solar physics. This is due to the intrinsic weakness of the field (e.g. $\sim$ 4G at a height of $0.1R_{\odot}$ above an active region) and the large thermal broadening of coronal emission lines. We propose using concurrent linear polarization measurements of near-infrared forbidden and permitted lines together with Hanle effect models to calculate the coronal vector magnetic field. In the unsaturated Hanle regime both the direction and strength of the magnetic field affect the linear polarization, while in the saturated regime the polarization is insensitive to the strength of the field. The relatively long radiative lifetimes of coronal forbidden atomic transitions implies that the emission lines are formed in the saturated Hanle regime and the linear polarization is insensitive to the strength of the field. By combining measurements of both forbidden and permitted lines, the direction and strength of the field can be obtained. For example, the SiX 1.4301μm line shows strong linear polarization and has been observed in emission over a large field-of-view (out to elongations of 0.5 $R_{\odot}$). Here we describe an algorithm that combines linear polarization measurements of the SiX 1.4301μm forbidden line with linear polarization observations of the HeI 1.0830μm permitted *coronal* line to obtain the vector magnetic field. To illustrate the concept we assume that the emitting gas for both atomic transitions is located in the plane of the sky. The further development of this method and associated tools will be a critical step towards interpreting the high spectral, spatial and temporal infrared spectro-polarimetric measurements that will be possible when the Daniel K. Inouye Solar Telescope (DKIST) is completed in 2019.

3.1 Introduction

Magnetometry using optical spectropolarimetry has yielded some of the most precise direct measurements of coronal magnetic fields (Kuhn 1995; Lin et al. 2000, 2004; Tomczyk et al. 2008). Earlier infrared(IR) coronal Zeeman observations (e.g., Arnaud & Newkirk 1987; Kuhn 1995) have used forbidden FeXIII transitions near 1 micron. The larger context of all coronal magnetometry techniques has been reviewed elsewhere (e.g., Penn 2014), but the great promise of the Daniel K. Inouye Solar Telescope (DKIST) will be to use near-IR coronal lines to routinely observe the so far seldom measured weak solar coronal magnetic field. Up until now attempts from the ground to measure the magnetic field strength have depended on the ability to detect very weak Zeeman splitting through Stokes-V (circular) polarization observations. A Gauss-scale coronal magnetic field creates very weak Stokes-V signals (typically 10^{-4}) in spectral lines that are dominated by much stronger linear scattering polarization amplitudes (e.g. Stokes-Q and U of order 10^{-2} and sometimes up to 10^{-1}, Lin et al. (2004)).

Most recently linear polarization observations of permitted lines combined with forward calculations of field configurations have been productive tools for understanding solar prominence magnetic fields (Bommier et al. 1981; López Ariste & Casini 2003; Merenda et al. 2006). A powerful coronal field diagnostic follows from simultaneous measurements of the optical scattering linear polarization of combined forbidden and permitted spectral lines. Early work on the possibility of using lines with different Hanle sensitivity used the HeI 0.5875μm and HeI 1.0830μm (hereafter HeI1083) lines for measuring the magnetic field in a prominence located in the plane of the sky (Bommier et al. 1981). Recently space spectropolarimetric observations of the permitted coronal Lyα line have been attempted (Ishikawa et al. 2011). The discovery of HeI1083 line far into the corona (Kuhn et al. 1996, 2007) has now made it feasible to measure coronal fields in the $0.1 - 10$G range using only linear polarimetry of the HeI1083 line and another forbidden coronal line – such as the newly characterized SiX 1.4301μm (hereafter SiX1430) line.

For practical reasons the IR spectrum is particularly useful for ground-based studies of the corona because spurious background noise from both the atmosphere and optical scattering in telescopes

and instruments decreases with increasing wavelength (Kuhn et al. 2003). Terrestrial thermal emission below 1.8 μm is also inconsequential. Observations (Kuhn et al. 1996) and calculations (Judge 1998) have described new IR forbidden lines that could be useful as spectropolarimetry diagnostics. Only the HeI1083 line has been observed as a promising IR permitted line for Hanle magnetometry. Some earlier measurements revealed diffuse coronal neutral triplet-state Helium associated with streamers (Kuhn et al. 1996). This initial measurement was eventually confirmed to have solar origin through ground-based spectro-polarimetric observations using the Scatter-free Observatory for Limb, Active Regions, and Coronae (SOLARC) telescope on Haleakala (Kuhn et al. 2007; Moise et al. 2010). The diffuse HeI emission is generated by scattering of photospheric radiation by the triplet state of HeI. The narrow line-width observed for this emission is consistent with the triplet states being produced primarily through electron collisional excitation of singlet-state neutral He in the higher density K-corona, rather than collisional recombination of He^+ ions (Moise et al. 2010).

3.2 Dual-line Hanle magnetic diagnostics

The Hanle effect causes a change in the polarization of atomically scattered optical radiation due to the presence of a magnetic field. The magnetic field splits atomic levels into 2J+1 magnetic sublevels (J is the total angular momentum) via the Zeeman effect. If sublevels of the upper level are unevenly populated through their coupling to an anisotropic solar radiation field, then the emission line can be polarized. When the Zeeman splitting is comparable to the energy spread of the upper level (i.e., the Larmor frequency is smaller than or comparable to the total line emission transition rate), quantum mechanically induced wavefunction interferences will modify the scattering polarization magnitude and rotate the polarization plane by an amount that depends on the field – this is the unsaturated Hanle effect.

The coronal vector magnetic field at a point in the corona is uniquely described by the magnetic flux density $|\mathbf{B}| \equiv \mathrm{B}$, the inclination angle θ_B (with respect to the local outward solar radial direction) and the azimuth angle χ_B in a plane perpendicular to the radial direction (Figure 3.1). For a scattering geometry where the emission takes place in the plane-of-sky (POS) we can freely

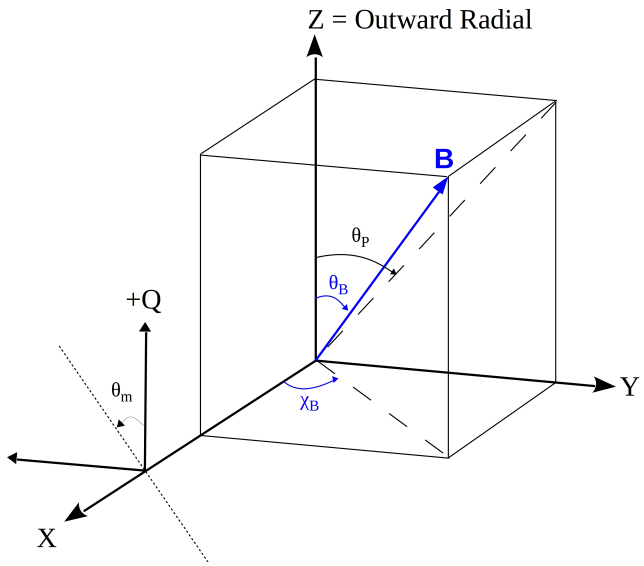

Figure 1. Observing geometry for a magnetic field located in the plane of the sky (corresponding to the ZY plane). The +Z direction indicates the local outward radial direction so moving around the solar limb corresponds to a rotation about the X axis which is taken to coincide with the line of sight. The projected angle of magnetic field on the plane sky $\theta_{\rm P}$ is measured clockwise, while the angle of polarization $\theta_{\rm m}$ is measured counter-clockwise adhering to the common polarimetric convention. The reference direction for the polarization measurement is oriented along the outward radial direction.

choose the reference axis for the $\chi_{\rm B}$ angle to coincide with the line of sight axis. In the unsaturated Hanle regime, when the atomic Larmor frequency is comparable to the inverse upper-level lifetime, the linear polarization of an emission line is sensitive to all three B-vector parameters, while in the saturated Hanle regime (when the Larmor frequency is much larger than the inverse lifetime) only the angles ($\theta_{\rm B}$, $\chi_{\rm B}$) influence the linear polarization. The B value at which the transition between the two regimes takes places is not a sharp value. In fact, a gradual loss of sensitivity takes place above the critical field strength $\rm B_H$, which depends on the Lande factor $\rm g'$ and the lifetime τ' of the upper level:

$$\rm B_H = \frac{\hbar}{\mu_B g' \tau'} \tag{3.2.1}$$

where $\mu_{\rm B}$ is the Bohr magneton.

The dual-line vector magnetometry technique we propose here relies on simultaneous observations of both permitted and forbidden coronal lines. Near-IR observable coronal lines such as

SiX1430, FeXIII 1.0747 μm (hereafter FeXIII1075) and HeI1083 have good polarized atomic modeling available (e.g., House 1974; Sahal-Brechot et al. 1977; Casini & Judge 1999; Asensio Ramos et al. 2008). The critical field strength $B_{\rm H}$ for the HeI1083 transition is 0.77G (Bommier et al. 1981) while the forbidden lines have critical field strengths in the 10^{-5}G range (House 1974). The two forbidden lines are firmly in the saturated Hanle regime, while the permitted HeI line maintains Hanle sensitivity up to $\sim$ 8G. In their analysis, Bommier et al. (1981) found the unsaturated Hanle magnetic sensitivity of the HeI1083 line to be significant between $0.1{\rm B_H} < {\rm B} < 10{\rm B_H}$.

The only known visible or IR coronal permitted line is HeI1083. Using current observatories like SOLARC, it is possible to combine near-IR observations of HeI1083 with the FeXIII1075 or SiX1430 lines. When DKIST comes on-line, potentially longer wavelength IR spectropolarimetry in the near-thermal IR will be possible. To date, emphasis has been placed on FeXIII1075 observations for coronal spectro-polarimetry (Tomczyk et al. 2008), although observations during the total solar eclipse on March 29, 2006 (Dima et al, 2016, in preparation) show that SiX1430 emission can be significantly brighter than FeXIII1075. The experiment for that eclipse used a wide-field fiber fed spectropolarimeter. Figure 3.2 gives a comparative view of the line signal/noise in each of the fibers. During the same eclipse HeI1083 emission was also observed, although that spectropolarimeter did not have the sensitivity to demonstrate Hanle magnetometry. Nevertheless, these IR measurements clearly point to the importance of the SiX1430 line. Since the FeXIII and SiX ion abundances peak at different temperatures this result highlights the need to have multiple coronal lines accessible for polarimetry that sample different temperature regimes of the corona. While the analysis and examples presented below discuss the SiX1430 line, they can apply equally well to FeXIII1075 observations since the two lines have very similar polarization properties (Judge et al. 2006).

3.3 Algorithm description

Forbidden lines like FeXIII1075 and SiX1430 have radiative decay rates that are not so different from the electron collision rate at coronal densities. Thus, isotropic collisions can depolarize the Zeeman substate populations in the upper levels of the lines. Mixing occurs through both electron collisions and indirectly through cascades from excited higher levels that can have substantially

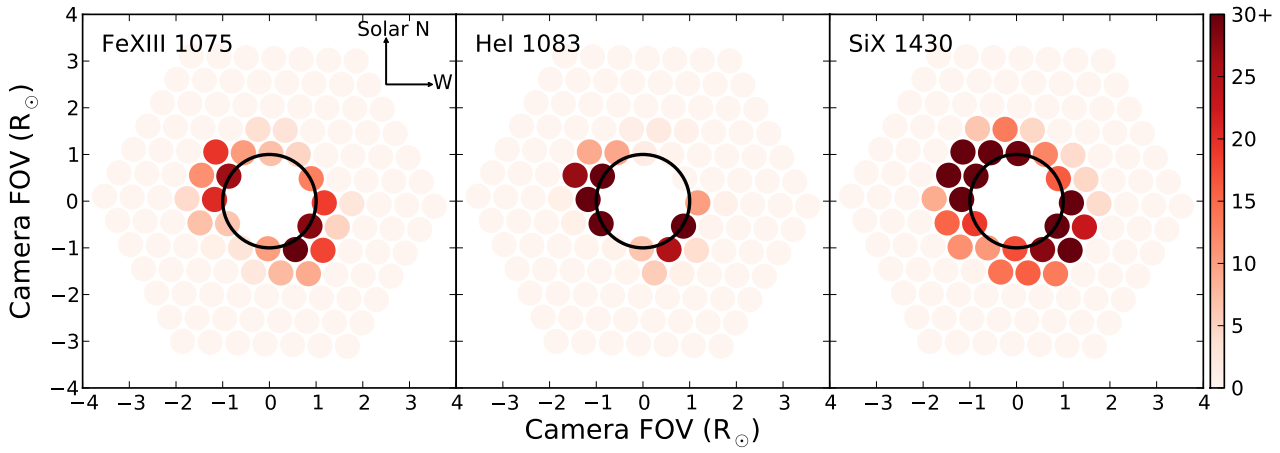

Figure 2. Spatial sampling of the corona during the March 29, 2006 total eclipse. A hexagonal array of 127 fibers sparsely sampled the coronal image plane. Each plot shows the signal/noise measured in each fiber for the lines indicated. One key result from these measurements is the large spatial extent of bright SiX1430 emission compared to FeXIII1075 emission.

higher downward transition rates (Sahal-Brechot et al. 1977; Judge et al. 2006). This collisional depolarization has a density dependence which is difficult to accurately model, but only affects the amplitude of the forbidden line polarization (Judge & Casini 2001). Consequently, our method in its current form only employs the polarization angle in the forbidden lines which is independent of isotropic collisional effects.

Lines in the saturated Hanle regime maintain a fixed angular relationship between the linear polarization plane (characterized by the polarization angle $\theta_{\rm m}$ and the projected magnetic field orientation on the plane of the sky (characterized by the projected angle $\theta_{\rm P}$) as shown in Figure 3.1. The magnetic field orientation angles ($\theta_{\rm B}$, $\chi_{\rm B}$) are related to the projected angle $\theta_{\rm P}$ by

$$\tan\theta_{\rm P} = \tan\theta_{\rm B}\sin\chi_{\rm B} \tag{3.3.1}$$

For magnetic dipole transitions like SiX1430 the polarization plane is parallel to the magnetic field when $\theta_{\rm B} < \theta_{\rm VV}$ or $\theta_{\rm B} > 180^\circ - \theta_{\rm VV}$ and perpendicular when $\theta_{\rm VV} < \theta_{\rm B} < 180^\circ - \theta_{\rm VV}$, where $\theta_{\rm VV} = 54.7^\circ$ is the Van Vleck angle. This effect leads to the Van Vleck ambiguity (e.g., House 1974): one measured pair of Stokes Q, U corresponds to at least two pairs of possible magnetic field orientation angles. This ambiguity only applies to a subset of possible field inclinations: all linearly

polarized emission from fields with $\theta_{\rm VV} < \theta_{\rm B} < 180^\circ - \theta_{\rm VV}$ is ambiguous with respect to a set of field inclinations outside this inclination domain.

In contrast, the HeI1083 permitted line has an upper level lifetime six orders of magnitude shorter. Collisions have a negligible effect on polarization amplitudes permitted lines at coronal densities. Thus, both the polarization angle and amplitude can be modeled without detailed knowledge of the coronal electron density. In our analysis synthetic Stokes I, Q, U profiles for the HeI1083 line are created using the Hanle and Zeeman Light (HAZEL)[1] code (Asensio Ramos et al. 2008). The HeI1083 line is a multiplet between the $2p^3S$ and 2s3S terms of the triplet system of HeI. The upper term has three levels with J=0,1,2 while the lower term has one level with J=1 with corresponding transition wavelengths: 10829.09Å, 10830.25Å and 10830.34Å. The blue component is not polarizable in emission because the upper level with J=0 has only one magnetic sublevel and is intrinsically unpolarizable. The final Stokes parameters are obtained from integrating the synthetic line profiles over the two red components which typically appear blended due to the small wavelength separation. For the analysis we choose to work in terms of the concepts of linear polarization angle and amplitude (degree) which are related to the line-profile integrated Stokes I, Q, U by the simple relations:

$$\text{Polarization amplitude} = \frac{\sqrt{\mathrm{Q}^2 + \mathrm{U}^2}}{I} \tag{3.3.2}$$

$$\text{Polarization angle} = 0.5 \tan^{-1}\left(\frac{\mathrm{U}}{\mathrm{Q}}\right) \tag{3.3.3}$$

To ensure the polarization angle is correctly calculated an "arctan2"-type function should be applied. This function accounts for the signs of the U an Q values and correctly maps the polarization angle over the domain $[-90^\circ, 90^\circ]$.

The algorithm steps for co-spatial sources in the plane of the sky proceed as follows:

1. From the measured forbidden line linear polarization angle $\theta_{\rm m}$ we generate two sets of angle pairs ($\theta_{\rm B}$, $\chi_{\rm B}$) satisfying Eq. 3.3.1 with $\theta_{\rm P} = -\theta_{\rm m}$ or $\theta_{\rm P} = -(\theta_{\rm m} + 90^\circ)$. The two sets correspond to the situations where the plane of polarization is respectively parallel or perpendicular to the projected magnetic field direction.

[1] http://www.iac.es/proyecto/magnetism/pages/codes/hazel.php

2. HAZEL is used to generate two model Stokes profile grids for each set of angle pairs together with a suitably chosen value range for the magnetic field strength ($0 < \mathrm{B} < 8\mathrm{G}$). Thus each point on the grid corresponds to one or more (B,θ_B,χ_B) magnetic fields. The two dimensional grids are expressed in terms of polarization angles and amplitudes calculated using Equations 3.3.2 and 3.3.3.

3. The measured HeI1083 polarization angle and amplitude are now compared to each of the model grids to find the magnetic field solution grid points consistent with the measurements and errors. If the measured linear polarization parameters only intersects the parallel model grid and lie outside the perpendicular model grid then the deduced magnetic field solution is not affected by the Van Vleck uncertainty. Alternatively if the measured value intersects both grids the deduced magnetic field has at least two degenerate solutions due to the Van Vleck uncertainty.

3.3.1 Example application

To demonstrate the method we use as examples two magnetic fields with different (B,θ_B,χ_B) parameters that are typical of coronal fields (Table 3.1). The fields, named Field I and II are influencing scattering points located in the plane of the sky at different heights, $0.26R_\odot$ and $0.08R_\odot$ respectively. We synthesize "measurements" using the assumed magnetic field parameters and height. HeI1083 measurements are calculated using the HAZEL code, while SiX1430 measurements are calculated using the FORWARD[2] code (Gibson et al. 2010) which generates polarized emission from a multi-level SiX atomic model (Judge & Casini 2001). To synthesize the SiX1430 polarized emission we also assumed coronal electron densities typical of the heights at which the two fields are located: $0.2 \times 10^8 \mathrm{cm}^{-3}$ for Field I and $2 \times 10^8 \mathrm{cm}^{-3}$ for Field II. The larger exciting radiation anisotropy and lower densities found at larger heights leads to an increase in the amplitude of the SiX1430 polarization. For observations that are not photon limited this leads to improved accuracy for measurements higher above the solar limb.

Following our algorithm two angle/amplitude grids are generated separately for Field I and

[2]http://www.hao.ucar.edu/FORWARD/

II from the SiX1430 polarization angle measurement. Figures 3.3 and 3.4 show the model grids generated for Field I and II respectively. By convention the polarization angle is defined over $[-90°, 90°]$, but we redefine it for display purposes over the interval $[0°, 180°]$ without any loss of information. This is done because the model grids shown below are easier to interpret over the modified domain. While the algorithm grid are arbitrarily dense, only some of the grid points are shown to avoid overcrowding the plot space. To visualize the variation with magnetic field strength B-isocontours are highlighted. The errors in the HeI1083 measurement are typical measurement errors of $\sim 0.5\%$ in the line intensity, although more accurate measurements are possible. The solution grids are not uniform so the same measurement error translates differently into inverted magnetic field errors depending on the strength of the field. Visually this is evident in the way the B-isocontours become closer together as the field strength increases. The top panel in each figure shows the full model domain while the lower panels show an enhanced view of each grid near the measured values.

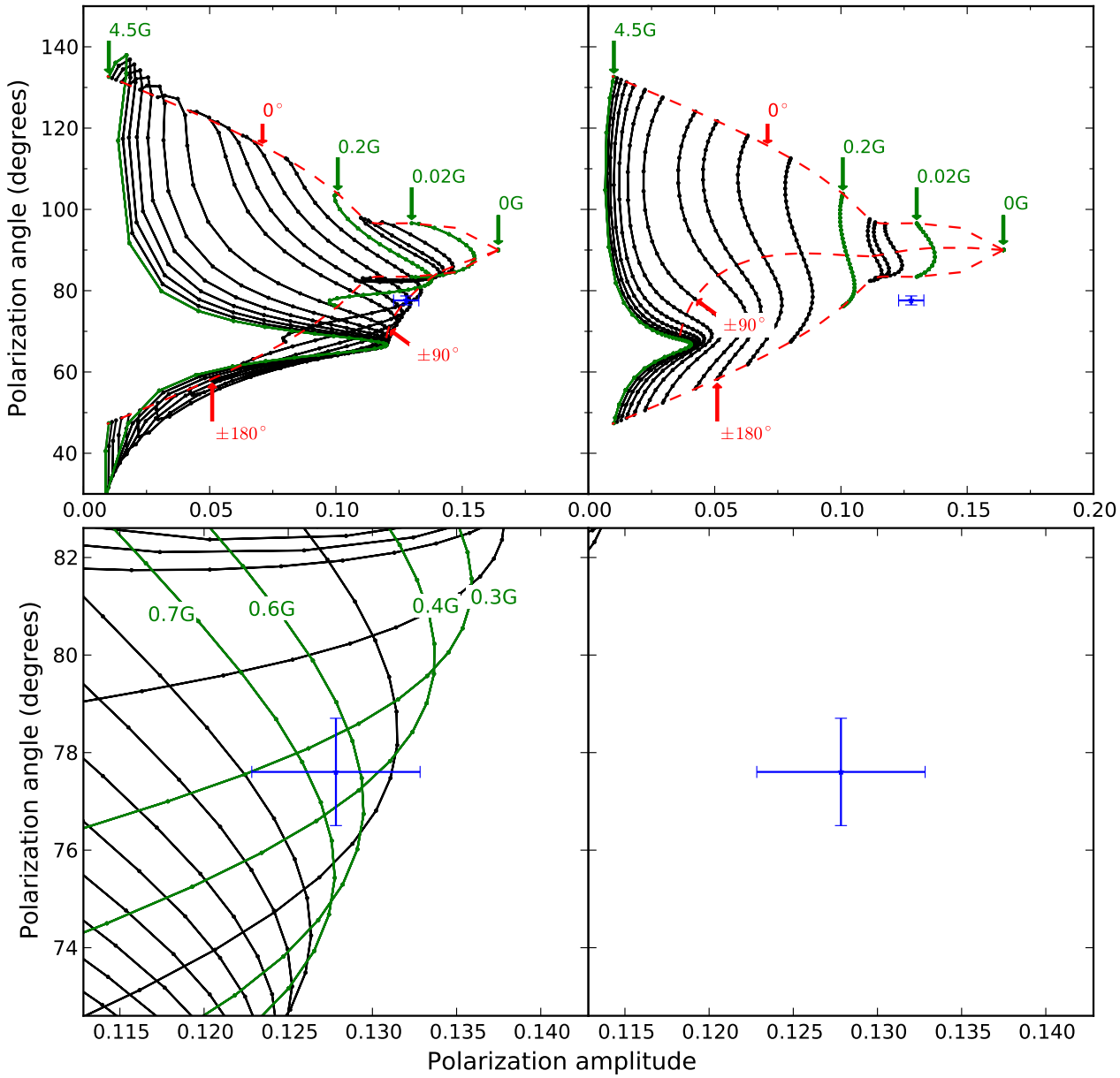

Figure 3. Field I model grids for HeI1083 linear polarization with polarization angle drawn against polarization amplitude. B-isocontours are drawn as solid black lines. *The top panel* shows the entire solution space with some B-isocontours highlighted and labeled in green three χ_B-isocontours drawn with red dashed. *The bottom panel* shows an enhanced region around the measured value for Field I with some B-isocontours highlighted in green. The B-isoncotours in the bottom panel are all separated by 0.1G. For both the top and bottom panels the left plot shows the model grids for plane of polarization parallel to the field projection, while the right plot shows the grid for the plane of polarization perpendicular to the field projection. The measured HeI1083 polarization value for Field I is drawn in blue with errors bars corresponding in size to intensity errors $\sim 0.5\%$. For Field I the measurement intersects only the parallel grid. This is consistent with an inclination measurement outside the Van Vleck uncertainty region.

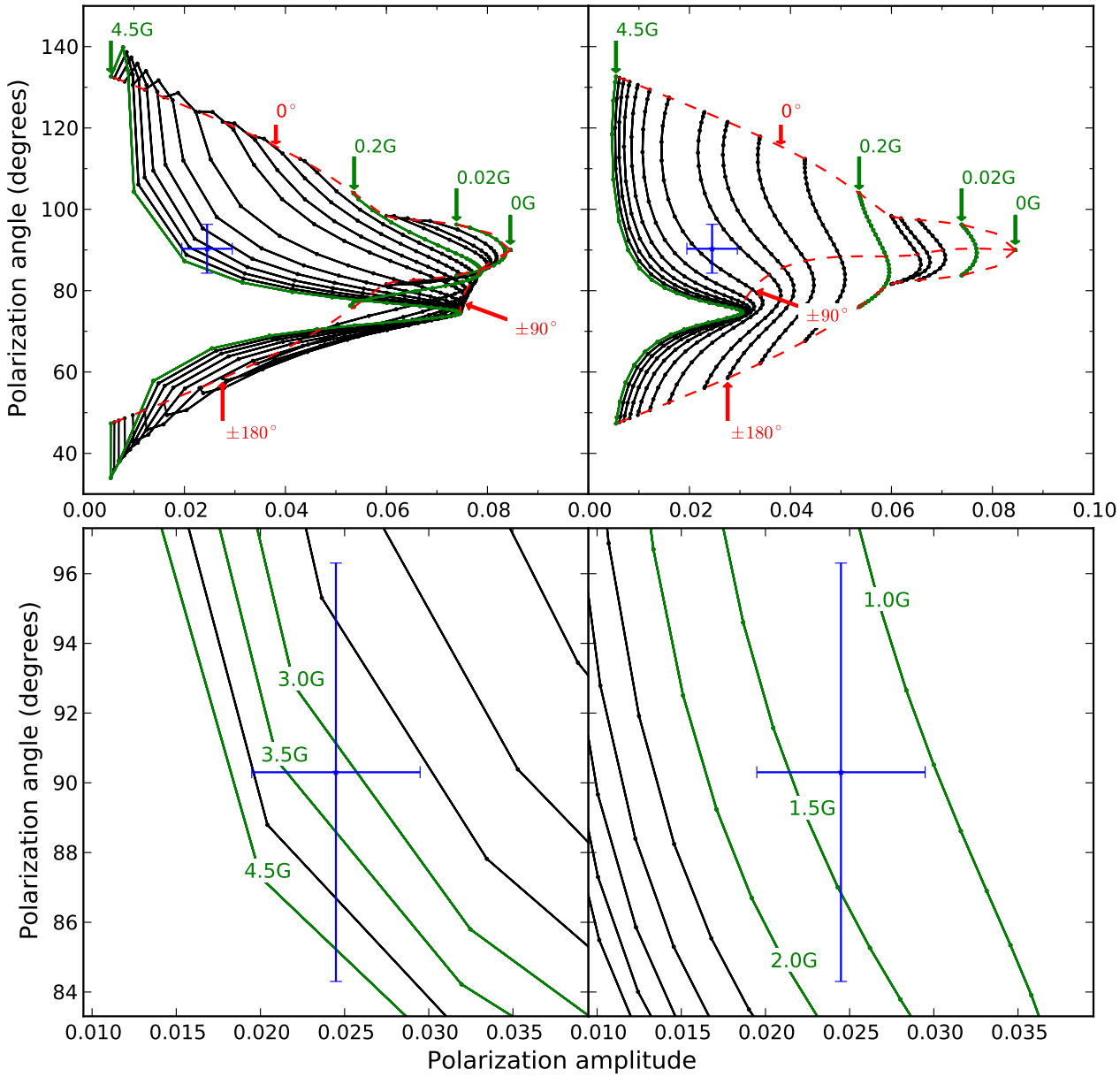

Figure 4. The same as Figure 3.3 for the Field II model grids. For the bottom panel only the B-isocontours spaced by 0.5G are drawn. For Field II the HeI1083 polarization measurement intersects both model grids which is consistent with inclination solutions inside the Van Vleck uncertainty region.

Table 3.1: Summary of parameters and algorithm solutions for two example magnetic field cases.

	Assumed values (B,θ_B,χ_B) Height($R_\odot$) Density(cm^{-3})	SiX1430 polarization (angle[b], amplitude[c])	HeI1083 polarization (angle[b], amplitude)	Solutions[a] (B,θ_B,χ_B)
Field I	(0.65G, 156°, -90°)	(-24±2°, 0.097±0.005)	(78±1°, 0.128±0.005)	$(0.65^{+0.15G}_{-0.15G}, 156^{+1°}_{-1°}, -90^{+10°}_{-15°})$
	0.26			$(0.65^{+0.15G}_{-0.15G}, 24^{+1°}_{-1°}, 90^{+15°}_{-10°})$
	0.2×10^8			$(0.35^{+0.15G}_{-0.10G}, 152^{+3°}_{-2°}, -125^{+10°}_{-5°})$
				$(0.35^{+0.15G}_{-0.10G}, 27^{+3°}_{-2°}, 125^{+5°}_{-10°})$
Field II	(1.3G, 76°, -63°)	(-16±14°, 0.01±0.005)	(-90±6°, 0.024±0.005)	$(1.3^{+0.4G}_{-0.3G}, 76^{+1°}_{-1°}, -63^{+8°}_{-7°})$
	0.08			$(1.3^{+0.4G}_{-0.3G}, 104^{+1°}_{-1°}, 63^{+7°}_{-8°})$
	2×10^8			$(3.2^{+1.8G}_{-0.9G}, 141^{+1°}_{-1°}, -22^{+3°}_{-3°})$
				$(3.2^{+1.8G}_{-0.9G}, 39^{+1°}_{-1°}, 22^{+3°}_{-3°})$

[a] Parameter errors only account for polarization errors in the HeI1083 line. The error contributions from SiX1430 polarization angle uncertainty is discussed in the text.

[b] Polarization angles are given in the $[-90°, 90°]$ domain and the reference direction is along the local solar radial.

[c] Polarization amplitude for SiX1430 are given to show amplitude/noise for each case, but the values themselves are not part of the algorithm.

For Field I four independent solutions are obtained as shown in Table 3.1. The four solutions can be divided into two solution pairs with unique values of the magnetic field strength B. For each pair with a unique B there are two degenerate solutions for the angle variables θ_B and χ_B. This "classical degeneracy" is independent of the Van Vleck degeneracy and is inherent in the matter-radiation interaction problem and plane of sky scattering geometry (Bommier 1980). The two ambiguous solutions can be obtained from each other by reflection of the B vector through the line of sight. For Field I it is evident that the measured polarization value does not intersect the solution grid for the case where the polarization plane is perpendicular to the magnetic field vector. This shows that the magnetic field is not in the Van Vleck degeneracy region.

The recovered solution space for Field II also consists of four independent solutions which can be broken down into two pairs of solutions with unique B values. Same as for Field I each pair with a unique B has two degenerate solutions for the angle variables due to the classical degeneracy. However, for Field II the origin of the different solutions for the magnetic field strength B lies in the Van Vleck degeneracy. This is seen from the fact that the measured polarization value intersects both model grids.

An important source of error in the analysis is the uncertainty in measuring the SiX1430 polarization angle. This uncertainty can be quite large as is the case for Field II due to the low radiation anisotropy and higher electron density. This uncertainty changes the parallel and perpendicular sets of (θ_B, χ_B) angles that satisfy Eq. 3.3.1. The effect this uncertainty has on the model grids is shown in Figures 3.5 and 3.6 for Field I and II respectively. To produce the variation shown the maximum uncertainty is added and subtracted to the measured SiX1430 polarization angle and new model grids are created using HAZEL. For Field I solutions the errors given in Table 3.1 are roughly one and a half time larger for all the parameters. Field II has a much larger uncertainty in measured SiX1430 polarization angle so the effect is larger but mostly concentrated in the angle determination with the variation in the angles increasing to $\pm 25^\circ$ while the magnetic field strength B uncertainty increases by one and a half times the values given in Table 3.1.

For these test cases we assume the line intensity measurement to be $\sim 0.5\%$ for both situation. Since the polarized signal for Field II is ten times weaker than the signal for Field I this translates

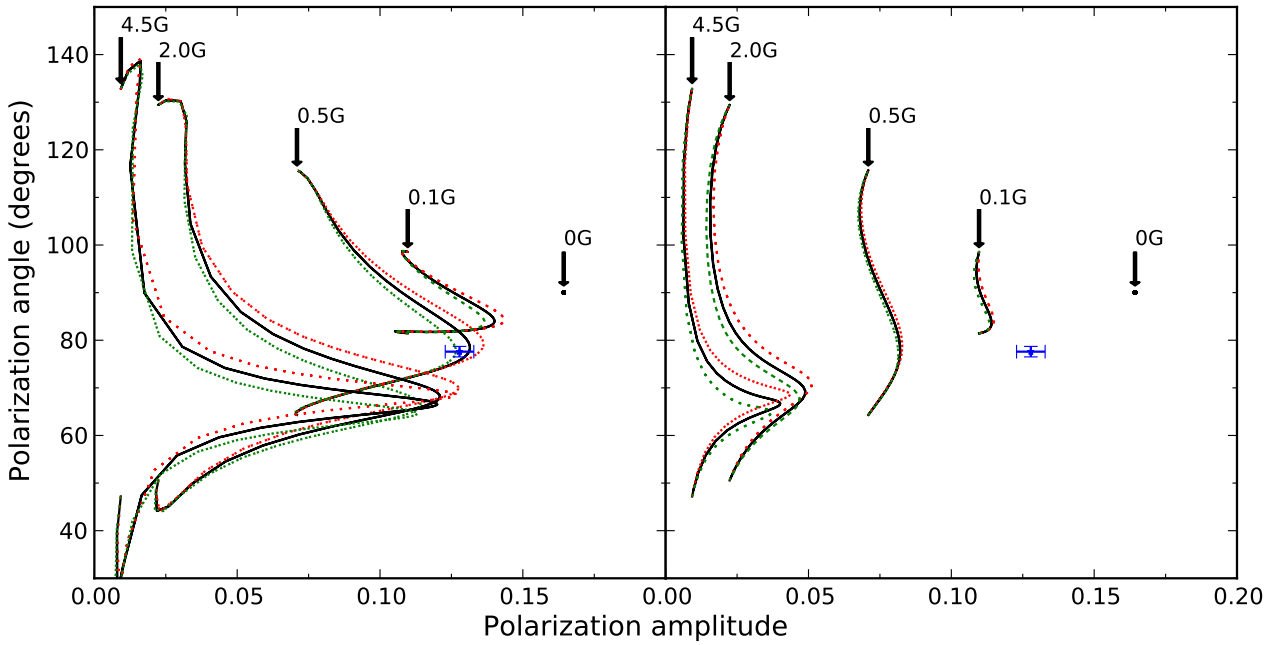

Figure 5. Shown in black are the parallel(left) and perpendicular(right) model grids for Field I as they also appear in Figure 3.3. The dotted lines represent added (red) and subtracted (green) uncertainties in the SiX1430 polarization angle. Only a few B-isocontours are shown and labeled to avoid overcrowding due to intersecting contour lines. The measured HeI1083 polarization parameters are shown with corresponding measurement uncertainties. Propagating the SiX1430 uncertainty requires new grids to be computed since the shapes of the grid changes as seen by the bending and crossing of model contours.

into a significant increase in the error of the calculated magnetic field strength. However, there is nothing fundamentally limiting about the uncertainty we adopted since the source of the uncertainty is random rather than systematic. For weak polarimetric signals we can increase the integration time to improve the the uncertainty to acceptable levels for errors in the calculated parameters. To achieve the quoted 0.5% accuracy using the current spectrograph on the 0.45m SOLARC telescope around 12 minutes of integration time is needed assuming a SiX1430 line brightness of $5 \times 10^{-6} B_{\odot}$ and a spatial resolution element 7" in diameter. The larger 4m telescope DKIST will have improved light collecting power as well as improved signal throughput. It will make this type of accuracy possible for an observation region 1" in diameter in less than 1s of integration time.

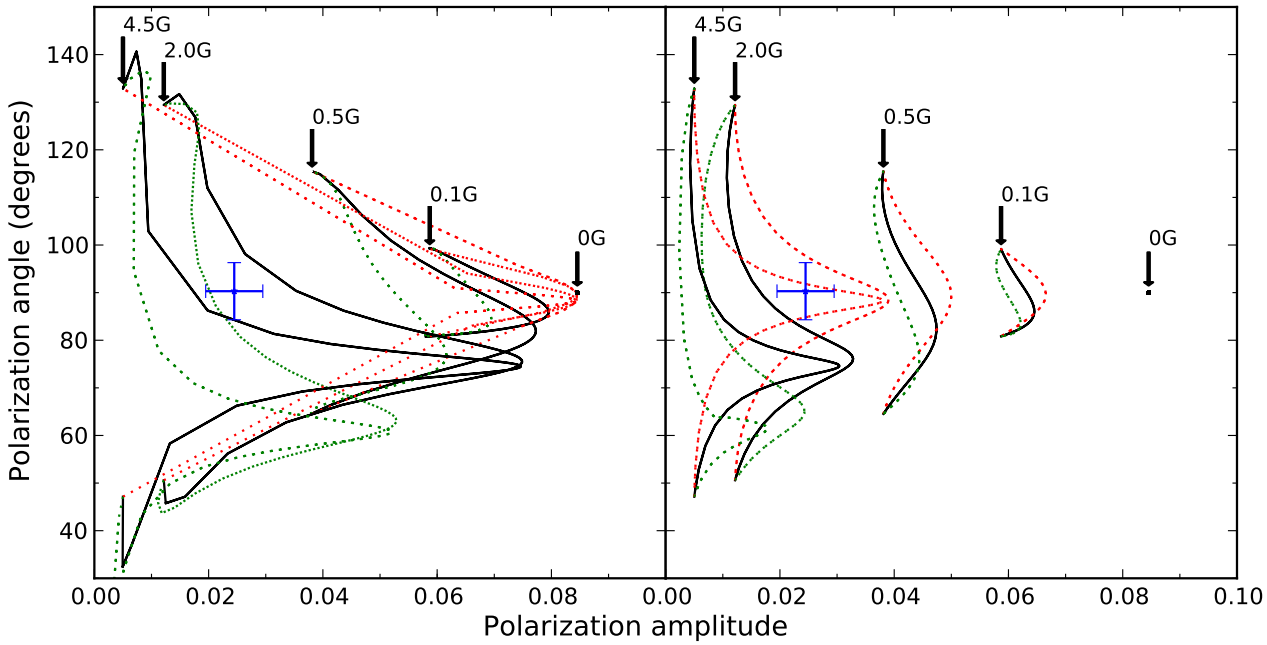

Figure 6. The same as Figure 3.5 but for the Field II model grids and corresponding errors. The SiX1430 linear polarization signal for Field II is weak and thus relatively uncertain for the selected realistic measurement accuracy. This uncertainty leads to the large distortions in the model grids. High accuracy forbidden line polarization directions will be required in this regime.

3.4 Discussion and conclusions

The method proposed provides important constraints on the coronal magnetic field and shows promise as a detailed magnetic field diagnostic, since it drastically constrains the coronal source region local magnetic field to four independent solutions using potentially high signal-to-noise IR linear polarization measurements. This is achieved without knowledge of polarization amplitudes for the forbidden lines that depends on the coronal electron density. It is interesting to note that the method obtains four degenerate solutions for magnetic fields located inside or outside the Van Vleck degeneracy region. Merenda et al. (2006) proposed a chromospheric algorithm that uses measured HeI1083 linear and circular polarization to determine the vector magnetic field for prominences located in the POS. Their method recovered two degenerate solutions for a magnetic field outside the Van Vleck region and four degenerate solutions for a field inside the Van Vleck region. However, all the examples analyzed by them were for field strengths in excess of 10G, which means the HeI1083

emission is in the saturated Hanle regime. From our solutions for Field I we conclude that the extra degeneracy (not related to the classical degeneracy) that appears even for fields outside the Van Vleck regions is due to the unsaturated Hanle effect. Independent knowledge of the electron density (or the forbidden line polarization amplitude) can reduce the degeneracy outside the Van Vleck region from four to two and uniquely recover the magnetic field strength B. For future work we are testing how accurate the density estimate needs to be in order to reliably distinguish between the degenerate solutions. It may be possible to exclude one pair of solutions even with an average electron model consistent with coronal white light observations.

In principle, the information on the electron density is contained in the polarization amplitude of the forbidden line which we excluded from the present algorithm. If it is possible to distinguish between the two solution pairs, we can then recover information about the electron density from the measured polarization amplitude.

Resolving the final ambiguity from the radiation field geometry requires more information. One solution to this problem is through forward modeling, using 3D coronal MHD models, perhaps constrained by photospheric magnetic field measurements. It is noticeable that these degenerate solutions have complementary values for the inclination angle, so constraints just from the photospheric magnetic polarity changes may provide the key to breaking this degeneracy. Note that similar degeneracies are encountered when measuring vector magnetic fields near the photosphere. Leka et al. (2009) summarizes the types of algorithms used to break the ambiguities in photospheric vector magnetograms. Another possibility involves using tomographic inferences from observing the same region over a few days of solar rotation. Bommier et al. (1981) successfully distinguished between ambigous solutions by observing a prominence as it rotates through the plane of the sky.

While detections of coronal HeI1083 emission shows strong correlation with streamers (Moise et al. 2010) more polarimetric observations of this line are needed to determine the exact geometry and line formation mechanisms of the emitting region. One of our principal assumptions is that the HeI1083 and forbidden line emission is co-spatial but a relaxed version of this assumption is that the emitters experience the same magnetic field. Since the magnetic field expands to fill the coronal volume it is not unreasonable to assume that some large volumes of the corona will experience

the same magnetic field. However, obtaining a better understanding and characterization of the HeI1083 coronal signal in the context of simultaneous forbidden line emission measurements will provide more information towards understanding the validity of this assumption. Currently we are pursuing a dedicated campaign to obtain co-spatial and quasi-simultaneous spectropolarimetric observations of the FeXIII1075, SiX1430 and HeI1083 lines in the solar corona using the SOLARC telescope on Haleakala. These observations will form the data set needed to test the proposed method.

BIBLIOGRAPHY

Kuhn, J. R. 1995, Infrared tools for solar astrophysics: What's next?, 89

Lin, H., Penn, M. J., & Tomczyk, S. 2000, ApJ, 541, L83

Lin, H., Kuhn, J. R., & Coulter, R. 2004, ApJ, 613, L177

Tomczyk, S., Card, G. L., Darnell, T., et al. 2008, Sol. Phys., 247, 411

Arnaud, J., & Newkirk, G., Jr. 1987, A&A, 178, 263

Penn, M. J. 2014, Living Reviews in Solar Physics, 11

Bommier, V., Sahal-Brechot, S., & Leroy, J. L. 1981, A&A, 100, 231

López Ariste, A., & Casini, R. 2003, ApJ, 582, L51

Merenda, L., Trujillo Bueno, J., Landi Degl'Innocenti, E., & Collados, M. 2006, ApJ, 642, 554

Ishikawa, R., Bando, T., Fujimura, D., et al. 2011, Solar Polarization 6, 437, 287

Kuhn, J. R., Coulter, R., Lin, H., & Mickey, D. L. 2003, Proc. SPIE, 4853, 318

Kuhn, J. R., Penn, M. J., & Mann, I. 1996, ApJ, 456, L67

Kuhn, J. R., Arnaud, J., Jaeggli, S., Lin, H., & Moise, E. 2007, ApJ, 667, L203

House, L. L. 1974, PASP, 86, 490

Sahal-Brechot, S., Bommier, V., & Leroy, J. L. 1977, A&A, 59, 223

Casini, R., & Judge, P. G. 1999, ApJ, 522, 524

Judge, P. G., Low, B. C., & Casini, R. 2006, ApJ, 651, 1229

Asensio Ramos, A., Trujillo Bueno, J., & Landi Degl'Innocenti, E. 2008, ApJ, 683, 542-565

Moise, E., Raymond, J., & Kuhn, J. R. 2010, ApJ, 722, 1411

Judge, P. G. 1998, ApJ, 500, 1009

Judge, P. G., & Casini, R. 2001, Advanced Solar Polarimetry – Theory, Observation, and Instrumentation, 236, 503

Gibson, S. E., Kucera, T. A., Rastawicki, D., et al. 2010, ApJ, 724, 1133

Bommier, V. 1980, A&A, 87, 109

Leka, K. D., Barnes, G., Crouch, A. D., et al. 2009, Sol. Phys., 260, 83

CHAPTER 4
SOLARC TELESCOPE TECHNICAL DESCRIPTION

The Scatter-free Observatory for Limb, Active Regions, and Coronae (SOLARC) is a 0.46 m reflecting coronographic solar telescope (Kuhn et al. 2003) located very near the top of Haleakalā (∼3048 m altitude) on the island of Maui. SOLARC has been used for coronal magnetometry using the Zeeman effect (Lin et al. 2004) and to observe the faint coronal HeI signature (Kuhn et al. 2007; Moise et al. 2010).

This telescope is particularly well suited for accurate spectropolarimetric measurements due to its off-axis unobscured optical system. The telescope itself is housed in a small dome attached to the Zodiacal Light (ZL) building (Figure 4.1a) near the construction site for the new 4m Daniel K. Inouye Solar Telescope (DKIST) telescope. Observations collected with the SOLARC telescope are relayed through an optical fiber bundle into an optical bench located inside the ZL building (Figure 4.1b-d).

4.1 Overview of SOLARC configurations

SOLARC is a hands-on research tool which must be changed depending on the nature of the observation targets. The optics have therefore been (re)configured several times during the telescope's lifetime (∼13 years). In the beginning, it was optimized to function as a coronal polarimeter, and polarized observations of FeXIII1075 and HeI1083 were obtained using a 256 fiber-bundle and an Ebert-Fastie spectrograph configuration (Lin et al. 2004; Kuhn et al. 2007). Later, this configuration was dismantled and optimized to enable limb and photospheric observations, as well as planetary observations. A different fiber bundle with 66 fibers was used along with a redesigned near-Littrow configuration for the polarimenter (Swindle 2014).

The user immediately before me changed the fore optics configuration described by Swindle (2014) for observations of the Venusian atmosphere using an infrared camera mounted at one of the Nasmyth focus positions on the telescope. Most of the fore optical elements inside the telescope had been removed to allow access to the light path for the Nasmyth mounted camera. Inside the

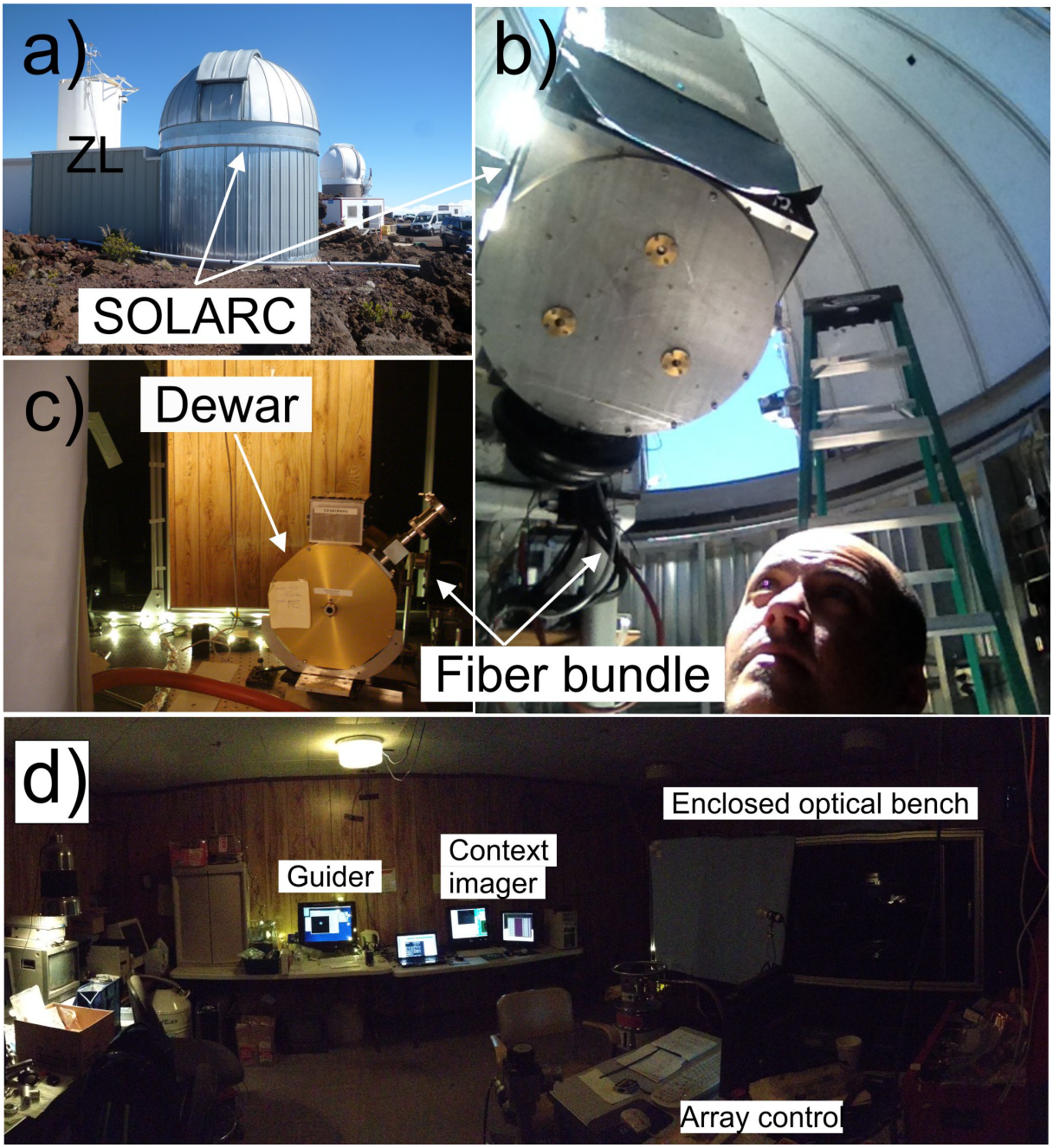

Figure 4.1: Photographs showing location and optical components of the SOLARC telescope. (a) Outside view of SOLARC and Zodiacal Light (ZL) building. (b) View from inside shot of the telescope. The light signal is carried from the telescope through a bundle of fiber optic cables to the optical bench. (c) The spectrograph is located inside the enclosed optical bench and can be accessed using a set of sliding doors. (d) The ZL bulding contains terminals for all three control systems for SOLARC so that dome access is only required to start/stop the day, or in emergencies.

optical bench the near-Littrow optics and configuration was undisturbed as described by Swindle (2014).

In order to collect observation for this project we removed the camera mounted at the Nasmyth focus and re-aligned all the fore optics inside the telescope until the setup described in Swindle (2014) was obtained. However, this configuration did not yield the required sensitivity needed for coronal observations since the system was optimized for observations on the solar disc where the flux levels are six orders of magnitude larger than in the corona. A slow, iterative process of modification started during which we re-configured the system to better suit the needs of our observations. By the end we had improved the signal to noise of the system by approximately two orders of magnitude.

A description of the final system configuration using similar nomenclature introduced by Swindle (2014) (e.g. fore and aft optics) is given below.

4.2 Fore optics

The term fore optics describes all the optical elements located inside the telescope. Light illuminates the 0.46m primary mirror (M1) (Figure 4.2) which then reflects the light through a tilt-angle of 10.5°. The beam passes though the M1 focus where a Field Stop blocks the solar disc and hits the secondary mirror (M2). The secondary mirror is also tilted by 10.5° and produces a focused beam offset by 5.3cm from the optical path of M1. The beam from M2 passes through a Lyot stop located at the same position as the Field Stop. The Lyot stop is designed to block the diffraction ring caused by the edge of the entrance aperture.

The fore optics are located inside the telescope right after the Lyot stop and before the M2 focus. An added benefit to the off-axis design is having enough room to include all optical elements between the Lyot stop and the focus point without vignetting the beam coming from M1. Each element is described below in the order in which it appears in the light path:

1) Two liquid crystal variable retarders (LCVRs, Meadowlark Optics) that modulate the phase of the beam allowing full Stokes polarimetry. Modifying the voltage across the LCVRs changes the phase between orthogonal polarized states passing through the crystals. To calibrate the

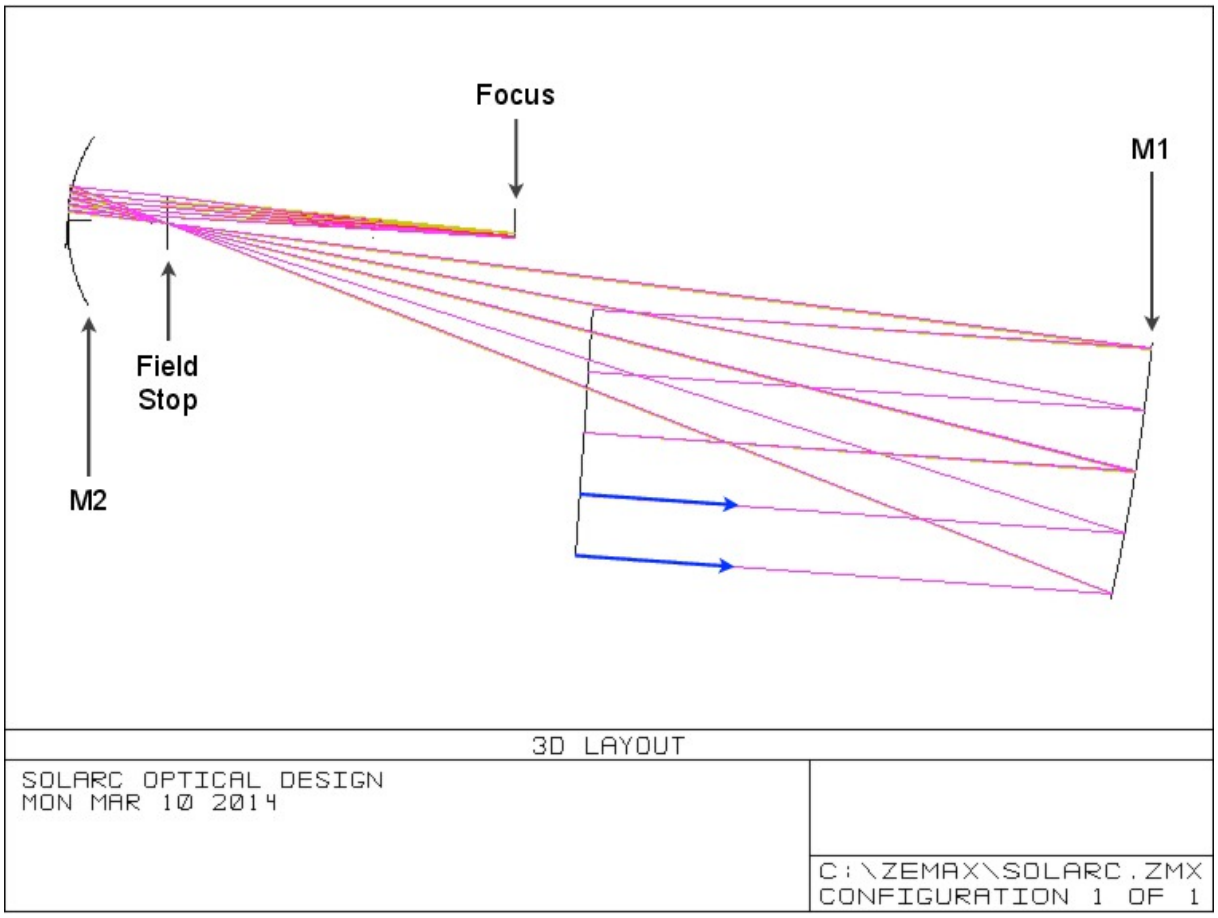

Figure 4.2: Zeemax optical design showing the light path inside the telescope. Note the M2 focus can be accessed without vignetting the beam coming from M1.

LCVRs two identical wiregrid linear polarizers (see below) are used. One polarizer is located in front of the crystals whereas the second polarizer is placed behind the LCVRs in a crossed position with the first polarizer. Each LCVR is calibrated individually by orienting the crystal such that its fast axis is rotated by 45° to both polarizers. In this configuration voltage across the crystal is modulated in 0.1 V increments between 0 and 10 V and the resulting intensity variation is recorded with a typical intensity curve shown in Figure 4.3. The voltage at peak of the transmitted intensity corresponds to half-wavelength retardance along the fast axis of the crystal. The mid-points of the intensity around the peak represent quarter and three-quarter retardance, respectively (Figure 4.3). Once each LCVR is individually calibrated they are placed back to back with their fast axes arranged at 45° to each other and calibrating linear

polarizer is removed from the beam path. The first LCRV in the beam has its fast axis parallel to the linear polarizer that follows the two crystals(Figure 4.4a). The task of the two LCVRs is to transform linear/circular polarized light into purely linearly polarized light along the fast axis of the linear polarizer that sits behind them in the beam.

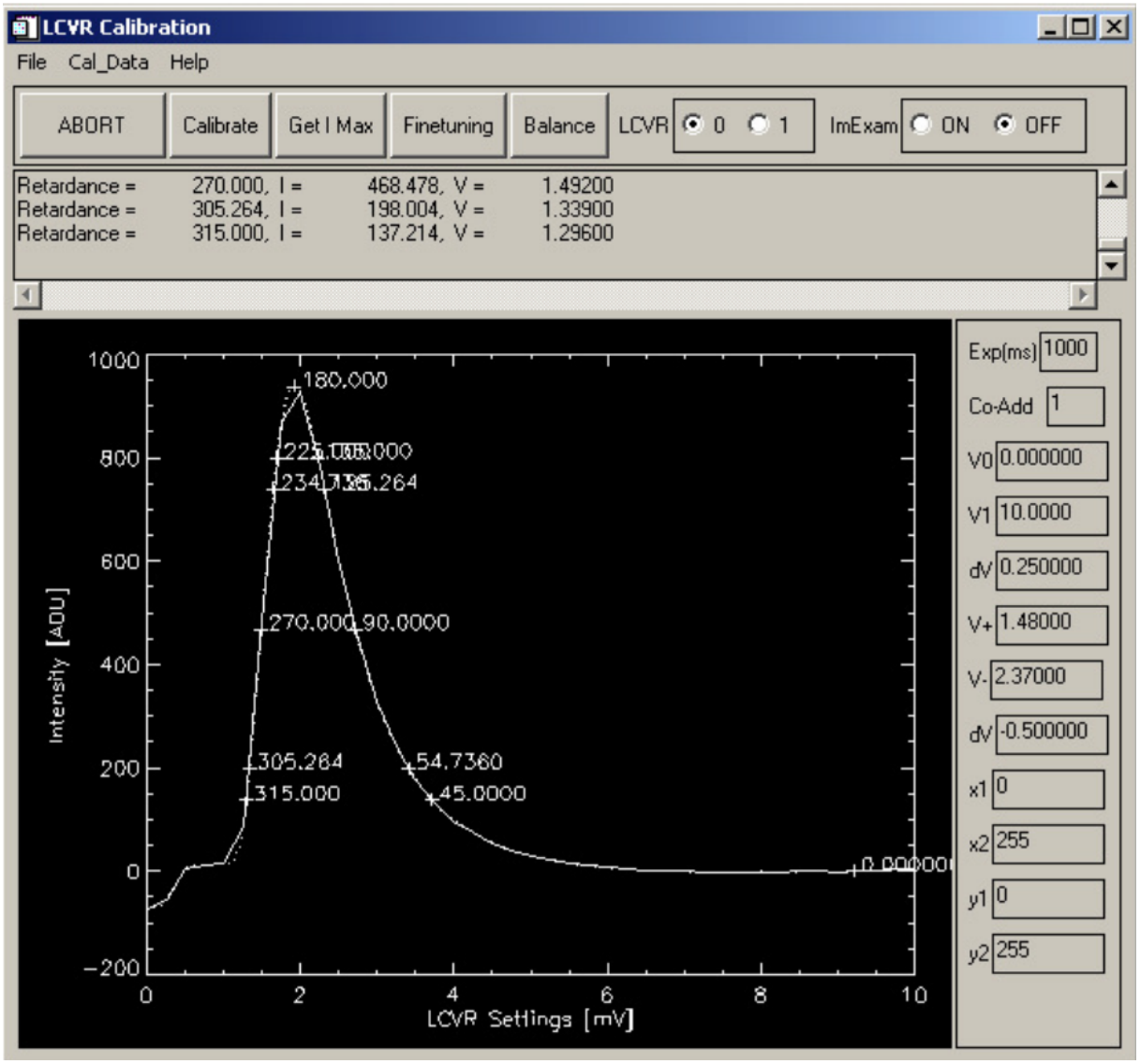

Figure 4.3: Computer screenshot showing LCVR calibration curve. The peak corresponds to half-wavelength (180°) retardance, whereas the mid-points represent three-quarter (270°) and one quarter (90°) retardance. At high voltages the crystals become optically inactive.

2) A wire grid polarizer that performs the role of an analyzer. The beam leaving the LCVRs

passes through a 25mm wire grid polarizer (Edmunds Optics, PN: 68-750). This element selectively passes light polarized along the transmission axis.

3) A piece of 1.5 mm-thick uncoated silica glass, rotated at 45°, is used to reflect ∼5% of the light into a context camera placed at 90° to the beam. The glass is housed in an opaque box to prevent as much scattering of light as possible (Figure 4.4). The reflectance of the glass is around 5% over the near-IR spectral region.

4) A coated bi-convex lens 25mm in diameter, with a focal length of 100mm. This element is used to demagnify the image and increase the plate scale of the instrument from 26 ″/mm to 92 ″/mm. The trade-off in spatial resolution is necessary to increase the signal-to-noise of the system by collecting more light into each fiber.

5) The entrance face of the fiber bundle, mounted on a three-axis holder, is located at the beam focus. Fibers entrances are distributed in a 16×16 pattern whereas fiber exits are re-arranged into 4×64 parallel columns of fibers. The exit columns are offset to prevent overlap between the spectra on the detector. Due to the configuration of the aft optics (see below) the fibers nonetheless do overlap when imaged on the detector. To avoid this problem, half the entrance fibers are blocked by a razor edge (see Figure 4.4c). Another razor edge is used at the exit point of the fibers to further restrict the number of fibers to 64 which can be imaged with minimal overlap on the array (Figure 4.5).

4.3 Aft Optics

The aft optics are arranged inside an enclosed optical bench (see Figure 4.1d) inside the ZL building. Light from the telescope is carried over the 25 m-long fiber bundle and the exit point of the bundle acts as the entry beam into an optical assembly arranged in a near-Littrow configuration (Figure 4.6). In this type of configuration, the same off-axis parabolic (OAP) mirror performs two roles simultaneously: (i) collect diverging light from the fiber exit and send plane parallel light towards the diffraction grating (Figure 4.6a); and (ii) collect parallel dispersed light from the diffraction

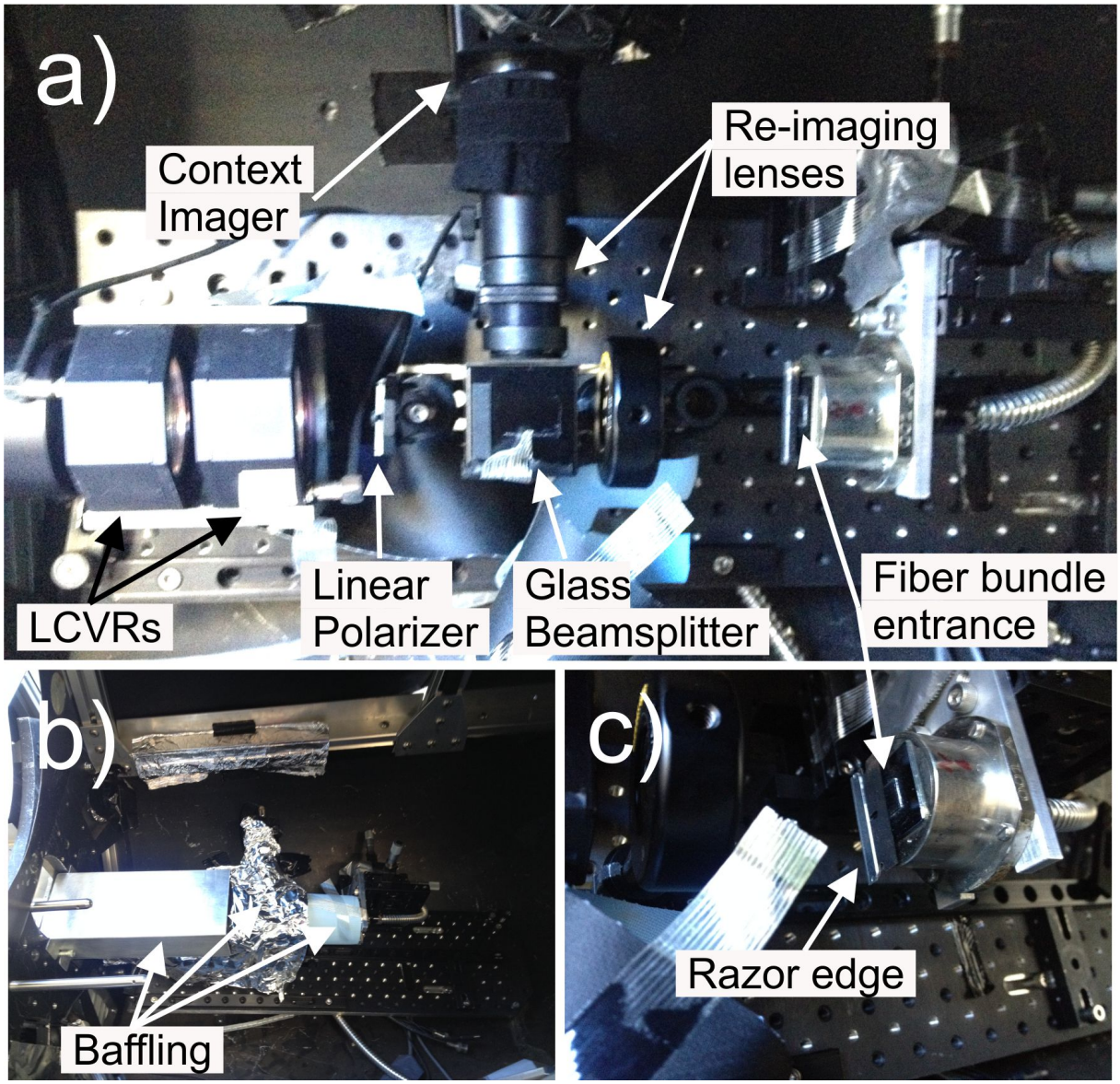

Figure 4.4: Photographs showing the fore optics arrangement on SOLARC. (a) Top view of the elements along the optical beam after removing all the baffling. (b) Similar top view of the setup but with all the baffling in place to minimize scattered light. (c) Close up view of the fiber bundle entrance face with half of the fibers blocked by a razor edge.

grating and create a converging beam onto the detector (Figure 4.6b). The optical elements of the aft optic are described below in the order they sit in the light path:

1) The illuminated exit end of the fiber bundle is arranged into two parallel columns of 64 fibers distributed parallel to the ruled direction of the diffraction grating. Attempts to include all

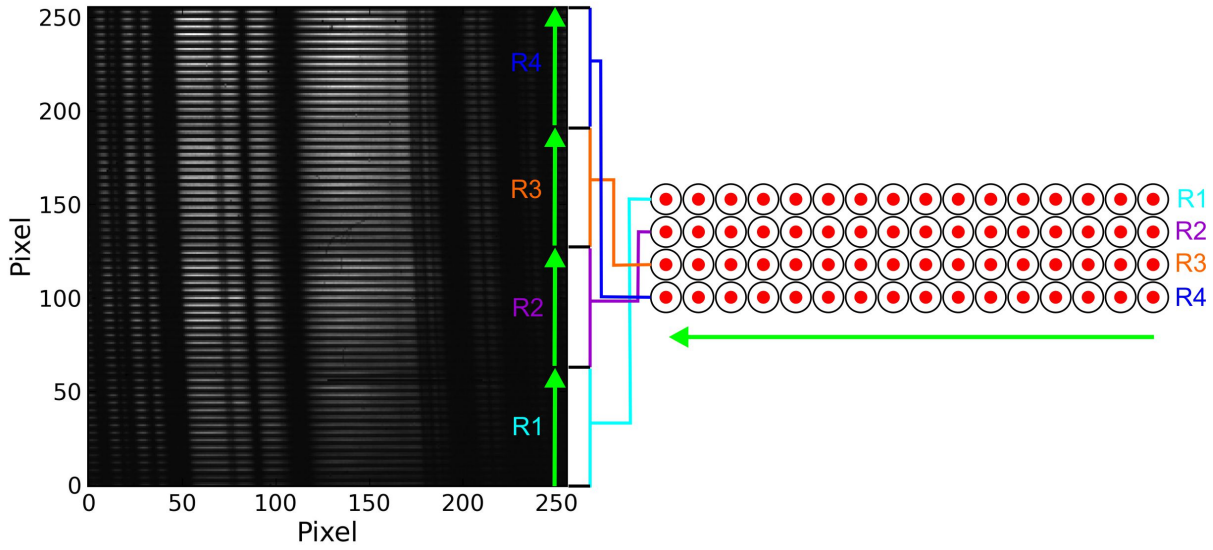

Figure 4.5: Fiber bundle mapping on the array. The perspective of the schematic is that of a person looking down on the entrance array of fibers. The green arrow indicates the order in which the fibers are imaged on the array.

128 spectra on the 256 x 256 IR array (see below) were problematic because this required focusing of the light into single pixel rows on the detector with only one empty row of pixels separating each dispersed spectrum. This creates too much overlap between fibers. Therefore we opted to obscure one row of fibers using another knife edge and only imaged one row of 64 fibers (Figure 4.6b).

2) A 175mm aperture OAP mirror with a 900mm focal length (Figure 4.6c) that collects diverging light from the fiber bundle exit and collimates it onto the dispersion grating. The fiber bundle exit is located at the focal plane of the OAP. Due to an undersized OAP only 60% of the diverging light from each fiber is captured.

3) Collimated light from the OAP falls onto a 79 line/mm echelle diffraction grating with a blaze angle of 64.5°. The grating disperses the light from each fiber and reflects it back towards the OAP which converges the beam onto a fold mirror (Figure 4.6b).

4) The fold mirror diverts the converging beam inside the dewar holding the camera. The Littrow configuration requires that the mirror is collinear with the exit beam from the fiber bundle.

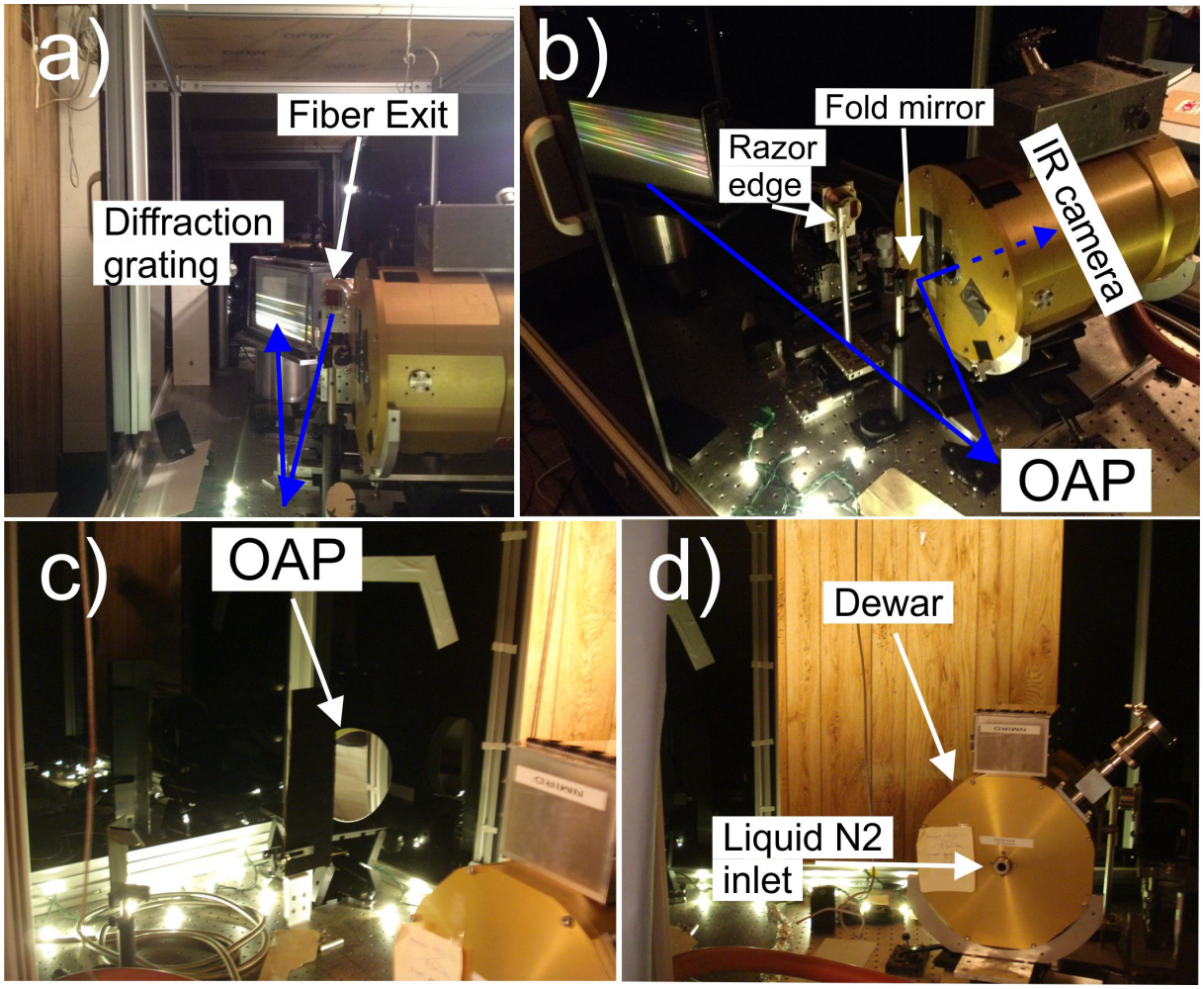

Figure 4.6: Photographs showing the optical bench setup. (a) View from the OAP showing the path which the light takes after it exits the fibers. (b) Path of the light after it is dispersed by the grating and collimated by the OAP onto the IR array. (c) Photo of the actual position of the OAP. (d) Backside of the camera dewar in which the feedthrough for the coolant is located. Abbreviations: OAP: off-axis parabolic mirror.

To avoid vignetting from the back of the fold mirror the exit beam from the fibers is slightly inclined with respect to the OAP axis to produce a height offset between the fold mirror and the exit beam.

5) Inside the dewar a cooled order-sorting filter wheel is located ahead of the IR array (Figure 4.7). The filter wheel is controlled by a mechanical feedthrough which allows for manual selection of the desired narrowband filters. Each of the filters is selected to be sufficiently

narrow so overlapping orders are blocked from being imaged simultaneously on the array. Only two filters are needed for these observations since the FeXIII1075 and HeI1083 lines are sufficiently close in wavelength that a single filter may be used for both, while a second filter is used to measure the SiX1430 line. Transmission profiles measured in house using a Cary 5000 spectrophotometer are shown Figure 4.8. The HeI1083 filter (Figure 4.8a) has peak transmissivity a little over half of the new SiX1430 filter we purchased (Figure 4.8c). The original SiX1430 filter used had too low throughput (Figure 4.8b) and so had to be replaced. Line profile widths are typically $\sim 2-3$ Å so both filters are sufficiently flat across the line profiles.

4.4 Guiding

SOLARC has three guiding systems that can be used for different observing scenarios.

The first system performs basic sidereal tracking through the RA/dec motors and allows the user to point the telescope at any location on the sky. It relies on 'The Sky6' software which includes an extensive map of the sky. This system is excellent for roughly pointing the telescope to the target of interest which can be the Sun or planets. However the tracking is purely mechanical and has no image feedback mechanisms. Any slipping of the RA/dec motors are not accounted for and the image can easily drift over time by many degrees if this is the only system used for tracking.

The second system referred to as the 'fast guider' performs corrections using piezoelectric actuators to apply small tip-tilt corrections to the M2 mirror with rates as fast at 10Hz. The fast guider camera is located inside the telescope (Figure 4.4a) and uses about 5% of light reflected from the beam coming from M2 that falls on the fiber entrance. Because coronal observations are very faint and the telescope is used in full aperture mode, no part of the disc light must make it through the Field Stop. At the CCD efficiency and exposure time used for the fast guider camera, coronal structures are too faint to guide on. Hence the fast guider is primarily used as a context imager to ensure disc light does not enter through the Field Stop due to unforeseen failures in the telescope or loss of guiding due to clouds.

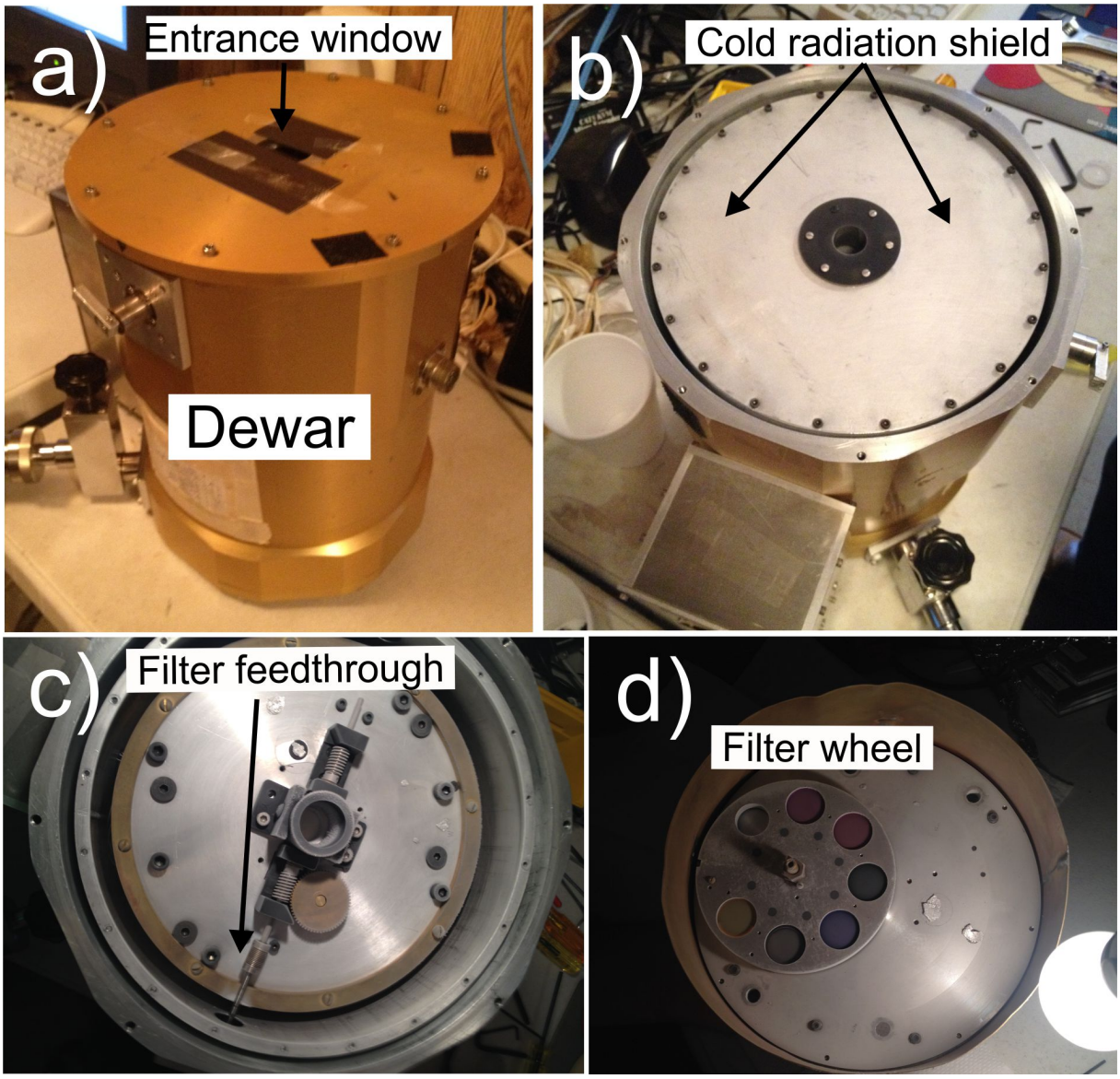

Figure 4.7: Photographs showing the dewar assembly. (a) An outside view of the intact dewar with the front vacuum sealing cover attached. (b) After removing the front cover there is a cooled radiation shield. (c) To access the filter wheel the mechanical feedthrough needs to be decoupled. (d) The top part of the assembly showing the filter together with the 1 inch filters. Only two of the filters are used for these observations.

The third system referred to as 'slow guider' performs corrections by issuing commands to the RA/dec motors and uses a small telescope/camera system mounted on the side of the telescope tube (Figure 4.9a) to get feedback on what the telescope is actually pointed at. A neutral density filter

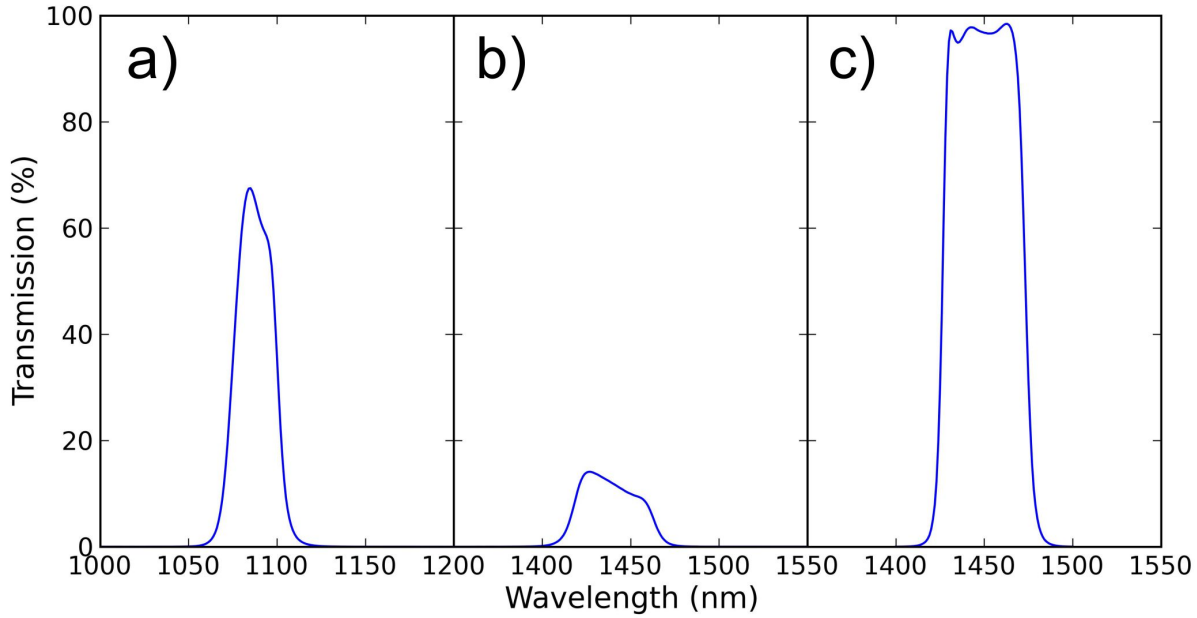

Figure 4.8: Filter transmission curves for: (a) HeI1083 and FeXIII1075; (b) Old SiX1430 filter; (c) New SiX1430 filter.

protects the CCD camera from being overexposed. The slow guider is a good option for keeping the telescope fixed on parts of the corona because of its large 5°×5°field of view (Figure 4.9b) and independent image acquisition. During operation, the slow guider software calculates the central position and radius of the solar disc based on a reference image flux established by the user when the image is visibly clear of obstructions. While observing, if the solar disc is obscured, the flux is affected and the guider incorrectly recalculates the size of the disc. This can potentially lead to catastrophic guiding errors and damage to the instruments. However, the guiding frequency is only around 0.1 Hz while the image acquisition with the slow guider is around 3 Hz. This 'delayed' guiding allows a vigilant observer to notice the change in the observing conditions and either decouple the guider or cover the telescope aperture to avoid damage. However, guiding errors with higher frequencies occur due to telescope jitter, atmospheric seeing variations and sudden slipping of the motors (sidereal tracking continues throughout the day). Apart from the RA/dec motors slipping, the other two processes induce random tip-tilt motions in the image with amplitudes $\sim 3-4''$ (Swindle 2014). Our demagnified plate scale ensures that the fibers collect light from a region $\sim 24\,''$ in diameter so

the small guiding errors are less of a concern since the fibers are already averaging over large areas in the image plane.

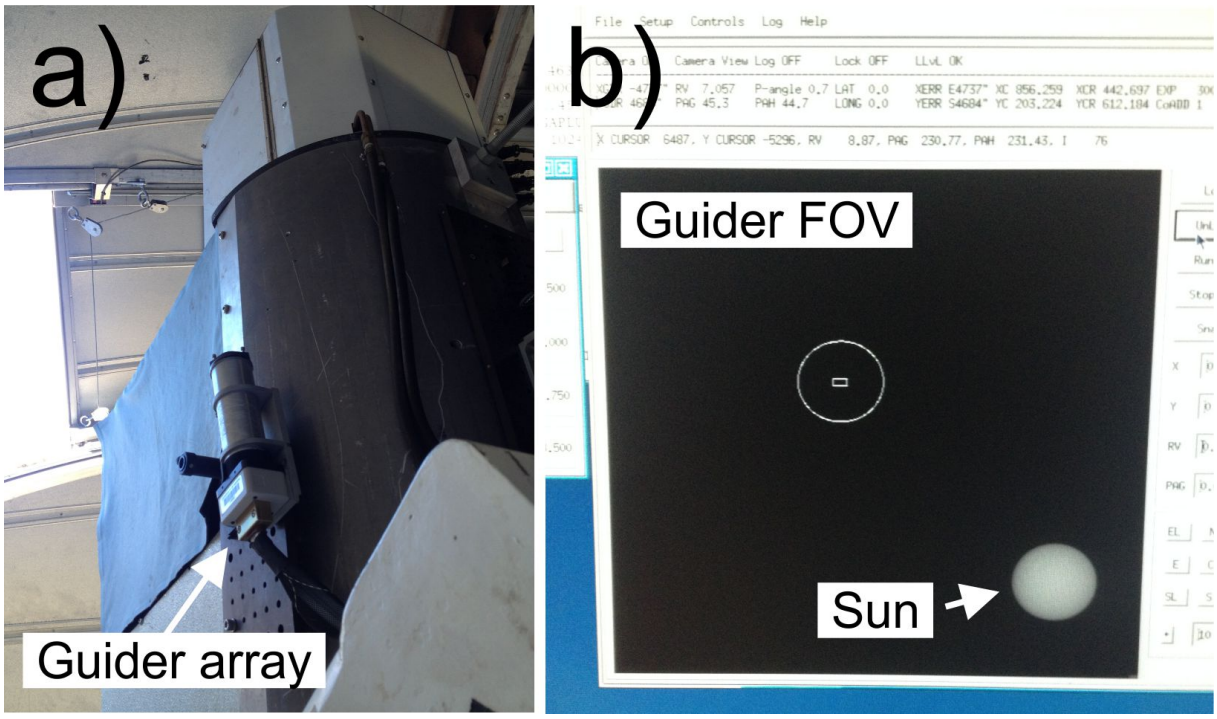

Figure 4.9: Photograph of the slow guider telescope and array (a) and computer screenshot showing the slow guider user interface and field of view (b).

4.5 Detector characteristics

The 256×256 IR detector is a HgCdTe $1 - 2.5\mu$m camera designed and built originally for the 1994 total solar eclipse (Kuhn et al. 1996). Frames are digitized at 16 bits/pixel and it uses a COM (serial) interface to connect to software written in C++. Maximum readout rates are around 20 frames per second but most of our data exposures are longer than one second. The software is integrated into an IDL graphical user interface (GUI) which allows exposures to be synchronized with modulations of the LCVRs to achieve full Stokes polarization exposures.

The camera is housed inside a sealed dewar (Figure 4.7) together with the filter wheel and can be cooled to 77K using liquid N_2. Typically the camera remains cold throughout one observing day

and requires cooling again at the start of each day. However, a very slow warming trend is observed during each working day with the slope in the warming dependent on the quality of the vacuum inside the dewar (Figure 4.10).

This vacuum inside the dewar lasts about 4 months before needing to be evacuated again using the turbo-pump available at the summit. The dewar is always evacuated warm so that impurities accumulated inside the charcoal getter inside are released. Hot pixels remain constant during the observing day and are usually removed though flat-fielding or dark subtraction. Among the problems encountered with data acquisition was troubleshooting a problem with cooling the camera dewar. It appeared as if the dewar had a leak since it would only reamin cold for a few hours when typically it would stay cold over the span of an entire day. This problem persisted for several months until we tracked the problem down to changing the purity of the charcoal used inside the dewar getter.

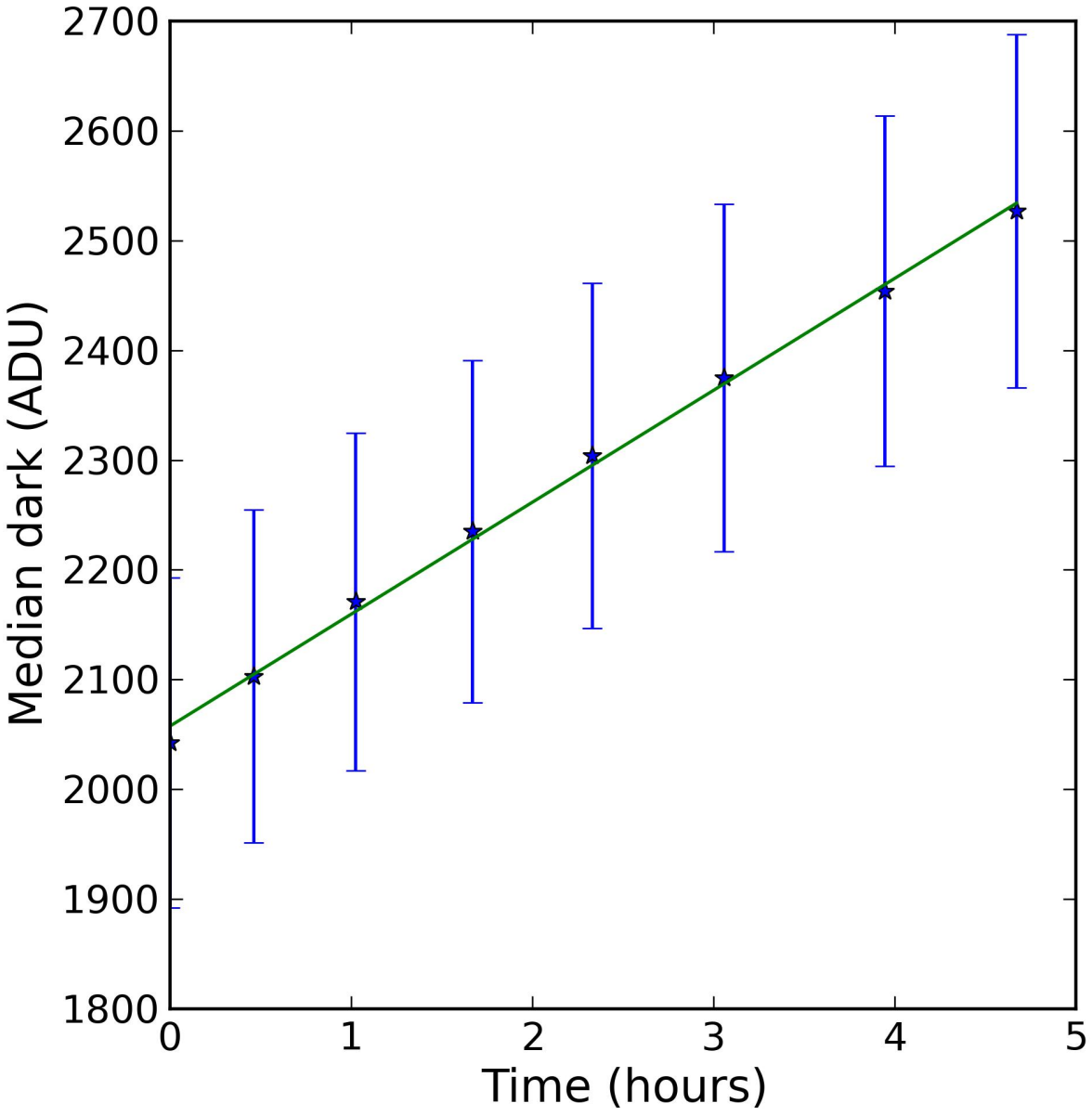

Figure 4.10: Graph showing average dark current evolution (3s exposure) during an observing day.

BIBLIOGRAPHY

Kuhn, J. R., Penn, M. J., & Mann, I. 1996, ApJ, 456, L67

Kuhn, J. R., Coulter, R., Lin, H., & Mickey, D. L. 2003, Proc. SPIE, 4853, 318

Kuhn, J. R., Arnaud, J., Jaeggli, S., Lin, H., & Moise, E. 2007, ApJ, 667, L203

Lin, H., Kuhn, J. R., & Coulter, R. 2004, ApJ, 613, L177

Moise, E., Raymond, J., & Kuhn, J. R. 2010, ApJ, 722, 1411

Swindle, T. R. 2014, Ph.D. Thesis

CHAPTER 5
DATA REDUCTION METHODS

Reduction methods are the sequence of procedures required for extraction of spectropolarametric data from the image array. These include:

- Elimination of modal noise.
- Dark and bias subtraction.
- Extracting individual spectra.
- Flat-fielding.
- Calculation of Stokes parameters from polarized spectra.
- Disc center calibration.

Each of these procedures and their modifications required for the acquisition of the present data are detailed below.

5.1 Modal noise

The fiber bundle present in the telescope when I started contained large time-varying modal noise structures. Optical fibers transmit power through constructive interference in an ensemble of modes (Baudrand & Walker 2001). Modal noise appears as a high-frequency structure seen in the entire spectrum (Figure 5.1a). This pattern cannot be calibrated since even small physical disturbances to the fibers, like the movement of the telescope due to tracking, changes the pattern. The types of fibers we use are ~ 50 μm in diameter and admit several thousand modes at infrared wavelengths. The interference pattern is sensitive to small changes in the fiber position, light injection into the fiber and wavelength. While the telecommunication industry can resort to very narrow single mode fibers to solve this issue, fibers of such small diameters are too inefficient for use in astronomy due to their low light throughput.

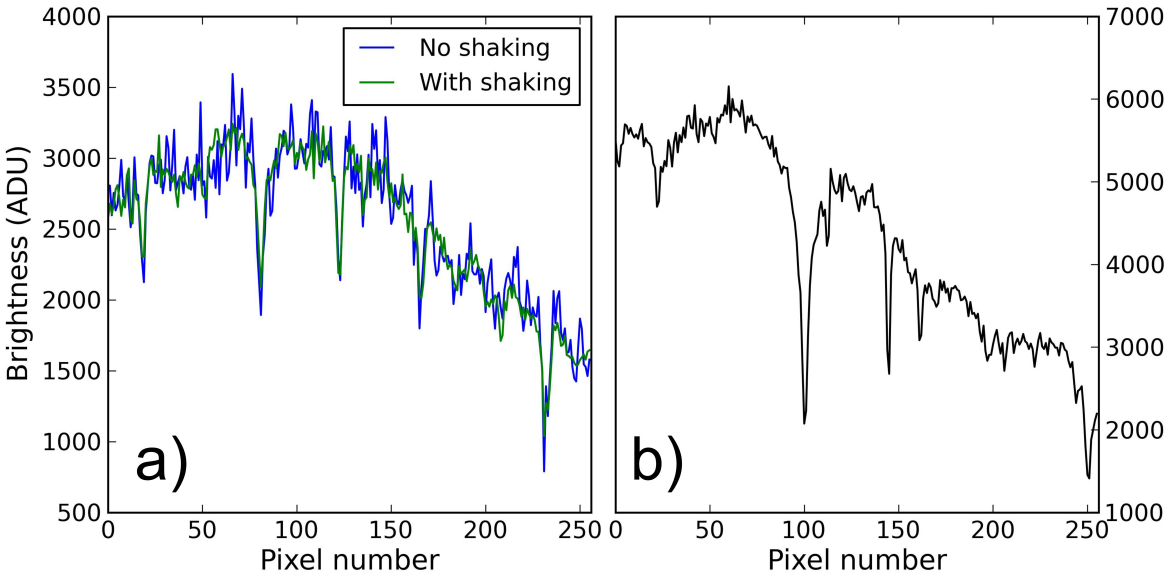

Figure 5.1: Plots showing modal noise spectra. a) Modal noise appears as a high-frequency structure seen in the entire spectrum. Shaking the fibers removes some of the modal noise and improves S/N. b) Spectrum obtained at disc center with the new fiber bundle shows significantly reduced modal noise without the need to shake the fibers.

This problem has been documented in the literature before (Baudrand et al. 1998; Baudrand & Walker 2001; McCoy et al. 2012). One simple and common solution to the modal noise structure is to shake the fibers as the exposures are taken. In principle this effectively mixes the interference patterns and averages out the modal noise leaving a clean spectrum. Experiments into the type of shaking suggest that small-amplitude shaking is best as long as the frequency is high enough that the averaging is over many patterns for the same exposure.

Typically, observatories build their own custom solutions to this problem and we also tested a few low cost solutions (e.g. modified desk-fan) to shake our fibers at 30 Hz. This frequency provides at least 15 cycles over the 500 ms disc center exposures and over 100 cycles for typical coronal exposure times. Figure 5.1a shows that shaking the fibers removes some of the modal noise and improves S/N. However, the improvement in S/N was not large enough to warrant using shakers for the long periods of time necessary to collect the observations.

In addition, we were concerned about the effect that prolonged high frequency shaking would have on the glass core of the fibers bundled inside the metal sheath. To fix this problem we replaced

the fiber bundle with the original 256 fiber bundle which had better performance in terms of modal noise (Lin et al. 2004). Apart from the improvement in modal noise, the new fiber bundle had a larger fiber core size which allowed for faster beams to enter the core of the fiber. Hence the fiber could collect light from larger areas on the sky.

The modal noise amplitude is observed to vary inversely with the f# of the input beam into the fibers. Since

$$\text{f\#} = \frac{focal\ length}{aperture\ diameter} \tag{5.1.1}$$

using the smallest circular aperture (diameter ~1.27 cm) to take disc center observations induced a greater amount of modal noise. Using a specially designed annular entrance aperture, which has the same f# as the full open aperture (diameter 0.46 m), helps alleviate the modal noise problem when taking disc center observations. Figure 5.1b shows a disc center spectrum obtained with the annular aperture.

5.2 Dark and bias calibration

The detector needs to be cooled to 77 K using liquid N_2. Once this temperature is reached the detector will stabilize around a median dark current at ~1100 ADU/s at 1083 nm, and 950 ADU/s at 1430 nm. The difference in the median dark levels is due to different thermal background intensities and the different profile shapes of the filters used for the two spectral regions (see Figure 4.8 for filter transmission profiles). Figure 5.2 shows examples of 100 co-added dark frames at 1083 and 1430 nm with 3 s exposure times. Dark frames were coadded automatically as the exposures were obtained to save disc memory and disk accessing time. Master dark frames coadded manually after saving each dark exposure individually were virtually identical to the automatically coadded ones.

In order to avoid introducing too much noise when subtracting the dark frames from data frames, we routinely coadded at least 100 dark frames exposures. To account for dark current variability during the day (see Figure 4.10), we obtained dark exposures every few hours and used a linear fit to the evolution to interpolate for dark current levels closer to the observation time during the day.

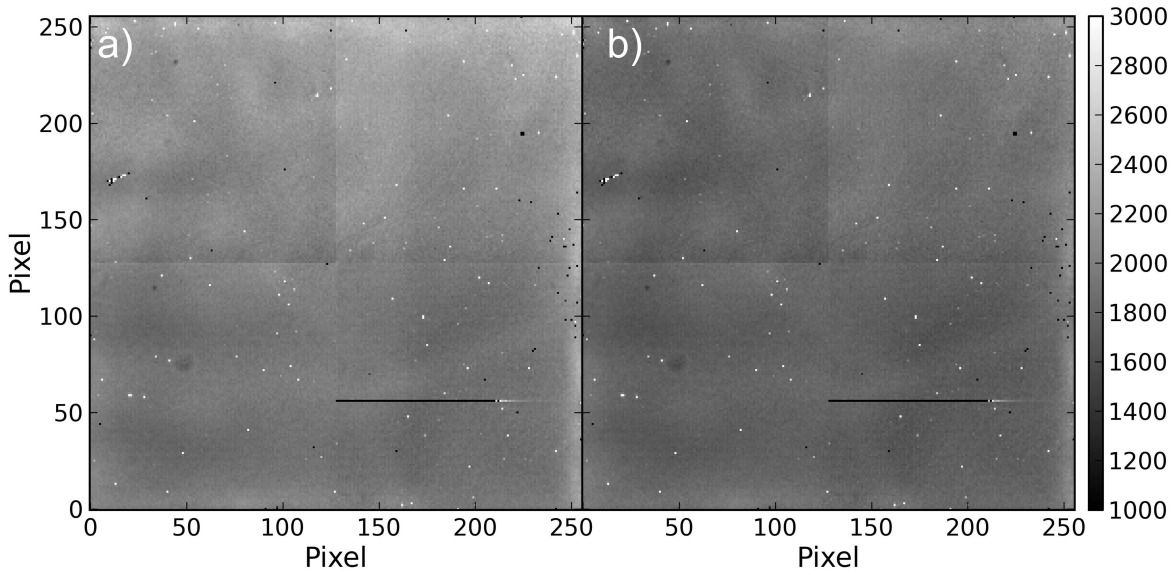

Figure 5.2: Dark frames obtained with 3 s exposures after coadding 100 exposures. The image scale is given in ADU. a) Dark frame obtained using the HeI 1083 filter; b) Dark frame obtained using the SiX 1430 filter.

5.3 Extracting individual spectra

For the present work, all data reduction was performed using custom software written using Python 2.7. Python is a free downloadable, extremely versatile and rapidly growing programming language that is being adopted across many scientific disciplines, including astrophysics. Importantly, data reduction pipelines for future DKIST instrument are also presently written in Python.

The data reduction pipeline for SOLARC was integrated into a graphical user interface (GUI) available for future users. The analysis GUI and reduction pipeline was specifically designed to be capable of recognizing and adapting to a range of observing scenarios such as: varying number of exposures recorded in a single file; varying numbers of fibers imaged across the array at different pixel positions; varying tilting of the spectra across the array. Appendix B shows screenshots and provides a brief summary for the GUI capabilities. The amount of data collected during a typical observing day with SOLARC sometimes involves hundreds of files with calibrations and exposures of different regions in the corona. To handle such a large number of files efficiently, the GUI has built-in assessment and display functions allowing the user the ability to quickly visualize which exposures

are useful for further analysis. This software is available on demand and can be distributed to potential users of SOLARC.

The spectra are oriented on the detector with the wavelength direction aligned horizontally whereas the vertical array direction corresponds to the linear arrangement of fibers across the array (see Figure 4.5 for sketch of fiber mapping across the array). The detector is oriented manually at the start of each day to ensure that the spectra have as little tilt as possible in the wavelength direction.

The pixels where the fiber centers are located in the vertical direction are determined algorithmically for each day of exposure. A sequence of high S/N disc center exposures is obtained using the annular aperture to determine the flatness of the array as well as fiber positioning across the array.

The extraction algorithm is as follows:

1) In image I(x,y) a reference column I(x_i,y)≡I_i(y) is selected at pixel x_i that has good signal contrast in all the fibers, typically locared near the center of the array.

2) Performing a Fourier transform for I_i(y) and calculating the power spectrum of we can calculated the average pixel spacing between fibers can be deduced. This spacing corresponds to the strongest peak in the Fourier power spectrum. However, this serves only as a first order estimate of the fiber positions and a more refined estimate is necessary to accurately deduce the central pixel row for each fiber.

3) Local maxima and minima in I_i(y) are found by calculating the quantity $M_i(y_k) = (I_i(y_k) - I_i(y_{k-1})) \times (I_i(y_k) - I_i(y_{k+1}))$ where $1 < k < 254$. Any pixel y_k with a positive $M_i(y_k)$ value is either a local maximum or minimum. To distinguish between the extrema we look at how the intensity in each of these pixels compares to the intensity of its nearest neighbor pixels. A first order polynomial is fit to the intensity of the minima pixels and subsequently I_i(y) is normalized by this polynomial. The first maxima pixel with normalized intensity >2 represents the first fiber center location.

4) Starting from the first fiber location and using the average spacing determined in step 2,

the approximate locations of the remaining fibers are deduced. We use a five pixel interval centered on these approximate locations to finally identify the precise fiber center location as the maxima in each interval.

5) The intensity column $I_i(y)$ is then cross-correlated with other columns $I_j(y)$ where $0 < j < 255$ to determine the warping and tilt of the spectrum across the array. Typically a simple linear tilt is observed which leads to a total shift $\sim$0.1 pixels over the entire 256 pixels of the array. The individual cross-correlation results are fit with a linear polynomial to remove any outliers due to low signal in parts of the spectrum. This is often the case for SiX1043 spectra as seen in Figure 5.3).

6) Once the central pixel location for each fiber are known, the spectrum for each fiber is extracted by averaging the intensity values over three pixels straddling the calculated pixel center in the spatial direction (y direction on the array).

5.4 Flat-Fielding

We attempted two approaches to flat fielding data frames.

5.4.1 Gain removal algorithm

The gain removal algorithm described in Kuhn et al. (1991) was applied to a sequence of shifted exposures of the solar disc center. This method is based on shifting a static image across the detector in two dimensions. Analyzing changes in the output signal provides information about the gain variation as long as the input signal remains constant during the shift. An iterative process converges on a solution for the gain variation across the detector typically over 20 cycles.

For our purposes the input signal represents the extracted and shifted disc center spectra from each fiber. The image movement is performed using the grating mounted on an electronically controlled rotating stage. This shifts the spectra in the horizontal (wavelength) direction across the array by varying the rotation of the grating. In theory, this slightly alters the dispersion power of the grating but in practice the shifts involved are so small ($\sim$ a few hundredths of a degree) that

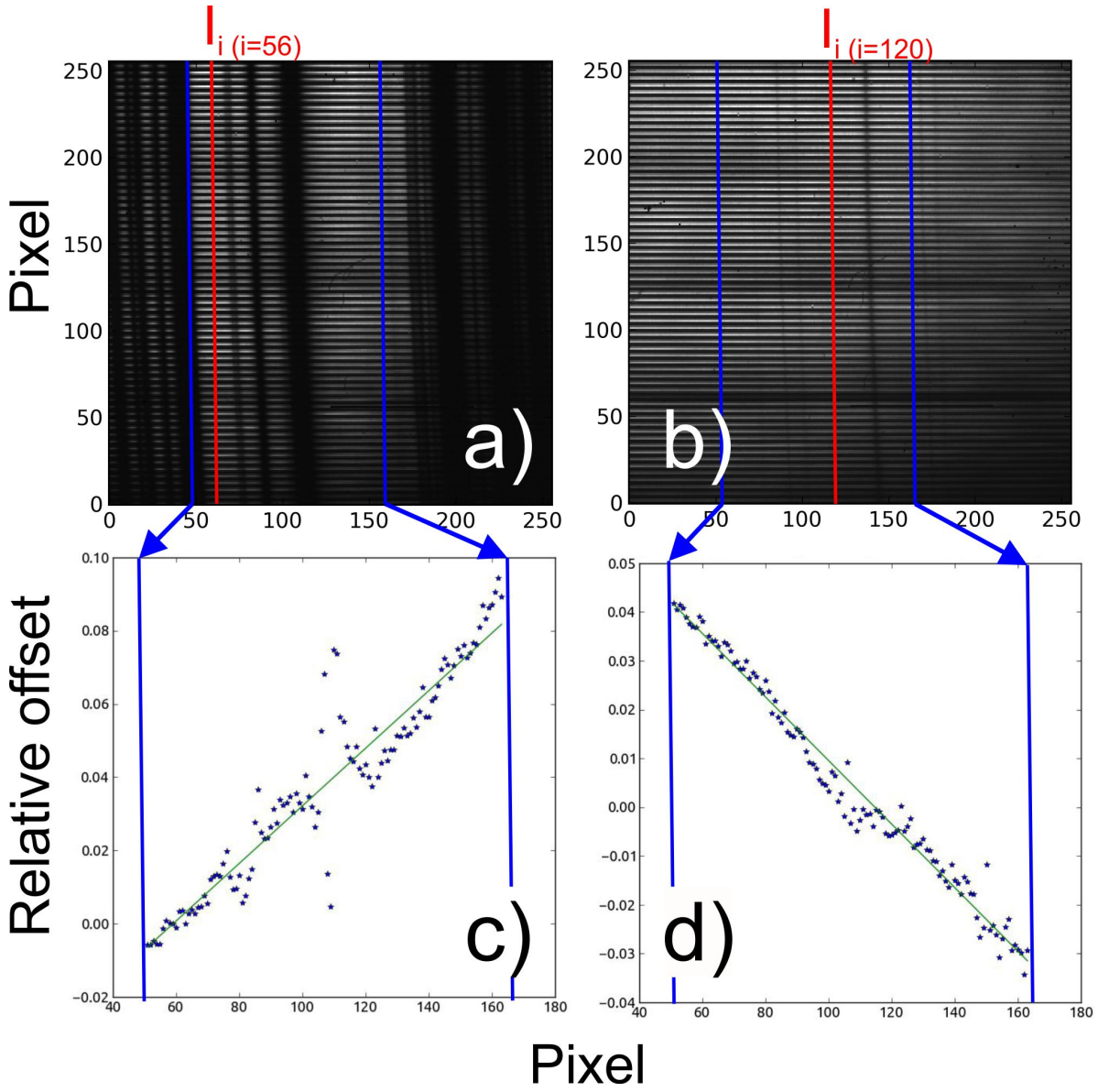

Figure 5.3: Cross-correlation shifts between the reference column $I_i(y)$ and all the columns with i between 56 and 120. On the left (a,c) is an exposure near SiX1403 and on the right (b,d) is an exposure near FeXIII1075. To determine the correct tilt of the spectra across the array a polynomial fit (green lines) is crucial for SiX1430 where strong absorption bands can produce spurious cross-correlation values.

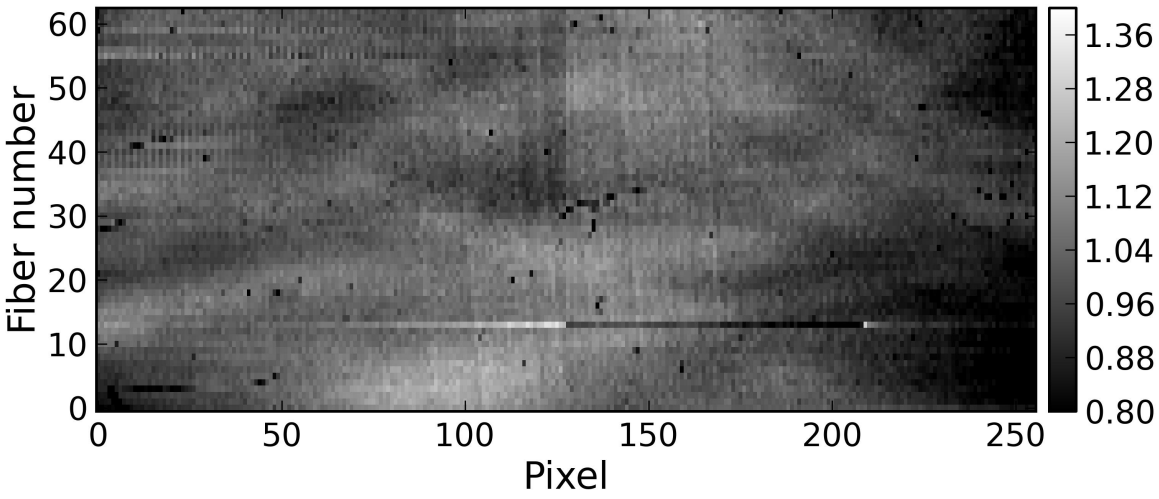

Figure 5.4: Gain map obtained by shifting the spectra across the detector using rotation of the dispersion grating.

we can treat the change in the dispersion as negligible. The smallest achievable movement is ∼5 pixels given the current rotating stage accuracy. An example of the gain map calculated using this method is shown in Figure 5.4.

Once a gain map is calculated the coronal spectra can be corrected through division with the map. This procedure does remove some of the gain pattern from the spectra but as can be seen in Figure 5.6, this procedure is better at filtering out high frequency gain patters but does not help with larger features.

5.4.2 Disc center flat fielding and calibration

Another way to flat field the coronal observations is by using exposures near the disc center where the illumination for all the fibers is uniform. In principle if the disc center spectra and the coronal spectra are imaged across the same array pixels, dividing one by the other will remove variations and lead to flatter spectra dominated by random variations (Figure 5.7).

Raw spectra extracted from the images are in analog-to-data-units (ADUs). To obtain a physically meaningful interpretation of the coronal measurements we use on-disc observations to calibrate off-disc data. To compute the calibrated coronal brightness value $F_c(x_i)$ in disc units at wavelength x_i the following formula applies:

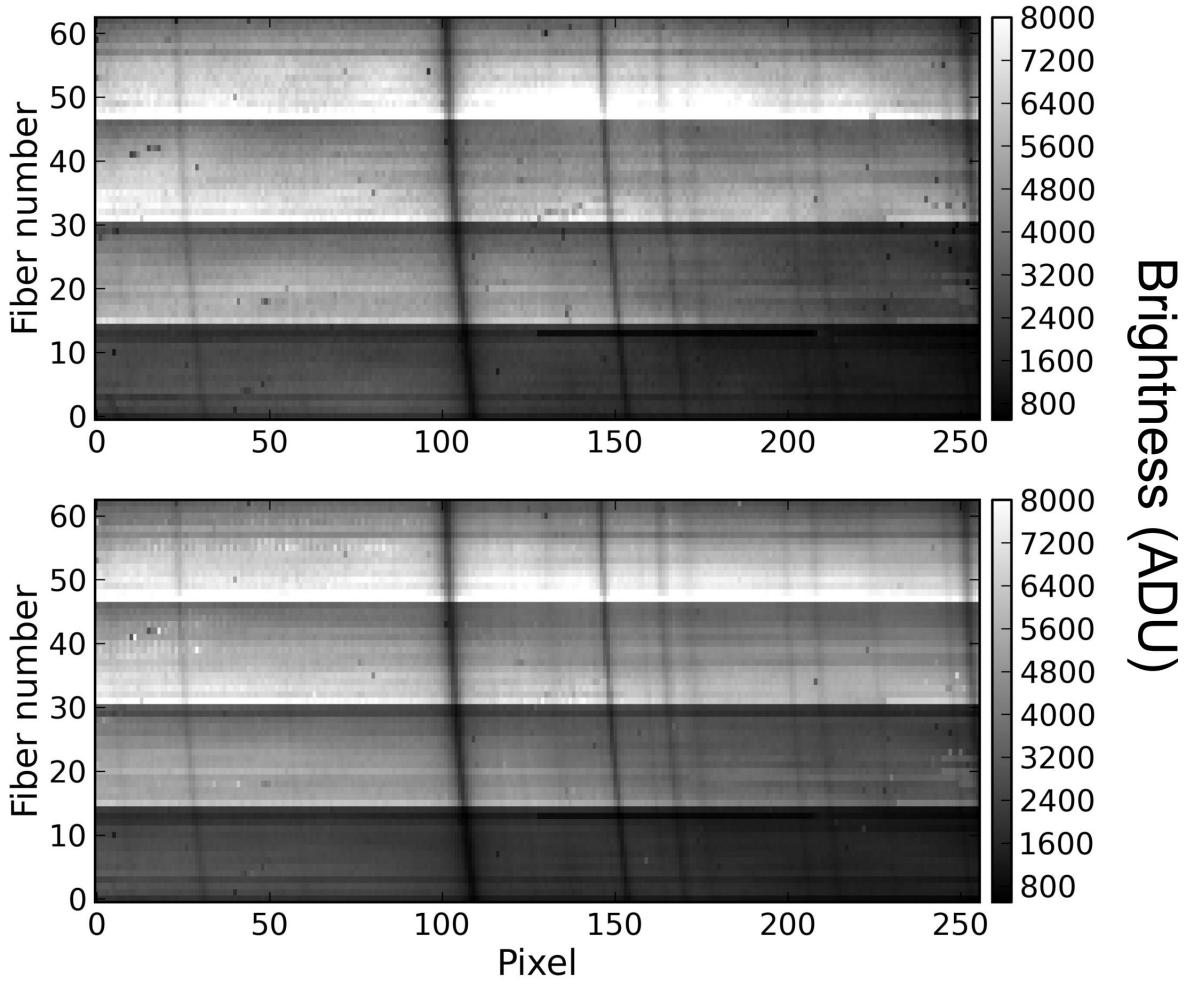

Figure 5.5: Coronal observation spectra for the region near HeI1083. Spectra without (top panel) and with (bottom) flat field correction using the flat shown in Figure 5.4. A lot of the high frequency features are corrected by the flat-fielding procedure.

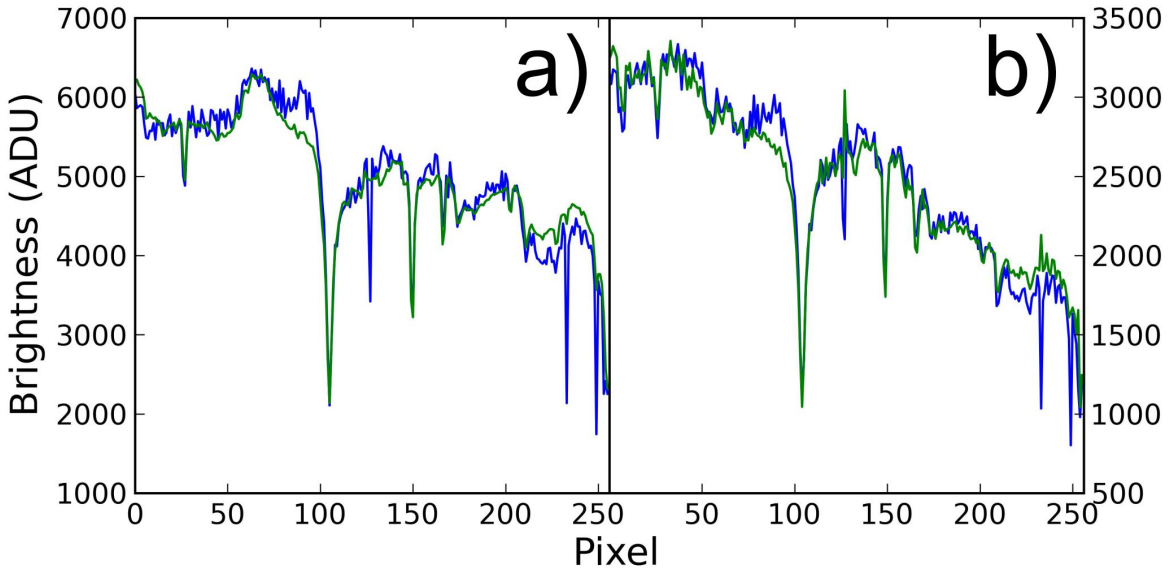

Figure 5.6: Comparison between original (blue) and flat-fielded spectra (green) for: (a) Disc center observations. (b) Coronal observations.

$$F_c(x_i)[B_\odot] = \frac{F_c(x_i)[ADU]}{F_\odot(x_i)[ADU]} \times \frac{t_\odot}{t_c} \times \frac{A_\odot}{A_c} \tag{5.4.1}$$

where the units for the brightness are made explicit in the square brakets, $F_\odot$ is the corresponding disc center brightness measured at the respective wavelength x_i, $t_\odot$ and t_c represent the exposure times for on disc and off disc respectively, and $A_\odot$ and A_c represent the aperture areas during on- and off-disc exposures respectively. Typically $A_\odot = 18.7\ cm^2$ for the annular aperture while $A_c = 1297.2\ cm^2$ for the fully open aperture.

To minimize pixel-to-pixel noise variations in the on-disc observations an average flux is computed over 20 pixels centered on x_i instead of directly using $F_\odot(x_i)$. Flat regions of the continuum spectrum are used for this averaging. The FeXIII1075 and HeI1083 coronal emission lines are located in areas of low absorption line density so regions of interest in the spectrum are not affected by this averaging. On-disc observation times are typically $t_\odot = 50$ ms since longer exposures cause some of the camera pixels to become saturated. An example of a coronal spectra calibrated using disc center calibrated observations is shown in Figure 5.8. Also noticeable are the large levels of scattered light that we observe in some of the coronal spectra.

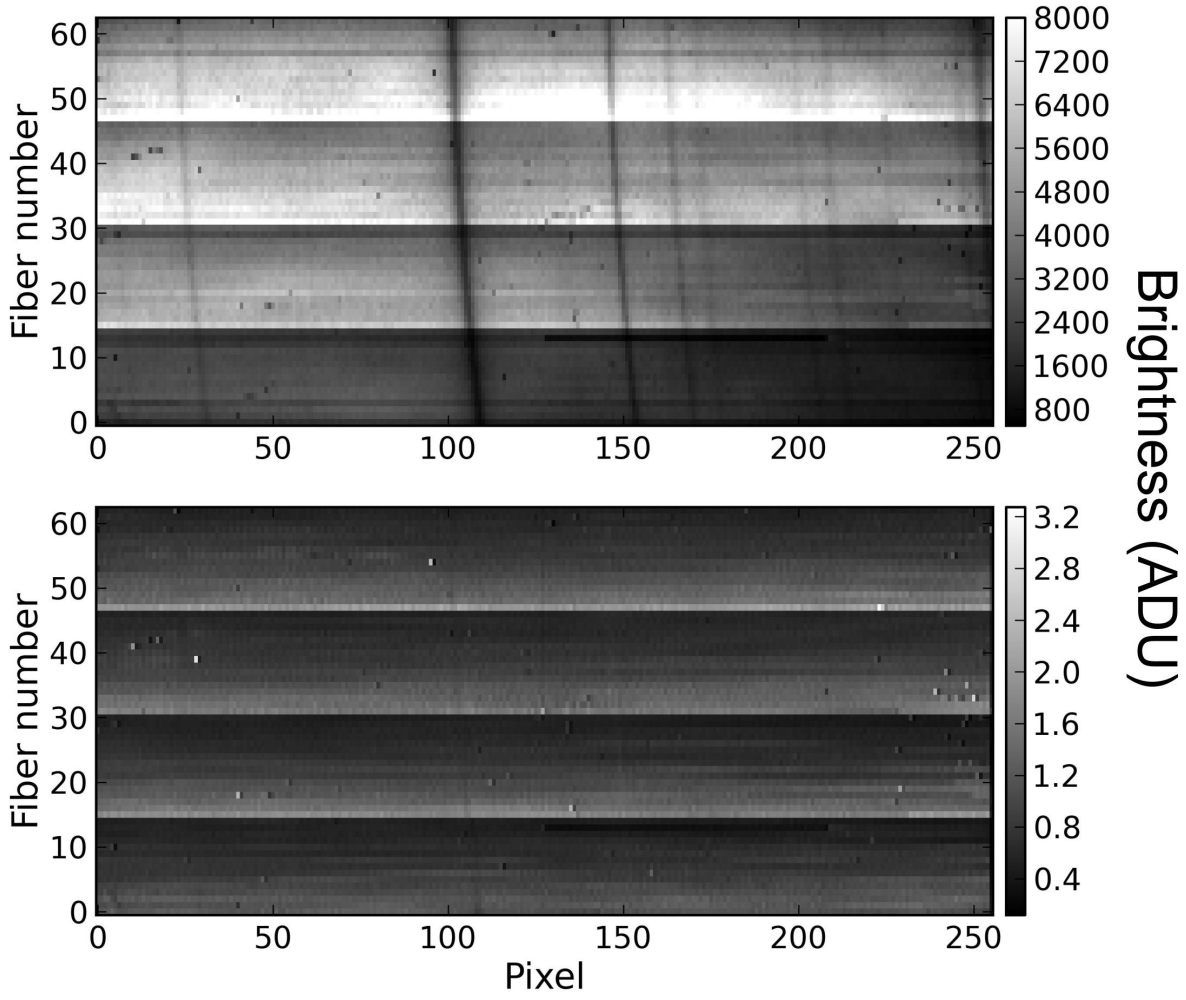

Figure 5.7: Coronal observation spectra for the region near HeI 1083. The top panel is not corrected while the bottom panel has been divided by the disc center spectra. Much of the larger scale structure disappears.

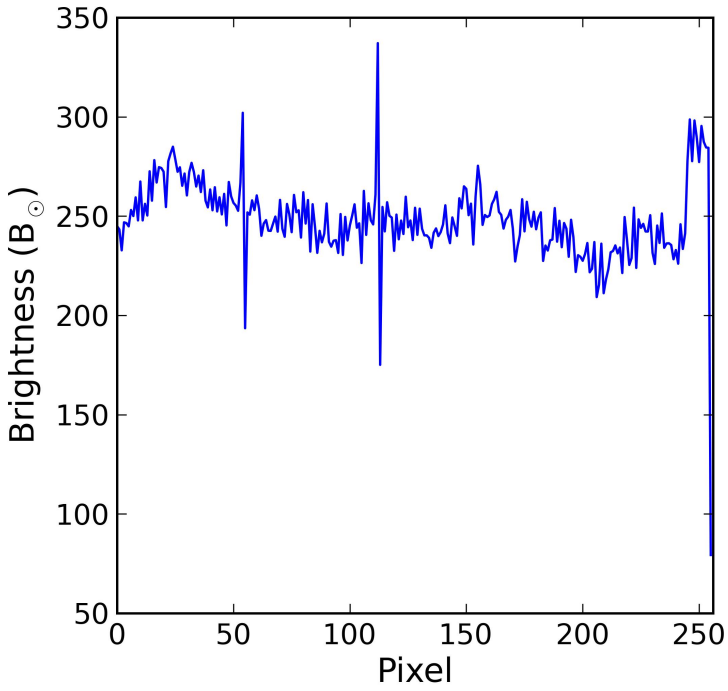

Figure 5.8: Single fiber normalized using the corresponding disc center spectrum imaged across almost the same pixels. The asymmetric spikes near pixel 50 and 110 are due to a slight sub-pixel misalignment between the two spectra.

5.5 Polarized spectra

A typical polarized frame obtained with SOLARC involves six individual images where the LCVRs modulate the polarization state of the incoming radiation using the following sequence: $(I+Q)_1$, $(I-Q)_2$, $(I+Q)_3$, $(I-Q)_4$, $(I+U)_5$, $(I-U)_6$, where the index numbers indicate the position of the image in the sequence and I, Q, U indicate the state of polarization observed. It was noted during previous use of the camera (Swindle 2014) that sometimes the array bias varies during the first two exposures in a sequence so the recommendation was to repeat the first two exposures for Stokes Q.

Individual exposures from each sequence are dark and bias corrected and then combined into Stokes "images" using the following sequence:

$$\begin{aligned} I_{img} &= \frac{(I+Q)_3 + (I-Q)_4 + (I+U)_5 + (I-U)_6}{4} \\ Q_{img} &= \frac{(I+Q)_3 - (I-Q)_4}{2} \\ U_{img} &= \frac{(I+U)_5 - (I-U)_6}{2} \end{aligned} \tag{5.5.1}$$

Since multiple frames are typically obtained for a single observing location these Stokes images are then coadded to further reduce random noise. From these final images Stokes I, Q and U spectra are extracted.

Presence of polarized photospheric absorption lines in the Q and U spectra indicates crosstalk from I spectra. The lines are narrow and are observed because of forward scattered disc light by the Earth's atmosphere. Bacause of the forward scattering angle we expect these lines to have negligible polarization. Crosstalk amounts vary with the telescope pointing so Q and U spectra must be corrected individually for each coronal target.

Spectral regions around the FeXIII1075 and HeI1083 lines allow for crosstalk removal through least square minimization. This is done by fitting crosstalk terms that remove the photospheric lines from the Stokes Q and U spectra. An important check on the accuracy of the correction is to compare the measured continuum linear polarization orientation with the expected orientation relative to the solar limb (Figure 5.9).

In contrast, the SiX1430 line region is characterized by strong atmospheric absorption bands

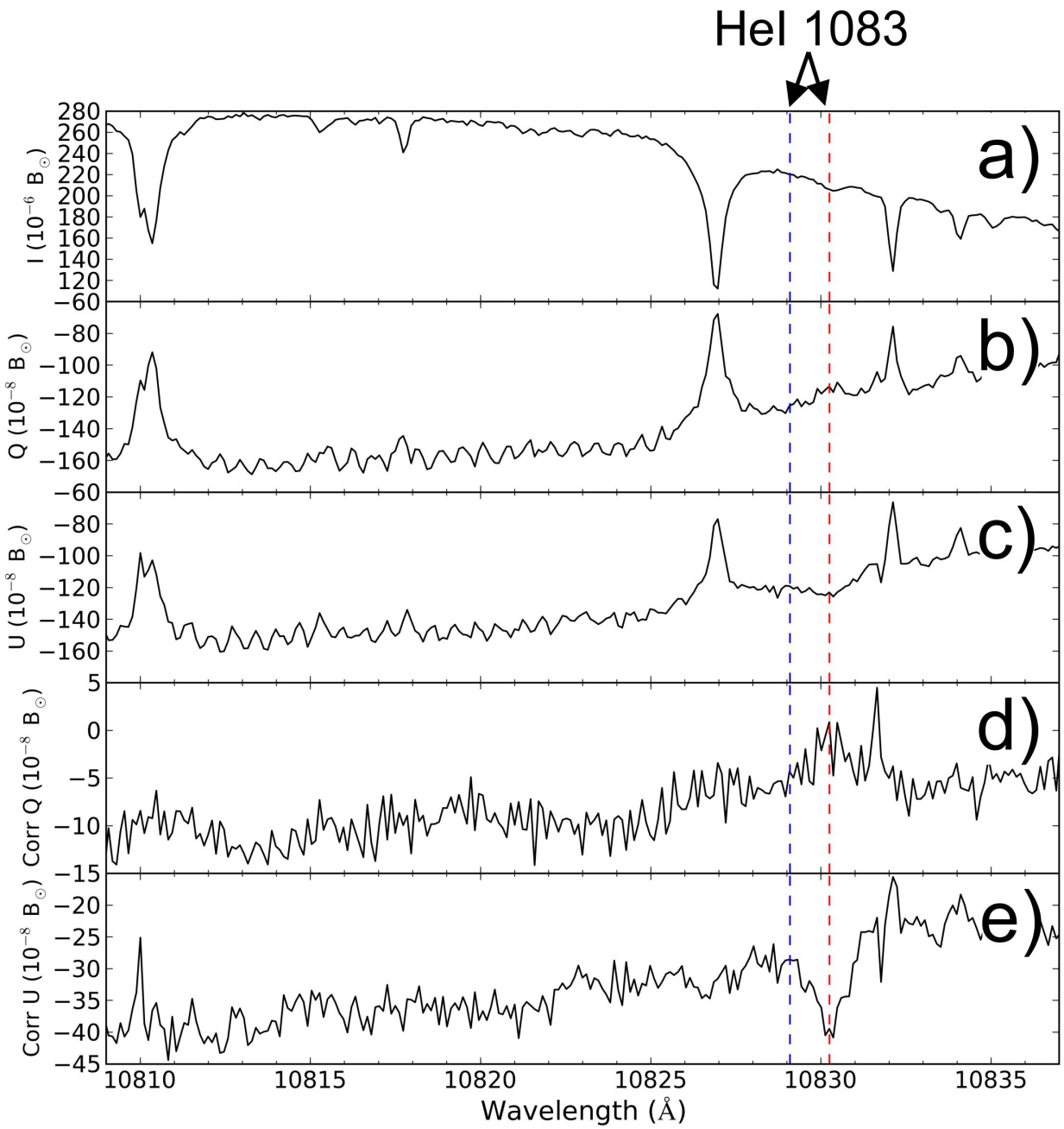

Figure 5.9: Effect of crosstalk removal from polarized spectra. (a) Stokes I spectrum near the HeI 1083 line. Stokes Q (b) and U (c) raw spectra extracted from the observations. Crosstalk corrected Q (d) and U (e) spectra. The photospheric emission lines are removed. The line near 10832 Å is a telluric absorption line so this is expected to appear in the polarized spectrum as well.

and very weak photospheric absorption lines. One alternative is to iterate over a range of crosstalk values until the continuum polarization orientation is tangential to the local solar radial direction. However, since we are interested in the emission line and not the continuum we can simply fit a coefficient to the atmospheric absorption bands that removes them completely from the spectrum. This will subtract both the crosstalk and continuum polarization. Hence, the resulting spectra consist of the SiX1430 line Q and U profiles (Figure 5.10).

Once the Stokes I crosstalk is removed the resulting spectrum will sometimes show large amplitude fringes due to interference in the optical elements. The fringing is strongly monochromatic so it is possible to use Fourier filtering to remove the ripple and recover photon noise limited spectra (Figure 5.11).

The final cleaned spectra show good line profiles at the expected wavelengths. The linear polarization orientations obtained from fitting the FeXIII and SiX lines for the same coronal region show good agreement as expected from two forbidden lines in the saturated Hanle regime. Line profiles are well approximated by Gaussian profiles within the noise limit of the measurements.

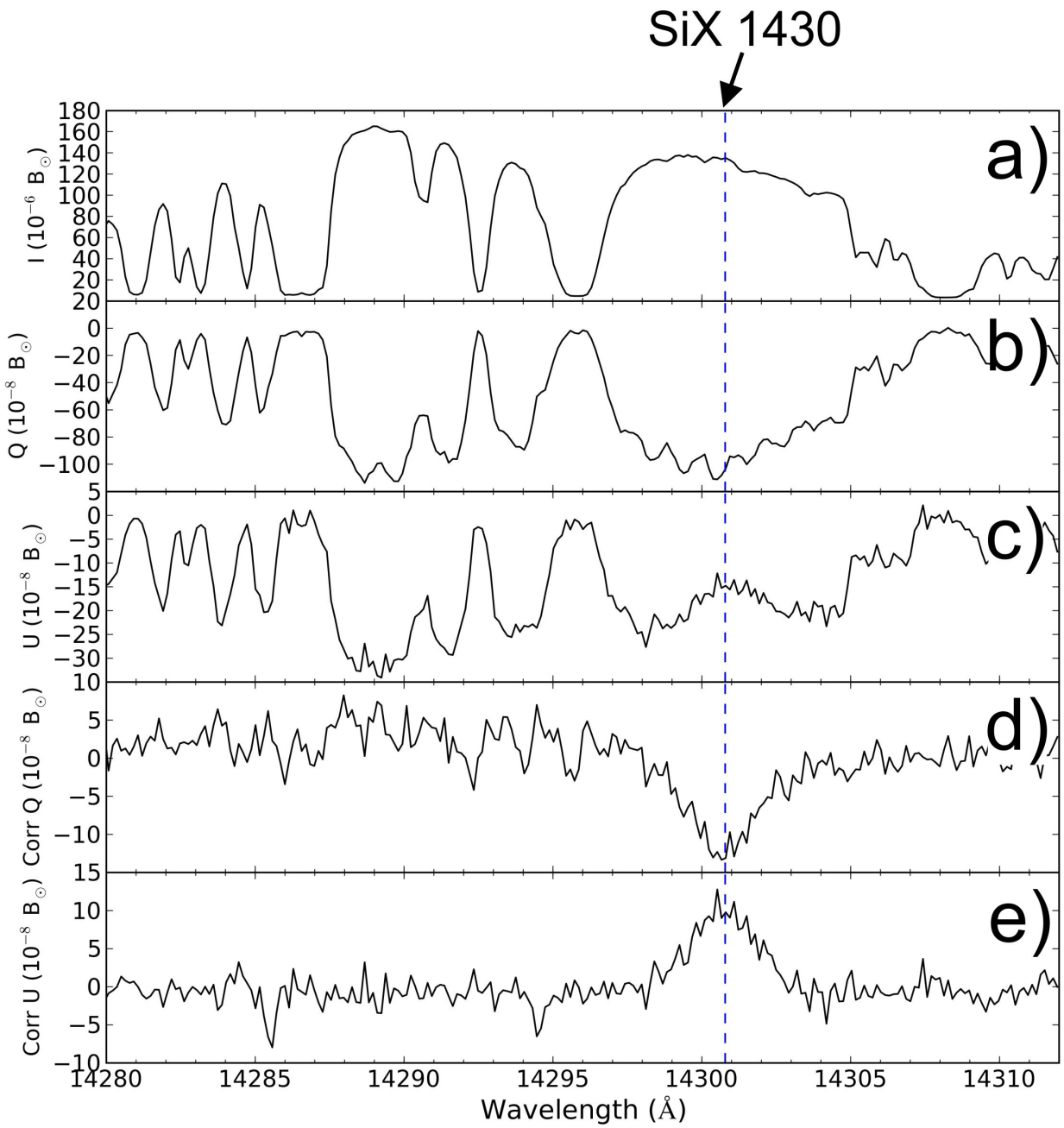

Figure 5.10: Similar to Figure 5.9 except for the region near SiX1430. Because of the lack of photospheric absorption lines near SiX1430 and the high density of telluric absorption lines a fraction of Stokes I is subtracted from the Q and U spectra until only the emission line is still present in the corrected spectra (d, e).

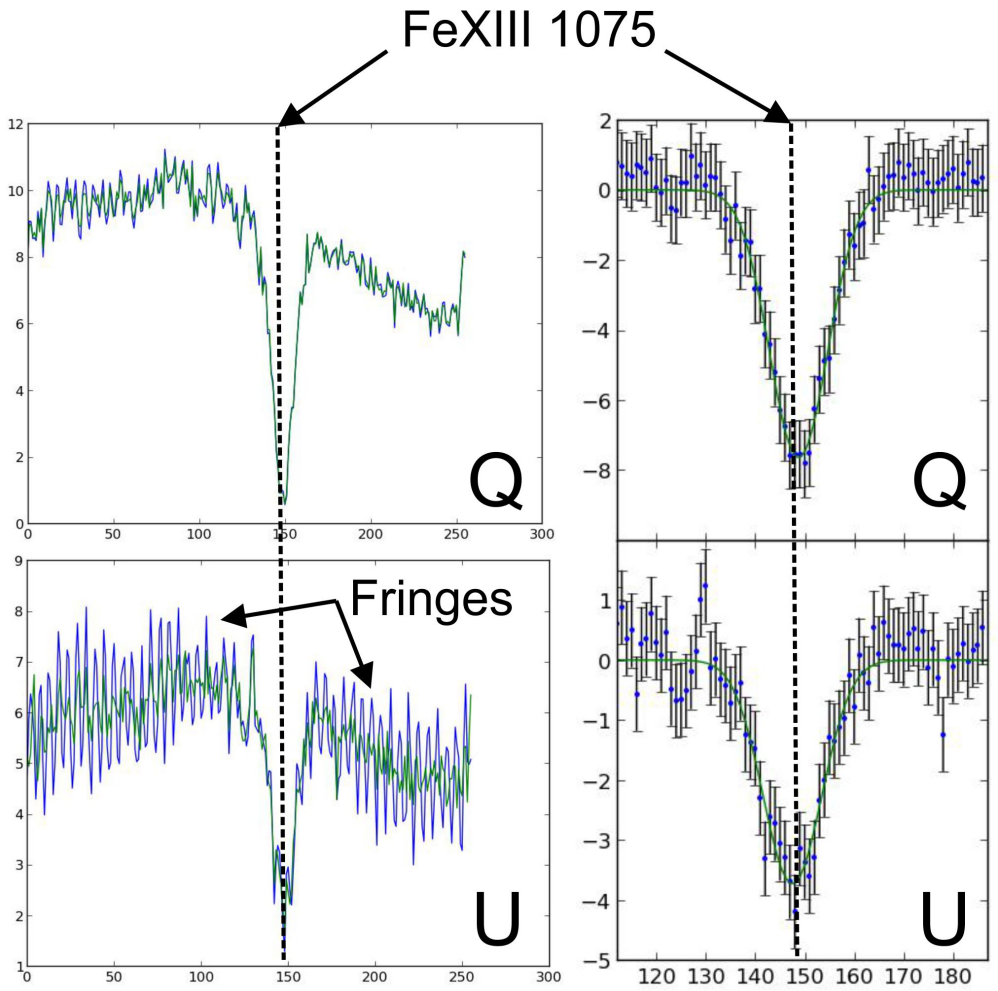

Figure 5.11: Similar to Figure 5.9 except for the region near SiX 1430. Because of the lack of photospheric absorption lines near SiX 1430 and the high density of telluric absorption lines a fraction of Stokes I is subtracted from the Q and U spectra until only the emission line is still present in the corrected spectra (d, e).

BIBLIOGRAPHY

Baudrand, J., & Walker, G. A. H. 2001, PASP, 113, 851

Baudrand, J., Guinouard, I., Jocou, L., & Casse, M. 1998, Fiber Optics in Astronomy III, 152, 32

Kuhn, J., Lin, H., Loranz, D., 1991, PASP, 103, 1097.

Lin, H., Kuhn, J. R., & Coulter, R. 2004, ApJ, 613, L177

McCoy, K. S., Ramsey, L., Mahadevan, S., Halverson, S., & Redman, S. L. 2012, Proc. SPIE, 8446, 84468J

Swindle, T. R. 2014, Ph.D. Thesis

CHAPTER 6
CORONAL OBSERVATIONS ANALYSIS

Coronal observations started early in 2015 but it was not until early 2016 that the final upgrades were performed on the system (e.g., new fiber bundle, increased plate scale, better baffling, etc.; see Chapter 4) that allowed the required sensitivity for detecting the coronal emission lines. Table A.1 (Appendix A) provides an summary of all the coronal data acquired with SOLARC after the upgrade took place. This table summarizes 25 days of observations with the new system when the sky was clear over 8 sessions, with lengths varying from 1 to 5 consecutive days of observation. In general, the longer sessions were better because of decreasing time each day necessary for cooling the dewar.

6.1 Instrument settings and data acquisition

A variety of observations were taken with different exposure times ranging from 200ms to 5s. Generally, exposures around 3s provide a good trade-off for increased sensitivity versus measurement error. Guiding was typically better before noon due to some imbalance in the telescope weight distribution that sometimes caused the drive motors to slip more during the afternoon. Whereas the hardware was optimized as discussed in Chapter 4, the variability in the settings depended mostly on computer software adjustments for data acquisition, i.e., exposure times and polarization sequences.

A typical day of observation involves the following procedures:

1. Cool down the array using liquid N_2. Depending on the starting temperature of the array, this can take between 20 minutes and two hours. To determine the array temperature the array is read out with the front window covered (i.e. dark mode). At 50ms exposures the the readout would typically stabilize around $\sim$100 ADU indicating the cooling is complete.

2. While the dewar cools the telescope is initialized on the center of the solar dics and the sidereal guiding is started. This is always done with the annular or small aperture mounted over the

telescope entrance to avoid overexposing the cameras. On-disc observations are not possible at full aperture with the current setup.

3. Once the array is cooled and the telescope is trained on the disc, optical components inside the optical bench are tuned to ensure the spectra are focused on the array and wavelength tilt is minimized.

4. A set of calibration images are taken at disc center with 50ms exposures. Exposing the disc center theoretically ensures uniform illumination of the fibers and can be used as a way to flat field the coronal spectra. Part of the calibration are also dark exposures at 50ms and 3s (typically coronal observation exposures). Thoroughout the day dark frames are recorded since there is a small but not negligible increase in the dark current during each day.

5. Once the calibrations are obtained, we shift the telescope to the limb of the Sun and initialize the slow guider. Checking the contrast between the on disc and off disc fibers the telescope focus can also be determined. If the image on the fibers is out of focus the limb will appear diffuse so the contrast will be low. The slow guider can now be engaged and coronal observations may begin.

6. Solar Dynamic Observatory / Atmospheric Imaging Assembly (SDO/AIA) satellite images of the solar corona for the day of observation are typically used to indicate interesting areas for observations, i.e., regions over streamers. These regions have been observed to correlated with increased HeI1083 emission.

The above preparation procedures for data acquisition took anywhere between 45 minutes and 2 hours depending on the time it took for the dewar to cool down. A number of $\sim$400 targets (individual positions in the corona) were observed during the entire observation campaign. The entire image dataset collected will be catalogued and made publicly available on one of the IfA servers.

6.2 Data reduction and assessment

A method of data reduction is required in order to translate the images at each target into usable spectra (see Chapter 5 for individual reduction steps).

There is ongoing work to try to improve the array flat field so the results presented here are still preliminary and rely primarily on the Stokes Q and U spectra where flat-fielding is not as big of an issue. Without an adequate flat-field and high background levels Stokes I measurements of the lines (with the possible of exception of FeXIII1075) is still not possible.

After screening the entire dataset, I present here only a selection of potentially interesting telescope targets that illustrate the goals of the observing campaign. Priority was given to target areas that had simultaneous measurements for multiple lines. The number of individual exposures for each target ranges from 20 to several hundred in the present dataset. In this chapter I present a number of 37 targets that were analyzed (Table 6.1) from which results were obtained for both SiX1430 polarization and Hanle inversions.

Table 6.1: Analyzed targets

Date	**UT Time**	**R[$R_\odot$]**	**PA[°]**	λ_c **[Å]**	t **[ms]**	**Frames**	**Coadds**	**Comments**
2016-05-03	19:15:06	1.25	100	10747	3000	1	20	Static
	19:23:47	1.25	90	10747	3000	1	20	Static
	19:31:26	1.25	80	10747	3000	1	20	Static
	19:39:25	1.25	70	10747	3000	1	20	Static
	19:47:09	1.25	60	10747	3000	1	20	Static
	19:54:46	1.25	50	10747	3000	1	20	Static
	20:02:30	1.25	40	10747	3000	1	20	Static
	20:10:12	1.25	30	10747	3000	1	20	Static
	20:17:51	1.25	20	10747	3000	1	20	Static
	20:26:00	1.22	10	10747	3000	1	20	Static
	20:33:38	1.22	0	10747	3000	1	20	Static
	20:47:44	1.27	270	10747	3000	1	20	Static
	20:55:45	1.27	260	10747	3000	1	20	Static
	21:03:36	1.29	250	10747	3000	1	20	Static
	21:11:17	1.29	240	10747	3000	1	20	Static
	21:19:19	1.29	230	10747	3000	1	20	Static
	22:00:55	1.25	60	14301	3000	1	50	Static
	22:21:25	1.22	50	14301	3000	1	50	Static
	22:41:31	1.22	40	14301	3000	1	50	Static
	23:03:30	1.32	230	14301	3000	1	50	Static

continued on next page...

Table 6.1, *continued*

Date	UT Time	R[$R_\odot$]	PA[°]	λ_c [Å]	t [ms]	Frames	Coadds	Comments
	23:38:38	1.32	230	14301	3000	1	100	Static
	23:58:04	1.35	240	14301	3000	1	50	Static
2016-05-04	00:17:11	1.35	250	14301	3000	1	50	Static
	00:54:45	1.35	260	14301	3000	1	100	Static
	01:14:28	1.31	270	14301	3000	1	50	Static
	01:34:07	1.25	300	14301	3000	1	50	Static
	01:54:54	1.2	90	14301	3000	1	50	Static
	02:33:05	1.2	60	14301	3000	1	100	Static
2016-06-08	21:06:09	1.27	100	10830	3000	1	20	Static
	21:21:30	1.27	90	10830	3000	1	20	Static
	21:37:10	1.27	80	10830	3000	1	20	Static
2016-06-09	00:11:41	1.27	270	10830	3000	20	1	Static
	01:13:11	1.31	200	10830	3000	20	1	Static
	01:28:00	1.31	200	10830	3000	1	20	Static
	01:38:23	1.31	200	10747	3000	20	1	Static
	01:47:01	1.31	270	10747	3000	20	1	Static

6.3 Data analysis and discussion

Our observation campaign with SOLARC had two important goals: (1) Obtain co-spatial measurements of HeI1083 and one forbidden line (either FeXIII1075 or SiX1430) to test the Hanle inversion method discussed in Chapter 3 (2) Detecting linearly polarized SiX1430 emission to compare with observations taken during the 2006 eclipse (Chapter 2) and improve understanding of its polarization properties and suitability as a coronal polarimetric diagnostic.

6.3.1 Hanle inversion analysis

Ideally, to apply the dual-line Hanle inversion method we need measurements of the polarization angle for the forbidden line and both polarization angle and amplitude for the HeI1083 permitted line. The entire dataset was screened for targets where measurements of more that one line are available. We discuss here two of promising targets that demonstrate the Hanle inversion method and the data analysis steps.

Table 6.2: Calculated polarized parameters for targets of interest (see text for additional explanation).

Date	Target			FeXIII1075		SiX1430		HeI1083		Solutions		
	Index	R[$R_\odot$]	PA[°]	angle[°]; amplitude	Timestamp	angle[°]; amplitude	Timestamp	angle[°]; amplitude	Timestamp	B[G]	θ_B[°]	χ_B[°]
2016-05-03	1	1.25	90	-80; na	092347	80; na	155454	na	xx	na	na	na
	2	1.25	60	73; na	094709	73; na	163305	na	xx	na	na	na
	3	1.25	50	42; na	095446	40; na	162125	na	xx	na	na	na
	4	1.25	40	20; na	100230	23; na	124131	na	xx	na	na	na
	5	1.29; 1.32	230	46; na	111919	53; na	130330	na	xx	na	na	na
	6	1.29; 1.35	240	77; na	111117	60; na	135804	na	xx	na	na	na
	7	1.29; 1.35	250	43; na	110336	56; na	141711	na	xx	na	na	na
	8	1.29; 1.35	260	72; na	105545	-82; na	145445	na	xx	na	na	na
	9	1.29; 1.31	270	-65; na	104744	-50; na	151428	na	xx	na	na	na
2016-06-09	10	1.31	200	37; na	153823	na	xx	-8; na	152800	na	na	na
								60; na	151311	na	na	na
	11	1.31	270	-77; na	154701	na	xx	4.5; >0.05	141141 142624	<7.5	135±15	-174±6
										<7.5	45±15	-174±6
										<2.5	84±2	-114±10
										<2.5	96±2	-114±10

Step 1: Assessing the individual fiber spectra

For each polarization sequence fibers are extracted from the images and aligned following the methods discussed in Chapter 5. Fibers are then organized into 2-dimensional fiber maps 66×256 (across I, Q and U) so a visual inspection can be performed for the presence of emission lines (Figure 6.1). Typically, FeXIII1075 was the easiest line to observe in individual spectra (e.g., 157401 timestamp). However, FeXIII1075 emission can also appear very faint like for the 153823 timestamp. The HeI1083 line usually appears much fainter and narrower than the FeXIII1075 line. Furthermore, it is generally too noisy to interpret for single fibers so we currently have to average over all the spectra to improve S/N, at the cost of spatial resolution. Fibers that are easily seen to have large signal fluctuation are removed from subsequent analysis with an automatic algorithm still being developed for faster fiber selection. For example, for timestamp 141141 fibers 13, 14, 30 and 46 are removed from subsequent analysis because their Stokes Q and U spectra clearly show anomalous behaviour. This could be due to gain variations or just telescope jitter during the exposures.

Step 2: Crosstalk removal

After removing bad fibers from each 2D map all remaining fibers are averaged to increase the S/N. The resulting average spectra show crosstalk from I to Q and I to U (Figure 6.2), demonstrated by the presence of polarized photospheric lines. Sharp photospheric lines observed in coronal spectra originate in scattered light from the Earth's atmosphere, and due to the low angle of scattering are expected to have negligible polarization. This information is used to remove the crosstalk though least-square fitting and removal of I in the Q and U spectra until the lines are no longer visible (Figure 6.3).

Step 3: Spectral line fitting

From the crosstalk corrected Q and U spectra the continuum is subtracted after fitting with a low order polynomial (Figure 6.4). Gaussian line profiles for HeI1083 and FeXIII1075 are fit in the Q and U spectra. The HeI1083 signal is comparatively noisy even after averaging over most of the fibers while the FeXIII1075 signal is significantly stronger.

Step 4: Calculating Stokes I values for the emission lines

The inversion method based on dual forbidden/permitted line polarimetry requires polarized mea-

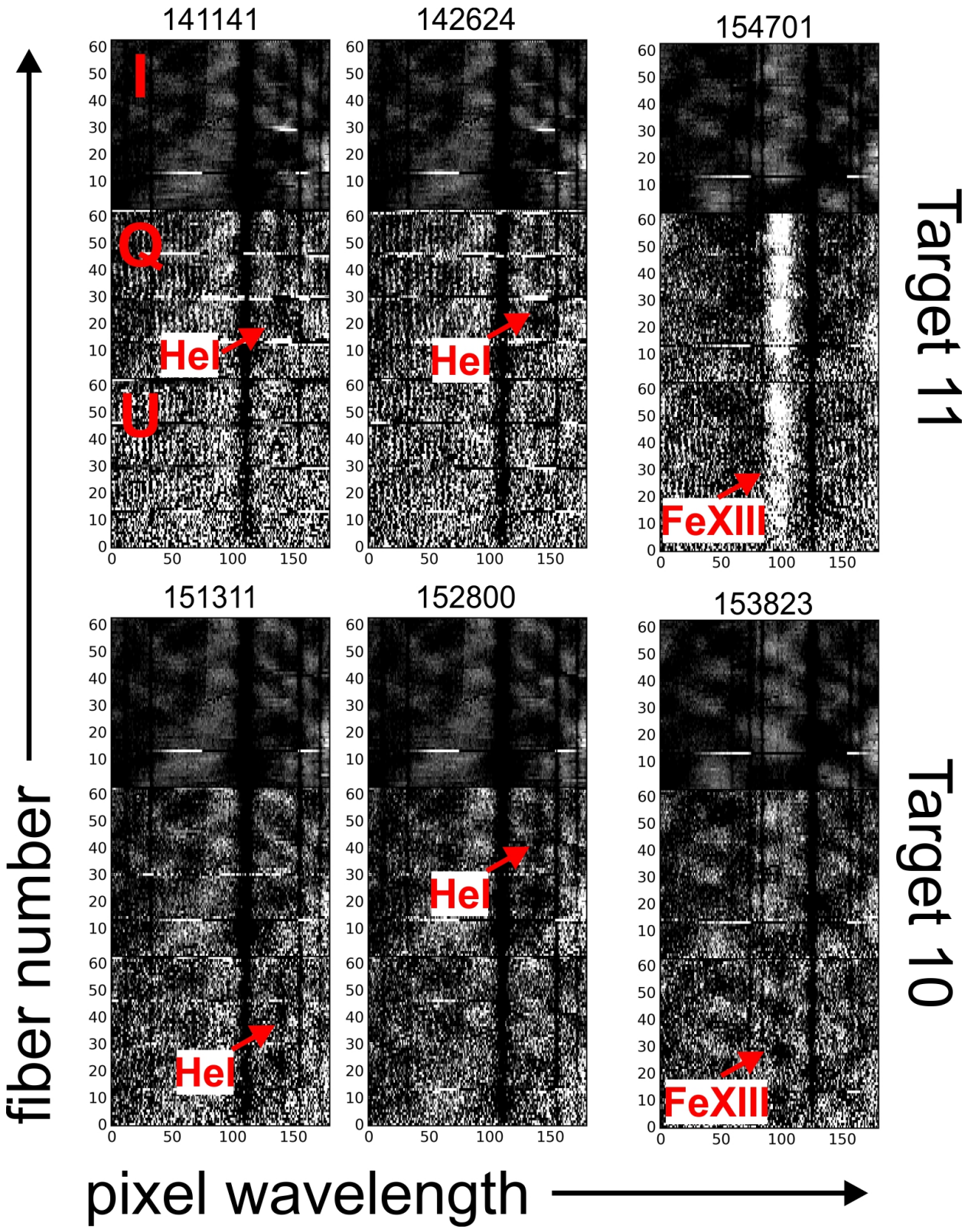

Figure 6.1: Extracted 2D Stokes I, Q, U spectra. To produce these plots an automated normalization with a polynomial fit to the continuum is performed. Color ranges are between 0.7 (black) and 1.3 (white). Timestamps for the observations are given as numbers at the top of each map. The top three panels refer to observing region named Target 11 while the bottom three panels refer to Target 10 (see Table 6.2).

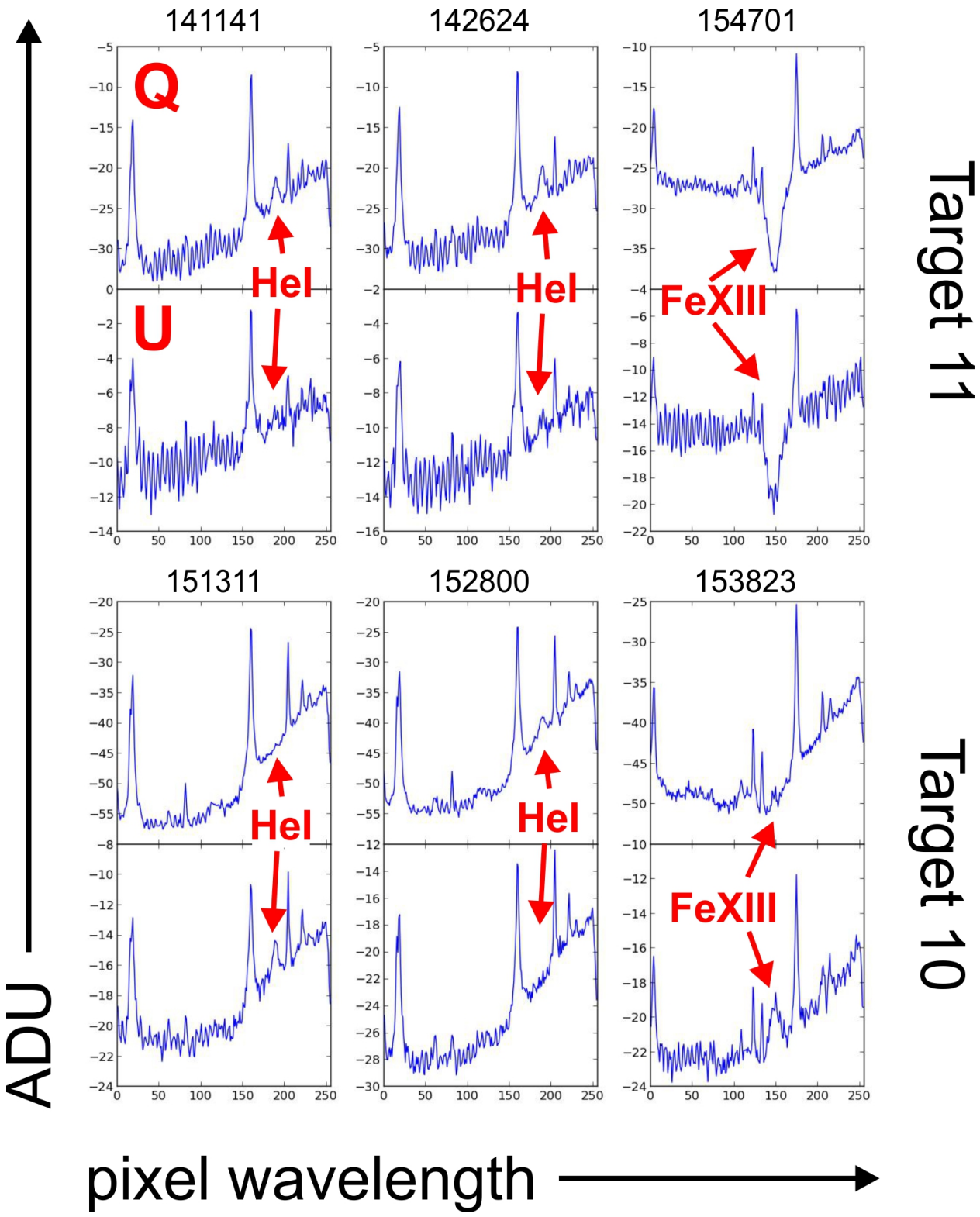

Figure 6.2: Averaged spectra with crosstalk for timestamps as marked showing Q and U polarized observations of HeI1083 and FeXIII1075.

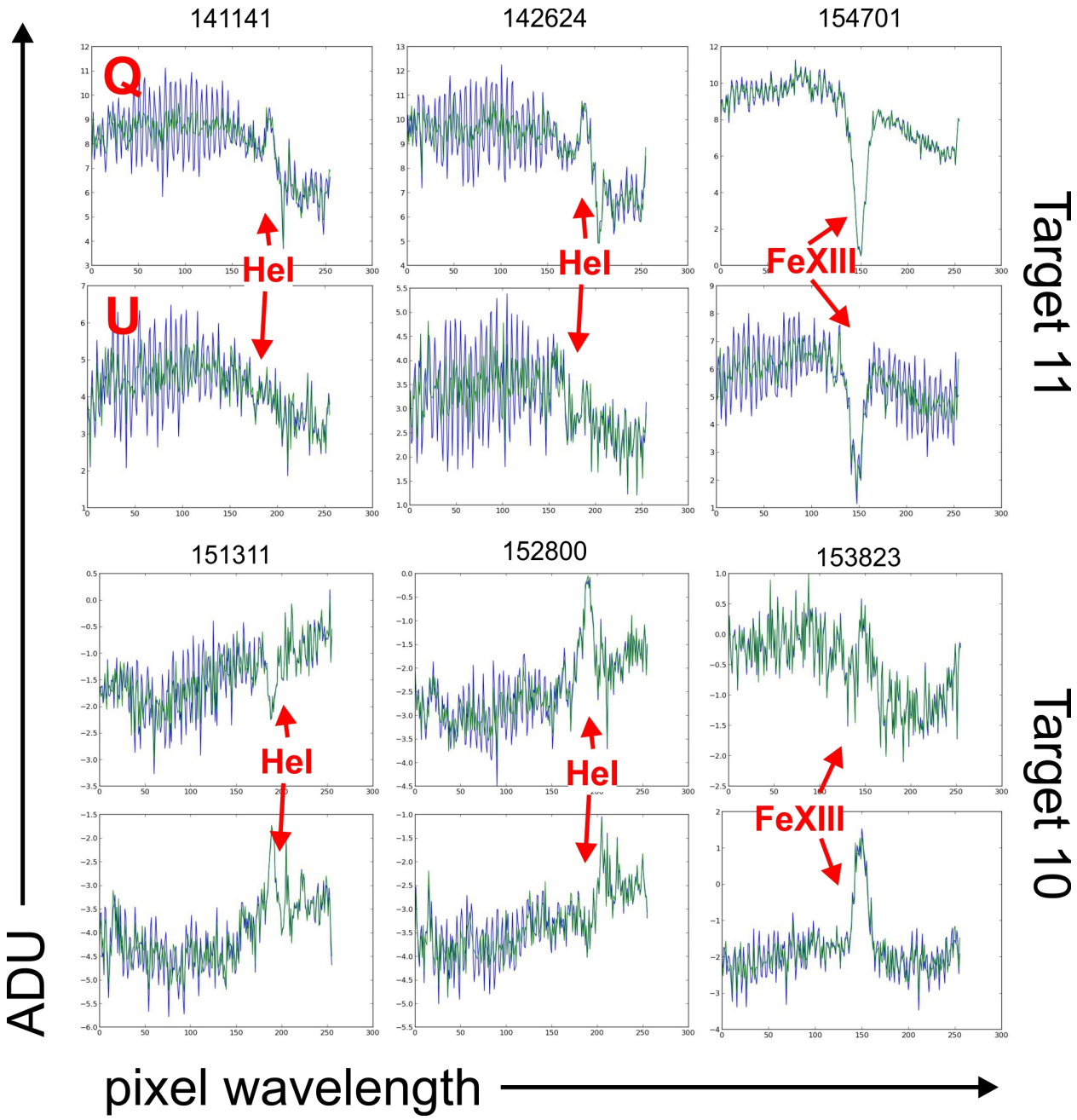

Figure 6.3: Crosstalk corrected spectra for timestamps as marked showing Q and U polarized observations of HeI1083 and FeXIII1075. Fringing is present in most of the spectra (blue line) but can be successfully Fourier filtered out (green).

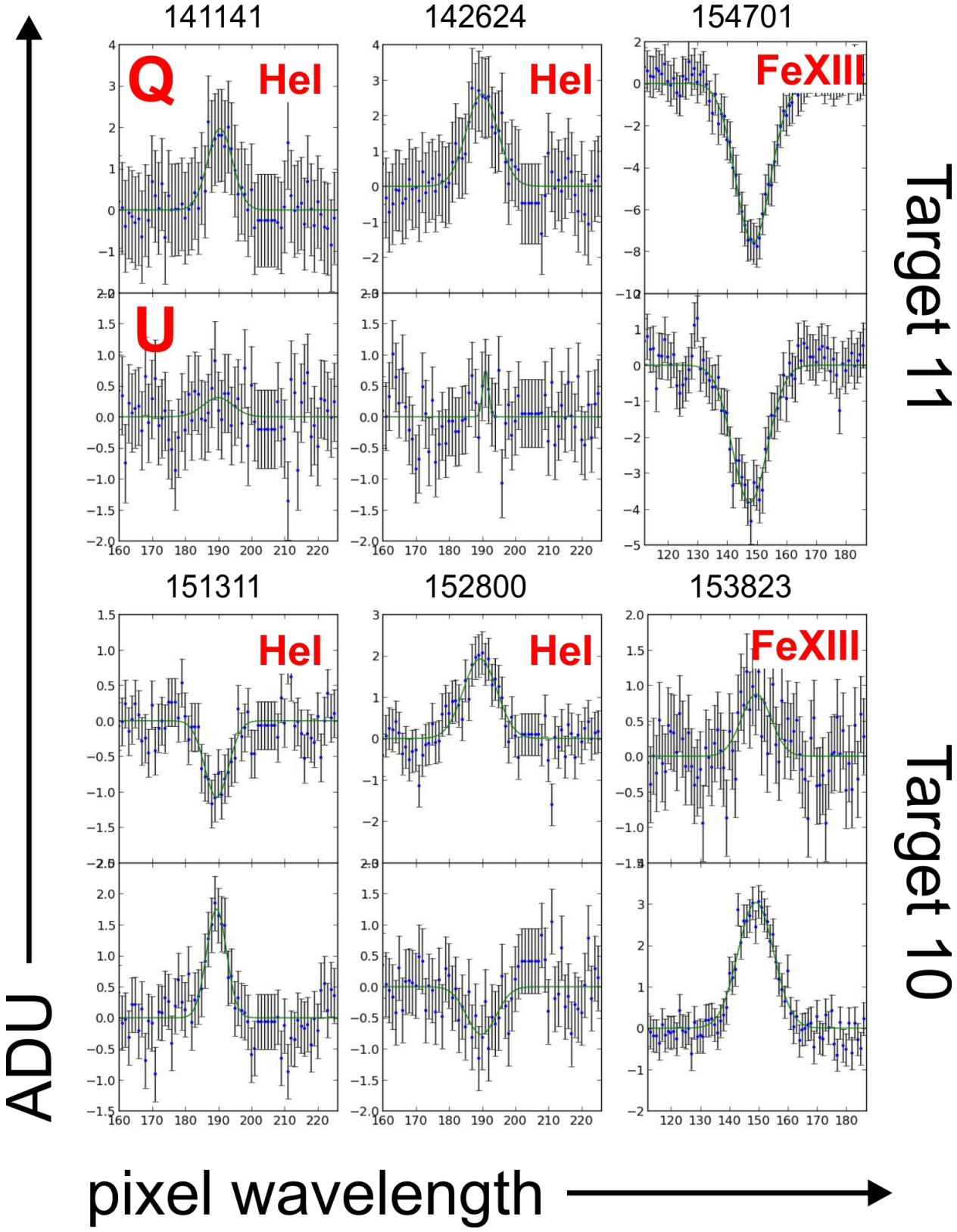

Figure 6.4: Continuum corrected averaged spectra (Q and U) for timestamps as shown at the top. Note low amplitude of HeI1083 signal in most cases compared to strong signals for FeXIII1075. Also noticeable is that the observed Q and U

surements for the HeI1083 (permitted) and FeXIII1075 or SiX1430 (forbidden) lines. In the case of the forbidden lines only the polarization angle is necessary, while for HeI1083 both polarization angle and amplitude are required to obtain a definite (within uncertainty) measurement of the magnetic field direction and strength. Polarization angle measurements are easier to obtain because polarized spectra generally do not need to be flat-fielded since photon noise always dominates. Background levels for our observations tend to be very high. For example the background levels tend to be close to 100×10^{-6} $B_{\odot}$, while the intensity signals for the lines we are intrested in can be as low as 5×10^{-7} $B_{\odot}$ for the HeI1083 lines. In order to measure such faint intensity signals we have to correct the array amplifier pixel-to-pixel gain variation to better than 0.5%. For the FeXIII1075 and SiX1430 lines which are typically closer to 20×10^{-6} $B_{\odot}$ and 5×10^{-6} $B_{\odot}$ respectively the gain noise is less of a concern.

To remove the flat field variation the most promising method so far has been to use disc center observations to normalize coronal spectra and divide out the gain variation. This method relies on the disc center spectra falling on exactly the same pixels as the coronal spectra and this is often not the case due to temperature variations inside the optical bench. These variations cause the camera dewar (and array) to shift by small amounts during the day such that spectra are imaged on slightly different pixels on the array. Figure 6.5 shows an example of a disc center calibrated spectra near the HeI1083 line where the data and calibration spectra are offset by a subpixel amount. The asymmetric profiles of the photospheric absorption lines in the calibrated spectra is an example of this offset. Shifting the calibration spectra by one pixel befor diving will change the asymmetry in calibrated spectra as shown. This problem is especially important for coronal HeI1083 emission because scattered chromospheric absorption at the same wavelength appears superposed. Having a misaligned disc center spectrum causes this absorption line to be poorly removed from the coronal spectrum and makes detection of the very faint coronal component challenging.

Currently we don't have a reliable way to emasure the intensity of the HeI1083 emission line so we estimate an upper limit based on the noise level across pixels near the line. This intensity upper limit can then be used in the Hanle inversion analysis to set upper limits on the strength of the magnetic field. One promising approach for improving the flat field correction relies on calculating

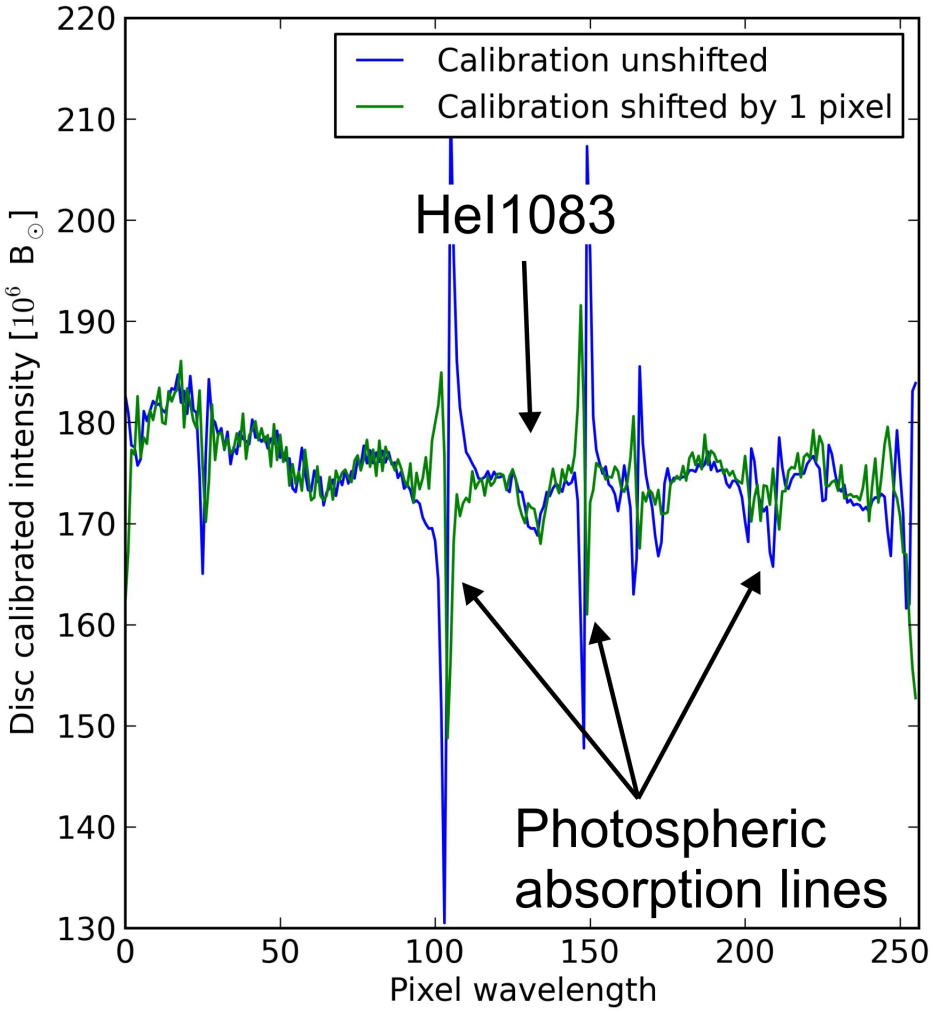

Figure 6.5: Calibrated Stokes I spectrum near the HeI 1083 line showing misalignment between the data and calibration spectra. This is representative of the type of data that is poorly constrained for further analysis using the Hanle inversion method. Shifting the calibration (green) by one pixel demonstrates large variation in the photospheric line correction. Note also the poorly calibrated photospheric HeI absorption line that significantly increases the noise where the coronal signal is expected (marked).

pixel-to-pixel amplifier variation maps from dark exposures of the entire array. The pixel-to-pixel variation derived from darks using different filters and exposures remains relatively constant in time (Figure 6.6). Variations on scales larger than a few pixels are still present but it may be possible to remove them using a Fourier filtering approach. This method may be useful up to a point since it does not account for variations in the spectrum due to any fringes that may be present in the spectra.

Step 5: Dual Hanle inversion analysis

Two targets that have co-spatial measurements of FeXIII1075 and HeI1083 emission are analyzed using the dual Hanle inversion algorithm (Table 6.2). From the analyzed Q and U spectra polarized angles are calculated for HeI1083 and FeXIII1075. We do not yet have the sensitivity to measure the Stokes I component for the HeI1083 line but we can establish upper limits on it based on the continuum variability where the line would be detected.

Following the inversion algorithm described in Chapter 3 the measured FeXIII1075 polarization line angle is used to generate sets of magnetic field orientation angles (θ_b, χ_b) which obey Equation 3.3.1. This equation expresses the geometric relationship between the polarization angle θ_m (through the projected angle θ_p and the magnetic field orientation angles (θ_B and χ_b) and encampsulates all the information provided by the FeXIII1075 line polarization angle.

Each set of possible angles, together with the height of the observations, is used as inputs into the HAZEL atomic model (Asensio Ramos et al. 2008) to produce HeI1083 polarization angle/amplitude model grids. One way to visualize these model grids is by plotting isocontours for constant χ_b and **B** (Figure 6.7 and 6.8, red and black lines, respectively) and then superposing the measured HeI polarized angle and amplitude measurements onto the grids (blue cross with errors). The location(s) where the HeI1083 measurement intersects the model grids corresponds to the magnetic field solutions constrained by the observations. The model grids are highly non-linear and sometimes fold in on themselves, which leads to degeneracies in the possible solutions.

In the case of target 10 two HeI1083 measurements yield different polarized angles. This discrepancy indicates a potential problem with the measurements for this target. In comparison Target 11 has two HeI1083 measurements that are consistent.

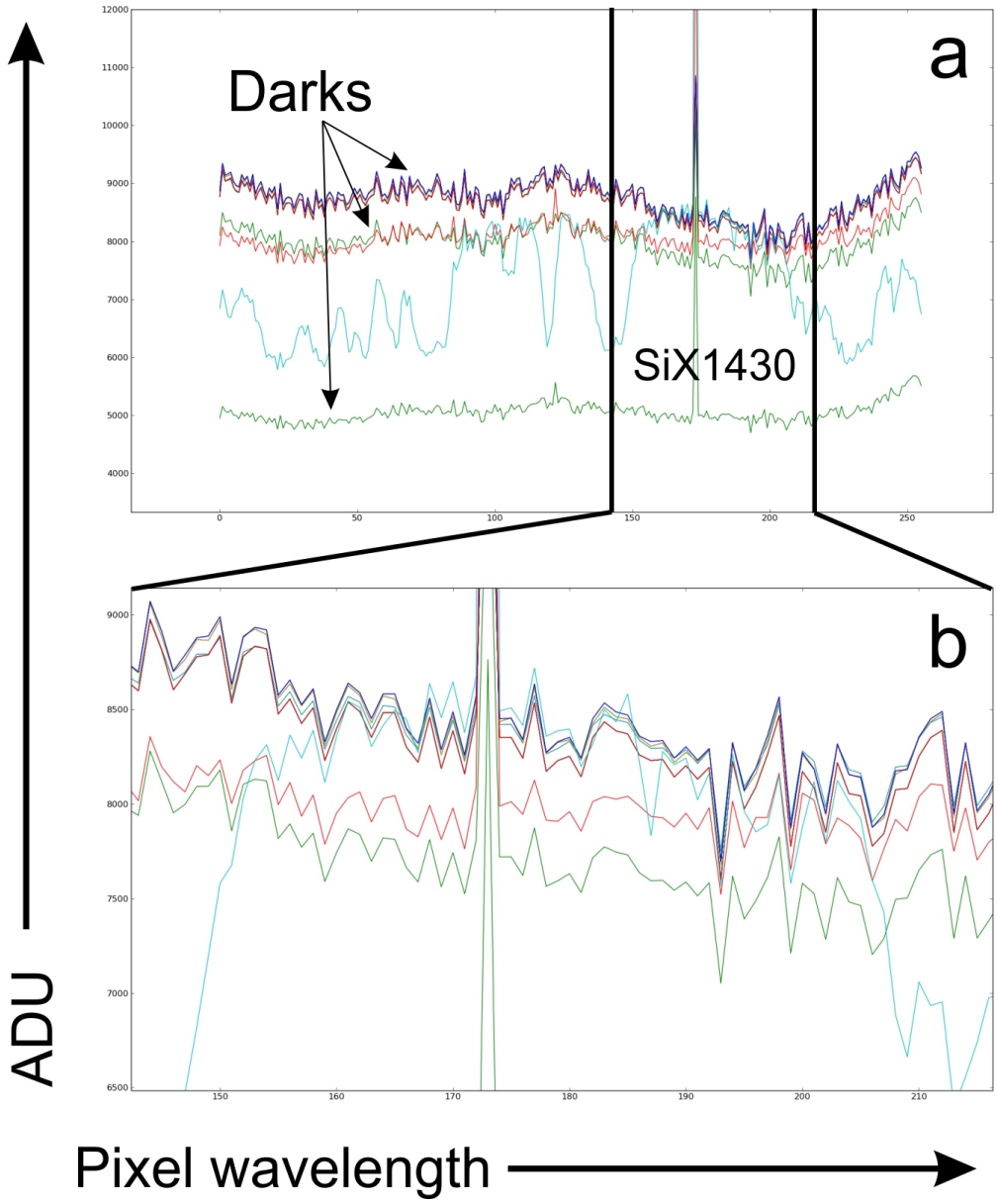

Figure 6.6: Example signal over an entire row of pixels (a) and an enhanced version of the same plot (b). Pixel-to-pixel gain variation correlates well over a variety of dark exposures. An example spectrum near the SiX1430 line, imaged over the same pixel row, also shows good correlation between the small scale variations.

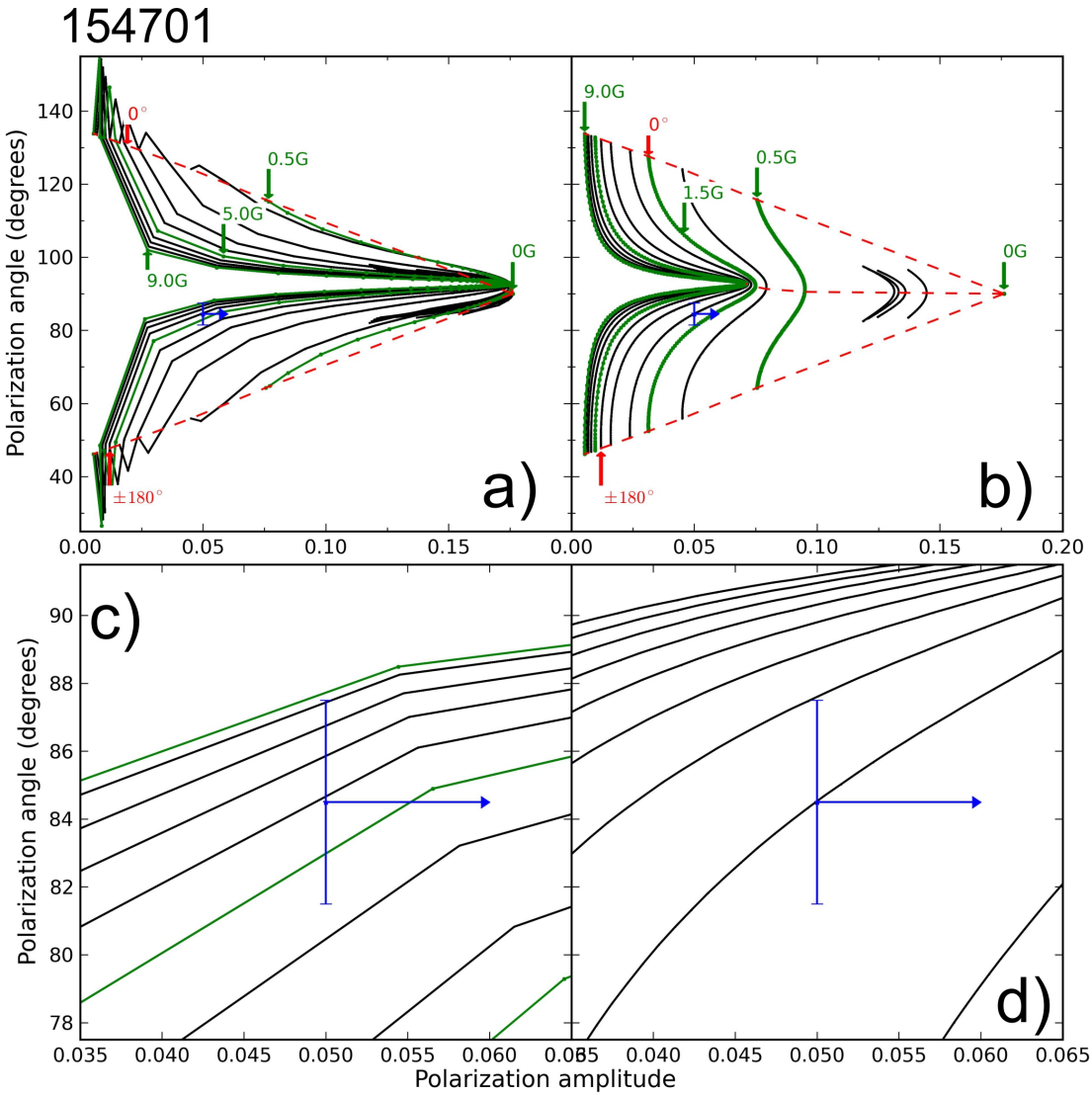

Figure 6.7: Model grids of HeI1083 polarized amplitudes and angles for magnetic field orientations constrained by FeXIII1075 polarization angle observations (timestamp as marked). Selected B-isocontours (black and labelled in green) are shown together with χ_b-isocontours (red dashed line). Blue crosses indicate the measured HeI polarized amplitude and angle for the same spatial region. The FeXIII1075 polarized angle is parallel (a), or perpendicular (b) to the projected magnetic field direction. The panels (c) and (d) show details of the grids near the measurements. For this pair of measurements we find a well constrained direction solution but only an upper limit for the magnetic field strength.

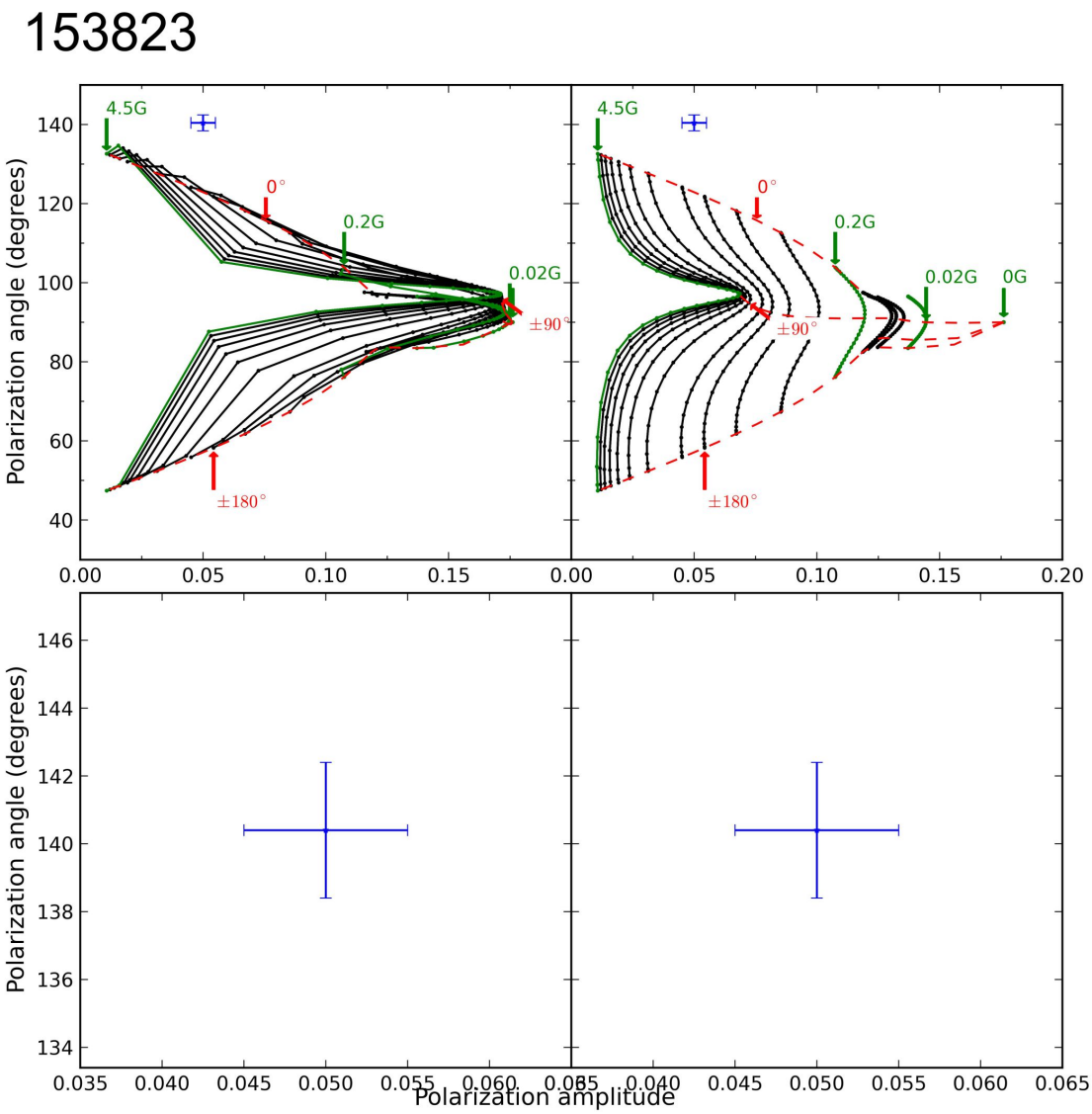

Figure 6.8: As for 6.7 except for observations at timestamp 153823. In this case the measured HeI1083 polarized measurements do not fall along the predicted model grid.

Assuming that the HeI1083 and FeXIII1075 emission are co-spatial and located near the plane of the sky solutions for the magnetic field can be calculated for case where the measurements intersect the model grids (Figure 6.7). For target 11, the inversion result also lies in the Van Vleck uncertainty region which adds more degeneracy to the solutions. Taking into account uncertainty in the HeI1083 measurement, the polarization angle and upper limit for the amplitude amplitude are compared to the values in the grid. All grid points that lie close to the measured value within the uncertainty are considered valid solutions.

For target 11 four solutions consistent with the measured polarization signals are found (Table 6.2). Of these, two are due to the Van Vleck uncertainty and 2 are due to the 180°-uncertainty inherent to the method assumptions. Two of the deduced magnetic field solutions are shown in Figure 6.9 overlaid on an SDO/AIA image obtained on the same day as the observations. The field of view for AIA is slightly smaller than the integrated field of view for the SOLARC fibers. The complementary solutions have the same projection but reversed orientations. The elongated filaments seen in the AIA image may correspond to gas tracing radial magnetic fields similar to the direction shown by the vector resulting from the inverted parallel solution (Figure 6.9a). However, low spatial resolution due to averaging over the region marked by the rectangle in the figure prohibits more meaningful interpretation. While no independent measurement exists currently to validate this inversion, having a self-consistent MHD model for the day of observations would provide a comparison to the inverted solution.

In contrast, when the measurement does not intersect either grid, as shown in Figure 6.8 for target 10, this indicates either possible problems with the underlying assumptions in the inversion, or measurement error that is not accounted for. The fundamental assumption in the Hanle inversion method states that the line emission is concentrated near the POS and the line-of-sight (LOS) integration is also assumed not to influence the measurement significantly.

Step 6: Magnetic field inversion sensitivity

There are two separate considerations that affect the reliability of the dual-Hanle inversions shown here. One is related to the accuracy of the emission model and the assumptions that go into it and the second one is the reliability of the measurements to which the model is applied. Getting

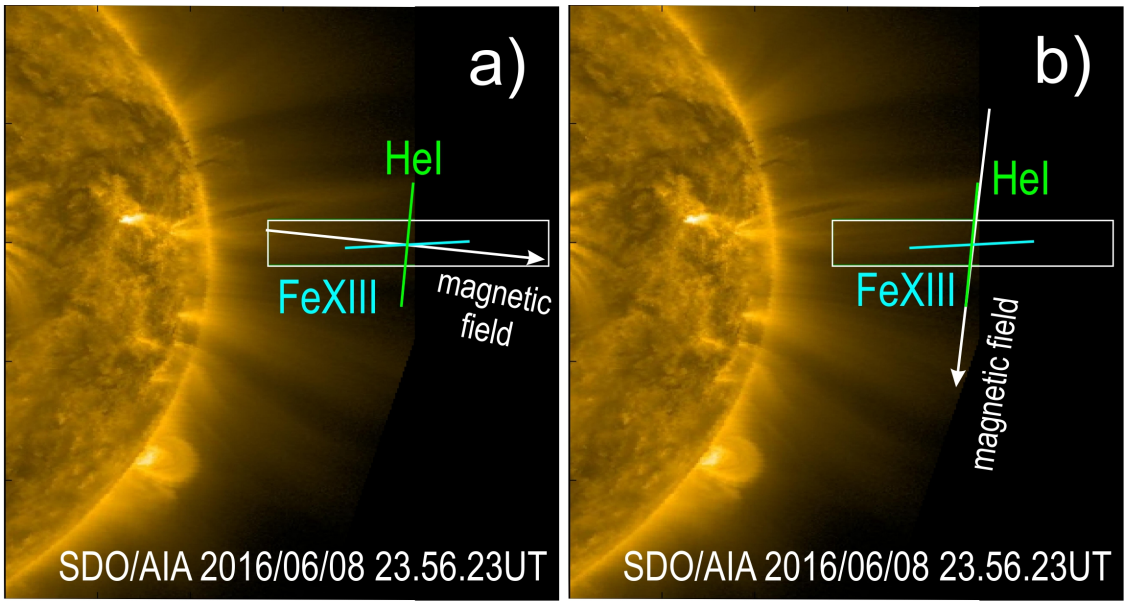

Figure 6.9: Plots of calculated vector magnetic field (as marked) for each corresponding grid in Figure 6.10. See text for additional explanations.

a handle on the reliability of the measurements is a simpler problem to treat than assessing the accuracy of the assumptions that go into the model.

Repeated observations of the same target region can help clarify if the measurements are consistent. For target 10 this is not the case and it could help explain the discrepancy between the measured HeI1083 polarization and the model grids. If the same outcome is obtained for repeated observations then a systematic error may be affecting the exposures. However, if inversions for different coronal regions taken during the same day and with the same instrumental setup do not show similar discrepancies it is unlikely that the error is due to a general problem with the system. The presence of systematic errors can also be detected through interpreting the continuum polarization. Continuum polarization parallel to the local solar limb is a strong indicator that there is no systematic effect in the measurements and this strongly indicates that the assumption underlying the inversion algorithm may not be valid in target region 10. However, for cases where the measurement is very close to the grid, a closer assessment needs to be undertaken to analyze how the forbidden line angle measurement errors, i.e., FeXIII1075 in this case, may influence the shape of the model grids.

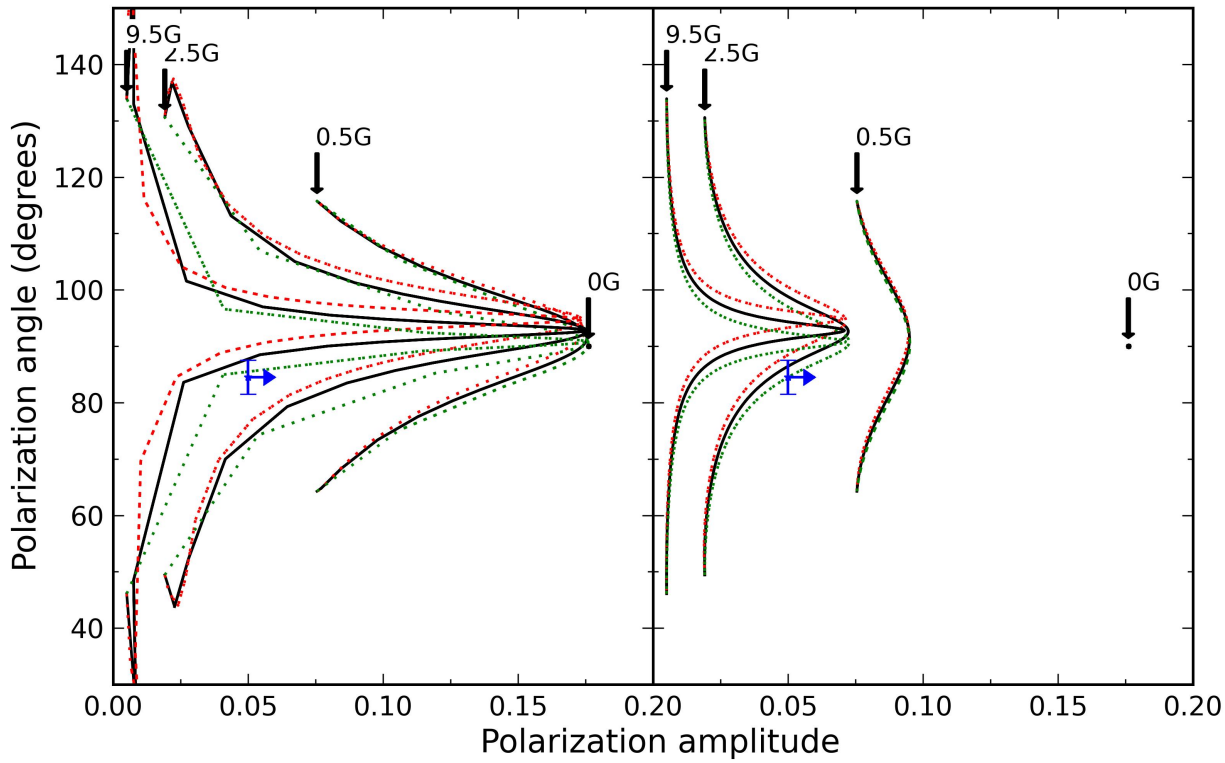

Figure 6.10: Parallel (left) and perpendicular (right) model grids (black) with added (red) and subtracted (green) uncertainties in the FeXIII1075 polarization angle for target 11. The measured HeI1083 polarization values (blue) are shown as upper limits in the polarization amplitude direction and corresponding measurement uncertainties in the angle direction. Propagating the FeXIII uncertainty requires new grids to be computed since the shape of the grids changes (bending and crossing of model contours).

The solution grids for HeI1083 are highly non-linear, so a 0.5% measurement error in the HeI1083 line intensity translates differently into inverted magnetic field errors depending on the strength of the magnetic field. This is also the case for the present analysis, i.e., compare Figure 3.3 with 6.7. Due to limited sensitivity of our observations only lower limits can be placed on the HeI1083 polarized amplitude. This translated into upper limits on the magnetic field strength of the inverted solution. For the theoretical situations considered in Chapter 3 the errors in the recovered field are on the order of 10-20% for the magnetic field strength, and $<$10% for the magnetic field orientation angles.

Accounting for measurement errors in the forbidden line polarization angles involves studying how the HeI1083 solution grids change (Figure 6.10). Overall this effect tends to increase the measurement errors to around 15-30% for the magnetic field strength and around 10-20% for the magnetic field orientation angles. At present time these values are estimates and the inherent limitations of these errors can only be understood through an independent method for estimating corona magnetic fields, e.g. MHD model for the same day or measurement of the line of sight field strength through circular polarization measurements.

6.3.2 SiX1430 coronal emission line

Infrared polarized coronal observations have so far been focused on the FeXIII1075 emission line. In contrast, the SiX1430 line has been the target for fewer observations in the corona. During the 2006 solar eclipse, we measured the linear polarization properties of SiX1430 (see Chapter 2) as well as the intensity ratios between SiX1430 and FeXIII1075 and showed how they can perform as a temperature diagnostic of the corona. During the observing campaign with SOLARC we followed up the eclipse measurements with higher spatial resolution simultaneous measurements of the FeXIII1075 and SiX1430 lines to test some of the results seen during the eclipse in regards to polarization orientation and line ratios. I present here results obtained during the observing day 2006-05-03 (Table 6.2) for nine targets observed at a variety of position angles around the solar limb.

Typically the SiX1430 polarized signal is fainter than the FeXIII1075 signal for the same target

regions, so that we still resort to coadding many fibers to obtain high enough S/N (Figure 6.11). In comparison, the FeXIII1075 polarized lines for the same target regions tend to be much stronger (Figure 6.12). Comparison of the polarization angles for the two lines shows significant correlation as expected for two lines in the saturated Hanle regime (Figure 6.13). We don't yet have an MHD model for the day of the observations, but using one of the available models for the solar corona from the 2006 solar eclipse and degrading the spatial resolution to SOLARC values we can see similar scatter in the correlation between the SiX1430 and FeXIII1075 polarized angles. The MHD model polarization angles are calculated for noise-free emission so the scatter must be due to some intrinsic difference in the line emission for the two lines along the LOS and in the emission regions sampled. An interesting prospect is that by increasing the spatial resolution of the observations the correlation will tighten and the scatter will provide some indication of the variation along the LOS. Thus by simultaneous observations of the two emission lines some understanding of the LOS uncertaining could be obtained.

Choosing regions in the corona to apply the inversion method is difficult because the LOS effect is not well understood yet. Using an MHD model it is possible to compare the effect LOS integration has on the measured polarization angle for the SiX1430 line (Figure 6.14). It is noticeable that in some regions of the corona the polarization angle measured from emission in the POS does not change appreciably compared to the polarization angle measured after integration along the LOS. If measurements of both FeXIII1075 and HeI1083 are obtained in areas where the LOS integration is problematic, then the inversion would not work since the grids are calculated assuming a specific geometry between the solar disc, the HeI emission region and the observer. We are currently working on ways to distinguish regions affected by the LOS problem using simultaneous measurements of both FeXIII1075 and SiX1430.

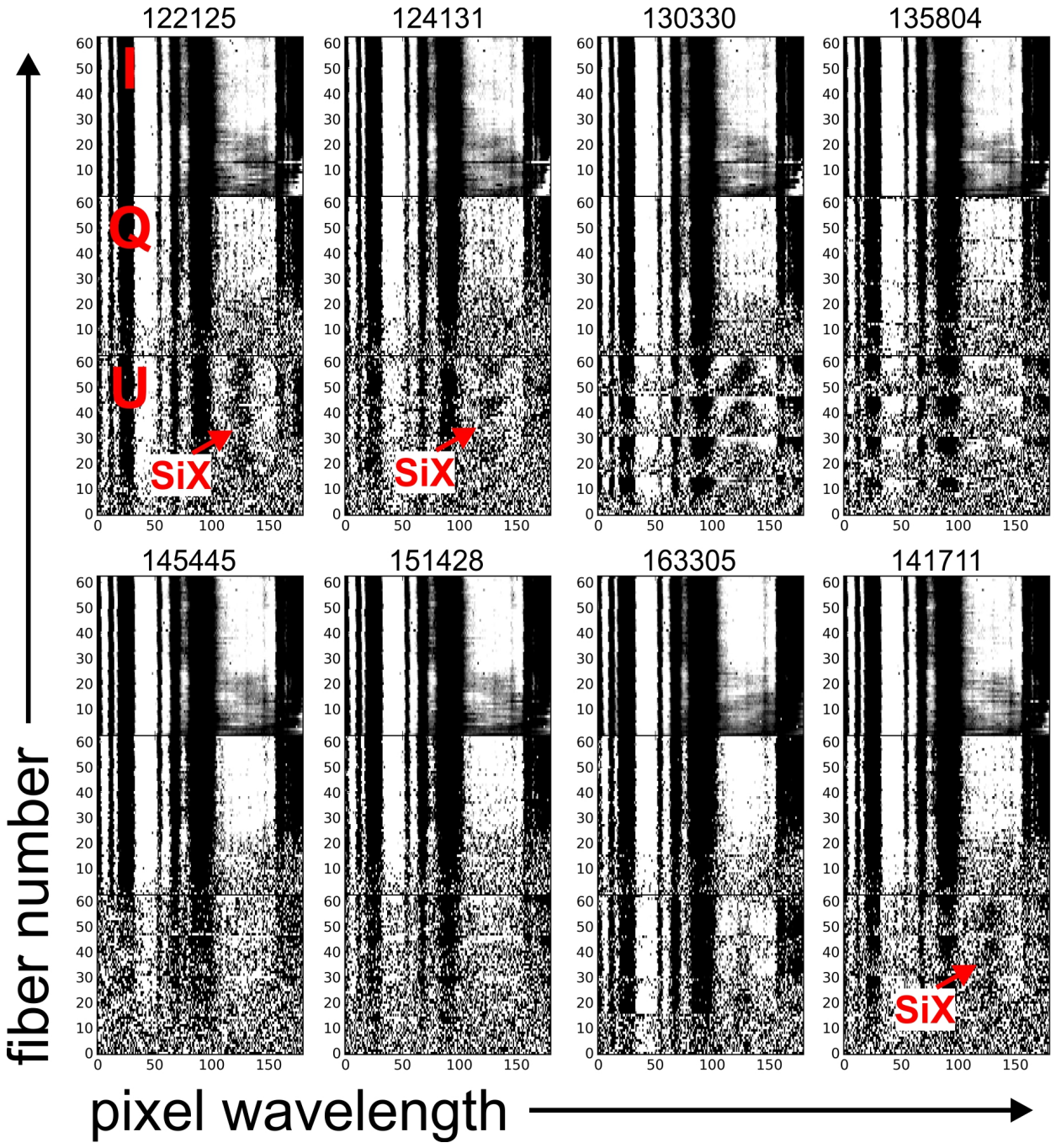

Figure 6.11: SiX1430 line (arrowed) 2D Stokes (I, Q, U as marked) spectra. Each spectrum was normalized with a polynomial fit to the continuum before plotting. Color ranges are between 0.7 (dark) and 1.3 (white).

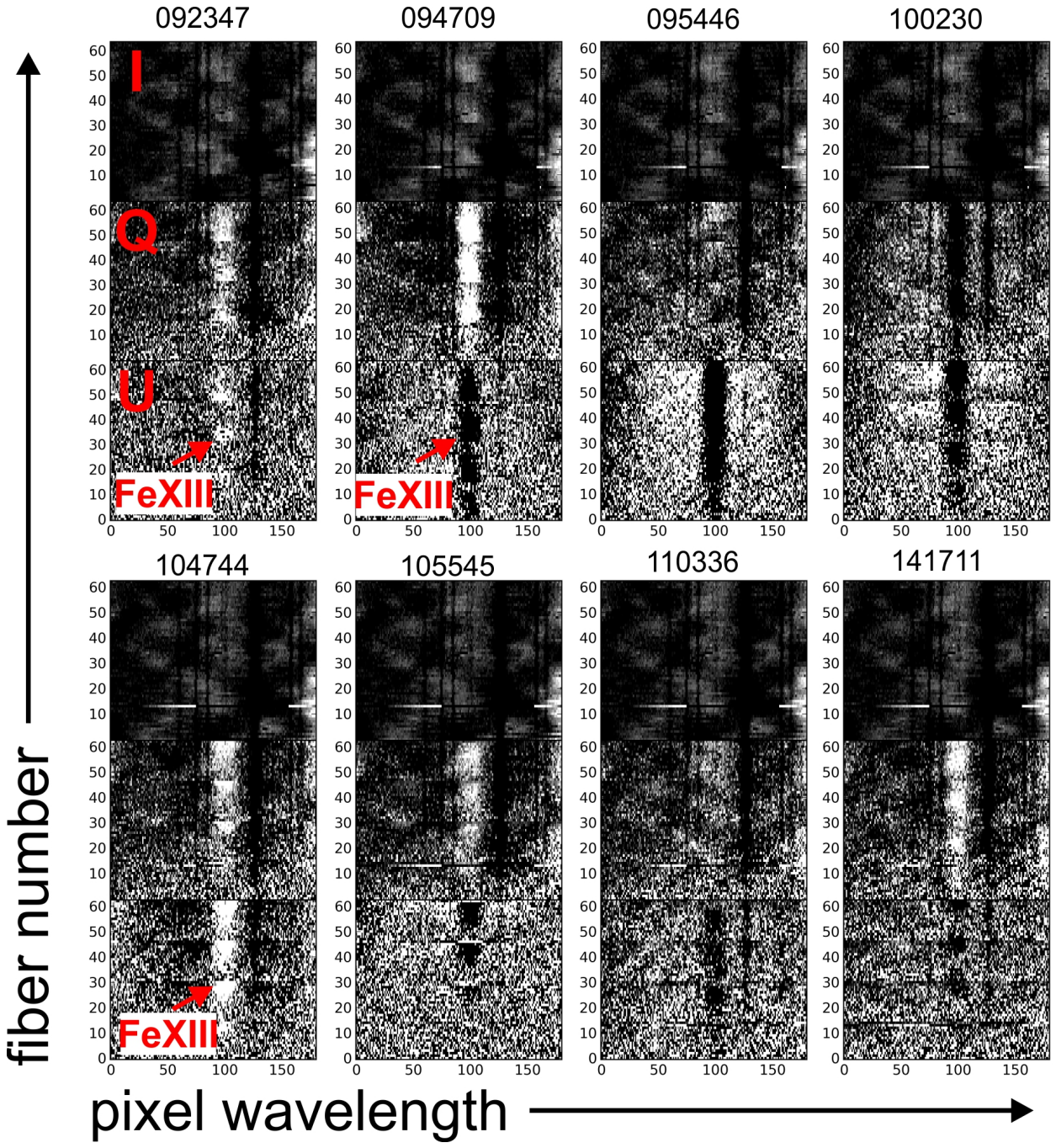

Figure 6.12: FeXIII line extracted (arrowed) 2D Stokes (I, Q, U as marked) spectra. Each spectrum was normalized with a polynomial fit to the continuum before plotting. Color ranges are between 0.7 (dark) and 1.3 (white).

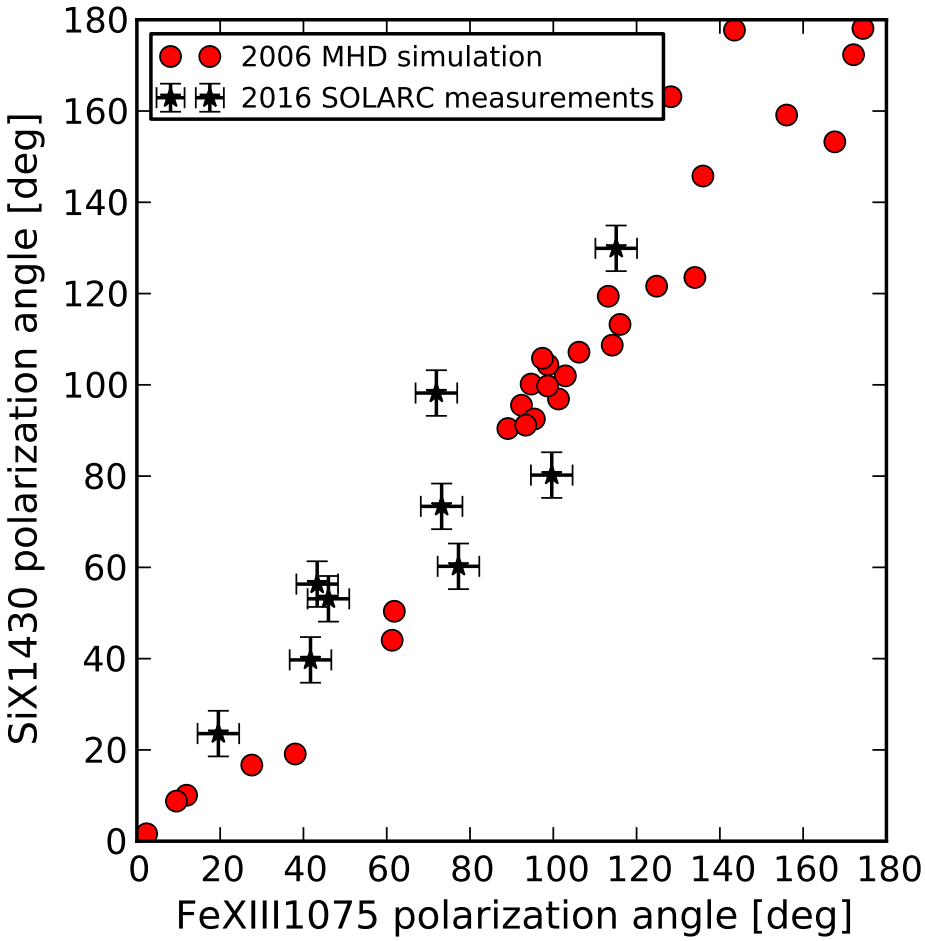

Figure 6.13: Plot showing the measured correlation between co-spatial SiX1430 and FeIII1075 polarized angle measurements (black stars) and the correlation of synthetic polarized angles obtained from forward integration through an MHD model for the 2006 solar eclipse. The angles are remapped from [-90°, 90°] to [0°, 180°]. Not all the scatter in the correlation is due to measurement errors and some scatter is evident even in the noise-free model.

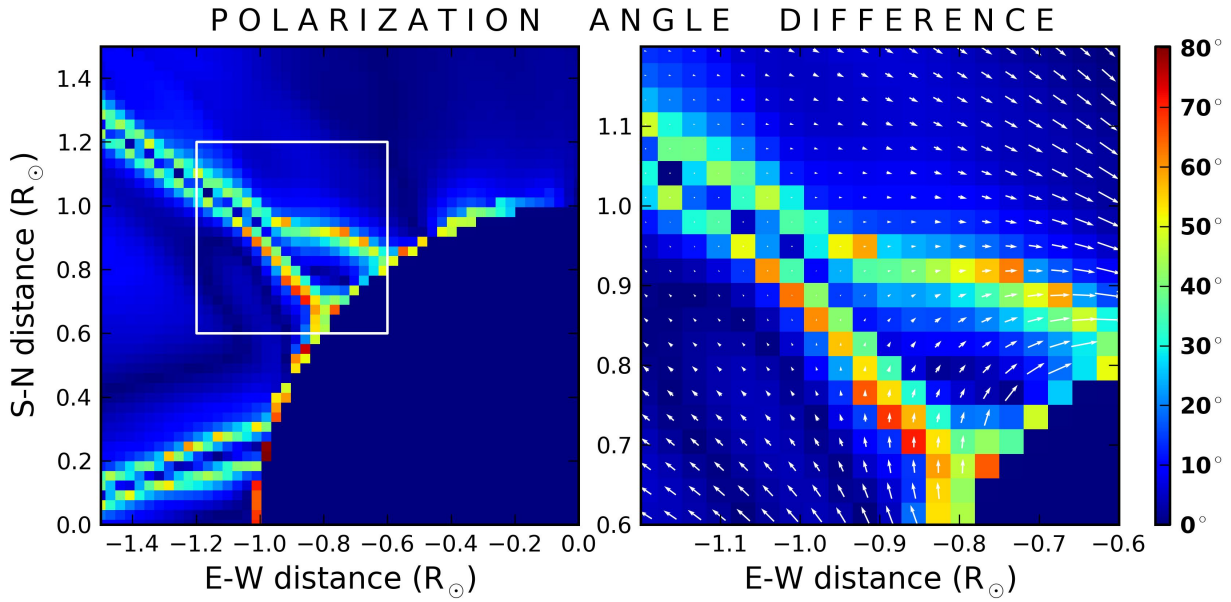

Figure 6.14: Absolute SiX1430 polarization angle differences between two forward integrals through the same MHD simulation for the global corona on March 29, 2006. One integral only measures emission from POS plasma while the second integral effectively measures all the emission along the LOS. The pixel scale is 0.03 $R_\odot$. Bluer colors indicate smaller deviations. Right panel shows a magnified view of the region enclosed by the white square in the left panel. The white arrows indicate the POS components of the magnetic field with lengths scaled to the relative POS strength of the field. Noticeable are large parts of the corona where deviations between the two measurements are less than 20°.

BIBLIOGRAPHY

Asensio Ramos, A., Trujillo Bueno, J., & Landi Degl'Innocenti, E. 2008, ApJ, 683, 542-565

Dima, G., Kuhn, J., & Berdyugina, S. 2016, Frontiers in Astronomy and Space Sciences, 3, 13

CHAPTER 7
SUMMARY AND OUTLOOK

In summary, the work reported during the PhD program has generated a number of significant outcomes:

- New infrared temperature diagnostic for the solar corona based on the FeXIII1075/SiX1430 emission line ratio.
- Characterization of the polarization properties of the SiX1430 emission line.
- Development of a new method to measure coronal magnetic fields based on Hanle effect.
- Optimization of the SOLARC telescope and camera system to acquire data with a S/N ratio sufficient for observing multiple faint coronal emission lines, and construction of a pipeline for reduction of the collected data.
- Obtained SOLARC linearly polarized measurements of SiX1430, FeXIII075 and HeI1083 – reference material for present and future analysis.
- Demonstration of the dual line Hanle inversion algorithm in application to the new SOLARC HeI1083 and FeXIII1075 observations.
- Work reported during the PhD program has shown that the decrease in sensitivity of measurement using SOLARC needs to be addressed in upgrading the system.

7.1 SiX1430 and FeXIII1075 intensities and linear polarization – temperature diagnostic

Through simultaneous observations of the SiX1430 and FeXIII1075 lines during the 2006 solar eclipse, it was shown that the relative intensities of the two lines can be used to distinguish between cooler and hotter MHD models for the corona. Because the ionization fraction of the two species

varies strongly with temperature, the intensity ratio FeXIII1075/SiX1430 can be used as a temperature diagnostic of the corona. While LOS integration still poses a problem with interpretation of the ratio, comparing forward integration through competing MHD models can reveal whether some regions can be inverted to yield an accurate estimate of the coronal temperature using the two lines.

The noisy 2006 eclipse observations hinted at a correlation between the polarization angle of the two forbidden lines through a statistical analysis. In contrast, the recent SOLARC observations confirmed, for the first time, the positive correlation between co-spatially measured polarized angles for the two lines, as predicted from forward simulations through MHD models. The scatter in the correlation plot is evident even in noise-free FORWARD integrals through MHD simulations (Figure 6.13), and thus it can be inferred that part of the scatter is due to the different spatial distributions of SiX ions relative to FeXIII throughout the corona and along the line of sight. Since both these lines are in the saturated Hanle regime we expect their polarization angles to aligned for emission from a single source region. We can infer that the observed scatter in the correlation is due to emission from multiple regions along the line of sight. Both eclipse and SOLARC observations of the two lines have coarse spatial resolutions ($\sim 6'$) so it's difficult to separate the effect of the line of sight from the distribution of emission inside the resolution element. By increasing the resolution of the measurements it may be possible to use the correlation between the polarized angles in the two lines to distinguish regions in the corona where line of sight integration is less problematic.

Due to limitations in data calibration we have not yet recovered line intensities for the two lines from SOLARC data. While the polarized signal measured for FeXIII1075 is larger than for SiX1430 in all of the observations analyzed so far, it is not straighforward to use this to infer an intensity value. Theoretically, SiX1430 and FeXIII1075 polarization amplitudes are different under identical scattering geometries. One key factor is the amount of depolarization in each line due to electron collisions (Judge et al. 2006). For the same electron density the linear polarization amplitude of the two lines is different due to different coupling to anisotropic exciting radiation (Judge & Casini 2001). If we believed the atomic models for the predicted polarized amplitudes and had a suitable MHD model for the solar corona it may be possible to infer the line intensities. However, comparisons of the predicted and observed polarization properties during the 2006 eclipse

for SiX1430 indicated that the models may underestimate the real polarization amplitude. We are working to obtain an MHD model for the days of observations with SOLARC to study whether we can use the polarized amplitudes to determine line intensities.

7.2 HeI1083 emission line – implications for the geometry of circumsolar dust

Results presented here have reconfirmed the handful of measurements of the HeI1083 emission line, reported for the first time from observations made during 1994 eclipse (Kuhn et al. 1996), and afterwards from ground-based SOLARC observations (Kuhn et al. 2007; Moise et al. 2010). None of the previous detections measured both Stokes Q and U as has been done in the present study. The 1994 experiment only reported line intensities, whereas later SOLARC observations only measured the Q polarization state, and assumed that U was negligible. These data led to an interpretation in which the HeI1083 line was scattered by neutral He produced due to desorption from circumsolar dust (Moise et al. 2010). This parametric model assumes that the circumsolar dust ring has an inner radius between 2-4 $R_{\odot}$ which acts to neutralize ionized He present in the solar wind. Beyond 2 $R_{\odot}$, the magnetic field is weak ($<$0.1 G) and only rotates the HeI1083 plane of polarisation by $<10^{\circ}$. Therefore one testable consequence of the Moise et al. (2010) models is that HeI1083 emission outside 2 $R_{\odot}$ must have an angle of polarization parallel to the solar limb.

This prediction can be tested using the present Stokes Q and U measurements since the polarization angle is now available for different locations around the limb. Even at current noise levels and decreased spatial resolution due to coadding, new SOLARC observations show a difference between continuum (parallel to the solar limb) and HeI1083 polarization angle (e.g., a difference of 11.7°for target 10), thus hinting at contradictions with the assumed geometry of the model. More sensitive measurements of the HeI1083 linear polarization with higher spatial resolution will help set more stringent limits on this deviation. This deviation raises the posibility that the emission comes from regions closer to the Sun where the magnetic field is stronger and can rotate the plane of polarization through the Hanle effect. Another interesting possibility raised by such measurements

is that dust may exist closer to the solar disc than expected, perhaps with sizes in the nanometric range where the solar flux is significantly depressed.

7.3 Dual-line Hanle magnetometry

The present work has generated a new method for calculating magnetic fields in the plane of sky using only linear polarization (Dima et al. 2016), and has also demonstrated its application to real observations (Chapter 6). This method does not depend on knowledge of the electron density and is thus independent of density models for the corona. Potentially, full vector magnetic fields can be obtained if accurate (>0.5% polarimetric sensitivity in terms of S/N) measurements are obtained and the assumptions for the inversion model hold. Such maps can be compared with MHD simulations for discriminating the topology and strength of magnetic fields obtained with different heating models.

7.4 Future perspectives

SOLARC is the world's largest reflecting coronagraph (Kuhn et al. 2003). It was used to establish the Zeeman sensitivity of IR emission lines for coronal magnetometry (Lin et al. 2004), and to observe the faint coronal HeI1083 signature. Its 256×256 HgCdTe detector is, however, $\sim$25 years old and the continuous thermal cycling has degraded the number of active pixels and their stable photometric sensitivity. Degradation of the SOLARC infrared detector is thus the largest apparent limitation to this technique – our line-of-sight (LOS) inversion and forward modelling calculations are now limited by the available dual-line polarimetric observations. Obtaining more data to better understand the HeI1083 line formation and upgrading the SOLARC detector are important for future advancement of the program. Doing so will teach us more about the coarse-resolution coronal structure and allow a demonstration of the full potential of this method at higher resolution and in preparation for the 4m Daniel K. Inouye Solar Telescope (DKIST).

Work reported during the PhD program has shown that the decrease in sensitivity needs to be addressed both in upgrading the system and data reduction pipeline. Currently over 30 minutes

of integration time is required to acquire I, Q and U spectra with enough sensitivity to detect the emission lines after co-adding data from all 64 fibers on the array. Improvements can be achieved by upgrading the IR camera: Relatively inexpensive deep-cooled InGaAs near-IR $640x512$ detectors with good quantum efficiency and stable electronic properties are now readily available. Such a camera will increase the signal to noise of our measurements by an order of magnitude and offer photometric performance exceeding early-generation HgCdTe arrays.

Upgrading the system would take advantage of the fiber-based design without having to sacrifice observing time. Upgrading of the system, besides acquisition of a new camera, would also require re-coating of the primary mirror to decrease the amount of scattered background light. Although new algorithms will be needed to interface with the camera and synchronise polarimetric observations, the concept behind such work is already well understood. Data reduction algorithms for the current camera have already been developed and thus we anticipate only small modifications are required to handle the upgraded camera system. Work would be done to (i) streamline raw data handling and (ii) output polarimetric observables (e.g. polarized amplitude and angle maps) that can be directly compared to FORWARD integrated observables or input into the dual-line Hanle inversion algorithm.

Substantial work on the core of the inversion algorithm has already been undertaken. Improvements to the algorithm will include the ability to accept polarized observable maps and return inverted magnetic field maps. Assessing the quality of such maps with respect to the real corona will depend critically on our understanding of the LOS integration uncertainty inherent in all single point inversion techniques. An important part of the problem is pinpointing the distribution of the HeI signal, which is possible with higher signal-to-noise HeI1083 polarimetry. The goals would be to (1) Constrain the geometry of the circumsolar dust and its presence within $<2\ R_{\odot}$; (2) Test LOS effects on dual-Hanle magnetometry to distinguish regions suitable for applying the inversion method; and (3) Use such regions to obtain coronal vector magnetic field maps. This would require a combination of several modelling tools. A new FORWARD module could be created to vary the inner radius of the dust ring which is essential in the production of HeI. Knowing there are regions in the corona where LOS integration does not significantly affect polarisation angle measurement

allows FORWARD integration of HeI lines through such regions to constrain the inner dust radius.

Measurements of neutral HeI1083 embedded in the million-degree corona are tantalizing hints that can open a new window into our understanding of this dusty plasma. Through our Hanle-based inversion method we can address this measurement problem at field strengths weaker than 8 G. These techniques, combined with the 4 m DKIST will bring a significant increase in sensitivity and spatial resolution. Such coronal magnetometric methods and modelling techniques improve the discrimination power of the observations for coronal magnetic models.

BIBLIOGRAPHY

Dima, G., Kuhn, J., & Berdyugina, S. 2016, Frontiers in Astronomy and Space Sciences, 3, 13

Judge, P. G., & Casini, R. 2001, Advanced Solar Polarimetry – Theory, Observation, and Instrumentation, 236, 503

Judge, P. G., Low, B. C., & Casini, R. 2006, ApJ, 651, 1229

Kuhn, J. R., Penn, M. J., & Mann, I. 1996, ApJ, 456, L67

Kuhn, J. R., Coulter, R., Lin, H., & Mickey, D. L. 2003, Proc. SPIE, 4853, 318

Kuhn, J. R., Arnaud, J., Jaeggli, S., Lin, H., & Moise, E. 2007, ApJ, 667, L203

Lin, H., Kuhn, J. R., & Coulter, R. 2004, ApJ, 613, L177

Moise, E., Raymond, J., & Kuhn, J. R. 2010, ApJ, 722, 1411

APPENDIX A
SOLARC OBSERVATIONS SUMMARY

This Appendix details all the observations obtained with SOLARC after the system was upgraded to have enough sensitivity to observe the emission lines.

Table A.1: Summary of observations.

Date	**UT Time**	**R[$R_\odot$]**	**PA[°]**	λ_c **[Å]**	t **[ms]**	**Frames**	**Coadds**	**Comments**
2016-07-29	20:56:43	1.28	130	10830	3000	7	20	Shifted
2016-07-29	21:45:43	1.28	130	10747	3000	7	20	Shifted
2016-07-29	22:52:17	1.25	90	10830	3000	7	20	Shifted
2016-07-29	23:42:22	1.25	90	10747	3000	7	20	Shifted
2016-07-30	00:46:52	1.25	280	10830	3000	7	20	Shifted
2016-07-30	01:36:09	1.25	280	10747	3000	7	20	Shifted
2016-07-30	02:37:20	1.30	320	10830	3000	1	50	Static
2016-07-28	20:51:12	1.25	90	14301	3000	1	10	Static
2016-07-28	21:09:17	1.25	90	14301	3000	1	50	Static
2016-07-28	21:27:37	1.25	70	14301	3000	1	50	Static
2016-07-28	21:47:58	1.25	50	14301	3000	1	50	Static
2016-07-28	22:07:46	1.25	110	14301	3000	1	50	Static
2016-07-28	22:42:46	1.25	110	14301	3000	1	100	Static
2016-07-28	23:02:17	1.28	130	14301	3000	1	50	Static
2016-07-28	23:22:16	1.3	230	14301	3000	1	50	Static
2016-07-28	23:40:44	1.3	250	14301	3000	1	50	Static
2016-07-29	00:05:40	1.3	270	14301	3000	1	50	Static
2016-07-29	00:34:32	1.25	290	14301	3000	1	50	Static
2016-07-29	00:59:19	1.25	310	14301	3000	1	50	Static
2016-07-29	01:27:13	1.23	130	10830	3000	1	20	Static
2016-07-29	01:44:57	1.23	130	10830	3000	1	50	Static
2016-07-29	01:55:00	1.28	110	10830	3000	1	20	Static
2016-07-29	02:03:27	1.28	90	10830	3000	1	20	Static
2016-07-29	02:21:11	1.28	280	10830	3000	1	20	Static
2016-07-29	02:29:06	1.28	280	10830	3000	1	20	Static
2016-07-29	02:37:35	1.28	300	10830	3000	1	20	Static
2016-07-29	02:45:51	1.28	320	10830	3000	1	20	Static
2016-06-21	01:23:19	1.27	80	10747	3000	1	5	Static
2016-06-21	01:26:05	1.24	90	10747	3000	1	5	Static
2016-06-21	01:29:28	1.24	90	10747	3000	1	5	Static
2016-06-21	01:32:28	1.24	80	10747	3000	1	5	Static
2016-06-21	01:35:19	1.24	70	10747	3000	1	5	Static
2016-06-21	01:38:06	1.24	60	10747	3000	1	5	Static
2016-06-21	01:56:48	1.24	60	14301	3000	1	5	Static
2016-06-21	02:00:20	1.26	70	14301	3000	1	5	Static

continued on next page...

Table A.1, *continued*

Date	UT Time	R[$R_\odot$]	PA[°]	λ_c [Å]	t [ms]	Frames	Coadds	Comments
2016-06-21	02:18:14	1.26	70	14301	3000	1	50	Static
2016-06-21	02:20:55	1.26	80	14301	3000	1	5	Static
2016-06-21	02:38:55	1.26	80	14301	3000	1	50	Static
2016-06-09	20:28:43	1.27	90	10747	3000	1	10	Static
2016-06-09	20:34:40	1.27	80	10747	3000	1	10	Static
2016-06-09	20:35:46	1.27	80	10747	3000	40	1	Static
2016-06-09	20:52:41	1.27	70	10747	3000	40	1	Static
2016-06-09	21:21:52	1.27	70	10747	3000	1	40	Static
2016-06-09	21:23:48	1.23	60	10747	3000	40	1	Static
2016-06-09	21:52:44	1.23	60	10747	3000	1	40	Static
2016-06-09	21:53:20	1.23	50	10747	3000	40	1	Static
2016-06-09	22:15:27	1.23	40	10747	3000	40	1	Static
2016-06-08	20:04:28	1.27	160	10830	3000	20	1	Static
2016-06-08	20:19:05	1.27	160	10830	3000	1	20	Static
2016-06-08	20:20:48	1.27	140	10830	3000	20	1	Static
2016-06-08	20:35:26	1.27	140	10830	3000	1	20	Static
2016-06-08	20:36:14	1.27	120	10830	3000	20	1	Static
2016-06-08	20:50:52	1.27	120	10830	3000	1	20	Static
2016-06-08	20:51:37	1.27	100	10830	3000	20	1	Static
2016-06-08	21:06:09	1.27	100	10830	3000	1	20	Static
2016-06-08	21:06:51	1.27	90	10830	3000	20	1	Static
2016-06-08	21:21:30	1.27	90	10830	3000	1	20	Static
2016-06-08	21:22:38	1.27	80	10830	3000	20	1	Static
2016-06-08	21:37:10	1.27	80	10830	3000	1	20	Static
2016-06-08	21:40:03	1.27	60	10830	3000	20	1	Static
2016-06-08	21:54:50	1.27	60	10830	3000	1	20	Static
2016-06-08	21:55:19	1.27	40	10830	3000	20	1	Static
2016-06-08	22:10:07	1.27	40	10830	3000	1	20	Static
2016-06-08	22:11:55	1.27	20	10830	3000	20	1	Static
2016-06-08	22:26:44	1.27	20	10830	3000	1	20	Static
2016-06-08	22:27:33	1.27	0	10830	3000	1	20	Static
2016-06-08	22:34:54	1.27	0	10830	3000	20	1	Static
2016-06-08	22:49:26	1.27	0	10830	3000	1	20	Static
2016-06-08	22:50:55	1.25	340	10830	3000	20	1	Static
2016-06-08	23:05:45	1.25	340	10830	3000	1	20	Static
2016-06-08	23:07:12	1.25	320	10830	3000	20	1	Static
2016-06-09	00:11:41	1.27	270	10830	3000	20	1	Static
2016-06-09	00:26:24	1.27	270	10830	3000	1	20	Static
2016-06-09	00:27:10	1.27	300	10830	3000	20	1	Static
2016-06-09	00:41:40	1.27	300	10830	3000	1	20	Static
2016-06-09	00:42:48	1.27	240	10830	3000	20	1	Static
2016-06-09	00:57:17	1.27	240	10830	3000	1	20	Static
2016-06-09	00:57:49	1.27	220	10830	3000	20	1	Static
2016-06-09	01:12:41	1.27	220	10830	3000	1	20	Static
2016-06-09	01:13:11	1.31	200	10830	3000	20	1	Static
2016-06-09	01:28:00	1.31	200	10830	3000	1	20	Static
2016-06-09	01:36:19	1.31	200	10747	200	20	1	Static

continued on next page...

Table A.1, *continued*

Date	UT Time	R[$R_\odot$]	PA[°]	λ_c [Å]	t [ms]	Frames	Coadds	Comments
2016-06-09	01:38:23	1.31	200	10747	3000	20	1	Static
2016-06-09	01:47:01	1.31	270	10747	3000	20	1	Static
2016-06-08	01:55:48	1.29	105	10830	200	100	1	Static
2016-06-08	02:05:41	1.29	105	10830	500	100	1	Static
2016-06-08	02:18:06	1.29	105	10830	1000	50	1	Static
2016-06-08	02:26:50	1.29	105	10830	2000	50	1	Static
2016-06-08	02:40:44	1.29	105	10830	3000	50	1	Static
2016-05-03	19:15:06	1.25	100	10747	3000	1	20	Static
2016-05-03	19:23:47	1.25	90	10747	3000	1	20	Static
2016-05-03	19:31:26	1.25	80	10747	3000	1	20	Static
2016-05-03	19:39:25	1.25	70	10747	3000	1	20	Static
2016-05-03	19:47:09	1.25	60	10747	3000	1	20	Static
2016-05-03	19:54:46	1.25	50	10747	3000	1	20	Static
2016-05-03	20:02:30	1.25	40	10747	3000	1	20	Static
2016-05-03	20:10:12	1.25	30	10747	3000	1	20	Static
2016-05-03	20:17:51	1.25	20	10747	3000	1	20	Static
2016-05-03	20:26:00	1.22	10	10747	3000	1	20	Static
2016-05-03	20:33:38	1.22	0	10747	3000	1	20	Static
2016-05-03	20:47:44	1.27	270	10747	3000	1	20	Static
2016-05-03	20:55:45	1.27	260	10747	3000	1	20	Static
2016-05-03	21:03:36	1.29	250	10747	3000	1	20	Static
2016-05-03	21:11:17	1.29	240	10747	3000	1	20	Static
2016-05-03	21:19:19	1.29	230	10747	3000	1	20	Static
2016-05-03	22:00:55	1.25	60	14301	3000	1	50	Static
2016-05-03	22:21:25	1.22	50	14301	3000	1	50	Static
2016-05-03	22:41:31	1.22	40	14301	3000	1	50	Static
2016-05-03	23:03:30	1.32	230	14301	3000	1	50	Static
2016-05-03	23:38:38	1.32	230	14301	3000	1	100	Static
2016-05-03	23:58:04	1.35	240	14301	3000	1	50	Static
2016-05-04	00:17:11	1.35	250	14301	3000	1	50	Static
2016-05-04	00:54:45	1.35	260	14301	3000	1	100	Static
2016-05-04	01:14:28	1.31	270	14301	3000	1	50	Static
2016-05-04	01:34:07	1.25	300	14301	3000	1	50	Static
2016-05-04	01:54:54	1.2	90	14301	3000	1	50	Static
2016-05-04	02:33:05	1.2	60	14301	3000	1	100	Static
2016-05-02	23:04:12	1.25	90	14301	3000	1	20	Static
2016-05-02	23:22:23	1.25	90	14301	3000	1	50	Static
2016-05-02	23:43:37	1.25	80	14301	3000	1	50	Static
2016-05-03	00:02:08	1.25	70	14301	3000	1	50	Static
2016-05-03	00:21:09	1.22	60	14301	3000	1	50	Static
2016-05-03	00:27:14	1.22	60	14301	3000	1	10	Static
2016-05-03	00:45:28	1.22	60	14301	3000	1	50	Static
2016-05-03	01:07:00	1.22	50	14301	3000	1	50	Static
2016-05-03	01:26:51	1.22	50	14301	3000	1	50	Static
2016-05-03	02:01:58	1.22	50	14301	3000	1	100	Static
2016-05-03	02:45:44	1.22	50	10747	3000	1	50	Static
2016-04-29	20:00:10	1.25	90	10830	100	100	1	Static

continued on next page...

Table A.1, *continued*

Date	UT Time	R[$R_\odot$]	PA[°]	λ_c [Å]	t [ms]	Frames	Coadds	Comments
2016-04-29	20:14:03	1.25	90	10830	100	1	100	Static
2016-04-29	20:20:44	1.25	90	10830	100	1	100	Static
2016-04-29	20:32:53	1.25	90	10830	100	1	200	Static
2016-04-29	20:52:35	1.25	90	10830	100	1	300	Static
2016-04-29	21:15:55	1.25	90	10830	100	1	400	Static
2016-04-29	21:45:19	1.25	90	10830	100	1	500	Static
2016-04-29	22:42:56	1.25	90	10830	100	1	1000	Static
2016-04-29	22:57:05	1.25	90	10830	4000	1	10	Static
2016-04-29	23:09:14	1.25	90	10830	3000	1	10	Static
2016-04-29	23:26:55	1.25	90	10830	3000	1	50	Static
2016-04-30	00:04:34	1.25	90	10830	3000	1	100	Static
2016-04-30	00:15:13	1.2	55	10830	3000	1	20	Static
2016-04-30	00:26:28	1.2	60	10830	3000	1	20	Static
2016-04-30	00:34:59	1.2	60	10747	3000	1	20	Static
2016-04-30	00:35:39	1.2	60	10747	3000	20	1	Static
2016-04-30	01:10:10	1.25	60	14301	3000	1	20	Static
2016-04-30	01:45:21	1.25	60	14301	3000	1	100	Static
2016-04-30	01:53:28	1.6	60	14301	3000	1	20	Static
2016-04-30	02:01:25	1.25	90	14301	3000	1	20	Static
2016-04-30	02:10:23	1.25	90	14301	3000	1	20	Static
2016-04-30	02:18:55	1.18	70	14301	3000	1	20	Static
2016-04-30	02:26:33	1.18	50	14301	3000	1	20	Static
2016-04-28	22:04:14	1.27	250	10747	200	1	10	Static
2016-04-28	22:06:18	1.27	250	10747	200	1	20	Static
2016-04-28	22:09:57	1.27	250	10747	200	1	50	Static
2016-04-28	22:17:48	1.27	250	10747	200	1	100	Static
2016-04-28	22:23:52	1.27	250	10830	200	1	10	Static
2016-04-28	22:25:57	1.27	250	10830	200	1	20	Static
2016-04-28	22:29:32	1.27	250	10830	200	1	50	Static
2016-04-28	22:37:01	1.27	250	10830	200	1	100	Static
2016-04-28	22:39:41	1.2	250	10830	200	1	20	Static
2016-04-28	22:43:37	1.2	250	10830	200	1	50	Static
2016-04-28	22:53:10	1.2	250	10830	200	1	100	Static
2016-04-28	23:00:55	1.2	250	10747	200	1	100	Static
2016-04-28	23:10:18	1.2	270	10747	200	1	100	Static
2016-04-28	23:17:23	1.2	270	10747	200	1	100	Static
2016-04-28	23:24:36	1.4	270	10747	200	1	100	Static
2016-04-28	23:31:50	1.4	270	10747	200	1	100	Static
2016-04-28	23:39:04	1.6	270	10747	200	1	100	Static
2016-04-28	23:45:49	1.6	270	10747	200	1	100	Static
2016-04-28	23:53:12	1.6	270	10830	200	1	100	Static
2016-04-29	00:01:50	1.23	290	10830	200	1	100	Static
2016-04-29	00:04:06	1.23	290	10830	200	100	1	Static
2016-04-29	00:38:18	1.4	270	10830	4000	10	1	Static,Sky calibration
2016-04-29	00:43:48	1.4	270	10830	3500	10	1	Static,Sky calibration
2016-04-29	00:44:56	1.4	270	10830	4500	10	1	Static,Sky calibration
2016-04-29	00:46:23	1.4	270	10830	5000	10	1	Static,Sky calibration

continued on next page...

Table A.1, *continued*

Date	UT Time	R[$R_\odot$]	PA[°]	λ_c [Å]	t [ms]	Frames	Coadds	Comments
2016-04-29	00:48:27	1.4	270	10830	3000	10	1	Static,Sky calibration
2016-04-29	00:49:26	1.4	270	10830	2500	10	1	Static,Sky calibration
2016-04-29	00:50:23	1.4	270	10830	2000	10	1	Static,Sky calibration
2016-04-29	00:51:53	1.4	270	10830	1500	10	1	Static,Sky calibration
2016-04-29	00:52:27	1.4	270	10830	1000	10	1	Static,Sky calibration
2016-04-29	00:57:48	1.4	270	10830	500	10	1	Static,Sky calibration
2016-04-29	00:58:30	1.4	270	10830	200	10	1	Static,Sky calibration
2016-04-29	01:53:43	1.23	90	10830	20	1	100	Static
2016-04-29	02:00:05	1.4	90	10830	20	1	100	Static
2016-04-29	02:05:37	1.4	90	10830	20	1	100	Static
2016-04-29	02:12:20	1.25	30	10830	20	1	100	Static
2016-04-29	02:18:03	1.25	30	10830	20	1	100	Static
2016-04-29	02:25:32	1.25	50	10830	20	1	100	Static
2016-04-29	02:31:04	1.25	50	10830	20	1	100	Static
2016-04-29	02:46:22	1.25	50	10830	1000	1	100	Static
2016-04-27	23:47:28	1.25	90	10830	200	1	10	Static
2016-04-27	23:48:57	1.25	90	10830	200	1	10	Static
2016-04-27	23:57:19	1.25	90	10830	200	1	100	Static
2016-04-28	00:04:22	1.25	90	10830	200	1	100	Static
2016-04-28	00:12:21	1.25	80	10830	200	1	100	Static
2016-04-28	00:19:42	1.25	80	10830	200	1	100	Static
2016-04-28	00:44:03	1.25	40	10830	200	1	100	Static
2016-04-28	00:53:24	1.25	30	10830	200	1	100	Static
2016-04-28	01:00:44	1.25	30	10830	200	1	100	Static
2016-04-28	01:10:40	1.2	10	10830	200	1	100	Static
2016-04-28	01:18:49	1.4	90	10830	200	1	100	Static
2016-04-28	01:25:43	1.4	90	10830	200	1	100	Static
2016-04-28	01:34:15	1.6	90	10830	200	1	100	Static
2016-04-28	01:41:30	1.8	90	10830	200	1	100	Static
2016-04-28	01:48:23	1.8	90	10830	200	1	100	Static
2016-04-28	01:58:19	1.27	270	10830	200	1	100	Static
2016-04-28	02:20:01	1.3	270	10830	200	1	100	Static
2016-04-28	02:27:16	1.5	270	10830	200	1	100	Static
2016-04-28	02:33:58	1.5	270	10830	200	1	100	Static
2016-04-22	20:00:20	1.23	85	10747	1000	50	1	Static
2016-04-22	20:16:39	1.23	85	10747	1000	1	50	Static
2016-04-22	20:31:37	1.23	85	10747	1000	1	100	Static
2016-04-22	21:04:25	1.23	85	10830	1000	1	100	Static
2016-04-22	21:05:09	1.23	85	10830	1000	1	100	Static
2016-04-22	21:19:51	1.23	85	10830	1000	100	1	Static
2016-04-22	21:37:08	1.23	85	10830	1000	100	1	Static
2016-04-22	22:53:10	1.3	210	10830	1000	100	1	Static
2016-04-22	23:12:12	1.3	220	10830	1000	1	10	Static
2016-04-22	23:22:06	1.3	220	10830	1000	1	50	Static
2016-04-22	23:24:55	1.3	225	10830	1000	1	10	Static
2016-04-22	23:52:37	1.3	225	10830	1000	1	20	Static
2016-04-23	00:07:28	1.3	225	10830	1000	1	100	Static

continued on next page...

Table A.1, *continued*

Date	UT Time	R[$R_\odot$]	PA[°]	λ_c [Å]	t [ms]	Frames	Coadds	Comments
2016-04-23	00:07:50	1.3	225	10830	1000	100	1	Static
2016-04-23	00:25:43	1.3	225	10830	1000	100	1	Static
2016-04-23	00:43:09	1.3	225	10830	1000	100	1	Static
2016-04-23	01:05:50	1.3	255	10830	1000	1	10	Static
2016-04-23	01:09:33	1.3	255	10830	1000	1	20	Static
2016-04-23	01:10:07	1.3	255	10830	1000	100	1	Static
2016-04-21	21:54:24	1.25	250	10747	1000	10	1	Static
2016-04-21	21:58:08	1.25	250	10747	1000	1	10	Static
2016-04-21	22:05:36	1.25	250	10747	1000	1	50	Static
2016-04-21	22:07:01	1.25	250	10830	1000	10	1	Static
2016-04-21	22:11:21	1.25	250	10830	1000	1	10	Static
2016-04-21	22:19:11	1.25	250	10830	1000	1	50	Static
2016-04-21	22:34:36	1.25	250	10830	1000	1	100	Static
2016-04-21	22:50:59	1.25	250	10830	1000	1	100	Static
2016-04-21	23:05:43	1.25	250	10830	1000	1	100	Static
2016-04-21	23:16:02	1.27	250	14301	1000	10	1	Static
2016-04-21	23:20:16	1.27	250	14301	1000	1	10	Static
2016-04-21	23:23:51	1.27	250	14301	1000	1	20	Static
2016-04-21	23:25:06	1.27	250	14301	1000	10	1	Static
2016-04-21	23:27:17	1.3	250	14301	1000	10	1	Static
2016-04-21	23:32:00	1.3	250	14301	1000	1	20	Static
2016-04-21	23:40:10	1.3	250	14301	1000	1	50	Static
2016-04-21	23:45:50	1.27	260	14301	1000	10	1	Static
2016-04-21	23:49:10	1.27	260	14301	1000	1	10	Static
2016-04-21	23:57:12	1.27	260	14301	1000	1	50	Static
2016-04-22	00:15:15	1.27	260	10747	1000	1	50	Static
2016-04-22	00:16:12	1.27	260	10747	1000	50	1	Static
2016-04-22	00:34:08	1.27	260	10830	1000	1	50	Static
2016-04-22	00:34:46	1.27	260	10830	1000	1	50	Static
2016-04-22	00:42:26	1.27	260	10830	1000	50	1	Static
2016-04-22	01:13:28	1.27	260	10830	1000	1	100	Static
2016-04-22	01:45:19	1.27	260	10830	1000	1	200	Static
2016-04-22	01:52:34	1.23	78	10830	1000	1	10	Static
2016-04-22	01:53:09	1.23	78	10830	1000	50	1	Static
2016-04-14	20:10:40	1.27	65	10747	1000	1	10	Static
2016-04-14	20:16:54	1.27	65	10747	1000	1	40	Static
2016-04-14	20:31:51	1.27	65	10747	1000	1	100	Static
2016-04-14	20:40:06	1.27	65	10747	2000	1	10	Static
2016-04-14	20:45:39	1.27	65	10747	2000	1	20	Static
2016-04-14	20:58:59	1.27	65	10747	2000	1	50	Static
2016-04-14	21:03:09	1.27	65	10830	2000	1	10	Static
2016-04-14	21:08:29	1.27	65	10830	2000	1	20	Static
2016-04-14	21:34:07	1.27	65	10830	1000	1	20	Static
2016-04-14	21:42:18	1.27	65	10830	1000	1	50	Static
2016-04-13	22:02:42	1.23	50	10747	2000	1	50	Static
2016-04-13	22:09:03	1.23	50	10747	1000	1	10	Static
2016-04-13	22:12:08	1.23	50	10747	1000	1	20	Static

continued on next page...

Table A.1, *continued*

Date	UT Time	R[$R_\odot$]	PA[°]	λ_c [Å]	t [ms]	Frames	Coadds	Comments
2016-04-13	22:16:16	1.23	50	10747	1000	1	20	Static
2016-04-13	22:31:37	1.23	50	10747	1000	1	100	Static
2016-04-13	22:42:47	1.23	50	10747	2000	1	10	Static
2016-04-13	22:54:29	1.23	50	10747	2000	1	10	Static
2016-04-13	23:00:01	1.23	44	10747	2000	1	10	Static
2016-04-13	23:05:09	1.23	44	10747	2000	1	20	Static
2016-04-12	20:54:00	1.31	40	14301	1000	1	10	Static
2016-04-12	21:02:30	1.31	40	14301	1000	1	50	Static
2016-04-12	21:13:38	1.29	50	14301	1000	1	50	Static
2016-04-12	21:17:03	1.29	60	14301	1000	100	1	Static
2016-04-12	21:40:55	1.29	60	14301	1000	1	40	Static
2016-04-12	21:56:40	1.29	60	14301	1000	1	100	Static
2016-04-12	22:07:33	1.29	60	14301	2000	1	20	Static
2016-04-12	22:20:21	1.29	60	14301	2000	1	50	Static
2016-04-12	22:24:21	1.29	70	14301	2000	1	10	Static
2016-04-12	22:37:36	1.29	70	14301	2000	1	50	Static
2016-04-12	23:04:09	1.29	70	14301	2000	1	100	Static
2016-04-12	23:38:09	1.29	70	14301	2000	1	10	Static
2016-04-12	23:53:03	1.29	70	14301	2000	1	50	Static
2016-04-13	00:18:37	1.29	70	14301	2000	1	100	Static
2016-04-13	00:26:54	1.27	280	14301	2000	10	1	Static
2016-04-13	00:35:33	1.27	280	14301	2000	1	20	Static
2016-04-13	00:48:17	1.27	280	14301	2000	1	50	Static
2016-04-13	00:49:23	1.27	280	14301	2000	100	1	Static
2016-04-13	01:19:56	1.27	270	14301	2000	1	10	Static
2016-04-13	01:33:59	1.27	270	14301	2000	1	50	Static
2016-04-13	01:37:48	1.27	260	14301	2000	1	10	Static
2016-04-13	01:50:36	1.27	260	14301	2000	1	50	Static
2016-04-13	02:02:47	1.27	90	14301	1000	1	20	Static
2016-04-13	02:17:51	1.27	90	14301	1000	1	100	Static
2016-04-11	21:45:24	1.25	80	14301	1000	1	10	Static
2016-04-11	21:53:21	1.25	80	14301	1000	1	20	Static
2016-04-11	22:02:14	1.25	80	14301	1000	1	50	Static
2016-04-11	22:06:11	1.25	70	14301	1000	1	10	Static
2016-04-11	22:14:59	1.25	70	14301	1000	1	50	Static
2016-04-11	22:39:27	1.25	70	14301	1000	1	10	Static
2016-04-11	22:41:39	1.25	60	14301	1000	1	10	Static
2016-04-11	22:45:05	1.25	60	14301	1000	1	20	Static
2016-03-31	20:16:30	1.25	90	14301	1000	1	10	Static
2016-03-31	20:20:18	1.25	90	14301	1000	1	20	Static
2016-03-31	20:25:42	1.25	90	14301	1000	1	30	Static
2016-03-31	20:33:13	1.25	90	14301	1000	1	40	Static
2016-03-31	20:41:15	1.25	90	14301	1000	1	50	Static
2016-03-31	20:41:49	1.25	90	14301	1000	50	1	Static
2016-03-31	20:59:11	1.25	80	14301	1000	1	10	Static
2016-03-31	21:06:52	1.25	80	14301	1000	1	50	Static
2016-03-31	21:22:04	1.25	80	14301	1000	1	100	Static

continued on next page...

Table A.1, *continued*

Date	UT Time	R[$R_\odot$]	PA[°]	λ_c [Å]	t [ms]	Frames	Coadds	Comments
2016-03-31	21:25:23	1.25	70	14301	1000	1	10	Static
2016-03-31	21:33:08	1.25	70	14301	1000	1	50	Static
2016-03-31	21:48:08	1.25	70	14301	1000	1	100	Static
2016-03-31	21:50:54	1.25	60	14301	1000	1	10	Static
2016-03-31	22:00:16	1.25	60	14301	1000	1	50	Static
2016-03-31	22:03:12	1.25	50	14301	1000	1	10	Static
2016-03-31	22:12:04	1.25	50	14301	1000	1	50	Static
2016-03-31	22:20:42	1.25	100	14301	1000	1	10	Static
2016-03-31	22:28:17	1.25	100	14301	1000	1	50	Static
2016-03-31	22:31:57	1.25	110	14301	1000	1	10	Static
2016-03-31	22:35:15	1.25	110	14301	1000	1	20	Static
2016-03-31	22:42:51	1.25	110	14301	1000	1	50	Static
2016-03-31	22:47:11	1.25	120	14301	1000	1	10	Static
2016-03-31	22:51:14	1.25	120	14301	1000	1	20	Static
2016-03-31	22:58:47	1.25	120	14301	1000	1	50	Static
2016-03-31	23:14:51	1.25	120	14301	1000	1	100	Static
2016-03-31	23:28:15	1.25	140	14301	1000	1	40	Static
2016-03-31	23:30:43	1.25	140	14301	1000	1	10	Static
2016-03-30	22:25:47	1.25	260	10747	1000	1	10	Static
2016-03-30	22:29:28	1.25	260	10747	1000	1	20	Static
2016-03-30	22:34:02	1.25	260	10747	1000	1	30	Static
2016-03-30	22:35:56	1.25	260	10747	1000	7	1	Static
2016-03-30	22:43:40	1.25	260	10747	1000	1	40	Static
2016-03-30	22:51:34	1.25	260	10747	1000	1	50	Static
2016-03-30	22:52:14	1.25	260	10747	1000	50	1	Static
2016-03-30	23:09:08	1.25	260	10830	1000	1	10	Static
2016-03-30	23:12:31	1.25	260	10830	1000	1	20	Static
2016-03-30	23:18:17	1.25	260	10830	1000	1	30	Static
2016-03-30	23:47:20	1.27	250	10747	1000	1	10	Static
2016-03-30	23:50:32	1.27	250	10747	1000	1	20	Static
2016-03-30	23:55:11	1.27	250	10747	1000	1	30	Static
2016-03-31	00:02:52	1.27	250	10747	1000	1	50	Static
2016-03-31	00:05:11	1.27	250	10830	1000	1	10	Static
2016-03-31	00:10:31	1.27	235	10830	1000	1	10	Static
2016-03-31	00:12:40	1.27	235	10747	1000	1	10	Static
2016-03-31	00:14:19	1.27	235	10747	1000	1	10	Static
2016-03-31	00:19:27	1.3	100	10747	1000	1	10	Static
2016-03-31	00:25:51	1.3	100	10747	1000	1	40	Static
2016-03-31	00:28:19	1.3	100	10830	1000	1	10	Static
2016-03-31	00:33:26	1.27	90	10830	1000	1	10	Static
2016-03-31	00:39:46	1.27	90	10830	1000	1	40	Static
2016-03-31	00:43:00	1.27	90	10747	1000	1	10	Static
2016-03-31	00:51:30	1.27	90	10747	1000	1	40	Static
2016-03-31	00:54:49	1.29	80	10747	1000	1	10	Static
2016-03-31	01:00:54	1.29	80	10747	1000	1	40	Static
2016-03-31	01:01:23	1.29	80	10747	1000	50	1	Static
2016-03-31	01:12:47	1.29	80	10830	1000	1	10	Static

continued on next page...

Table A.1, *continued*

Date	UT Time	R[$R_\odot$]	PA[°]	λ_c [Å]	t [ms]	Frames	Coadds	Comments
2016-03-31	01:15:08	1.29	80	10830	1000	1	10	Static
2016-03-31	01:21:23	1.29	80	10830	1000	1	40	Static
2016-03-31	01:22:13	1.29	80	10830	1000	20	1	Static
2016-03-31	01:27:55	1.29	70	10830	1000	1	10	Static
2016-03-31	01:31:20	1.29	70	10830	1000	1	20	Static
2016-03-31	01:37:43	1.29	70	10830	1000	1	40	Static
2016-03-31	01:40:24	1.29	70	10830	1000	1	10	Static
2016-03-31	01:42:14	1.29	70	10747	1000	1	10	Static
2016-03-31	01:48:25	1.29	70	10747	1000	1	40	Static
2016-03-31	01:57:17	1.29	60	10747	1000	1	40	Static
2016-03-31	01:59:41	1.29	60	10830	1000	1	10	Static
2016-03-31	02:07:42	1.29	60	10830	1000	1	40	Static
2016-03-29	21:59:23	1.27	75	10747	1000	7	1	Static
2016-03-29	22:01:15	1.27	90	10747	1000	7	1	Static
2016-03-29	22:04:20	1.27	90	10747	1000	1	10	Static
2016-03-29	22:46:07	1.23	90	10747	1000	1	5	Static
2016-03-29	22:47:46	1.23	90	10747	1000	1	10	Static
2016-03-29	22:50:36	1.25	80	10747	1000	1	10	Static
2016-03-29	22:55:02	1.25	80	10747	1000	1	20	Static
2016-03-29	22:57:48	1.27	70	10747	1000	1	10	Static
2016-03-29	23:00:39	1.27	70	10747	1000	1	10	Static
2016-03-29	23:03:59	1.27	70	10747	1000	1	20	Static
2016-03-29	23:13:46	1.27	100	10747	1000	1	20	Static
2016-03-29	23:21:26	1.23	260	10747	1000	1	5	Static
2016-03-29	23:24:40	1.23	260	10747	1000	1	20	Static
2016-03-29	23:25:06	1.23	260	10747	1000	40	1	Static
2016-03-29	23:34:40	1.23	270	10747	1000	1	10	Static
2016-03-29	23:37:11	1.23	270	10747	1000	50	1	Static
2016-03-29	23:53:25	1.21	262	10747	1000	1	5	Static
2016-03-12	00:57:29	1.24	90	10747	1000	1	5	Static
2016-03-12	00:59:54	1.24	90	10747	1000	1	10	Static
2016-03-12	01:01:36	1.24	90	10747	1000	20	1	Static
2016-03-12	01:10:56	1.24	90	10747	1000	1	10	Static
2016-03-12	01:13:44	1.24	90	10747	1000	1	10	Static
2016-03-12	01:15:54	1.24	80	10747	1000	1	5	Static
2016-03-12	01:19:09	1.24	80	10747	1000	1	10	Static
2016-03-12	01:21:28	1.24	90	10747	1000	1	10	Static
2016-03-12	01:25:07	1.24	90	10747	1000	1	20	Static
2016-03-12	01:30:31	1.17	270	10747	1000	1	5	Static
2016-03-12	01:32:39	1.17	270	10747	1000	1	10	Static
2016-03-12	01:35:07	1.17	280	10747	1000	1	10	Static
2016-03-12	01:37:32	1.2	290	10747	1000	1	10	Static
2016-03-12	01:39:39	1.2	300	10747	1000	1	10	Static
2016-03-12	01:43:02	1.18	260	10747	1000	1	10	Static
2016-03-12	01:44:57	1.18	260	10747	1000	1	10	Static
2016-03-12	01:47:34	1.18	250	10747	1000	1	10	Static
2016-03-12	01:53:34	1.18	265	10747	1000	1	10	Static

continued on next page...

Table A.1, *continued*

Date	**UT Time**	**R[$R_\odot$]**	**PA[°]**	λ_c **[Å]**	t **[ms]**	**Frames**	**Coadds**	**Comments**
2016-03-12	02:09:55	1.18	265	14301	1000	1	10	Static
2016-03-12	02:14:23	1.18	265	14301	1000	1	20	Static
2016-03-12	02:21:20	1.16	260	14301	1000	1	20	Static
2016-03-12	02:23:00	1.9	260	14301	1000	20	1	Static
2016-03-11	00:39:59	1.35	90	14301	1000	1	5	Static
2016-03-11	00:47:07	1.35	80	10747	1000	1	5	Static
2016-03-11	00:49:27	1.35	70	10747	1000	1	5	Static
2016-03-11	01:02:54	1.29	90	10830	1000	1	5	Static
2016-03-11	01:06:32	1.29	90	10830	1000	1	5	Static
2016-03-11	01:08:27	1.29	70	10747	1000	1	5	Static
2016-03-11	01:13:00	1.17	270	10747	1000	1	5	Static
2016-03-11	01:13:54	1.17	270	10747	1000	1	5	Static
2016-03-11	01:16:17	1.17	270	10747	1000	1	10	Static
2016-03-11	01:18:49	1.17	270	10747	1000	1	10	Static

APPENDIX B
DATA REDUCTION PIPELINE FOR SOLARC

This Appendix provides an overview of the data reduction pipeline I constructed using Python v2.7. The tools are assembled into a user-friendly graphical user interface (GUI) to facilitate easy viewing and selection of data collected during the course of an observing day.

Work on the GUI is ongoing and features still to be added include

- Interaction with fibers after extraction from the images and manual selection and exclusion of fibers from the 2D fiber images that are obviously nonphysical.
- Adding more physically meaningful units to the plots.
- Adding tool tips and help guides to help users with the GUI.

B.1 Main GUI operation

The Maui GUI window allows the user overview over the current selected data directory and all the files inside that directory as well as the ability to select files, perform data reduction, gain calibration and fiber extraction (Figure B.1).

1. At the top are two menus that control interaction with files outside the GUI (Figure B.2). The functions in each menu are:
    - "Save GUI state" saves the current selected variables in the GUI like data directories and file settings so analysis can be started from the same location when the GUI is started again.
    - "Save analysis state" will be phased out in future instances. Currently it saves the current analysis point in a format that can accessed from an external Python routine that mimics the functionality of the GUI.

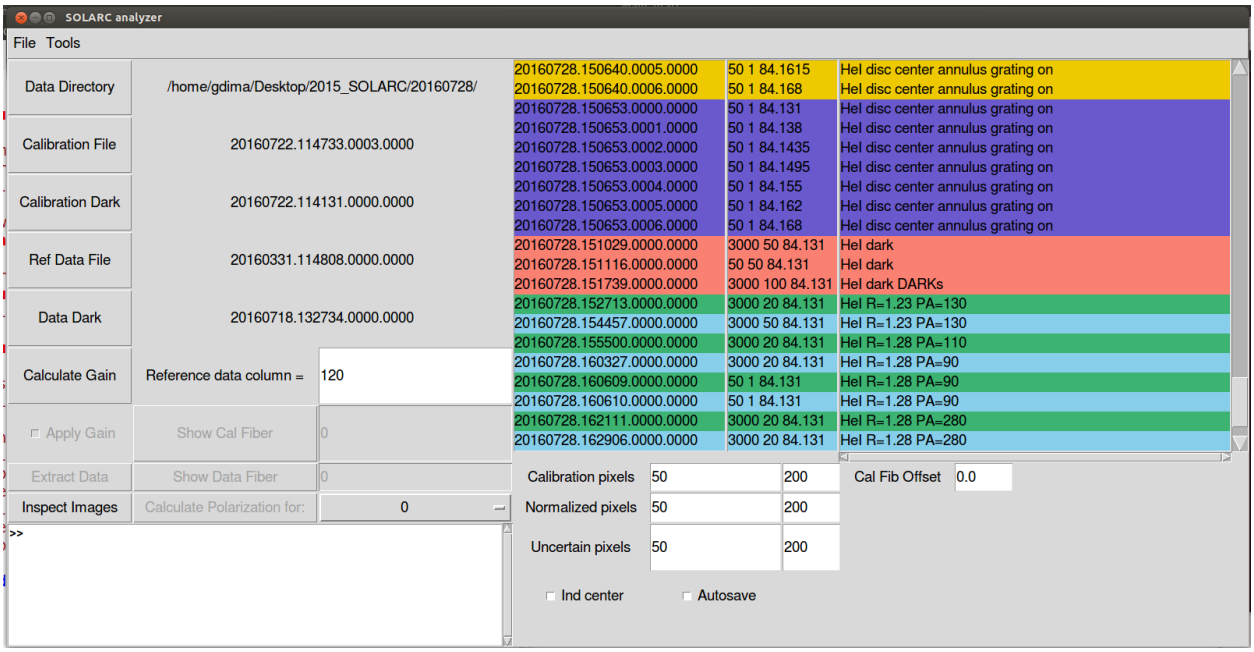

Figure B.1: Screenshot of the main GUI window showing all the elements discussed in the text.

- "Save extracted data arrays" saves all the extracted fiber arrays and calibration files to a file that can be manipulated by external routines or by GUI later in time.
- "Load extracted data arrays" can load and read the information in the file saved by "Save extracted data arrays"
- "Exit" will exit the GUI without saving.
- "Inspect folder" performs a manual review of the current "Data Directory" to find and load all valid SOLARC data files into the GUI listboxes. The information is stored inside an intermediate text file inside each folder called "file_descriptions.txt".
- "Modify file headers" enable manual modification of the comments in the data headers.

2. On the left side of the GUI are a range of buttons for selecting files to analyze the data as well as textboxes to show the files currently being used (Figure B.3). Some of the buttons are not immediately available (e.g. Show Cal Fiber, Extract data) since they rely of previous information being computed first (e.g. Calculate Gain).

   In summary the buttons perform the following functions:

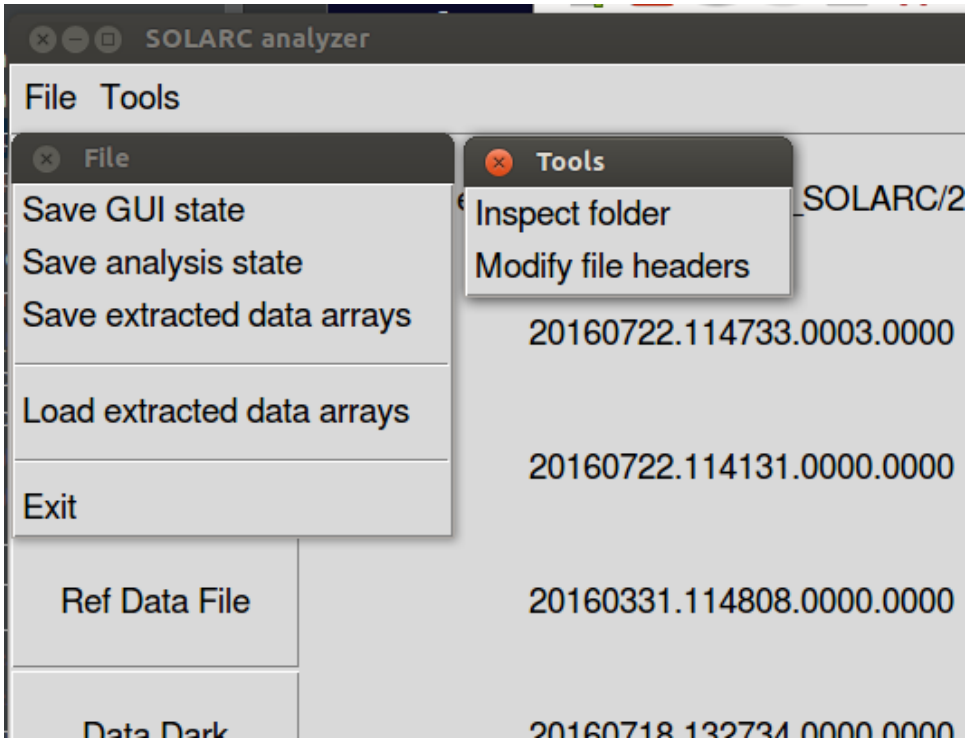

Figure B.2: Screen-shot of menu options (description in text).

- "Data Directory" selects the desired work directory shown to the right of the button.
- "Calibration File" selects the file for one of the disc center calibration files in a shifted sequence.
- "Calibration Dark" selects the dark file corresponding to the calibration exposure time.
- "Ref Data File" selects the science data exposure which may also contain polarized sequences.
- "Data Dark" selects the dark file corresponding to the data exposure time.
- "Calculate Gain" computes the column shifted gain map based on the calibration file and using the value entered under "Reference data column" as a reference (see Chapter 5). As the gain is calculated a new window will appear (Figure B.4) that provides an overview of the gain calculation process as well as calculate the tilt of the spectra across the array and the central pixel rows where the fibers are located.
- "Extract Data" performs the dark correction of the selected data exposures and extracts

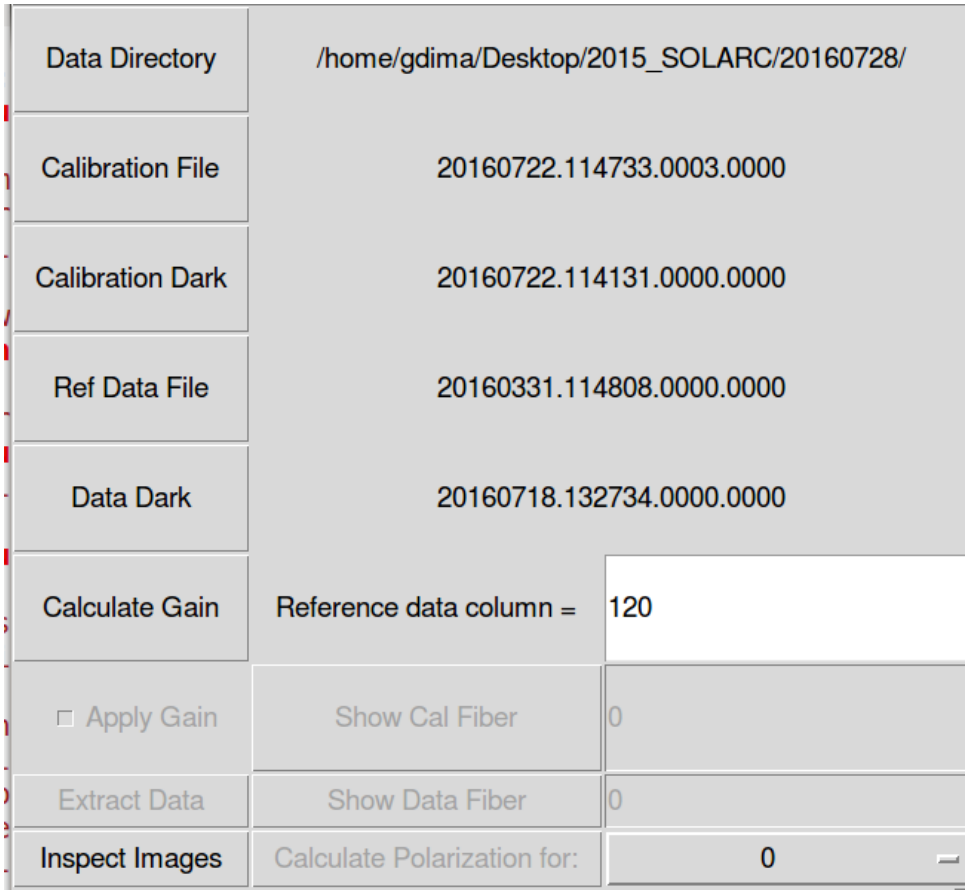

Figure B.3: Screen-shot of functional buttons (description in text).

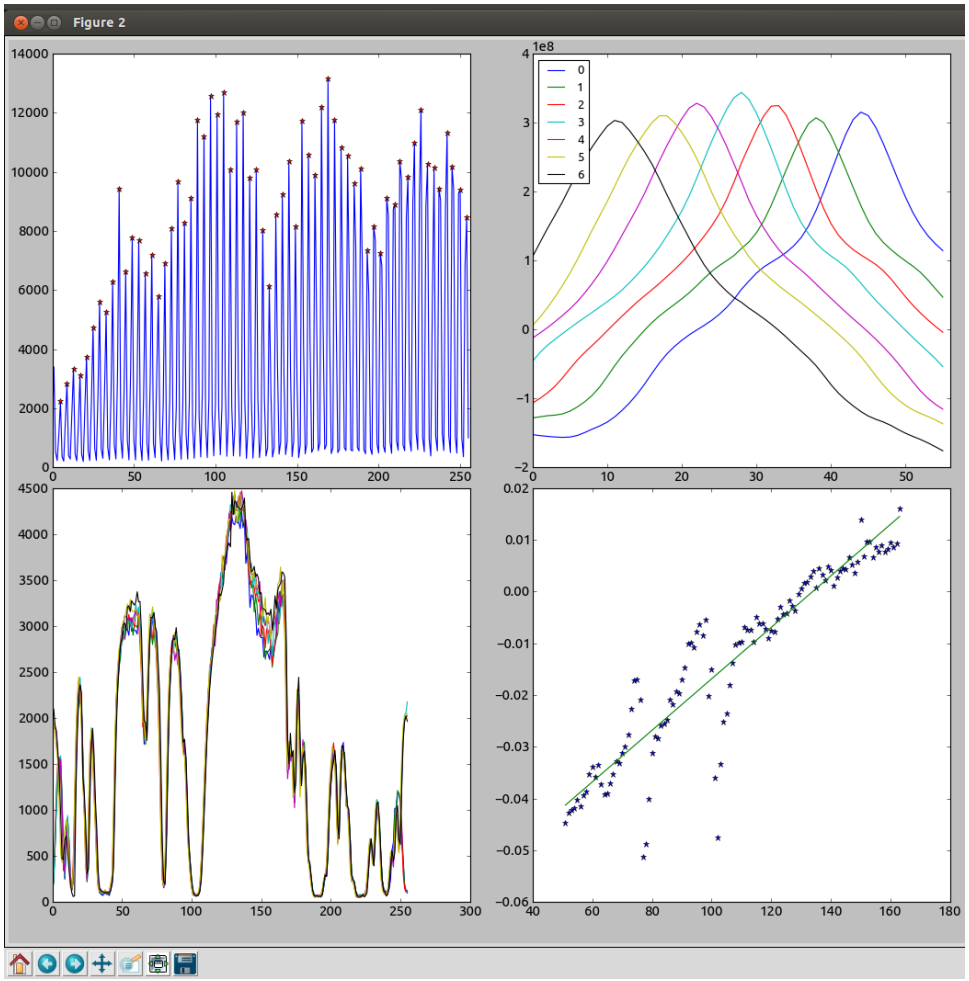

Figure B.4: Screen-shot of the external window that calculates the gain using the grating shift method. The top left plot shows the determination of central fiber rows at the reference column and provides a sanity check that the routine is locating the fiber positions correctly. The bottom right plot shows the fit through the fiber tilt across the array. As this is a SiX1430 spectral region (bottom left plot) parts of the spectra have steep drops in intensity.

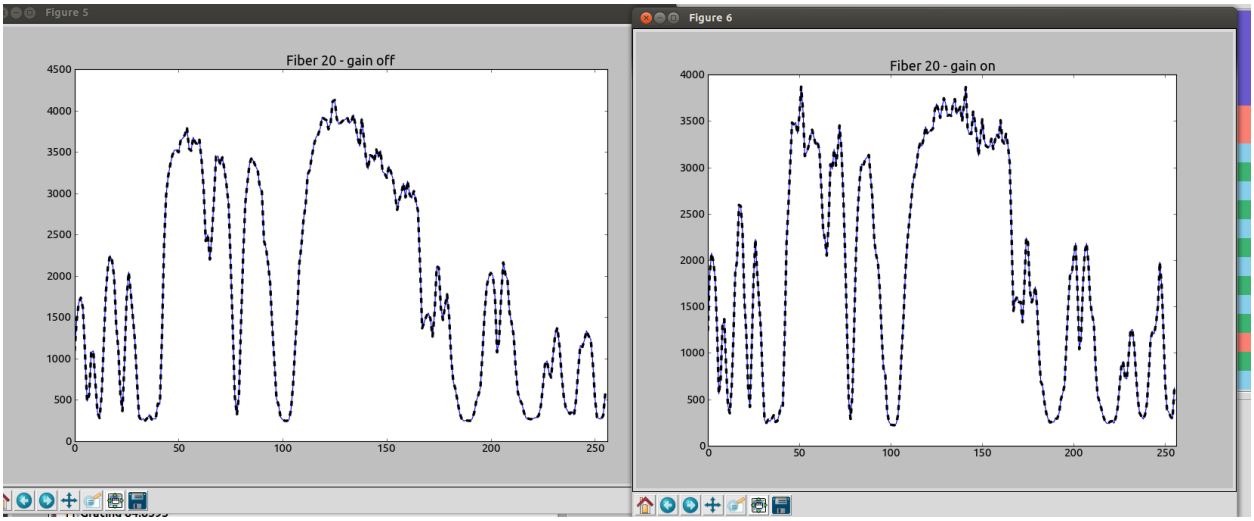

Figure B.5: Examples of the same extracted data fiber 20 with (left) and without (right) the gain correction applied. Some differences are apparent but it is not clear how good the correction is.

the I, Q, U spectra.

- "Show Cal Fiber" and "Show Data Fiber" provide a quick way to check how a fiber looks like once it is extracted. This is combine with the the "Apply Gain" check-button to determine is gain application is desired (Figure B.5)
- "Inspect Images" will open an external tool that enables the analysis of the selected data image without any extraction (Figure B.6). This is very useful for quick visual inspection of a data file.

3. To the right are coordinated listsboxes (Figure B.7) that show information about valid data files located in the present directory.

   - The first listbox shows the file names which are date and time-stamped automatically when recorded at SOLARC. Each file is labeled with the [date].[HST time].[sequence number].[index in a sequence].
   - The middle listbox indicates: exposure time (in ms), number of internally co-added exposures, position angle of the diffraction grating.
   - The right listbox shows the observer comments in the each file header. These can be modified manually using the GUI in case files need to be discarded or are mislabeled.

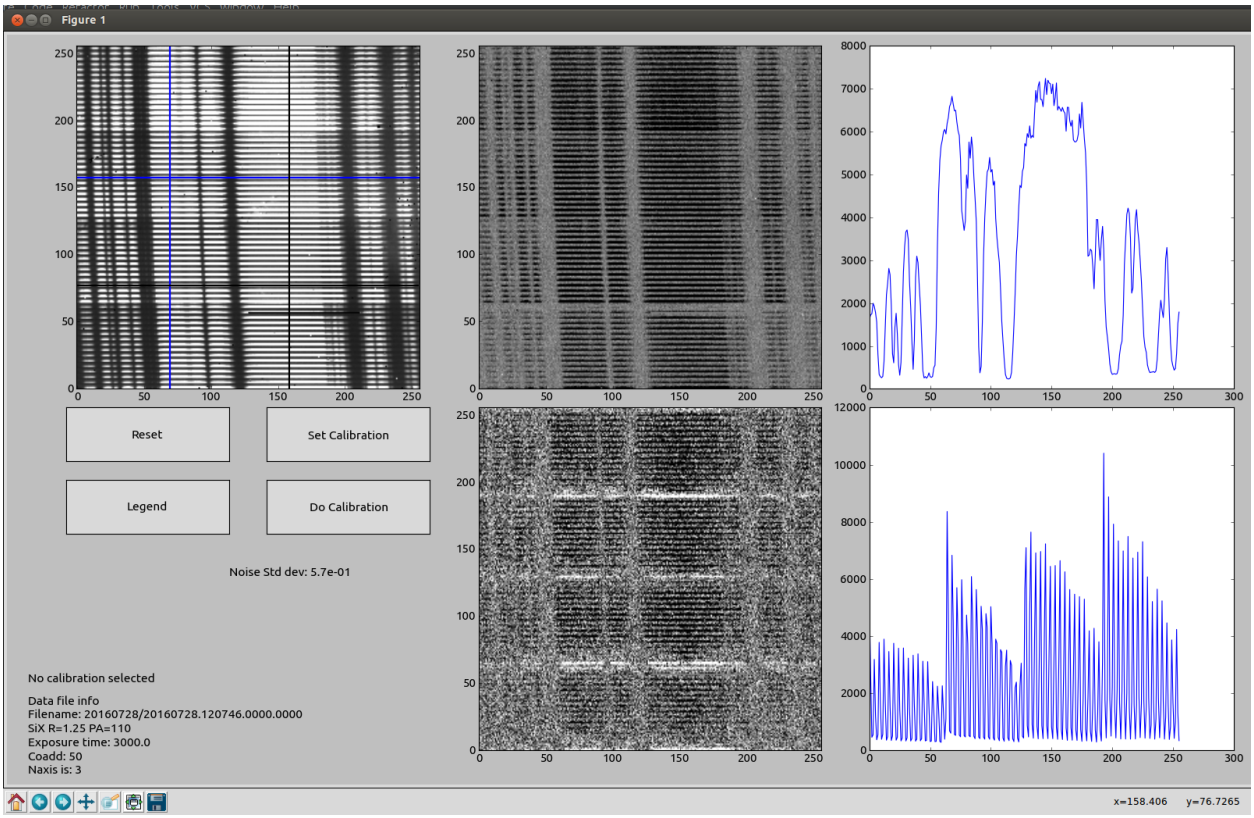

Figure B.6: Screen-shot of the custom imager for visualizing I, Q, U images from the same data file. It is also possible to visualize columns or rows of pixels to see if emission lines are visible.

The varying color scheme uses the presence of keywords in the comments to separate out files that contain calibration, dark or data exposures so that users can more easily sort through the available files.

- Below the listboxes are entry boxes used when extracting data from each data file. The pixel entryboxes are not currently used for anything but they are meant to be used at some point for custom fitting to specific pixel ranges.
- The checkbox "Ind center" decides if the central fibers for each exposures should be calculated using the data file, rather than the locations determined from using the calibration exposures. This is sometimes necessary if the fibers shifted across the array during the day compared to the calibrations.

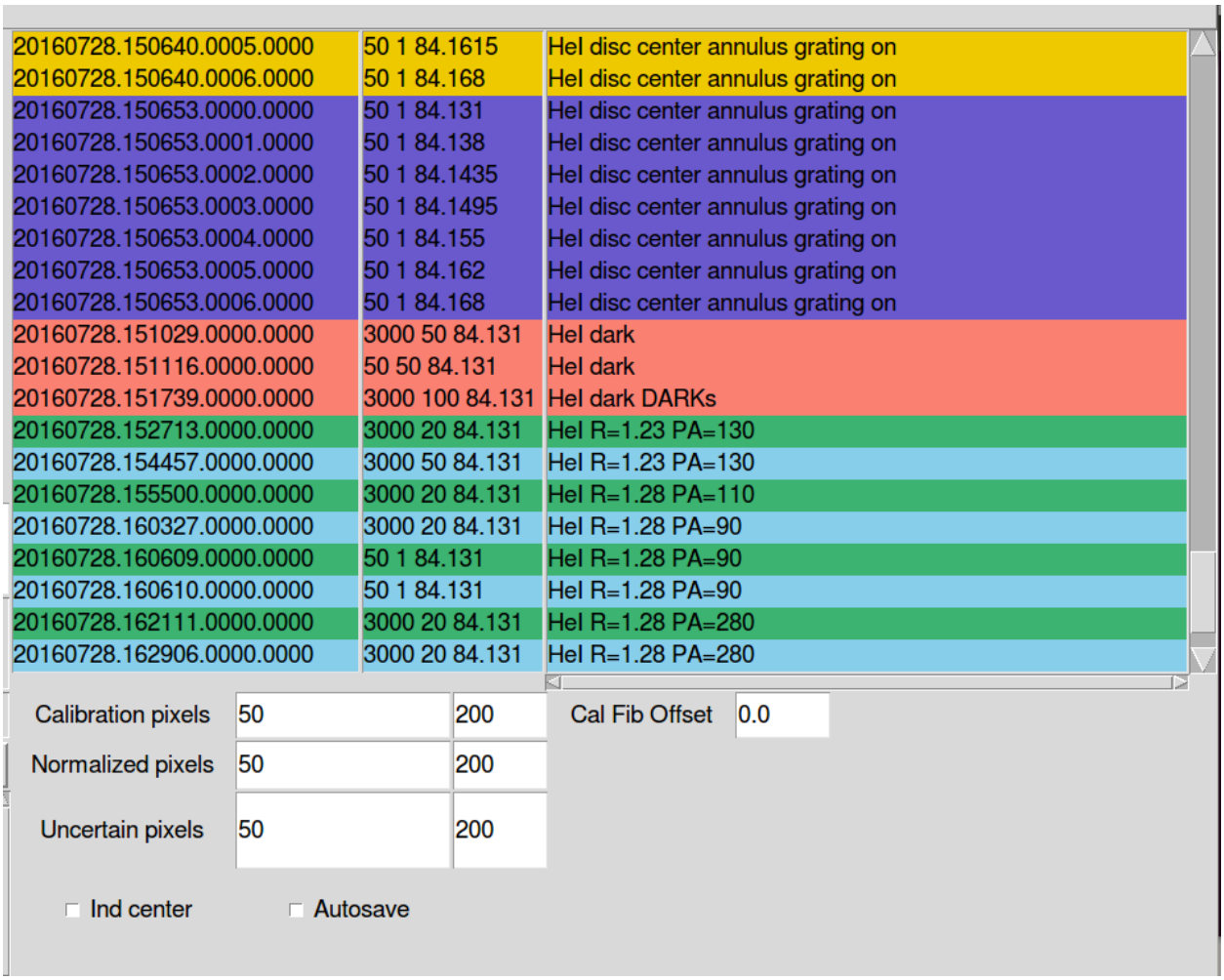

Figure B.7: The listboxes that display filenames (left), exposure times and grating positions (center) as well as observer comments present in the header of each file (right).